



**Max-Planck-Institut für Metallforschung
Stuttgart**

**The effect of substrate orientation on the kinetics and
thermodynamics of initial oxide-film growth on metals**

Friederike Reichel

Dissertation
an der
Universität Stuttgart

Bericht Nr. 209
November 2007

The effect of substrate orientation on the kinetics and thermodynamics of initial oxide-film growth on metals

Von der Fakultät Chemie der Universität Stuttgart
zur Erlangung der Würde eines Doktors der Naturwissenschaften (Dr. rer. nat.)
genehmigte Abhandlung

vorgelegt von

Friederike Reichel

aus Aachen

Hauptberichter:	Prof. Dr. Ir. E. J. Mittemeijer
Mitberichter:	Prof. Dr. Dr. h. c. M. Rühle
Prüfer:	Prof. Dr. F. Aldinger
Prüfungsvorsitzender:	Prof. Dr. H. Bertagnolli

Tag der Einreichung:	28.09.2007
Tag der mündlichen Prüfung:	19.11.2007

MAX-PLANCK-INSTITUT FÜR METALLFORSCHUNG STUTTGART
INSTITUT FÜR METALLKUNDE DER UNIVERSITÄT STUTTGART

Stuttgart 2007

Contents

1. General Introduction	7
1.1. The initial oxidation of bare metals	8
1.1.1. Kinetics.....	8
1.1.2. Thermodynamics.....	9
1.2. Thin oxide films on bare Al single-crystals.....	10
1.2.1. Thermal oxidation of bare Al substrates	10
1.2.2. Modifications of alumina	11
1.2.3. Applications of thin Al ₂ O ₃ films.....	11
1.3. Methods of characterization	12
1.3.1. Angle-Resolved X-ray Photoelectron Spectroscopy (AR-XPS).....	12
1.3.2. Real-time In-situ Spectroscopic Ellipsometry (RISE).....	14
1.3.3. Low Energy Electron Diffraction (LEED).....	15
1.3.4. High-Resolution Transmission Electron Microscopy (HR-TEM).....	16
1.4. Outline	18
References	18
2. Thermodynamic model of oxide overgrowth on bare metals.....	23
2.1. Introduction	23
2.2. Theory	25
2.2.1. Basis of the model.....	25
2.2.2. Interfacial energies.....	27
2.2.3. Misfit-dislocation energy	31
A) The Semi-infinite Overgrowth (SIO) approach.....	31
B) The Large Dislocation Distance (LDD) approach.....	35
C) The Extrapolation (EXTR) approach.....	35
D) The First Approximation (APPR) approach.....	36
E) The Ball approach	37
F) The Volterra (VOLT) approach.....	38
2.2.4. Minimization of $\gamma_{\langle M \rangle - \langle M_x O_y \rangle}$; numerical procedure	39
2.2.5. General remarks about the misfit-dislocation energy	40
2.3. Energetics of chromium-oxide films on chromium substrates.....	40
2.3.1. Bulk Gibbs energies of the $\{Cr_2O_3\}$ and $\langle Cr_2O_3 \rangle$ cells.....	41
2.3.2. Surface energies of the $\{Cr_2O_3\}$ and $\langle Cr_2O_3 \rangle$ cells.....	43
2.3.3. Interfacial energies of the $\{Cr_2O_3\}$ and $\langle Cr_2O_3 \rangle$ cells.....	46

A) The interface energy of the crystalline-amorphous $\langle \text{Cr} \rangle - \{ \text{Cr}_2\text{O}_3 \}$ interface	46
B) The interface energy of the crystalline-crystalline $\langle \text{Cr} \rangle - \langle \text{Cr}_2\text{O}_3 \rangle$ interface	47
C) Difference in interface energy of the crystalline and amorphous overgrowths	57
2.4. Relative stabilities of amorphous and crystalline oxide films.....	59
2.4.1. Model predictions	59
2.4.2. Experimental observations versus model predictions	60
2.5. Conclusion	61
References	63
3. The thermodynamic stability of amorphous oxide overgrowths on metals ..	65
3.1. Introduction.....	65
3.2. Theory and calculation	67
3.2.1. Basics of the model	67
3.2.2. Bulk energy differences.....	69
3.2.3. Surface energy differences	70
3.2.4. Interface energy differences.....	71
A) The crystalline-amorphous interface energy	71
B) The crystalline-crystalline interface energy	72
3.3. Model predictions.....	76
3.3.1. System specific details and results	76
A) Al/Al ₂ O ₃	76
B) Ni/NiO	79
C) Cu/CuO ₂	81
D) Cr/Cr ₂ O ₃	81
E) Fe/FeO and Fe/Fe ₃ O ₄	82
F) Mg/MgO	84
G) Zr/ZrO ₂	87
H) Ti/TiO ₂	87
I) Si/SiO ₂	88
3.3.2. Thermodynamic stability of amorphous oxide film on various metals.....	89
3.4. Conclusions	92
Appendix 3.A. Estimation of the density of an amorphous oxide.....	94
Appendix 3.B. Estimation of the surface energies of the oxide overgrowths	95
3.B.1. Amorphous oxides	95
3.B.1. Crystalline oxides.....	97
Appendix 3.C. Enthalpy of mixing O in $\langle M \rangle$	101
References	102

4. The origin of high mismatch orientation relationships for ultra-thin oxide overgrowths.....	107
4.1. Introduction	107
4.2. Experimental.....	109
4.2.1. Material and surface preparation	109
4.2.2. Oxidation	109
4.2.3. AR-XPS analysis and quantification	110
4.2.4. HR-TEM sample preparation and analysis	111
4.3. Thermodynamics of oxide overgrowths on metals; summary of theoretical background	112
4.4. Experimental results and discussion	114
4.4.1. The oxidized Al{111} substrate	114
4.4.2. The oxidized Al{100} substrate	118
4.5. Experiment versus model predictions.....	124
4.6. Conclusions.....	128
Appendix 4.A. Electron-radiation-induced changes of the oxide-film microstructure.....	129
References.....	131
5. The amorphous-to-crystalline transition for oxide overgrowths on Al substrates	133
5.1. Introduction	133
5.2. Experimental details	135
5.3. AR-XPS spectral reconstruction and quantification	137
5.3.1. Resolving the metallic Al 2p PZL intensity of the bare metal.....	137
5.3.2. Resolving the metallic and oxidic Al 2p PZL intensities of the oxidized metal	139
5.3.3. Resolving the O 1s PZL intensities of the oxidized metal.....	141
5.3.4. Quantification	141
5.4. Oxide-film microstructure before and after annealing.....	143
5.4.2. Oxide films on Al{111}.....	145
5.4.3. Oxide films on Al{100}.....	147
5.4.4. Oxide films on Al{110}.....	148
5.5. Discussion: the stability of amorphous oxide films.....	150
5.5.1. Amorphous oxide films on Al{111}.....	150
5.5.2. Amorphous oxide films on Al{100}.....	152
5.5.3. Amorphous oxide films on Al{110}.....	153
5.6. Conclusions.....	155
Appendix 5.A. Procedures for the AR-XPS quantification.....	156

5.A.1. Expressions for the PZL photoelectron intensities	156
5.A.2. Calculation of oxide-film composition and thickness	158
Appendix 5.B. Calculation of effective depths of resolved species	161
References	161
6. The effect of substrate orientation on the kinetics of ultra-thin oxide-film growth on Al single-crystals	163
6.1. Introduction.....	164
6.2. Experiment	166
6.3. Data evaluation	166
6.4. Model description of the oxide-film growth kinetics	169
6.4.1. Theoretical background.....	169
6.4.2. Application to oxide-film growth on Al	171
6.5. Results and Discussion	174
6.5.1. Formation of a closed oxide film	174
6.5.2. Oxidation-induced reconstruction of the Al{110} face	177
6.5.3. Oxide-film growth kinetics	179
6.5.4. Oxide-film growth mechanisms	182
6.6. Conclusions	186
References	188
7. Summary	191
8. Zusammenfassung in deutscher Sprache.....	201
Symbols and abbreviations	211
List of publications	215
Danksagung	217
Curriculum Vitae	219

Chapter 1

General Introduction

The chemical reaction of oxygen gas with a solid metal surface ($x \cdot M + \frac{y}{2} \cdot O_2 \rightleftharpoons M_xO_y$), leading to the growth of a thin (i.e. thickness < 10 nm) oxide film on top of the metal, is of great scientific and technological interest, because thermally grown oxide films are employed in many application areas such as catalysis [1-3], microelectronics [4-6] and surface coatings for enhanced wear and corrosion resistance [7, 8]. The chemical and physical properties of such oxide films (e.g. their electronic and thermal conductivity, chemical and mechanical stability, corrosion resistance, adhesion properties, as well as its friction and wear resistance) will depend on their microstructure, which comprises e.g. the chemical composition, morphology, state-of-stress and crystallographic and defect structure of the oxide film. Evidently, the microstructure of a thermally grown oxide film, in turn, depends on the growth conditions such as the temperature (T), the partial pressure of oxygen (p_{O_2}), as well as the cleanliness, roughness and crystallographic orientation of the parent metal substrate surface [9].

To date, the technological potential to optimize and control the chemical and physical properties of thin oxide films by tailoring their microstructure is still limited by a lack of fundamental and comprehensive knowledge on the kinetics and thermodynamics of thin oxide growth as function of the growth conditions [10]. For example, previous kinetic studies on the thermal oxidation of bare metals surfaces have mainly addressed the empirical relationships between the oxide-film growth rate, the developing oxide-film microstructure and the oxidation conditions, but often failed to identify the governing mechanism(s) and rate-limiting (or rate-determining) step(s) of the oxidation process. Further, only very recently, the first thermodynamic studies on the microstructural evolution of the initial oxide overgrowth on a bare metal have been reported, which not only acknowledge, but also strive to account for the crucial role of surface and interfaces in such thin film systems [11].

This thesis addresses in particular the effect of substrate orientation on the kinetics and thermodynamics of initial oxide overgrowth on bare (i.e. without native oxide film) single-crystalline metals. To this end, the microstructural evolution of ultra-thin (< 5 nm) oxide

overgrowths on different bare metals (Al, Ni, Cu, Cr, Fe, Mg, Zr and Ti) was calculated on a *thermodynamic* basis as function of the metal-substrate orientation and the oxide growth temperature, while accounting for the important role of surface and interface energetics in such thin film systems (see Chapters 2 to 4). Experimental verification of the thermodynamic model predictions for initial oxide overgrowth on Al{111}, Al{110} and Al{100} metal surfaces was performed using a combined analytical approach by angle-resolved X-ray Photoelectron Spectroscopy (AR-XPS), Low Energy Electron Diffraction (LEED) and High-Resolution Transmission Electron Microscopy (HR-TEM) (see Chapters 4 and 5). Therefore, bare Al single-crystalline substrates were exposed to pure oxygen gas at a p_{O_2} of 1×10^{-4} Pa in the temperature range from 350 K to 700 K in an especially designed Ultra-High Vacuum (UHV) system for specimen preparation, processing and in-situ analysis. At the same time, the *kinetics* of oxide film growth on the bare Al{111}, Al{110} and Al{100} metal surfaces were established by Real-time In-situ Spectroscopic Ellipsometry (RISE). Finally, the governing growth mechanism and rate-limiting steps of the oxidation process of Al single-crystalline substrates were revealed by modelling the oxide-film growth kinetics as function of the growth conditions (see Chapter 6).

1.1. The initial oxidation of bare metals

1.1.1. Kinetics

The initial formation of a closed oxide film covering the entire metal surface involves a series of concurrent steps, such as transport and subsequent physisorption of oxygen molecules to the metal surface, (dissociative) chemisorption, oxide nucleation and growth. After formation of a closed oxide film on the metal surface, further oxide-film growth is decelerated, because the initial oxide film provides a diffusion barrier between the two reactants (i.e. parent metal substrate and oxygen gas). It follows that continued oxide-film growth can only proceed if (charged) reactant species (as, possibly, cations, anions, electrons, holes and vacancies) are transported through the developing oxide film towards the reacting oxide/gas and/or metal/oxide interfaces.

To describe the observed oxidation rates as function of the oxidation conditions, it is usually sufficient to consider only the *rate-determining* steps of the oxidation process, which correspond to those processes required to accurately describe the observed oxide-film growth kinetics. If transport of a single charged species through the growing oxide film is much slower than that of all the others, it is said to be the *rate-limiting* step of the oxidation process.

Then a balance will be established during oxidation between the transport fluxes of charged species, such that the rate-limiting transport step proceeds at the maximum possible rate. The resulting oxide-film growth under the influence of both a chemical (related to the concentration) and an electrostatic potential is the basis of various models proposed to describe the low temperature oxidation of metals [12-17].

In the coupled-currents approach of Fromhold and Cook [14, 15], which provides a comprehensive treatment of the low temperature oxidation, at least one electronic current (by quantum-mechanical tunnelling and/or thermionic emission) and one ionic current (diffusion of cations and/or anions) are considered. These currents of charged species are then coupled by the constraint that no net electric charge is transported through the film (so called coupled-currents constraint). In Chapter 6, the kinetics of oxide-film growth on bare Al single-crystal surfaces at low temperatures was successfully modelled on the basis of coupled currents of electrons (by both tunnelling and thermionic emission) and cations under influence of a surface-charge field setup up by (negatively charged) chemisorbed oxygen species at the growing oxide-film surface [14, 15, 18]. As such, activation-energy barriers for the transport of electrons and cations into and/or through the oxide film were obtained as function of the oxidation conditions.

1.1.2. Thermodynamics

To date, the growth kinetics has been used as the principle tool for studying the initial overgrowth of ultra-thin oxide films (< 5 nm) on bare metal surfaces. The thermodynamics of initial oxide overgrowth, which states the conditions of e.g. temperature, pressure, oxide-film thickness, chemical composition, and parent metal-substrate orientation under which a given thermodynamically stable oxide phase can form on its bare metal surface, have received only very little attention.

In this work, the thermodynamic model developed in Ref. [11], which describes the microstructural evolution of an initial oxide overgrowth on its bare metal, has been extended (and thereby improved considerably) to account for the relaxation of elastic growth strain in the crystalline oxide film by the introduction of misfit dislocations (i.e. plastic deformation) at the metal/oxide interface. This improvement allows the application of the model to larger oxide-film thicknesses and metal/oxide systems with large initial lattice mismatch between the parent metal substrate and the crystalline oxide overgrowth (Chapter 2). The extended model was applied to various metal/oxide systems to reveal the correlations between

properties of the metals and their oxides and the developing oxide-film microstructure, including a possible amorphous-to-crystalline transition (Chapter 3).

Furthermore, the thermodynamic model was successfully used to explain the observed occurrence of a crystallographic orientation relationship (COR) of exceptionally high lattice mismatch between the metal substrate and its oxide overgrowth (Chapter 4). This striking observation, as reported here for the initial oxide overgrowth on a single-crystalline Al{100} substrate, is in contrast with the general assumption that a COR corresponding with low lattice mismatch is preferred. However, as demonstrated here by thermodynamic model calculations, the relatively large energy contributions due to residual growth strain and misfit dislocations in such thin overgrowths can be overcompensated by the relatively low sum of the surface and interface energies. Neglecting the role of the surface energy and/or the interface energy contributions, as e.g. in the commonly applied Bollmann's method [19], leads to wrong theoretical predictions of CORs for ultra-thin overgrowths.

1.2. Thin oxide films on bare Al single-crystals

1.2.1. Thermal oxidation of bare Al substrates

Till now, initial oxidation of polycrystalline (cf. [20-23]) and single-crystalline Al substrates has been investigated for various oxidation conditions (mostly at different T and p_{O_2}), thereby using a wide range of different surface analysis techniques [24-37]. However, sometimes the parent metal substrate was not prepared under UHV conditions [24-27], so that a 2 nm to 3 nm thick native oxide was already present on the Al surface at the onset of oxidation. Further, many experimental works (cf. [29-31]), as well as some first principle simulations (cf. [38]), mainly focussed on the very initial stages of interaction of oxygen with the bare metal surface (i.e. adsorption, chemisorption, oxygen incorporation); i.e. these studies did not address the subsequent stages of 3-dimensional oxide nucleation and continued growth. Some experimental investigations and theoretical studies (using molecular dynamics [39]) are reported on the developing oxide-film microstructure [28, 36, 37] and/or the oxide growth-kinetics [32-34, 39] as function of the oxidation conditions for the initial oxidation of *bare Al single-crystalline* substrates. However, in these studies the effect of substrate orientation on the oxide-film growth kinetics and the developing oxide microstructure remains largely unaddressed. As shown in this thesis, the metal-substrate orientation can have a pronounced effect on both the kinetics and thermodynamics of the oxidation process (Chapters 4 to 6).

1.2.2. Modifications of alumina

Alumina (Al_2O_3) exists in a variety of different modifications, e.g. α - Al_2O_3 , γ - Al_2O_3 , η - Al_2O_3 , δ - Al_2O_3 , θ - Al_2O_3 , κ - Al_2O_3 and amorphous Al_2O_3 [40]. The only thermodynamically stable *bulk* modification is α - Al_2O_3 which possesses a hexagonal corundum structure, in which all Al^{3+} cations are octahedrally coordinated by the O^{2-} anions.

γ - Al_2O_3 is a thermodynamically stable modification for thin oxide films and nanocrystals [11, 41] and can be described as a defect spinel with 32 O anions on an fcc lattice and 24 octahedral and tetrahedral cation sites, which are occupied by $21\frac{1}{3}$ Al cations and $2\frac{2}{3}$ intrinsic cation vacancies [42]. Calculations based on classical molecular dynamics and Monte Carlo simulations in conjunction with *ab initio* calculations [42, 43] showed that cation vacancies in octahedral and tetrahedral sites of the oxygen sublattice of γ - Al_2O_3 are about equally stable (octahedral sites are energetically only slightly preferred), so that at finite temperatures above 0 K both types of intrinsic cation vacancies sites are likely to be present.

As demonstrated in Ref. [11] and Chapter 3, amorphous Al_2O_3 (further designated as *am*- Al_2O_3) can be considered as a thermodynamically stable modification of alumina for ultra-thin (< 1 nm) oxide films on Al substrates. Its structure is built up by neighbouring 'building blocks' of edge- and/or corner-sharing $[\text{AlO}_4]$ and $[\text{AlO}_6]$ polyhedra. Thereby, the O^{2-} anions form a distorted fcc packing with Al^{3+} cations distributed over tetrahedral and octahedral sites [44-47].

Different transition oxides between *am*- Al_2O_3 and γ - Al_2O_3 exists [47-49], which are sometimes designated as γ' - Al_2O_3 in the literature [47, 48]. These transition oxides usually only deviate from the ideal structure of γ - Al_2O_3 in their different atomic arrangement of the Al^{3+} cations in the interstices of the oxygen sublattice and/or the degree of long range order of the oxygen sublattice (as reflected by slightly different lattice parameters with respect to that of γ - Al_2O_3). The number of octahedrally coordinated cations increases with increasing density (and with progressing development of long range order in the amorphous oxide) from *am*- $\text{Al}_2\text{O}_3 \rightarrow \gamma'$ - $\text{Al}_2\text{O}_3 \rightarrow \gamma$ - $\text{Al}_2\text{O}_3 \rightarrow \alpha$ - Al_2O_3 [46, 47, 49].

1.2.3. Applications of thin Al_2O_3 films

Owing to their specific physical and chemical properties, such as a high dielectric strength, high resistivity, low refractive index, radiation resistance and high transparency, thin alumina films find numerous applications in optics and microelectronics (e.g. tunnel junctions, gate dielectrics, laser mirrors, waveguides, amplifiers and switches) [50-57]. Further, alumina is stable in contact with Si, which is of crucial import in many microelectronic applications [50].

Because of their high hardness, wear resistance, thermal stability and chemical inertness (durability against hostile environments), alumina films are also applied as wear and corrosion resistant coatings (e.g. on metal reflectors). Other possible applications of alumina films are heat sinks due to their high thermal conductivity or as sensor materials (e.g. capacitance humidity sensors) [52-54].

For many of the abovementioned technological applications, either an amorphous or an epitaxial single-crystalline oxide film in the nanometer thickness range is desirable, because of the absence of grain boundaries in both these types of oxide films. Grain boundaries in the grown oxide films may act as paths for fast atom or electron transport, thereby deteriorating material properties such as the electrical resistivity, corrosion resistance and/or catalytic activity [2, 5-9, 57-61]. In particular for technological applications in the field of microelectronics, thin amorphous oxide films are required, because of their uniform thickness and specific microstructure (no grain-boundaries, moderate bond flexibility, large free volume, negligible growth strain) and related properties (e.g., passivating oxide-film growth kinetics, low leakage current, high isotropic dielectric constant, high corrosion resistance, no permanent dipoles) [5, 6, 51, 52, 60, 61]. Sometimes single-crystalline oxide films are preferred, because they are denser and thermally more stability than the amorphous films [57]. Thicker films (micrometers range) consisting of the modifications α -Al₂O₃ and κ -Al₂O₃ are technologically used as e.g. wear-resistant cutting tools [62].

1.3. Methods of characterization

An ultra-high vacuum (UHV) chamber in combination with in-situ surface-sensitive analytical techniques is a prerequisite to investigate the initial oxidation of bare metal surfaces. In the present work, a combined experimental approach by angle-resolved X-ray photoelectron spectroscopy (AR-XPS), real-time in-situ ellipsometry (RISE), low energy electron diffraction (LEED) and high-resolution transmission electron microscopy (HR-TEM) has been used to study the microstructural evolution and growth kinetics of ultra-thin oxide overgrowths on Al single-crystals.

1.3.1. Angle-Resolved X-ray Photoelectron Spectroscopy (AR-XPS)

AR-XPS is based on the photon-induced emission of electrons from characteristic (core-electron) energy levels of the elements in a solid. The measured energy spectra (i.e. electron intensity versus binding energy, BE) of the detected photoelectrons provide information about the composition of the surface region and the chemical state of the elements in the

investigated material. The investigated depth below the surface depends on the effective attenuation length of the emitted electrons in the solid (λ^{eff}) and their angle of detection with respect to the sample surface normal (α) as expressed by the information depth ($3\lambda^{\text{eff}} \cdot \cos \alpha$). It follows that the information depth for the photoelectrons excited from metal and oxide surfaces (with $\lambda^{\text{eff}} \sim 2.5$ nm) by Al K α X-ray irradiation (as used here) varies in the range from 1 nm to 7 nm for photoelectrons detected at grazing and near-normal detection angles of 23° and 83°, respectively. [63]

For the state-of-the-art AR-XPS equipment employed in the present study, the emitted photoelectrons were simultaneously detected over the entire angular detection range from $\alpha = 23^\circ$ to $\alpha = 83^\circ$ in eight ranges of 7.5° each. As such, different information depths of the sample are probed for each angular detection range, which provides valuable information on e.g. the depth distribution of the detected chemical species within the grown oxide film. For example, from the quantitative analysis of a series of measured Al 2p and O 1s AR-XPS spectra recorded at different detection angles from an oxidized Al single-crystalline substrate, information was obtained on the oxide-film thickness, the chemical composition, as well as the existence of different valence states of the Al cations in the oxide film adjacent to the metal/oxide interface (Chapter 5).

For the accurate quantitative analysis of the measured AR-XPS spectra, the total primary zero loss intensity of each resolved spectral component, which comprises all recorded photoelectrons that have been emitted from the concerned core level and left unaffected until recorded (i.e. all recorded elastically scattered and unscattered photoelectrons), has to be determined separately. This implies that the sum of the backgrounds of inelastically scattered electrons associated with each resolved spectral component has to be subtracted from the measured spectrum. For example, the measured Al 2p core-level spectrum recorded from the oxidized Al metal substrate contains at least one metallic and one oxidic component (see Fig. 1.1), which each have to be resolved from the measured spectrum (together their individual inelastic backgrounds) by e.g. fitting the measured Al 2p spectrum with a combination of asymmetric and symmetric lineshape functions (such as e.g. a Doniach-Sunjic or Gauss-Lorentz function).

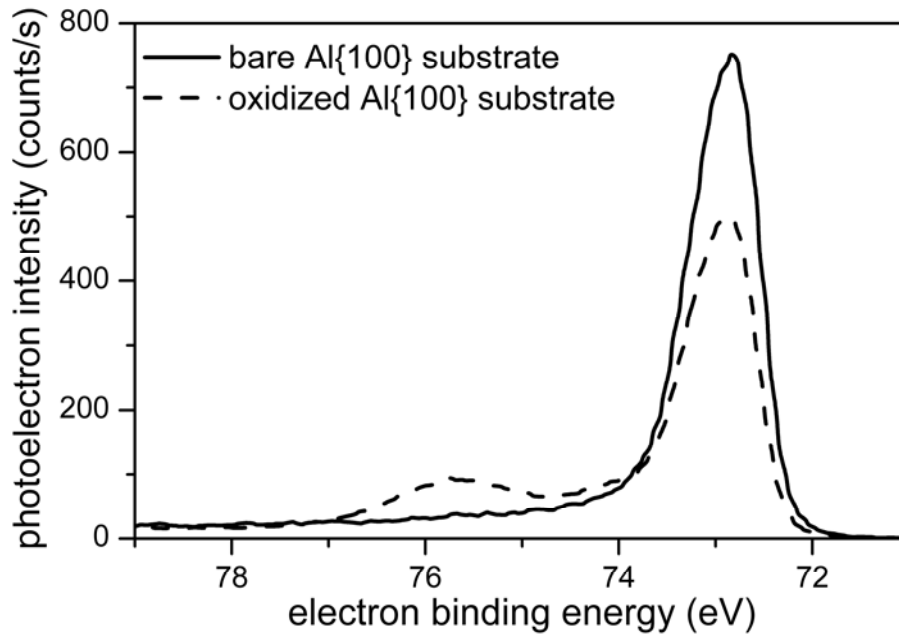


Figure 1.1. Measured Al 2p photoelectron spectra as recorded from an bare and oxidized Al{100} substrate by XPS employing a detection angle of $\alpha = 41.25^\circ$ with respect to the surface normal. The oxidized spectrum pertains to the Al{100} substrate after thermal oxidation at $T = 500$ K and $p_{\text{O}_2} = 1 \times 10^{-4}$ Pa for $t = 6000$ s (dashed line). Note that the oxidized spectrum shows the presence of both a metallic and oxidic spectral component, as originating from Al atoms in the metal substrate and in the oxide film, respectively.

1.3.2. Real-time In-situ Spectroscopic Ellipsometry (RISE)

Ellipsometry is a non-destructive optical technique based on the measurement of the change in phase and amplitude of polarized light upon interaction with a sample surface (*here*: a thin oxide film on a metal substrate). For the in situ investigation of film growth kinetics by ellipsometry, the changes in the ellipsometric amplitude-ratio and phase-shift dependent parameters ψ and Δ as function of oxidation time are measured simultaneously for various wavelengths of the incident polarized light. The tangent of the angle Ψ equals the ratio of the amplitude attenuation (or magnification) upon reflection between p and s polarisations and Δ is the difference between phase shifts experienced upon reflection of p and s polarisations, where p and s polarisations are the components of the electric field components of the polarized light vibrating in the plane of incidence and perpendicular to it, respectively [64].

In the present work, real-time in-situ spectroscopic ellipsometry (RISE), employing a Xe source operating in the wavelength range of $\lambda = 350 - 800$ nm, was used to determine the oxide-film growth kinetics from the measured changes in $\psi(\lambda)$ and $\Delta(\lambda)$ with increasing oxidation time (see Fig. 1.2), as recorded during oxidation of bare Al single-crystalline substrates. To this end, a suitable model for the evolving substrate/oxide-film system (which

includes the optical constants of the metal substrate and the oxide film) was adopted to fit the measured changes in $\psi(\lambda)$ and $\Delta(\lambda)$ as function of oxidation time (Chapter 6).

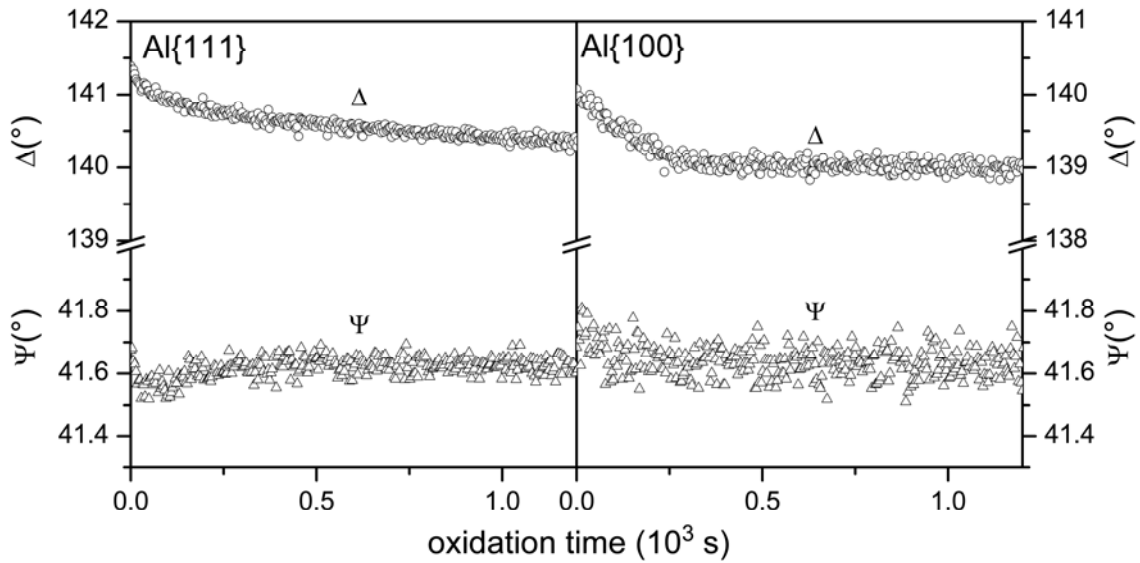


Figure 1.2. Measured changes of the amplitude-ratio and phase-shift dependent parameters Ψ and Δ (at a wavelength of $\lambda = 589$ nm) with increasing oxidation time (t) for the oxidation of Al{111} (left panel) and Al{100} (right panel) substrate at $T = 350$ K and $p_{\text{O}_2} = 1 \times 10^{-4}$ Pa.

1.3.3. Low Energy Electron Diffraction (LEED)

LEED is based on the principle that incident electrons with a kinetic energy in the range of about 20 eV to 500 eV are scattered by the atomic arrangement at a solid sample surface. The elastically scattered electrons can be detected on a fluorescence screen and the thus obtained electron diffraction pattern then contains information about the atom arrangement at the surface region of the sample (the recorded LEED pattern mainly depends on the two dimensional symmetry of the surface region atoms; see Fig. 1.3). The investigated depth of the sample is only about 2 to 5 atom layers (increases with increasing incident electron energy), because of the small attenuation lengths of the low energy electrons in solids (cf. [65]).

LEED was used to determine the microstructure of the grown oxide films on the Al single-crystals, in particular whether the grown oxide films are amorphous or crystalline (Chapters 4 and 5). For the case of a crystalline oxide overgrowth on the Al substrate, the crystallographic orientation relationship (COR) between the oxide film and the metal substrate could also be determined. Further, LEED was applied to check the crystallinity and

cleanness of bare metal substrates prior to oxidation, as well as the occurrence of reconstruction phenomena at the bare and oxidized Al metal surfaces (see Chapter 5).

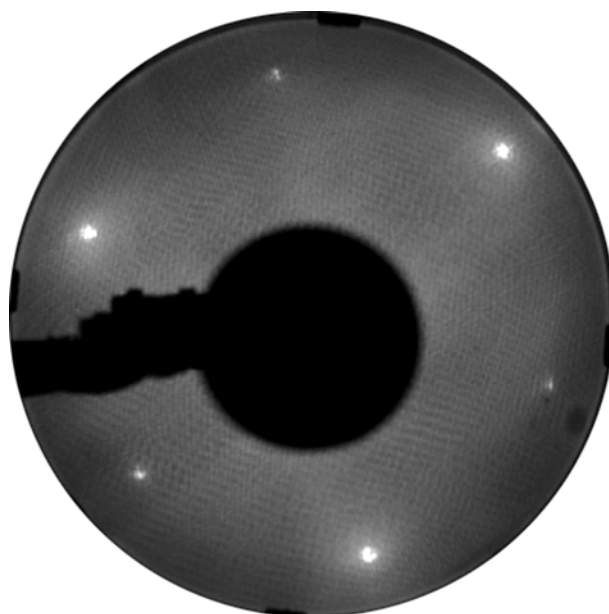


Figure 1.3. LEED pattern as recorded (at a primary electron energy of 78 eV) from the bare Al{111} substrate.

1.3.4. High-Resolution Transmission Electron Microscopy (HR-TEM)

Transmission electron microscopy (cf. [66]) is applied to obtain an image of the specimen at high resolution. Therefore, electrons are emitted from a solid by thermal or field emission, accelerated using high voltage and focussed by the use of magnetic lenses. The HR-TEM image is formed, when electrically scattered electrons pass through the specimen, by complex interference of various diffracted beams and the direct beam. A subsequent lens system magnifies the exit wave function onto a screen. The image depends on the imaging conditions and the thickness of the specimen, which should be very thin (< 100 nm) to be transparent for the electrons and avoid large contrast-losses due to inelastic scattering. The negatives of the recorded micrographs are digitized for further quantitative evaluation. Using HR-TEM, detailed information on the atomic structure (i.e. defects, interfaces) of the investigated sample area can be obtained.

In this study, HR-TEM analysis of metal/oxide cross sections (as prepared from oxidized Al single-crystals) was performed to study the microstructure and morphology of the thermally grown oxide films on an atomic scale, as well as to establish the crystallographic orientation relationships between the crystalline oxides films and the differently oriented Al substrates (Chapters 4 and 5). Preparation and analysis of the HR-TEM metal/oxide cross-sections requires that the oxidized Al single-crystals are removed from the UHV system. To

protect the grown oxide films from further oxidation upon exposure to atmospheric conditions, the films were sealed by a ~ 150 nm thick Al capping layer prior to their removal from the UHV system (see Fig. 1.4). The Al seal was deposited in-situ by Molecular Beam Epitaxy (MBE), while cooling the specimen (holder) containing the oxidized single-crystal with liquid nitrogen to prevent any microstructural changes of the oxide film and to minimize the chemical interaction of the Al capping layer with the oxide-film surface. Subsequently, a very thin TEM-lamella (thickness: 80 – 100 nm; size: $3 \mu\text{m} \times 4 \mu\text{m}$) was cut from the oxidized Al single-crystal with Al capping layer (after its removal from the UHV system) using a dual Focused Ion Beam with 30 keV Ga^+ ions.

Transmission electron microscopic analysis of the thus obtained metal/oxide cross-sections was performed with a very high acceleration voltage of 1250 kV and a point-to-point resolution with the side entry lens of 0.12 nm [67]. To retard the occurrence of microstructural changes in the irradiated area of specimen, as inflicted by the high-energy electron beam, the TEM-lamellae were cooled with liquid nitrogen during the HR-TEM analysis.

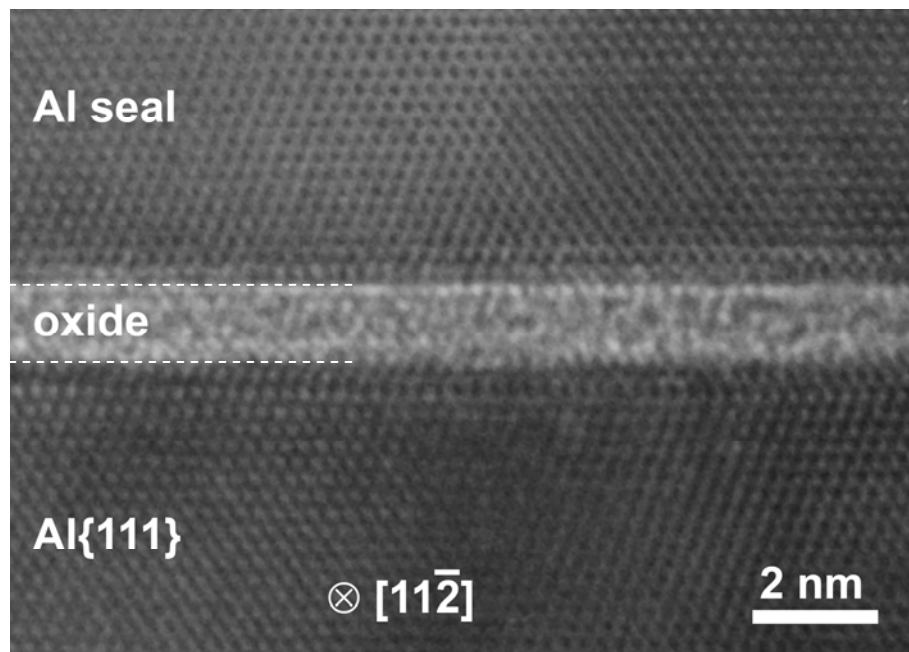


Figure 1.4. High-resolution transmission electron micrograph of the crystalline Al_2O_3 overgrowth on $\text{Al}\{111\}$ after oxidation at $T = 373$ K and $p_{\text{O}_2} = 1 \times 10^{-4}$ Pa for $t = 6000$ s. The direction of the primary electron beam was along the zone axis (\otimes) $[11\bar{2}]$ of the $\text{Al}\{111\}$ substrate. The dashed lines roughly indicate the boundaries between the oxide and the $\text{Al}\{111\}$ substrate and the oxide and the Al seal, respectively.

1.4. Outline

In Chapter 2 a thermodynamic model is presented that predicts the initial growth of either a (semi-)coherent crystalline oxide phase or an amorphous oxide phase (with a subsequent amorphous-to-crystalline transition) on a bare metal as function of the substrate orientation, growth temperature and film thickness. The model accounts for possible relaxation of growth stresses by plastic deformation (i.e. the accommodation of growth strain by the formation of misfit dislocations at the metal/oxide interface). In Chapter 3 the thermodynamic model is applied to several metal/oxide systems (Ni, Cu, Cr, Fe, Mg, Zr, Ti and Si) to reveal the material properties that govern the microstructural evolution of the oxide overgrowths. The occurrence and thermodynamic explanation of a crystallographic orientation relationship (COR) of exceptionally high lattice mismatch between a Al{100} substrate and its crystalline oxide overgrowth is reported in Chapter 4. Chapter 5 is devoted to verify our thermodynamic model predictions in Chapter 3 of the occurrence of a stable amorphous phase for the initial oxide overgrowth on bare Al substrates. To this end, the oxide-film thickness and microstructure of oxide overgrowths on Al single-crystals were investigated as function of the oxidation temperature by AR-XPS, LEED and HR-TEM. Furthermore, the thermal stability of the amorphous oxide films was confirmed by in-situ UHV annealing above the growth temperature. Finally, the effect of the substrate orientation on the observed oxidation kinetics of bare Al substrates (as experimentally determined by RISE) is revealed by establishing the underlying mechanisms and rate-controlling steps of the oxidation process as function of the oxidation conditions (Chapter 6).

References

- [1] H.-J. Freund, Surf. Sci. **601** (2007) 1438.
- [2] I. E. Wachs, Catal. Today **100** (2005) 79.
- [3] D. W. Goodman, J. Catal. **216** (2003) 213.
- [4] P. F. Ladwig, J. J. Yang, Y. Yang, Y. A. Chang, F. Liu, B. B. Pant and A. E. Schultz, Appl. Phys. Lett. **87** (2005) 061901.
- [5] C. J. Först, K. Schwarz and P. E. Blöchl, Phys. Rev. Lett. **95** (2005) 137602.
- [6] S. Miyazaki, J. Vac. Sci. Technol. B **19** (2001) 2212.
- [7] J. Ma, Y. He, D. Wang and W. Gao, Mater. Lett. **58** (2004) 807.
- [8] H. L. Wang, C. H. Lin and M. H. Hon, Thin Solid Films **310** (1997) 260.

- [9] K. R. Lawless, Rep. Prog. Phys. **37** (1974) 231.
- [10] A. Pasquarello and A. M. Stoneham, J. Phys.: Condens. Matter **17** (2005) V1.
- [11] L. P. H. Jeurgens, W. G. Sloof, F. D. Tichelaar and E. J. Mittemeijer, Phys. Rev. B **62**, (2000) 4707.
- [12] N. F. Mott, Trans. Faraday Soc. **43** (1947) 429.
- [13] N. Cabrera and N. F. Mott, Rep. Prog. Phys. **12** (1949) 163.
- [14] A. T. Fromhold, Jr. and E. L. Cook, Phys. Rev. **158** (1967) 600.
- [15] A. T. Fromhold, Jr. and E. L. Cook, Phys. Rev. **163** (1967) 650.
- [16] F. P. Fehlner and N. F. Mott, Oxid. Met. **2** (1970) 59.
- [17] E. Fromm, *Kinetics of Metal-Gas Interactions at Low Temperatures; Hydriding, Oxidation, Poisoning* (Springer, Berlin, 1998).
- [18] L. P. H. Jeurgens, A. Lyapin and E. J. Mittemeijer, Acta Mater. **53** (2005) 4871.
- [19] W. Bollmann, *Crystal Defects and Crystalline Interfaces*, (Springer, Berlin, 1970) p. 143.
- [20] L. P. H. Jeurgens, W. G. Sloof, F. D. Tichelaar and E. J. Mittemeijer, J. Appl. Phys. **92**, (2002) 1649.
- [21] L. P. H. Jeurgens, W. G. Sloof, F. D. Tichelaar and E. J. Mittemeijer, Surf. Sci. **506**, (2002) 313.
- [22] L. P. H. Jeurgens, W. G. Sloof, F. D. Tichelaar and E. J. Mittemeijer, Thin Solid Films **418**, (2002) 89.
- [23] T. Do and N. S. McIntyre, Surf. Sci. **440** (1999) 438.
- [24] K. Thomas and M. W. Roberts, J. Appl. Phys. **32** (1961) 70.
- [25] P. E. Doherty and R. S. Davis, J. Appl. Phys. **34** (1963) 619.
- [26] K. Hart and J. K. Maurin, Surf. Sci. **20** (1970) 285.
- [27] K. Shinohara, T. Seo and H. Kyogoku, Z. Metallkde. **73** (1982) 774.
- [28] F. Jona, J. Phys. Chem. Solids **28** (1967) 2155.
- [29] I. P. Batra and L. Kleinman, J. Electron Spectr. Related Phenomena **33** (1984) 175.
- [30] J. Trost, H. Brune, J. Witterling, R. J. Behm and G. Ertl, J. Chem. Phys. **108** (1998) 1740.
- [31] I. Popova, V. Zhukov and J. T. Yates, Jr., J. Appl. Phys. **87** (2000) 8143.
- [32] P. Hofmann, W. Wyrobisch and A. M. Bradshaw, Surf. Sci. **80** (1979) 344.

- [33] B. E. Hayden, W. Wyrobisch, W. Oppermann, S. Hachicha, P. Hofmann and A. M. Bradshaw, *Surf. Sci.* **109** (1981) 207.
- [34] C. Ocal, S. Ferrer, N. Garcia, *Surf. Sci.* **163** (1985) 335.
- [35] A. Bianconi, R. Z. Bachrach, S. B. M. Hagstrom and S. A. Flodström, *Phys. Rev. B* **19** (1979) 2837.
- [36] J. I. Eldridge, R. J. Hussey, D. F. Mitchell and M. J. Graham, *Oxid. Met.* **30** (1988) 301.
- [37] K. Shimizu, A. Gotoh, K. Kobayashi, G. E. Thompson and G. C. Wood, in: M. J. Bennett and G. W. Lorimer (ed.), *Microscopy of oxidation* (The Institute of Metals, 1991) p. 144.
- [38] Y. F. Zhukovskii, P. W. M. Jacobs and M. Causá, *J. Phys. Chem. Solids* **64** (2003) 1317.
- [39] A. Hasnaoui, O. Politano, J. M. Salazar and G. Aral, *Phys. Rev. B* **73** (2006) 035427.
- [40] I. Levin and D. Brandon, *J. Am. Ceram. Soc.* **81** (1998) 1995.
- [41] J. M. McHale, A. Auroux, A. J. Perrotta and A. Navrotsky, *Science* **277** (1997) 788.
- [42] G. Gutiérrez, A. Taga and B. Johansson, *Phys. Rev. B* **65** (2001) 012101.
- [43] F. H. Streitz and J. W. Mintmire, *Phys. Rev. B* **60** (1999) 773.
- [44] P. Lamparter and R. Kniep, *Physica B* **234-236** (1997) 405.
- [45] L. A. Aleshina, E. A. Nikitina and A. D. Fofanov, *Cryst. Rep.* **42** (1997) 836.
- [46] G. Gutiérrez and B. Johansson, *Phys. Rev. B* **65** (2002) 104202.
- [47] U. Bardi, A. Atrei and G. Rovida, *Surf. Sci.* **268** (1992) 87.
- [48] R. S. Alwitt, C. K. Dyer and B. Noble, *J. Electrochem. Soc.* **129** (1982) 711.
- [49] H. J. van Beek and E. J. Mittemeijer, *Thin Solid Films* **122** (1984) 131.
- [50] J.-S. Kim, M. Shahjahan, H. K. Mosammat, K. Sawada and M. Ishida, *Jap. J. Appl. Phys.* **45** (2006) 5107.
- [51] M. G. El-Shaarawy and W. A. A. Bayoumy, *Mater. Chem. Phys.* **78** (2002) 405.
- [52] H. Momida, T. Hamada, Y. Takagi, T. Yamamoto, T. Uda and T. Ohno, *Phys. Rev. B* **73** (2006) 054108.
- [53] B. J. H. Stadler, M. Oliveria and L. O. Bouthillette, *J. Am. Ceram. Soc.* **78** (1995) 3336.
- [54] K. S. Shamala, L. C. S. Murthy and K. Narasimha Rao, *Mater. Sci. Eng. B* **106** (2004) 269.
- [55] M. Aguilar-Frutis, M. Garcia and C. Falcony, *Appl. Phys. Lett.* **72** (1998) 1700.

- [56] P. J. Kelly and R. D. Arnell, *J. Vac. Sci. Technol. A* **17** (1999) 945.
- [57] S. Oh, K. Cicak, R. McDermott, K. B. Cooper, K. D. Osborn, R. W. Simmonds, M. Steffen, J. M. Martinis and D. P. Pappas, *Supercond. Sci. Technol.* **18** (2005) 1396.
- [58] C.-C. Shih, S.-J. Lin, K.-H. Chung, Y.-L. Chen and Y.-Y. Su, *J. Biomed. Mater. Res.* **53** (2000) 323.
- [59] A. Tschöpe, *J. Electroceram.* **14** (2005) 5.
- [60] F. P. Fehlner, *Low-temperature Oxidation: The Role of Vitreous Oxides* (Wiley-Interscience, New York, 1986).
- [61] A. G. Revesz and F. P. Fehlner, *Oxid. Met.* **15** (1981) 297.
- [62] P. Hansson, M. Halvarsson and S. Vuorinen, *Surf. Coat. Technol.* **76/77** (1995) 256.
- [63] D. Briggs and J. T. Grant (ed.), *Surface Analysis by Auger and X-ray Photoelectron Spectroscopy* (IM Publications, Charlton and SurfaceSpectra Limited, Manchester, 2003).
- [64] R. M. A. Azzam and N. M. Bashara, *Ellipsometry and Polarized Light* (North-Holland, Amsterdam, 1987).
- [65] M. A. Van Hove, W. H. Weinberg and C.-M. Chan, *Low-Energy Electron Diffraction: Experiment, Theory and Surface Structure Determination*, (Springer, Berlin, 1986).
- [66] P. R. Buseck, J. M. Cowley and L. Eyring, *High-Resolution Transmission Electron Microscopy and Associated Techniques* (Oxford University Press, New York, 1988).
- [67] F. Phillipp, R. Höschel, M. Osaki, G. Möbus and M. Rühle, *Ultramicroscopy* **56** (1994) 1.

Chapter 2

Thermodynamic model of oxide overgrowth on bare metals

Relaxation of growth strain by plastic deformation

F. Reichel, L. P. H. Jeurgens and E. J. Mittemeijer

Abstract

A thermodynamic model has been developed which predicts the growth of either an initial (semi-)coherent, strained crystalline oxide phase or an initial amorphous oxide phase (with a possible amorphous-to-crystalline transition) on the bare single-crystalline metal substrate as function of the metal-substrate orientation, the growth temperature and the oxide-film thickness. The model accounts for relaxation of residual stresses in a crystalline oxide overgrowth by plastic deformation (i.e., through the introduction of misfit dislocations at the metal/oxide interface). As an example, the microstructural evolution of the initial oxide film grown on the {111}, {110} and {100} crystallographic surfaces of a bare Cr substrate has been modelled as function of the growth temperature and the oxide-film thickness (< 5 nm). The initial oxide-film growth on the bare Cr{100} and Cr{111} substrates is predicted to proceed by the initial formation and growth of an amorphous oxide film up to a critical thickness of about 0.5 nm and 0.9 nm, respectively. On the other hand, the onset of oxidation on a bare Cr{110} substrate should proceed by the direct overgrowth of a semi-coherent, strained crystalline oxide film. These model predictions provide understanding for experimental observations reported in the literature.

2.1. Introduction

Upon oxidation of a bare (i.e., without a native oxide), single-crystalline metal or semiconductor substrate, the microstructure of the developing oxide film can be variable. For metals (or semiconductors) such as Al, Si and Ta, an initially amorphous oxide film develops on the bare metal surface, which transforms into a crystalline oxide film if the thickness exceeds a critical value at higher temperatures (e.g., Refs. [1, 2] and Refs. therein). For other metals such as Cu, Ni and Fe, oxidation starts with the nucleation and growth of a (semi-)

coherent, elastically strained crystalline oxide film (e.g., Refs. [1, 2] and Refs. therein). After attaining some critical oxide-film thickness, the built-up growth strain in the oxide film is released by the formation of misfit dislocations (i.e., plastic deformation occurs), which are initiated at the metal/oxide interface.

For many technological applications (e.g., microelectronics, surface coatings and catalysis), the growth of either an amorphous or a coherent, single-crystalline oxide film is desired, because of the absence of grain boundaries in both these types of oxide films [3-5]: Grain boundaries in the grown oxide films may act as paths for fast atom or electron transport, thereby deteriorating material properties such as the electrical resistivity, corrosion resistance or catalytic activity [2, 6]. In particular for technological applications in the field of microelectronics, thin amorphous oxide films are required, because of their uniform thickness and specific microstructure (no grain-boundaries, moderate bond flexibility, large free volume, negligible growth strain) and related properties (e.g., passivating oxide-film growth kinetics, low leakage current, high dielectric constant, high corrosion resistance) [2, 3, 5].

As shown by recent model calculations by Jeurgens et al. [1] on the relative thermodynamic stability of an amorphous oxide film on its metal substrate (with respect to that of the corresponding elastically-strained, crystalline oxide film on the same substrate), an amorphous structure for the initially grown oxide film can be thermodynamically (instead of kinetically) preferred due to the lower sum of the interfacial and surface energies for the amorphous-oxide-film/metal-substrate configuration as compared to the crystalline-oxide-film/metal-substrate configuration. However, in this model, which was applied to the oxidation of Al, the possible relaxation of growth strain in the crystalline oxide overgrowth (and/or the parent metal substrate) by introduction of misfit dislocations at the metal/oxide interface is not considered, which is only justified up to a certain oxide-film thickness and for a small initial lattice mismatch between the metal substrate and the oxide overgrowth.

In the present contribution, the original model description [1] has been extended and thereby improved considerably to account for the relaxation of growth strain (originating from the initial lattice mismatch between a crystalline oxide overgrowth and its parent metal substrate) by plastic deformation. The resulting model can be applied to distinctly larger oxide-film thicknesses, as well as to metal/oxide systems of high initial lattice mismatch. A general expression has been derived for the assessment of the energy of the interface between a metal substrate and its corresponding coherent or semi-coherent crystalline oxide overgrowth. Further, the different approaches as reported in the literature for the estimation of the misfit-dislocation energy contribution to the interface energy have been outlined and a

numerical procedure has been presented to calculate the value of the interface energy of the corresponding semi-coherent interface as function of the growth temperature and oxide-film thickness.

The new model description has been applied to the Cr/Cr₂O₃ system, which not only represents a case of very large lattice mismatch, but also exhibits pronouncedly different mismatches along different directions in the boundary plane between the metal substrate and the oxide film (i.e., the crystalline oxide film exhibits anisotropic growth strain). On the basis of the model calculations, the thermodynamic stability of an amorphous Cr₂O₃ film on different crystallographic faces of the Cr substrate, as compared to that of the corresponding crystalline Cr₂O₃ film on the same crystallographic faces of the Cr substrate, has been evaluated as function of the growth conditions. Finally, the model predictions for the microstructural evolution of thin oxide films grown on bare, single-crystalline Cr substrates have been compared with experimental observations as obtained by low energy electron diffraction (LEED) [7-9], reflection high energy electron diffraction (RHEED) [7, 10, 11], X-ray scattering [12] and valence band spectra of the oxidized metal as recorded by ultraviolet (UPS) and X-ray photoelectron spectroscopy (XPS) [13].

2.2. Theory

2.2.1. Basis of the model

Consider an homogeneous oxide film, M_xO_y ¹, of uniform thickness, $h_{M_xO_y}$, on its single-crystalline metal substrate, $\langle M \rangle$. In one case, the oxide film is amorphous, denoted as $\{M_xO_y\}$, with thickness $h_{\{M_xO_y\}}$. In the other case, the oxide film is crystalline, denoted as $\langle M_xO_y \rangle$, with thickness $h_{\langle M_xO_y \rangle}$. The braces $\{ \}$ and the brackets $\langle \rangle$ refer to the amorphous state and the crystalline state, respectively. The composition of the amorphous and crystalline oxides is the same, and both films have been formed from the same molar quantity of oxygen on identical substrates.

¹ It is noted that the stoichiometry of the oxide phase is denoted here with M_xO_y (with x and y being the number of cations and anions per oxide molecule, respectively) instead of MO_x as in Ref. [1], since in the present calculations the number of metal ions per oxide molecule becomes relevant (see Chapter 3, Appendix 3.B).

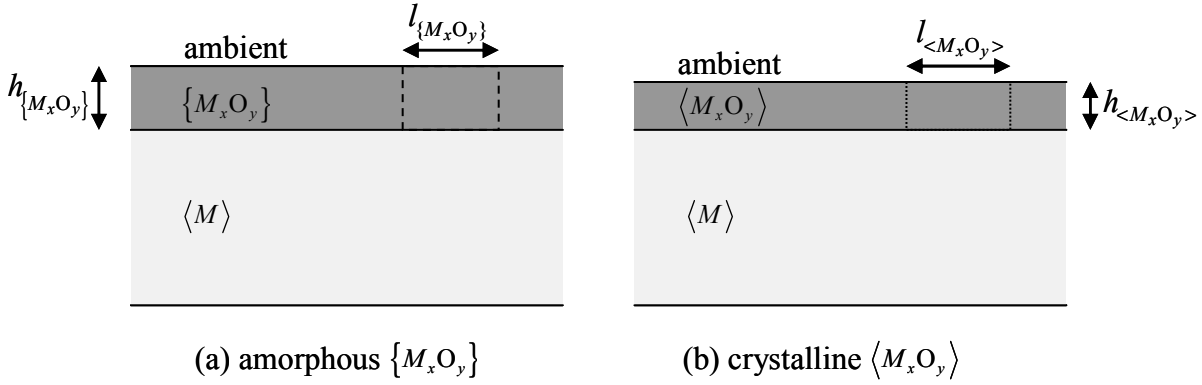


Figure 2.1. Schematic drawing of a homogeneous M_xO_y oxide film of uniform thickness, $h_{M_xO_y}$, on top of its single crystalline metal substrate, $\langle M \rangle$, in contact with the ambient (e.g., vacuum, a gas atmosphere or an adsorbed layer). (a) represents the case of an amorphous oxide film $\{M_xO_y\}$ of uniform thickness, $h_{\{M_xO_y\}}$, on the $\langle M \rangle$ substrate, while (b) represents the case of the corresponding crystalline oxide-film $\langle M_xO_y \rangle$ of uniform thickness, $h_{\langle M_xO_y \rangle}$, on the $\langle M \rangle$ substrate. Both films have been formed from the same molar quantity of oxygen on identical substrates. The two competing cells of volume $h_{\{M_xO_y\}} \times l_{\{M_xO_y\}}^2$ and $h_{\langle M_xO_y \rangle} \times l_{\langle M_xO_y \rangle}^2$, as indicated in (a) and (b), respectively, contain the same molar quantity of oxide.

To assess the thermodynamic stability of the amorphous oxide film on the metal substrate with respect to that of the corresponding crystalline oxide film on the metal substrate, the energetics of the $\langle M \rangle - \{M_xO_y\}$ and $\langle M \rangle - \langle M_xO_y \rangle$ configurations will be compared for cells of volume $h_{\{M_xO_y\}} \times l_{\{M_xO_y\}}^2$ and $h_{\langle M_xO_y \rangle} \times l_{\langle M_xO_y \rangle}^2$, respectively (see Figs. 2.1a and b). Both cells contain the same molar quantity of oxide. The difference in total Gibbs energy between the amorphous and crystalline cells, $\Delta G = G_{\{M_xO_y\}} - G_{\langle M_xO_y \rangle}$, can be given as:

$$\Delta G = h_{\{M_xO_y\}} \left(\frac{\Delta G_{\{M_xO_y\}}^f - \Delta G_{\langle M_xO_y \rangle}^f}{V_{\{M_xO_y\}}} \right) + \gamma_{\{M_xO_y\}-\text{amb}} + \gamma_{\langle M \rangle - \{M_xO_y\}} - \chi \left(\gamma_{\langle M_xO_y \rangle - \text{amb}} + \gamma_{\langle M \rangle - \langle M_xO_y \rangle} \right), \quad (2.1)$$

where $\Delta G_{\{M_xO_y\}}^f$ and $\Delta G_{\langle M_xO_y \rangle}^f$ are the Gibbs energies of formation of the amorphous and the crystalline oxide, respectively; $V_{\{M_xO_y\}}$ is the molar volume of the amorphous oxide; $\gamma_{\{M_xO_y\}-\text{amb}}$ and $\gamma_{\langle M_xO_y \rangle - \text{amb}}$ are the surface energies of the amorphous oxide and the crystalline oxide in contact with the ambient, respectively; $\gamma_{\langle M \rangle - \{M_xO_y\}}$ and $\gamma_{\langle M \rangle - \langle M_xO_y \rangle}$ are the interfacial energies of the interface between the metal substrate and the amorphous oxide and the metal

substrate and the crystalline oxide, respectively; χ denotes the ratio of the surface areas of the unstrained amorphous cell and the (strained) crystalline cell (see Sec. 2.2.2 and Ref. [1]):

$$\chi = \frac{l_{\langle M_x O_y \rangle}^2}{l_{\{M_x O_y\}}^2}. \quad (2.2)$$

If $\Delta G < 0$ the amorphous oxide cell is more stable, whereas for $\Delta G > 0$ the crystalline oxide cell is more stable.

2.2.2. Interfacial energies

Experimental values for the solid-solid interfacial energies between a metal substrate and its amorphous or crystalline oxide overgrowth [i.e., values for $\gamma_{\langle M \rangle - \{M_x O_y\}}$ and $\gamma_{\langle M \rangle - \langle M_x O_y \rangle}$ in Eq. (2.1)] as function of the growth conditions are generally not available. Therefore approximative expressions have been derived on the basis of the macroscopic atom approach [14].

The *crystalline-amorphous* interface $\langle M \rangle - \{M_x O_y\}$ is conceived as an interface between a crystalline solid (i.e., metal $\langle M \rangle$) and a configurationally frozen liquid (as a model for the amorphous oxide, $\{M_x O_y\}$). Because of the relatively large free volume and moderate bond flexibility of an amorphous phase, it is assumed that no mismatch strain resides in the amorphous oxide film (and consequently the metal substrate) at the oxide-growth temperature. It then follows that the energy, $\gamma_{\langle M \rangle - \{M_x O_y\}}$, of the interface between the metal substrate and the amorphous oxide film (per unit area of the interface) can be expressed as the resultant of three additive energy contributions (for details, see Ref. [1]), i.e.

$$\gamma_{\langle M \rangle - \{M_x O_y\}} = \gamma_{\langle M \rangle - \{M_x O_y\}}^{\text{interaction}} + \gamma_{\langle M \rangle - \{M_x O_y\}}^{\text{entropy}} + \gamma_{\langle M \rangle - \{M_x O_y\}}^{\text{enthalpy}}. \quad (2.3)$$

The (relatively large) negative interaction contribution, $\gamma_{\langle M \rangle - \{M_x O_y\}}^{\text{interaction}}$, arises from the chemical bonding between the amorphous oxide and the metal substrate across the interface. The positive entropy contribution, $\gamma_{\langle M \rangle - \{M_x O_y\}}^{\text{entropy}}$, results from the ordering (i.e., the decrease of configurational entropy) of the amorphous oxide *near* the interface with the crystalline metal substrate (for experimental confirmation see Ref. [15]). Finally, the (relatively small) positive enthalpy contribution, $\gamma_{\langle M \rangle - \{M_x O_y\}}^{\text{enthalpy}}$, arises from the relative increase in enthalpy of the metal

substrate atoms *at* the interface (as compared to the bulk) due to the liquid-type of bonding with the amorphous oxide at the interface (see further Ref. [1]).

The energy, $\gamma_{\langle M \rangle - \langle M_x O_y \rangle}$, of the coherent or semi-coherent *crystalline-crystalline* interface, $\langle M \rangle - \langle M_x O_y \rangle$, is the resultant of two energy contributions:

$$\gamma_{\langle M \rangle - \langle M_x O_y \rangle} = \gamma_{\langle M \rangle - \langle M_x O_y \rangle}^{\text{interaction}} + \gamma_{\langle M \rangle - \langle M_x O_y \rangle}^{\text{mismatch}}. \quad (2.4a)$$

The interaction contribution, $\gamma_{\langle M \rangle - \langle M_x O_y \rangle}^{\text{interaction}}$, represents the chemical interaction between the crystalline oxide film and the metal substrate across the interface (see also above) and the mismatch contribution, $\gamma_{\langle M \rangle - \langle M_x O_y \rangle}^{\text{mismatch}}$, is due to the mismatch between the lattices of the metal substrate and the crystalline oxide film at the interface plane. Here it is noted that, an enthalpy term as present in Eq. (2.3) is absent in Eq. (2.4a) of the crystalline-crystalline interface energy, since for the case of a fully coherent oxide film, the changes in the metal atom positions at the interface are assumed to be negligible small, and otherwise a possible change in the positions of the substrate metal atoms at the interface is accounted for in the misfit dislocation energy term.

For a fully coherent crystalline-crystalline interface, $\langle M \rangle - \langle M_x O_y \rangle$, all lattice mismatch is accommodated fully elastically by the thin, epitaxially grown oxide film. This limiting case, which results in a homogeneous strain² in the epitaxial oxide film, will be further referred to as the '*elastic regime*' (Fig. 2.2). With increasing oxide-film thickness, as well as initially for $\langle M \rangle - \langle M_x O_y \rangle$ systems of large initial lattice mismatch (larger than, say, $\sim 7\%$), any homogeneous mismatch/growth strain in the crystalline oxide film may partly or fully be relaxed by built-in misfit dislocations at the metal/oxide interface (see Refs. [16, 17]). This intermediate case is characterized by a residual homogeneous strain and misfit dislocations in the crystalline oxide film and will be further referred to as the '*mixed regime*' (Fig. 2.2). Upon further increase of the oxide-film thickness, more and more misfit dislocations are generated at the semi-coherent $\langle M \rangle - \langle M_x O_y \rangle$ interface in the crystalline

² If the lateral extent of the oxide film is not infinite, as is the case for e.g., coherent oxide islands on the bare metal surface, a heterogeneous strain occurs in the oxide. However, it is assumed in our model that the system (i.e., metal and oxide film) is of infinite length in the directions parallel to the metal/oxide interface, which is a valid assumption for the very thin (< 5 nm) oxide overgrowths considered in this study.

oxide film until all residual strain within the grown oxide film has been fully relaxed. Then the (fully) '*plastic regime*' has been entered (see Fig. 2.2).

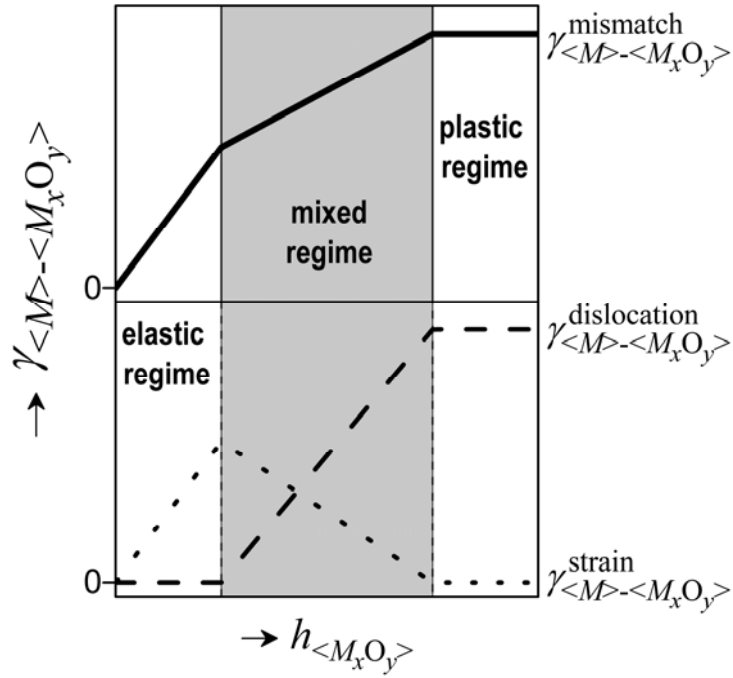


Figure 2.2. Schematic drawing of the separate energy contributions due to (i) residual homogeneous strain, $\gamma_{\langle M \rangle - \langle M_x O_y \rangle}^{\text{strain}}$, and (ii) misfit dislocations, $\gamma_{\langle M \rangle - \langle M_x O_y \rangle}^{\text{dislocation}}$, to the total mismatch energy, $\gamma_{\langle M \rangle - \langle M_x O_y \rangle}^{\text{mismatch}}$, as function of crystalline oxide-film thickness $h_{\langle M_x O_y \rangle}$ in the various growth regimes. The elastic, mixed and plastic regimes, as defined in Sec. 2.2.2, have been indicated.

The relaxation of growth strain in the crystalline oxide film by the generation of dislocations (plastic deformation) is accounted for by substituting the original mismatch contribution, $\gamma_{\langle M \rangle - \langle M_x O_y \rangle}^{\text{mismatch}}$, in Eq. (2.4a) (as introduced in Ref. [1]) by two separate energy contributions $\gamma_{\langle M \rangle - \langle M_x O_y \rangle}^{\text{strain}}$ and $\gamma_{\langle M \rangle - \langle M_x O_y \rangle}^{\text{dislocation}}$ due to the residual homogeneous strain and the induced misfit dislocations in the crystalline oxide film, respectively. Hence [see Eq. (2.4a)]:

$$\gamma_{\langle M \rangle - \langle M_x O_y \rangle} = \gamma_{\langle M \rangle - \langle M_x O_y \rangle}^{\text{interaction}} + \gamma_{\langle M \rangle - \langle M_x O_y \rangle}^{\text{strain}} + \gamma_{\langle M \rangle - \langle M_x O_y \rangle}^{\text{dislocation}}. \quad (2.4b)$$

In the mixed regime the residual homogeneous strain can thought to be superimposed on the periodic, inhomogeneous strain field, resulting from the sum of strain fields associated with each of the misfit dislocations. With increasing density of misfit dislocations at the semi-coherent $\langle M \rangle - \langle M_x O_y \rangle$ interface, the strain contribution, $\gamma_{\langle M \rangle - \langle M_x O_y \rangle}^{\text{strain}}$, decreases, whereas the

dislocation term, $\gamma_{\langle M \rangle - \langle M_x O_y \rangle}^{\text{dislocation}}$, increases (see Fig. 2.2 and e.g., Ref. [17]). Because the energy contributions due to the residual homogeneous strain and the misfit dislocations in the crystalline oxide film are attributed (here) to the interface energy instead of to the bulk energy of the film [see Eq. (2.1) in Sec. 2.2.1], the interface energy $\gamma_{\langle M \rangle - \langle M_x O_y \rangle}$ exhibits a pronounced dependence on the oxide-film thickness (see Fig. 2.2).

The interaction energy contribution, $\gamma_{\langle M \rangle - \langle M_x O_y \rangle}^{\text{interaction}}$, per unit area of the $\langle M \rangle - \langle M_x O_y \rangle$ interface [see Eq. (2.4b)] is given by

$$\gamma_{\langle M \rangle - \langle M_x O_y \rangle}^{\text{interaction}} = \frac{p \Delta H_{\text{O in } \langle M \rangle}^{\infty}}{A_{\langle O \rangle}^{\text{unstr}}} (1 + \bar{\epsilon}_{11})(1 + \bar{\epsilon}_{22}), \quad (2.4c)$$

where p is a constant fraction that depends on the shape of the Wigner-Seitz cell of oxygen in the oxide (*here*: $p = \frac{1}{3}$; see Ref. 1); $\Delta H_{\text{O in } \langle M \rangle}^{\infty}$ denotes the enthalpy of mixing at infinite dilution of 1-mol O(g) atoms in the solid crystalline metal $\langle M \rangle$; the molar interface area $A_{\langle O \rangle}^{\text{unstr}}$ is defined as the area of the $\langle M \rangle - \langle M_x O_y \rangle$ interface containing 1-mol O atoms for the case of the *unstrained* crystalline oxide film, which differs from the corresponding molar interface area $A_{\langle O \rangle}$ in the original treatment [1], as defined for the *strained* crystalline oxide film. To correct for the area difference between the strained and unstrained crystalline oxide film, the term $(1 + \bar{\epsilon}_{11})(1 + \bar{\epsilon}_{22})$ is introduced here, where $\bar{\epsilon}_{11}$ and $\bar{\epsilon}_{22}$ denote the *residual*, homogeneous, normal strains in the oxide in perpendicular directions 1 and 2, respectively, at the $\langle M \rangle - \langle M_x O_y \rangle$ interface plane.

The strain energy $\gamma_{\langle M \rangle - \langle M_x O_y \rangle}^{\text{strain}}$ due to the *residual* homogeneous strain in the crystalline oxide film, is obtained from

$$\gamma_{\langle M \rangle - \langle M_x O_y \rangle}^{\text{strain}} = h_{\langle M_x O_y \rangle} \bar{\sigma}_{ij} \bar{\epsilon}_{ij} = h_{\langle M_x O_y \rangle} C_{ijkl} \bar{\epsilon}_{ij} \bar{\epsilon}_{kl} \quad (i, j, k, l = 1, 2, 3), \quad (2.4d)$$

where $\bar{\sigma}_{ij}$ is the stress tensor, C_{ijkl} is the fourth-rank stiffness tensor and $\bar{\epsilon}_{ij}$ is the *residual* homogeneous strain tensor of $\langle M_x O_y \rangle$. The perpendicular directions 1 and 2 are parallel to the $\langle M \rangle - \langle M_x O_y \rangle$ interface plane, whereas direction 3 is perpendicular to the interface plane.

The *initial* lattice mismatch within the $\langle M \rangle - \langle M_x O_y \rangle$ interface plane is characterized by the mismatch values f_1 and f_2 in the two perpendicular directions 1 and 2 within the interface plane:

$$f_i = \frac{{}^i a_{\langle M \rangle} - {}^i a_{\langle M_x O_y \rangle}}{{}^i a_{\langle M_x O_y \rangle}} \quad (i = 1, 2), \quad (2.5a)$$

where ${}^i a_{\langle M \rangle}$ and ${}^i a_{\langle M_x O_y \rangle}$ denote values of *unstrained* lattice spacings corresponding to direction 1 and 2 of the metal substrate $\langle M \rangle$ and the $\langle M_x O_y \rangle$ film, respectively. For the case of a semi-coherent $\langle M \rangle - \langle M_x O_y \rangle$ interface in the mixed regime (see Fig. 2.2), the *residual* normal strains, $\bar{\epsilon}_{ii}$, within the $\langle M_x O_y \rangle$ film in directions 1 and 2 depend on the corresponding *residual* lattice spacings, ${}^i \bar{a}_{\langle M_x O_y \rangle}$, of the $\langle M_x O_y \rangle$ film according to

$$\bar{\epsilon}_{ii} = \frac{{}^i \bar{a}_{\langle M_x O_y \rangle} - {}^i a_{\langle M_x O_y \rangle}}{{}^i a_{\langle M_x O_y \rangle}} \quad (i = 1, 2). \quad (2.5b)$$

Finally, the contribution of the dislocation energy, $\gamma_{\langle M \rangle - \langle M_x O_y \rangle}^{\text{dislocation}}$, to the total interface energy, $\gamma_{\langle M \rangle - \langle M_x O_y \rangle}$ in Eq. (2.4b), equals the sum of the total energies of the arrays of misfit dislocations, ${}^1 \gamma_{\langle M \rangle - \langle M_x O_y \rangle}^{\text{dislocation}}$ and ${}^2 \gamma_{\langle M \rangle - \langle M_x O_y \rangle}^{\text{dislocation}}$, with Burgers vectors parallel to directions 1 and 2, respectively:

$$\gamma_{\langle M \rangle - \langle M_x O_y \rangle}^{\text{dislocation}} = {}^1 \gamma_{\langle M \rangle - \langle M_x O_y \rangle}^{\text{dislocation}} + {}^2 \gamma_{\langle M \rangle - \langle M_x O_y \rangle}^{\text{dislocation}}. \quad (2.4e)$$

In the following Sec. 2.2.3 various treatments are outlined to estimate the misfit-dislocation energy terms ${}^i \gamma_{\langle M \rangle - \langle M_x O_y \rangle}^{\text{dislocation}}$ ($i = 1, 2$).

2.2.3. Misfit-dislocation energy

A) The Semi-infinite Overgrowth (SIO) approach

In the Frank-van der Merwe approach (e.g., Refs. [17, 18]) the energy of an array of misfit dislocations at a semi-coherent solid-solid interface is calculated by adopting an interfacial

force between the atoms on each side of the interface that varies periodically with the atomic registry (e.g., Refs. [17, 18]).

In the semi-infinite overgrowth (SIO) approach, the limiting case of a semi-infinite (i.e., infinitely thick) overgrowth (*here*: the $\langle M_x O_y \rangle$ oxide film) on top of a semi-infinite substrate (*here*: the metal substrate $\langle M \rangle$) is considered. Accordingly, all mismatch is assumed to be fully compensated by a rectangular grid of misfit dislocations at the interface, i.e., only the plastic regime is considered. Further, a sinusoidal interfacial potential energy density function between the substrate with lattice spacings ${}^1a_{\langle M \rangle}$ and ${}^2a_{\langle M \rangle}$ and the overgrowth with lattice spacings ${}^1a_{\langle M_x O_y \rangle}$ and ${}^2a_{\langle M_x O_y \rangle}$ is adopted that is a function of the relative displacements of the atoms on either side of the interface with respect to their equilibrium positions in the unstrained case. Additional assumptions of the SIO approach are listed in Table 2.1.

The periodic distance, d_i , between adjacent, parallel misfit dislocations at the interface is equal to the vernier period of the mismatch, P_i , as defined in units of the lattice spacing of the overgrowth:

$$d_i = P_i {}^i a_{\langle M_x O_y \rangle} = (P_i \pm 1) {}^i a_{\langle M \rangle} \quad (i = 1, 2). \quad (2.6a)$$

Then, a reference lattice with lattice spacings c_i ($i = 1, 2$) can be defined by

$$d_i = \left(P_i \pm \frac{1}{2} \right) c_i \quad (i = 1, 2) \quad (2.6b)$$

with

$$c_i = \frac{2 {}^i a_{\langle M \rangle} {}^i a_{\langle M_x O_y \rangle}}{{}^i a_{\langle M \rangle} + {}^i a_{\langle M_x O_y \rangle}} \quad (i = 1, 2). \quad (2.6c)$$

Accordingly, the lattices of the metal substrate, $\langle M \rangle$, and the crystalline oxide film, $\langle M_x O_y \rangle$, can be conceived as generated from the reference lattice by a homogeneous compression or a homogeneous expansion equal to $\frac{1}{2} c_i$ of the span $(P_i + 1)c_i$ or $P_i c_i$, respectively [17].

Table 2.1. Assumptions made in the Semi-Infinite Overgrowth (SIO), Large Dislocation Distance (LDD), Extrapolation (EXTR), First Approximation (APPR), Ball (BALL) and Volterra (VOLT) approaches, for estimation of the misfit-dislocation energy (see Sec. 2.2.3). The approximate thickness range (in oxide monolayers; ML) for which an approach is valid has also been indicated.

Assumption	SIO	LDD	EXTR	APPR	BALL	VOLT
$\langle M \rangle$ and $\langle M_x O_y \rangle$ phase:						
- initial dislocations present	no	no	no	no	no	no
- Hookeian behavior (outside dislocation core)	yes	yes	yes	yes	yes	yes
- isotropic	yes	yes	yes	yes	yes	yes
Dislocations:						
- long and straight	yes	yes	yes	yes	yes	yes
- located at the interface	yes	yes	yes	yes	yes	yes
- only edge character	yes	yes	yes	yes	yes	no
- Burgers vectors in interface plane	yes	yes	yes	yes	yes	no
- arranged in a rectangular grid	yes	yes	yes	yes	yes	yes
- regularly spaced	yes	yes	yes	yes	yes	yes
- dislocation core energy included	no	no	no	no	no	yes
- interactions at crossings of dislocation lines	no	no	no	no	no	no
- same dislocation energy as in bulk	no	no	no	no	no	yes
$\langle M \rangle$–$\langle M_x O_y \rangle$ interface:						
- atomically smooth interface	yes	yes	yes	yes	yes	yes
- normal stress in interface plane	no	no	no	no	no	no
- strain gradient perpendicular to interface plane	yes	yes	yes	yes	no	yes
- interaction of dislocations with surface	no	no	yes	yes	yes	yes
Approximate thickness range (ML)	∞	> 20	> 10	several	< 10	> 20

The maximum amplitude W_0 of the interfacial potential energy density function determines the maximum interfacial force for disregistered atoms on each side of the interface and depends on the strength of bonding between the adjacent solids and hence on the adhesion

energy. Estimations for W_0 based on simple bond concepts lead to the value of one third of the adhesion energy, $\gamma_{\langle M \rangle - \langle M_x O_y \rangle}^{\text{adhesion}}$ [17, 19], i.e.,

$$W_0 = \frac{1}{3} \gamma_{\langle M \rangle - \langle M_x O_y \rangle}^{\text{adhesion}} = \frac{1}{3} \left(\gamma_{\langle M \rangle - \text{amb}} + \gamma_{\langle M_x O_y \rangle - \text{amb}} - \gamma_{\langle M \rangle - \langle M_x O_y \rangle}^{\text{interaction}} \right), \quad (2.6d)$$

where $\gamma_{\langle M \rangle - \text{amb}}$ and $\gamma_{\langle M_x O_y \rangle - \text{amb}}$ are the surface energies of the metal $\langle M \rangle$ and the crystalline oxide $\langle M_x O_y \rangle$ in contact with the ambient (see Sec. 2.2.1) and the interaction energy $\gamma_{\langle M \rangle - \langle M_x O_y \rangle}^{\text{interaction}}$ as defined in Sec. 2.2.2. Further, the interfacial shear modulus μ_i is related to the amplitude W_0 by [17]:

$$\mu_i = \frac{2\pi W_0}{c_i} \quad (i = 1, 2). \quad (2.6e)$$

This results in the following expression for the energy ${}^i \gamma_{\langle M \rangle - \langle M_x O_y \rangle}^{\text{dislocation}}$ of an array of misfit dislocations with a Burgers vector parallel to direction i , per unit area of the semi-coherent $\langle M \rangle - \langle M_x O_y \rangle$ interface, according to the SIO approach [17]:

$${}^i \gamma_{\langle M \rangle - \langle M_x O_y \rangle}^{\text{dislocation}} = \frac{\mu_i c_i}{4\pi^2} \left\{ \frac{1}{2} \left[1 + \left(\frac{1}{2} \beta_i - 1 \right) B_i - \beta_i \ln(1 - B_i^2) \right] \right\} \quad (i = 1, 2). \quad (2.7a)$$

The parameter B_i in Eq. (2.7a) is defined as

$$B_i = \sqrt{1 + \beta_i^2} - \beta_i \quad (i = 1, 2), \quad (2.7b)$$

with

$$\beta_i = \frac{2\pi \lambda^{\text{av}} c_i}{d_i \mu_i} \quad (i = 1, 2). \quad (2.7c)$$

The parameter λ^{av} in Eq. (2.7c) expresses the average elastic properties of the substrate-overgrowth system according to

$$\frac{1}{\lambda^{\text{av}}} = \frac{1 - \nu_{\langle M \rangle}^{\text{el}}}{\mu_{\langle M \rangle}^{\text{el}}} + \frac{1 - \nu_{\langle M_x O_y \rangle}^{\text{el}}}{\mu_{\langle M_x O_y \rangle}^{\text{el}}}, \quad (2.7d)$$

where $\mu_{\langle M \rangle}^{\text{el}}$ and $\mu_{\langle M_x O_y \rangle}^{\text{el}}$ and $\nu_{\langle M \rangle}^{\text{el}}$ and $\nu_{\langle M_x O_y \rangle}^{\text{el}}$ are the shear moduli and the Poisson ratios of the metal substrate, $\langle M \rangle$, and the oxide overgrowth, $\langle M_x O_y \rangle$, respectively.

The energy term ${}^i \gamma_{\langle M \rangle - \langle M_x O_y \rangle}^{\text{dislocation}}$ according to Eq. (2.7a) incorporates the energy of disregistry at the interface, as well as the energy of the localized, inhomogeneous strain fields around each misfit dislocation (as is also the case for the following approaches presented in Secs. 2.2.3B–F). In the SIO approach, the strain field radius of the dislocations is taken equal to half of the dislocation spacing (i.e., $\frac{1}{2} d_i$).

B) The Large Dislocation Distance (LDD) approach

For very small initial lattice mismatches and thick overgrowths (more than 20 atom layers), the expression for the dislocation energy as obtained using the SIO approach for the case of a semi-infinite overgrowth on a semi-infinite substrate [see Eq. (2.7a) in Sec. 2.2.3A] can also be used to estimate the corresponding dislocation energy if the overgrowth is of *finite* thickness. Further assumptions of this so-called large dislocation distance (LDD) approach are listed in Table 2.1.

Since residual homogeneous strain can be present in an overgrowth of finite thickness, the unstrained lattice spacing ${}^i a_{\langle M_x O_y \rangle}$ of the overgrowth in Eqs. (2.6a) to (2.6c) of the SIO approach in Sec. 2.2.3A has to be replaced by the residual strain affected lattice spacing ${}^i \bar{a}_{\langle M_x O_y \rangle}$, which also influences the calculated constants μ_i , B_i and β_i [see Eqs. (2.6e), (2.7b) and (2.7c), respectively]. Further, for thick overgrowths with large dislocation distances d_i , it is assumed that $\frac{c_i^2}{d_i^2} \approx 0$. This results in the following expression for the energy ${}^i \gamma_{\langle M \rangle - \langle M_x O_y \rangle}^{\text{dislocation}}$ of an array of misfit dislocations with a Burgers vector parallel to direction i , per unit area of the semi-coherent $\langle M \rangle - \langle M_x O_y \rangle$ interface, according to the LDD approach [20]:

$${}^i \gamma_{\langle M \rangle - \langle M_x O_y \rangle}^{\text{dislocation}} = \frac{\lambda^{\text{av}} c_i^2}{2\pi d_i} \left[\ln \left(\frac{\mu_i d_i}{4\pi \lambda^{\text{av}} c_i} \right) + 1 \right] \quad (i = 1, 2). \quad (2.8)$$

C) The Extrapolation (EXTR) approach

The SIO model for the case of a semi-infinite overgrowth [see Eq. (2.7a) in Sec. 2.2.3A] can be extrapolated to the case of a thin overgrowth of finite thickness, $h_{\langle M_x O_y \rangle}$, by adopting the

so-called extrapolation (EXTR) approach. Then, as for the LDD approach in Sec. 2.2.3B, the unstrained lattice spacing ${}^i a_{\langle M_x O_y \rangle}$ of the overgrowth has to be replaced by the residual strain affected lattice spacing ${}^i \bar{a}_{\langle M_x O_y \rangle}$. However, in the EXTR approach the interactions of the individual strain fields of the dislocations with each other and with the free surface are now approximately accounted for (see Table 2.1) by defining an effective range for the strain field of a dislocation. In the SIO approach, the strain field radius of the dislocations is taken equal to half of the dislocation spacing (i.e., $\frac{1}{2} d_i$), whereas in the EXTR approach the strain field radius is taken equal to $\frac{1}{2} q_i$ [21], which is defined by:

$$q_i = \begin{cases} \frac{4h_{\langle M_x O_y \rangle} d_i^2}{d_i^2 + 4h_{\langle M_x O_y \rangle}^2}; d_i \geq 2h_{\langle M_x O_y \rangle} \\ d_i; & d_i \leq 2h_{\langle M_x O_y \rangle} \end{cases} \quad (i = 1, 2) . \quad (2.9a)$$

This results in the following expression for the energy ${}^i \gamma_{\langle M \rangle - \langle M_x O_y \rangle}^{\text{dislocation}}$ of an array of misfit dislocations with a Burgers vector parallel to direction i , per unit area of the semi-coherent $\langle M \rangle - \langle M_x O_y \rangle$ interface, according to the EXTR approach [21]:

$${}^i \gamma_{\langle M \rangle - \langle M_x O_y \rangle}^{\text{dislocation}} = \frac{q_i \mu_i c_i}{d_i 4\pi^2} \left\{ \frac{1}{2} \left[1 + \left(\frac{1}{2} \beta_i^* - 1 \right) B_i^* - \beta_i^* \ln(1 - B_i^{*2}) \right] \right\} \quad (i = 1, 2) , \quad (2.9b)$$

where the parameters B_i^* and β_i^* are calculated according to Eqs. (2.7b) and (2.7c) by replacing d_i by q_i .

The EXTR approach is only a good approximation for films thicker than about ten atom layers, because for smaller film thicknesses the adopted interfacial potential energy density function (as taken from the SIO approach for semi-infinite overgrowths; see Sec. 2.2.3A) differs too much from the actual potential energy density function at the interface between a thin film and a semi-infinite substrate [17].

D) The First Approximation (APPR) approach

In the first approximation (APPR) approach [17], a different atom displacement function is derived (i.e., different from that used for the SIO, LDD and EXTR approaches; e.g., Refs. [17, 18]) to arrive at an improved description for the disregistry of the atoms at the interface for the case of a *finite* overgrowth on a semi-infinite substrate (see Table 2.1).

This results in the following expression for the energy ${}^i\gamma_{\langle M \rangle - \langle M_x O_y \rangle}^{\text{dislocation}}$ of an array of misfit dislocations with a Burgers vector parallel to direction i , per unit area of the semi-coherent $\langle M \rangle - \langle M_x O_y \rangle$ interface, according to the APPR approach [17]:

$${}^i\gamma_{\langle M \rangle - \langle M_x O_y \rangle}^{\text{dislocation}} = \frac{\mu_i c_i}{8\pi^2} (1 - B_i + \beta_i B_i) + \frac{\mu_i c_i}{4\pi^2} \beta_i \sum_{n=1}^{\infty} \frac{(\sinh^2 \zeta_i - \zeta_i^2) B_i^{2n}}{n \lambda^{\text{av}} \left[\frac{(\sinh^2 \zeta_i - \zeta_i^2) \cdot (1 - \nu_{\langle M \rangle})}{\mu_{\langle M \rangle}} + \frac{(\sinh \zeta_i \cosh \zeta_i - \zeta_i) \cdot (1 - \nu_{\langle M_x O_y \rangle})}{\mu_{\langle M_x O_y \rangle}} \right]}, \quad (2.10a)$$

$(i = 1, 2)$

with

$$\zeta_i = \frac{2\pi n}{d_i} h_{\langle M_x O_y \rangle}. \quad (2.10b)$$

The APPR approach is a useful approximation for finite overgrowths, but underestimates the strain energy associated with misfit dislocations in the monolayer regime [17].

E) The Ball approach

In the approach by Ball, which is also based on the theoretical concepts proposed by Frank and van der Merwe [16, 22], a parabolic representation of the interfacial potential energy is used to arrive at an improved description for the disregistry of the atoms at the interface for the case of an *ultra-thin* overgrowth (up to only a few atom layers; treated as a “monolayer” of thickness $h_{\langle M_x O_y \rangle}$) on a semi-infinite substrate (see Table 2.1). In the BALL approach, the strain gradient perpendicular to the surface/interface plane is neglected, which is a reasonable assumption for ultra-thin overgrowths [17].

In the BALL approach the elastic strain in both the semi-infinite substrate and the ultra-thin overgrowth, due to the misfit dislocations, is considered. Further, the interfacial modulus μ_i [see Eq. (2.6e) in Sec. 2.2.3A] is modified (symbol: μ'_i) to approximately correct for errors introduced by the unrealistic parabolic interfacial potential energy density function [16], i.e.,

$$\mu'_i = \mu_i \frac{8}{\pi^4} \left[\sqrt{2} + \ln(1 + \sqrt{2}) \right] \quad (i = 1, 2). \quad (2.11a)$$

This results in the following expression for the energy ${}^i\gamma_{\langle M \rangle - \langle M_x O_y \rangle}^{\text{dislocation}}$ of an array of misfit dislocations with a Burgers vector parallel to direction i , per unit area of the semi-coherent $\langle M \rangle - \langle M_x O_y \rangle$ interface, according to the BALL approach [16]:

$${}^i\gamma_{\langle M \rangle - \langle M_x O_y \rangle}^{\text{dislocation}} = \frac{\mu'_i c_i}{4\pi^2} \cdot \sum_{n=1}^{\infty} \left[n^2 + n/\beta'_i + \frac{1}{2} \cdot \left(\frac{\mu'_i d_i^2}{4\pi\mu_{\langle M_x O_y \rangle} (1 - \nu_{\langle M_x O_y \rangle}) h_{\langle M_x O_y \rangle} c_i} \right) \right]^{-1} \quad (i = 1, 2), \quad (2.11b)$$

with

$$\beta'_i = \frac{2\pi\lambda^{\text{av}} c_i}{d_i \mu'_i}. \quad (2.11c)$$

F) The Volterra (VOLT) approach

In the VOLT approach, which has been extensively used by Matthews [23, 24], a theoretical treatment on the basis of an adopted interfacial potential energy density function and correspondingly derived atom displacement function (as for the approaches in Secs. 2.2.3A–E) is no longer employed. Instead, the substrate and the overgrowth are considered as a homogeneous solid with elastic properties equal to the weighted properties of the substrate and the film, i.e. without a real interface as in the aforementioned models. Thereby a variation of the chemical bond strength across the interface is not accounted for and, consequently, the VOLT approach becomes inaccurate for small film thicknesses and/or misfit strains larger than about 10-15% [21, 24]. Since Hooke's law is no longer valid within the dislocation core, in addition to the outer cut-off radius of the strain field of an individual dislocation, an inner cut-off radius has to be defined in the VOLT approach, such that the core energy is effectively included (see below).

This results in the following expression for the energy ${}^i\gamma_{\langle M \rangle - \langle M_x O_y \rangle}^{\text{dislocation}}$ of an array of misfit dislocations with a Burgers vector parallel to direction i , per unit area of the semi-coherent $\langle M \rangle - \langle M_x O_y \rangle$ interface, according to the VOLT approach [24]:

$${}^i\gamma_{\langle M \rangle - \langle M_x O_y \rangle}^{\text{dislocation}} = \frac{\lambda^{\text{av}} |\vec{b}_i|^2}{2\pi d_i} \cdot \ln \left(\frac{R_i}{|\vec{b}_i|} + 1 \right) \quad (i = 1, 2), \quad (2.12a)$$

with the outer cut-off radius of the dislocation strain field taken as

$$R_i = \begin{cases} \frac{d_i}{2}; & h_{\langle M_xO_y \rangle} \geq \frac{d_i}{2} \\ h_{\langle M_xO_y \rangle}; & h_{\langle M_xO_y \rangle} \leq \frac{d_i}{2} \end{cases} \quad (i = 1, 2). \quad (2.12b)$$

The absolute of the Burgers vector, i.e., $|\vec{b}_i|$, in the logarithmic term of Eq. (2.12a) is taken as an approximate for the inner cut-off radius of the dislocation strain field. The energy of the associated dislocation core is taking into account by adjustment (i.e. a decreasing) of the inner cut-off radius of the dislocation strain field (as approximated here by the empirical summand one in the logarithmic term of Eq. (2.12a); see Ref. [24]). As reflected by Eq. (2.12a), imperfect misfit dislocations (i.e., with realistic Burgers vectors inclined to the interface or with mixed edge-screw-character, as observed from experiment) can be considered in the calculation of the misfit-dislocation energy according to the Volterra (VOLT) approach (see Table 2.1). If the actual Burgers vector for the system under study is not known, its absolute value can be estimated by the lattice spacing of the reference lattice $|\vec{b}_i| \approx c_i$ [see Eq. (2.6c)].

2.2.4. Minimization of $\gamma_{\langle M \rangle - \langle M_xO_y \rangle}$; numerical procedure

Since the energy contributions due to residual homogeneous strain and misfit dislocations in the crystalline oxide film are assigned to the interface energy $\gamma_{\langle M \rangle - \langle M_xO_y \rangle}$, instead of to the bulk energy of the film [see Eq. (2.1) in Sec. 2.2.1], it follows that a minimum in the total Gibbs energy of the crystalline cell (thermodynamic equilibrium; see Fig. 2.1b) is attained if $\gamma_{\langle M \rangle - \langle M_xO_y \rangle}$ is at its minimum value.³ To determine the minimum value of $\gamma_{\langle M \rangle - \langle M_xO_y \rangle}$ the residual strain affected lattice spacings ${}^1\bar{a}_{\langle M_xO_y \rangle}$ and ${}^2\bar{a}_{\langle M_xO_y \rangle}$ of the crystalline $\langle M_xO_y \rangle$ film are solved simultaneously by minimization of $\gamma_{\langle M \rangle - \langle M_xO_y \rangle}$ with respect to the residual homogeneous strain in the film for a given oxide-film thickness, $h_{\langle M_xO_y \rangle}$, and growth temperature, T , i.e.,

$$\frac{\partial \gamma_{\langle M \rangle - \langle M_xO_y \rangle}}{\partial \bar{\epsilon}_{ij}} = 0, \quad (2.13)$$

³ Since the dislocations form regular arrays the crystals can be considered as almost perfect and entropy differences play an insignificant role in the following considerations [11].

where $\bar{\varepsilon}_{ij}$ is the residual strain tensor [see Eq. (2.5b) in Sec. 2.2.2]. The boundary conditions for the minimization are absence of in-plane shear strain in the $\langle M \rangle - \langle M_x O_y \rangle$ interface plane (i.e., $\bar{\varepsilon}_{12} = 0$), as well as absence of stress perpendicular to the interface plane (i.e., $\bar{\sigma}_{13} = \bar{\sigma}_{23} = \bar{\sigma}_{33} = 0$). The unstrained *initial* lattice spacings ${}^1a_{\langle M_x O_y \rangle}$ and ${}^2a_{\langle M_x O_y \rangle}$ are used as starting estimates for ${}^1\bar{a}_{\langle M_x O_y \rangle}$ and ${}^2\bar{a}_{\langle M_x O_y \rangle}$. The minimization has been performed by adopting the Nelder-Mead simplex method as implemented in Matlab [25].

2.2.5. General remarks about the misfit-dislocation energy

Different approaches for the calculation of the dislocation energy have been presented in Secs. 2.2.3A–F: While the SIO, the LDD and the VOLT approaches are suitable for thick overgrowths, the EXTR, the APPR and the BALL approaches are more suitable for thinner overgrowths (see Table 2.1), whereupon the APPR approach has the greatest overall accuracy [21].

The dislocation density in a thin film system, as observed from experiment, is generally lower than the value calculated theoretically (i.e., according to one of the equilibrium models discussed in Secs. 2.2.3A–F). This is mainly because *kinetic* constraints as illustrated by the occurring activation energies for generation and movement of dislocations due to the Peierl's force (e.g., Ref. [23]) and the formation of stacking faults and/or surface steps (which can accompany the introduction of misfit dislocations) are not accounted for in the *equilibrium* models [20]. Also, in practice, for the system under study, suitable glide systems may lack (thereby prohibiting the built-in and movement of dislocations) and/or a growth mode deviating from ideal layer-by-layer growth (e.g., islands or islands-by-layer growth) may occur. Island (-by-layer) growth mode can lead to introduction of grain and/or domain boundaries which reduces the growth strain and thereby the number of mismatch dislocations.

2.3. Energetics of chromium-oxide films on chromium substrates

The thermodynamic model presented in Sec. 2.2 is applied here to the case of a thin Cr_2O_3 film of variable, uniform thickness (“overgrowth”) on the $\{110\}$, $\{100\}$ and $\{111\}$ crystallographic faces of a single-crystalline (body centered cubic) Cr substrate, $\langle \text{Cr} \rangle$, for growth temperatures in the range of 298 K to 1000 K. An amorphous nature of the Cr_2O_3 film, further denoted as $\{\text{Cr}_2\text{O}_3\}$, competes with a crystalline $\alpha\text{-Cr}_2\text{O}_3$ (trigonal, corundum crystal

structure; see e.g., Ref. [26]) nature of the film, further designated as $\langle \text{Cr}_2\text{O}_3 \rangle$, whether or not containing misfit dislocations.

To calculate the total Gibbs energies of the amorphous $\{\text{Cr}_2\text{O}_3\}$ and crystalline $\langle \text{Cr}_2\text{O}_3 \rangle$ cells (see Fig. 2.1 and Sec. 2.4), first the corresponding bulk, surface and interfacial energy contributions [see Eq. (2.1) in Sec. 2.2.1] have to be determined (see Secs. 2.3.1, 2.3.2 and 2.3.3, respectively). The crystalline-crystalline $\langle \text{Cr} \rangle - \langle \text{Cr}_2\text{O}_3 \rangle$ interfacial energy contribution has been calculated according to the approach presented in this chapter (Sec. 2.2.2) involving different estimations of the misfit-dislocation energy contributions, ${}^i \gamma_{\langle \text{Cr} \rangle - \langle \text{Cr}_2\text{O}_3 \rangle}^{\text{dislocation}}$, to the total $\langle \text{Cr} \rangle - \langle \text{Cr}_2\text{O}_3 \rangle$ interface energy (see Sec. 2.2.3), made by employing the numerical procedure presented in Sec. 2.2.4. The corresponding bulk and surface energy contributions of the $\{\text{Cr}_2\text{O}_3\}$ and $\langle \text{Cr}_2\text{O}_3 \rangle$ cells (Secs. 2.3.1 and 2.3.2, respectively), as well as the crystalline-amorphous $\langle \text{Cr} \rangle - \{\text{Cr}_2\text{O}_3\}$ interfacial energy contribution (Sec. 2.3.3), were calculated according to the procedure described detailed in Ref. [1] (see also Chapter 3).

2.3.1. Bulk Gibbs energies of the $\{\text{Cr}_2\text{O}_3\}$ and $\langle \text{Cr}_2\text{O}_3 \rangle$ cells

The bulk Gibbs energies of formation, $\Delta G_{\{\text{Cr}_2\text{O}_3\}}^f$ and $\Delta G_{\langle \text{Cr}_2\text{O}_3 \rangle}^f$, of $\{\text{Cr}_2\text{O}_3\}$ and $\langle \text{Cr}_2\text{O}_3 \rangle$, respectively, have been taken from Ref. [27]. The bulk Gibbs energy of formation of liquid Cr_2O_3 below the glass-transition temperature has been adopted as an approximate for the value of $\Delta G_{\{\text{Cr}_2\text{O}_3\}}^f$ for amorphous $\{\text{Cr}_2\text{O}_3\}$, treated as a configurationally frozen liquid (see Ref. [1]). The corresponding molar volumes of $\{\text{Cr}_2\text{O}_3\}$ and $\langle \text{Cr}_2\text{O}_3 \rangle$ at $T_0 = 298$ K are shown in Table 2.2.

The calculated difference in bulk Gibbs energy contribution [see Eq. (2.1)], $h_{\{\text{Cr}_2\text{O}_3\}} \cdot (\Delta G_{\{\text{Cr}_2\text{O}_3\}}^f - \Delta G_{\langle \text{Cr}_2\text{O}_3 \rangle}^f) / V_{\{\text{Cr}_2\text{O}_3\}}$, per unit area of the $\langle \text{Cr} \rangle - \{\text{Cr}_2\text{O}_3\}$ interface, has been plotted in Fig. 2.3 as function of the thickness, $h_{\{\text{Cr}_2\text{O}_3\}}$, of the $\{\text{Cr}_2\text{O}_3\}$ cell for both $T_0 = 298$ K and $T = 1000$ K. Obviously, if only the bulk Gibbs energies of the competing cells are considered, the crystalline $\langle \text{Cr}_2\text{O}_3 \rangle$ cell is thermodynamically preferred. The bulk Gibbs energy difference between the competing cells decreases with increasing temperature (equal values of ΔG^f occur at the $\langle \text{Cr}_2\text{O}_3 \rangle$ melting point).

Table 2.2. Unstrained lattice parameters, \tilde{a}^0 and \tilde{c}^0 , and molar volumes, V , at $T_0 = 298$ K of $\langle \text{Cr} \rangle$ and $\langle \text{Cr}_2\text{O}_3 \rangle$. The unstrained lattice parameters and the corresponding molar volumes at a given growth temperature were calculated using the linear thermal expansion coefficient as defined by $\alpha(T) = \alpha_A + \alpha_B T + \alpha_C T^2$.

Phase	Symbol	Value	Unit	Ref.	Remark
$\langle \text{Cr} \rangle$	$\tilde{a}_{\langle \text{Cr} \rangle}^0$	2.8849×10^{-10}	m	26	
$\langle \text{Cr}_2\text{O}_3 \rangle$	$\tilde{a}_{\langle \text{Cr}_2\text{O}_3 \rangle}^0$	4.9573×10^{-10}	m	26	
	$\tilde{c}_{\langle \text{Cr}_2\text{O}_3 \rangle}^0$	13.5923×10^{-10}	m	26	
$\langle \text{Cr} \rangle$	α_A	9.983×10^{-7}	K^{-1}	} 34	for $T < 795$ K
	α_B	2.153×10^{-8}	K^{-2}		
	α_C	-1.152×10^{-11}	K^{-3}		
$\langle \text{Cr} \rangle$	α_A	1.097×10^{-5}	K^{-1}	} 34	for $T > 795$ K
	α_B	-3.402×10^{-9}	K^{-2}		
	α_C	4.089×10^{-12}	K^{-3}		
$\{\text{Cr}_2\text{O}_3\}$	α_A	1.038×10^{-5}	K^{-1}	} 35	data for poly-crystalline Cr_2O_3
	α_B	-6.244×10^{-9}	K^{-2}		
	α_C	3.186×10^{-12}	K^{-3}		
$\langle \text{Cr}_2\text{O}_3 \rangle$	α_A	1.376×10^{-5}	K^{-1}	} 35	along the a-axis
	α_B	-1.200×10^{-9}	K^{-2}		
	α_C	1.628×10^{-12}	K^{-3}		
$\langle \text{Cr}_2\text{O}_3 \rangle$	α_A	3.785×10^{-6}	K^{-1}	} 35	along the c-axis
	α_B	4.758×10^{-8}	K^{-2}		
	α_C	-1.377×10^{-12}	K^{-3}		
$\{\text{Cr}_2\text{O}_3\}$	$V_{\{\text{Cr}_2\text{O}_3\}}^0$	3.160×10^{-5}	$\text{m}^3\text{mol}^{-1}$	29	estimated (see App. 3.A in Chapter 3)
$\langle \text{Cr}_2\text{O}_3 \rangle$	$V_{\langle \text{Cr}_2\text{O}_3 \rangle}^0$	2.903×10^{-5}	$\text{m}^3\text{mol}^{-1}$	26	

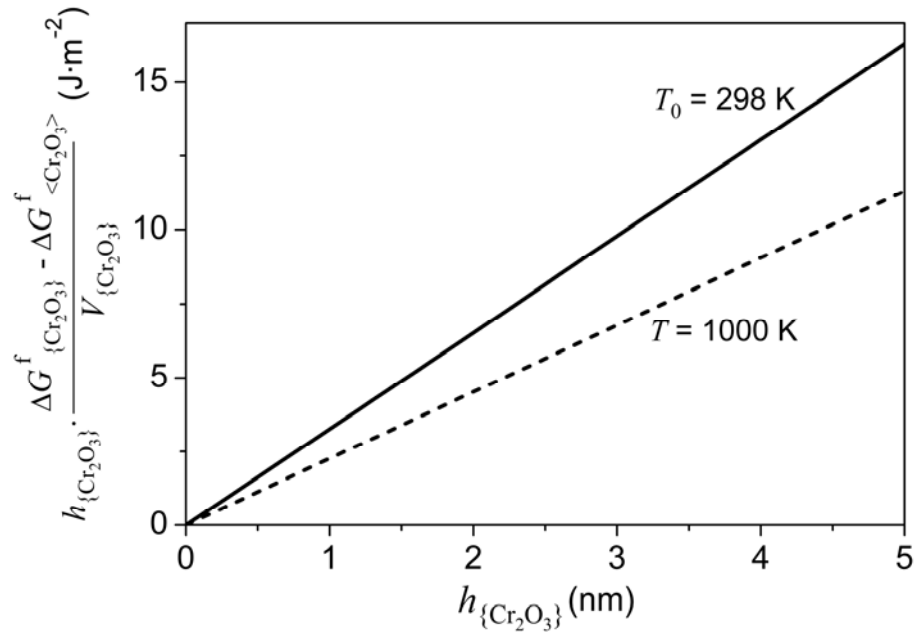


Figure 2.3. Difference in bulk Gibbs energy of formation of the amorphous $\{Cr_2O_3\}$ and the crystalline $\langle Cr_2O_3 \rangle$ cells, per unit area of the $\langle Cr \rangle - \{Cr_2O_3\}$ interface [see Eq. (2.1) in Sec. 2.2.1 and see Fig. 2.1], as function of the thickness, $h_{\{Cr_2O_3\}}$, of the amorphous $\{Cr_2O_3\}$ overgrowth at $T_0 = 298$ K and $T = 1000$ K.

2.3.2. Surface energies of the $\{Cr_2O_3\}$ and $\langle Cr_2O_3 \rangle$ cells

For the calculation of the $\langle Cr \rangle - \langle Cr_2O_3 \rangle$ interface (Sec. 2.3.3) and surface energy contributions, the following orientation relationship between the $\{110\}$, $\{100\}$ and $\{111\}$ faces of the body centered cubic (bcc) $\langle Cr \rangle$ substrate and the trigonal (corundum) $\langle Cr_2O_3 \rangle$ film has been adopted: $(110)_{\langle Cr \rangle} \parallel (0001)_{\langle Cr_2O_3 \rangle}$ and $[1\bar{1}0]_{\langle Cr \rangle} \parallel [01\bar{1}0]_{\langle Cr_2O_3 \rangle}$ (as experimentally observed for thin crystalline Cr_2O_3 films grown on $\{110\}$ and $\{111\}$ faces of single-crystalline Cr substrates by thermal oxidation [7, 12, 28]). Consequently, the $Cr_2O_3\{0001\}$, $Cr_2O_3\{\bar{1}\bar{1}26\}$ and $Cr_2O_3\{\bar{1}104\}$ crystallographic planes constitute the surfaces of the crystalline $\langle Cr_2O_3 \rangle$ overgrowths on the $Cr\{110\}$, $Cr\{100\}$ and $Cr\{111\}$ substrates, respectively.

The values adopted for the surfaces energies of the $\{Cr_2O_3\}$ and $\langle Cr_2O_3 \rangle$ cells (and their temperature dependence) have been gathered in Table 2.3. The employed temperature dependence of the $\langle Cr_2O_3 \rangle$ surface energies (Table 2.3) represents an empirical estimate as obtained from the averaged temperature dependence for various crystalline oxide surfaces

[29, 30]. The employed temperature dependence of the $\{\text{Cr}_2\text{O}_3\}$ surface energy (Table 2.3) represents an empirical estimate as obtained from the averaged temperature dependence of various liquid and amorphous oxides (see Appendix 3.B in Chapter 3) [29, 31].

Table 2.3. Surface energies, $\gamma_{\langle\text{Cr}\rangle\text{-vac}}$, $\gamma_{\langle\text{Cr}_2\text{O}_3\rangle\text{-vac}}$ and $\gamma_{\{\text{Cr}_2\text{O}_3\}\text{-vac}}$, at $T_0 = 298$ K and their temperature dependence, $\partial\gamma_{\text{phase-vac}}/\partial T$, for the differently oriented $\langle\text{Cr}\rangle$ substrates and the $\{\text{Cr}_2\text{O}_3\}$ and $\langle\text{Cr}_2\text{O}_3\rangle$ cells of the corresponding overgrowths (see Fig. 2.1), as adopted in the model calculations.

Phase	Crystallographic surface plane	$\gamma_{\text{phase-vac}}$ ($\text{J}\cdot\text{m}^{-2}$)	$\partial\gamma_{\text{phase-vac}}/\partial T$ ($\text{J}\cdot\text{m}^{-2}\cdot\text{K}^{-1}$)	Ref.
$\langle\text{Cr}\rangle$	$\{110\}$	2.62	} -3×10^{-4}	33, 36-38
	$\{100\}$	2.24		
	$\{111\}$	2.50		
$\{\text{Cr}_2\text{O}_3\}$	-	1.21	-1×10^{-4}	29, 33
$\langle\text{Cr}_2\text{O}_3\rangle$	$\{0001\}$	1.61	} -4×10^{-4}	29, 30, 32, 39
	$\{\bar{1}\bar{1}26\}$	2.47		
	$\{\bar{1}104\}$	2.57		

The literature value for the surface energy of the relaxed $\text{Cr}_2\text{O}_3\{0001\}$ surface has been obtained by atomistic lattice simulations performed at $T = 0$ K [32]. No literature values for the $\text{Cr}_2\text{O}_3\{\bar{1}\bar{1}26\}$ and $\text{Cr}_2\text{O}_3\{\bar{1}104\}$ surface energies could be found. Therefore, literature values for the energies of the relaxed $\text{Cr}_2\text{O}_3\{0001\}$ and $\text{Cr}_2\text{O}_3\{11\bar{2}0\}$ surfaces [32] have been employed to estimate the surface energy of the $\text{Cr}_2\text{O}_3\{\bar{1}\bar{1}26\}$ surface at $T = 0$ K, by conceiving the stepped $\text{Cr}_2\text{O}_3\{\bar{1}\bar{1}26\}$ surface as constituted of $\text{Cr}_2\text{O}_3\{0001\}$ and $\text{Cr}_2\text{O}_3\{\bar{1}\bar{1}20\}$ crystallographic planes (facets). Similarly, the energy of the stepped $\text{Cr}_2\text{O}_3\{\bar{1}104\}$ surface at $T = 0$ K has been estimated from literature values for the relaxed $\text{Cr}_2\text{O}_3\{0001\}$ and $\text{Cr}_2\text{O}_3\{10\bar{1}0\}$ surfaces (see Appendix 3.B in Chapter 3). The thus obtained surface energies of the concerned crystalline $\langle\text{Cr}_2\text{O}_3\rangle$ cells obey $\gamma_{\langle\text{Cr}_2\text{O}_3(0001)\rangle\text{-vac}} < \gamma_{\langle\text{Cr}_2\text{O}_3(\bar{1}\bar{1}26)\rangle\text{-vac}} < \gamma_{\langle\text{Cr}_2\text{O}_3(\bar{1}104)\rangle\text{-vac}}$ (see Table 2.3).

The surface energy at $T = 0$ K of the amorphous $\{\text{Cr}_2\text{O}_3\}$ cell (on all three crystallographic faces of the $\langle\text{Cr}\rangle$ substrate) is approximated to be $\frac{3}{4}$ of the corresponding, most densely packed crystalline oxide surface, i.e., the $\text{Cr}_2\text{O}_3\{0001\}$ surface (see Refs. [29, 33] and Appendix 3.B in Chapter 3).

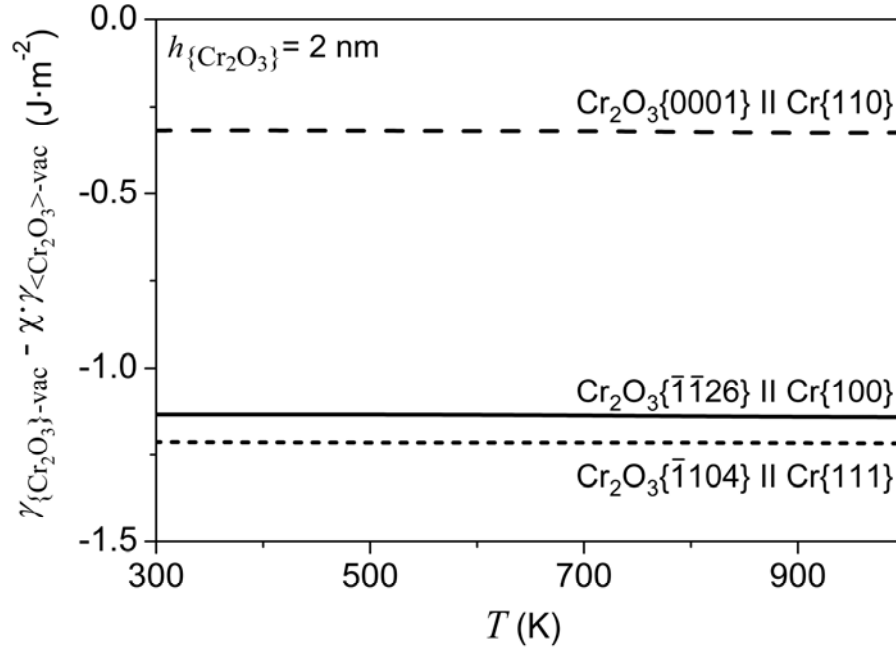


Figure 2.4. Surface energy difference, $\gamma_{\{\text{Cr}_2\text{O}_3\}\text{-vac}} - \chi \cdot \gamma_{\langle\text{Cr}_2\text{O}_3\rangle\text{-vac}}$, per unit area of the $\{\text{Cr}_2\text{O}_3\}$ surface, as function of the growth temperature, T , for the competing amorphous $\{\text{Cr}_2\text{O}_3\}$ and crystalline $\langle\text{Cr}_2\text{O}_3\rangle$ cells on the $\{110\}$, $\{100\}$ and $\{111\}$ faces of the $\langle\text{Cr}\rangle$ substrate [and for a thickness of the $\{\text{Cr}_2\text{O}_3\}$ overgrowth of $h_{\{\text{Cr}_2\text{O}_3\}} = 2$ nm; see Eq. (2.1) and Fig. 2.1]. The surface plane of the $\langle\text{Cr}_2\text{O}_3\rangle$ overgrowth corresponds with the $\text{Cr}_2\text{O}_3\{0001\}$, the $\text{Cr}_2\text{O}_3\{\bar{1}\bar{1}26\}$ and the $\text{Cr}_2\text{O}_3\{\bar{1}\bar{1}04\}$ crystallographic faces, respectively.

The calculated difference in surface energy, $\gamma_{\{\text{Cr}_2\text{O}_3\}\text{-vac}} - \chi \cdot \gamma_{\langle\text{Cr}_2\text{O}_3\rangle\text{-vac}}$ [cf. Eq. (2.1)], per unit area of the $\{\text{Cr}_2\text{O}_3\}$ surface, has been plotted in Fig. 2.4 as function of T for oxide growth on the $\text{Cr}\{110\}$, $\text{Cr}\{100\}$ and $\text{Cr}\{111\}$ substrates for $h_{\{\text{Cr}_2\text{O}_3\}} = 2$ nm. The surface energy difference decreases slightly with increasing $h_{\{\text{Cr}_2\text{O}_3\}}$ (up to about 1 nm thickness), as a consequence of the concurrent change of the surface area ratio, χ , of the competing cells in the mixed regime [see Eq. (2.2) in Sec. 2.2.1]. Therefore, the results in Fig. 2.4 have been given for a specific thickness within the plastic regime (i.e. $h_{\{\text{Cr}_2\text{O}_3\}} = 2$ nm). It follows from

Fig. 2.4 that the surface energy of the amorphous $\{\text{Cr}_2\text{O}_3\}$ cell is in all cases lower than that of the corresponding crystalline $\langle\text{Cr}_2\text{O}_3\rangle$ cell, which is a factor contributing to a possible stabilization of the amorphous $\{\text{Cr}_2\text{O}_3\}$ cell (see Sec. 2.4). The surface energy difference is least negative for the most densely packed $\text{Cr}_2\text{O}_3\{0001\}$ surface. Further, the surface energy difference increases with increasing T due to the stronger (negative) temperature dependence of the crystalline surface energy.

2.3.3. Interfacial energies of the $\{\text{Cr}_2\text{O}_3\}$ and $\langle\text{Cr}_2\text{O}_3\rangle$ cells

A) The interface energy of the crystalline-amorphous $\langle\text{Cr}\rangle-\{\text{Cr}_2\text{O}_3\}$ interface

The interface energy, $\gamma_{\langle\text{Cr}\rangle-\{\text{Cr}_2\text{O}_3\}}$, of the crystalline-amorphous $\langle\text{Cr}\rangle-\{\text{Cr}_2\text{O}_3\}$ interface is the resultant of the interaction, entropy and enthalpy contributions [cf. Eq. (2.3)]. Values for the interaction, entropy and enthalpy contributions have been calculated as function of the growth temperature and oxide-film thickness according to the procedure outlined in Ref. [1], employing the data gathered in Table 2.2 and Refs. [1, 27].

The thus obtained values of $\gamma_{\langle\text{Cr}\rangle-\{\text{Cr}_2\text{O}_3\}}^{\text{interaction}}$, $\gamma_{\langle\text{Cr}\rangle-\{\text{Cr}_2\text{O}_3\}}^{\text{entropy}}$, $\gamma_{\langle\text{Cr}\rangle-\{\text{Cr}_2\text{O}_3\}}^{\text{enthalpy}}$ and of the resultant $\gamma_{\langle\text{Cr}\rangle-\{\text{Cr}_2\text{O}_3\}}$ for amorphous oxide growth on the $\text{Cr}\{110\}$, $\text{Cr}\{100\}$ and $\text{Cr}\{111\}$ substrates have been given in Table 2.4 for various growth temperatures. It follows that the (negative) interaction contribution is the largest energy contribution, overruling the minor (positive) entropy and enthalpy contributions, resulting in a negative value for the interface energy, $\gamma_{\langle\text{Cr}\rangle-\{\text{Cr}_2\text{O}_3\}}$. The enthalpy contribution depends on the orientation of the $\langle\text{Cr}\rangle$ substrate and is larger for a more densely packed substrate surface (approximately independent of the growth temperature). The resultant interface energy, $\gamma_{\langle\text{Cr}\rangle-\{\text{Cr}_2\text{O}_3\}}$, only slightly increases (i.e., becomes less negative) with temperature, due to the increase of the interaction (via the temperature dependence of the lattice spacings) and entropy contributions.

Table 2.4. Values of the interaction, $\gamma_{\langle\text{Cr}\rangle-\{\text{Cr}_2\text{O}_3\}}^{\text{interaction}}$, entropy, $\gamma_{\langle\text{Cr}\rangle-\{\text{Cr}_2\text{O}_3\}}^{\text{entropy}}$, and enthalpy, $\gamma_{\langle\text{Cr}\rangle-\{\text{Cr}_2\text{O}_3\}}^{\text{enthalpy}}$, energy contributions to the resultant $\langle\text{Cr}\rangle-\{\text{Cr}_2\text{O}_3\}$ interfacial energy, $\gamma_{\langle\text{Cr}\rangle-\{\text{Cr}_2\text{O}_3\}}$, for the overgrowth of the amorphous $\{\text{Cr}_2\text{O}_3\}$ cell (see Fig. 2.1a) on the differently oriented $\langle\text{Cr}\rangle$ substrates for various growth temperatures, T , and film thicknesses, $h_{\{\text{Cr}_2\text{O}_3\}}$. All data have been calculated according to the procedure outlined in Ref. [1], employing the data reported in Table 2.2 and Refs. [1, 27] (see also Sec. 2.2.2).

T (K)	$\gamma_{\langle\text{Cr}\rangle-\{\text{Cr}_2\text{O}_3\}}^{\text{interaction}}$ (J m ⁻²)	$\gamma_{\langle\text{Cr}\rangle-\{\text{Cr}_2\text{O}_3\}}^{\text{entropy}}$ (J m ⁻²)	$\gamma_{\langle\text{Cr}\rangle-\{\text{Cr}_2\text{O}_3\}}^{\text{enthalpy}}$ (J m ⁻²)			$\gamma_{\langle\text{Cr}\rangle-\{\text{Cr}_2\text{O}_3\}}$ (J m ⁻²)		
			{110}	{100}	{111}	{110}	{100}	{111}
298	-1.73	0.07	0.25	0.17	0.10	-1.42	-1.49	-1.56
500	-1.71	0.11	0.24	0.17	0.10	-1.35	-1.50	-1.42
1000	-1.56	0.22	0.24	0.17	0.10	-1.10	-1.17	-1.24

B) The interface energy of the crystalline-crystalline $\langle\text{Cr}\rangle-\langle\text{Cr}_2\text{O}_3\rangle$ interface

The interface energy, $\gamma_{\langle\text{Cr}\rangle-\langle\text{Cr}_2\text{O}_3\rangle}$, of the crystalline-crystalline $\langle\text{Cr}\rangle-\langle\text{Cr}_2\text{O}_3\rangle$ interface is the resultant of the interaction contribution and the mismatch contribution [Eq. (2.4a)], which is latter further subdivided into a contribution due to the presence of residual strain in the $\langle\text{Cr}_2\text{O}_3\rangle$ overgrowth and a contribution due to the misfit dislocations at the $\langle\text{Cr}\rangle-\langle\text{Cr}_2\text{O}_3\rangle$ interface [Eq. (2.4b)]. Values for the interaction and mismatch contributions have been calculated as function of the growth temperature and oxide-film thickness according to the numerical procedure outlined in Sec. 2.2.4, employing Eqs. (2.4c) to (2.4e) and (2.5b) and the data reported in Tables 2.2, 2.3, 2.5, 2.6 and Refs. [1, 27]. The calculations have been performed for each of the different expressions of the misfit-dislocation energy contribution, $\gamma_{\langle\text{Cr}\rangle-\langle\text{Cr}_2\text{O}_3\rangle}^{\text{dislocation}}$, presented in Secs. 2.2.3B–F. The thus obtained resultant interfacial energies, $\gamma_{\langle\text{Cr}\rangle-\langle\text{Cr}_2\text{O}_3\rangle}$, have been plotted in Figs. 2.5a-c as function of the crystalline oxide-film thickness, $h_{\langle\text{Cr}_2\text{O}_3\rangle}$, for a $\langle\text{Cr}_2\text{O}_3\rangle$ overgrowth on the Cr{110}, Cr{100} and Cr{111} substrates, respectively. Additionally, values of $\gamma_{\langle\text{Cr}\rangle-\langle\text{Cr}_2\text{O}_3\rangle}$ have been plotted in Fig. 2.5 for the two limiting cases that (i) all lattice mismatch is fully accommodated by either elastic strain (i.e., only the elastic regime is considered; as calculated according to Ref. [1]) or (ii) all

lattice mismatch is fully accommodated by misfit dislocations (i.e., only the plastic regime is considered; as calculated using the SIO approach discussed in Sec. 2.2.3A). The equivalent thickness in number of oxide monolayers (see abscissa at top of Fig. 2.5) has been obtained by taking the approximate thickness $\tilde{c}_{\langle\text{Cr}_2\text{O}_3\rangle}^0 \cong 0.23 \text{ nm}$.

Table 2.5. Single-crystal elastic compliances, C_{ij} , shear modulus, μ^{el} , and Poisson ratios, ν^{el} , of $\langle\text{Cr}\rangle$ and $\langle\text{Cr}_2\text{O}_3\rangle$ as taken from Refs. [40, 41]. The abbreviation 'n.a.' stands for 'not available' (to indicate that no literature values or estimates are available).

Symbol	Unit	$\langle\text{Cr}\rangle$	$\langle\text{Cr}_2\text{O}_3\rangle$
C_{11}	Pa	355.0×10^9	374×10^9
C_{12}	Pa	46.0×10^9	148×10^9
C_{13}	Pa	C_{12}	175×10^9
C_{14}	Pa	0	-19×10^9
C_{33}	Pa	C_{11}	362×10^9
C_{44}	Pa	104.0×10^9	159×10^9
$\partial C_{11}/\partial T$	$\text{Pa}\cdot\text{K}^{-1}$	-2.0×10^7	n.a.
$\partial C_{22}/\partial T$	$\text{Pa}\cdot\text{K}^{-1}$	6.0×10^7	n.a.
$\partial C_{44}/\partial T$	$\text{Pa}\cdot\text{K}^{-1}$	-1.0×10^7	n.a.
μ^{el}	Pa	120.4×10^9	187×10^9
ν^{el}	-	0.193	0.192
$\partial \mu^{\text{el}}/\partial T$	$\text{Pa}\cdot\text{K}^{-1}$	-1.7×10^7	n.a.
$\partial \nu^{\text{el}}/\partial T$	K^{-1}	6×10^{-5}	n.a.

To discuss these results it is first noted that a much larger initial lattice mismatch, f , [see Eq. (2.5a)] exists along the defined direction 1 (i.e., $f_1 \sim -18\%$ to -14%) than along the perpendicular direction 2 (i.e., $f_2 \sim -3\%$ to $+1\%$) within the $\langle\text{Cr}\rangle$ – $\langle\text{Cr}_2\text{O}_3\rangle$ interface plane (see Table 2.6). Consequently, a large anisotropic strain resides within the $\langle\text{Cr}_2\text{O}_3\rangle$ film at the onset of growth: a large compressive stress along direction 1 and either a small tensile or small compressive stress along direction 2. Since the thermal expansion coefficients of $\langle\text{Cr}\rangle$ and $\langle\text{Cr}_2\text{O}_3\rangle$ are of the same order of magnitude (Table 2.2), the initial lattice mismatch

values f_1 and f_2 only slightly change (i.e., increase with about 0.2%) with increasing temperature up to 1000 K.

Table 2.6. The directions 1 and 2 in the $\langle \text{Cr} \rangle - \langle \text{Cr}_2\text{O}_3 \rangle$ interface plane and the unstrained lattice spacings in the same directions of the $\langle \text{Cr} \rangle$ substrate, $^1a_{\langle \text{Cr} \rangle}$ and $^2a_{\langle \text{Cr} \rangle}$, and of the $\langle \text{Cr}_2\text{O}_3 \rangle$ overgrowth, $^1a_{\langle \text{Cr}_2\text{O}_3 \rangle}$ and $^2a_{\langle \text{Cr}_2\text{O}_3 \rangle}$, at $T_0 = 298$ K for the $\langle \text{Cr}_2\text{O}_3 \rangle$ overgrowth on the $\{110\}$, $\{100\}$ and $\{111\}$ crystallographic faces of the $\langle \text{Cr} \rangle$ substrate. The corresponding *initial* lattice mismatches f_1 and f_2 along the perpendicular directions 1 and 2 [see Eq. (2.5a) in Sec. 2.2.2] have also been indicated.

Symbol	on Cr $\{110\}$	on Cr $\{100\}$	on Cr $\{111\}$
direction 1	$[1\bar{1}0]_{\langle \text{Cr} \rangle} \parallel [11\bar{2}0]_{\langle \text{Cr}_2\text{O}_3 \rangle}$	$[0\bar{1}0]_{\langle \text{Cr} \rangle} \parallel [11\bar{2}1]_{\langle \text{Cr}_2\text{O}_3 \rangle}$	$[1\bar{1}0]_{\langle \text{Cr} \rangle} \parallel [11\bar{2}0]_{\langle \text{Cr}_2\text{O}_3 \rangle}$
direction 2	$[001]_{\langle \text{Cr} \rangle} \parallel [1\bar{1}00]_{\langle \text{Cr}_2\text{O}_3 \rangle}$	$[001]_{\langle \text{Cr} \rangle} \parallel [1\bar{1}00]_{\langle \text{Cr}_2\text{O}_3 \rangle}$	$[\bar{1}\bar{1}2]_{\langle \text{Cr} \rangle} \parallel [2\bar{2}01]_{\langle \text{Cr}_2\text{O}_3 \rangle}$
$^1a_{\langle \text{Cr} \rangle}$	$\sqrt{2}\tilde{a}_{\langle \text{Cr} \rangle}$	$2\tilde{a}_{\langle \text{Cr} \rangle}$	$\sqrt{2}\tilde{a}_{\langle \text{Cr} \rangle}$
$^1a_{\langle \text{Cr}_2\text{O}_3 \rangle}$	$\tilde{a}_{\langle \text{Cr}_2\text{O}_3 \rangle}$	$\frac{1}{3}\sqrt{9\tilde{a}_{\langle \text{Cr}_2\text{O}_3 \rangle}^2 + \tilde{c}_{\langle \text{Cr}_2\text{O}_3 \rangle}^2}$	$\tilde{a}_{\langle \text{Cr}_2\text{O}_3 \rangle}$
$^2a_{\langle \text{Cr} \rangle}$	$3\tilde{a}_{\langle \text{Cr} \rangle}$	$3\tilde{a}_{\langle \text{Cr} \rangle}$	$3\sqrt{\frac{3}{2}}\tilde{a}_{\langle \text{Cr} \rangle}$
$^2a_{\langle \text{Cr}_2\text{O}_3 \rangle}$	$\sqrt{3}\tilde{a}_{\langle \text{Cr}_2\text{O}_3 \rangle}$	$\sqrt{3}\tilde{a}_{\langle \text{Cr}_2\text{O}_3 \rangle}$	$\frac{1}{2}\sqrt{12\tilde{a}_{\langle \text{Cr}_2\text{O}_3 \rangle}^2 + \tilde{c}_{\langle \text{Cr}_2\text{O}_3 \rangle}^2}$
f_1 (%)	-17.7	-14.1	-17.7
f_2 (%)	0.8	0.8	-3.2

Because the initial lattice mismatch for the investigated Cr-Cr₂O₃ system is large, the assumption that all mismatch is accommodated fully elastically leads to a severe overestimation of the interface energy, $\gamma_{\langle \text{Cr} \rangle - \langle \text{Cr}_2\text{O}_3 \rangle}$, beyond an oxide-film thicknesses of one oxide monolayer (see bold dashed lines in Fig. 2.5). On the other hand, if it is assumed that all lattice mismatch is fully accommodated by plastic deformation, the resulting value of $\gamma_{\langle \text{Cr} \rangle - \langle \text{Cr}_2\text{O}_3 \rangle}$ may lead to large overestimation of the interface energy within the submonolayer thickness regime (see bold solid lines in Fig. 2.5).

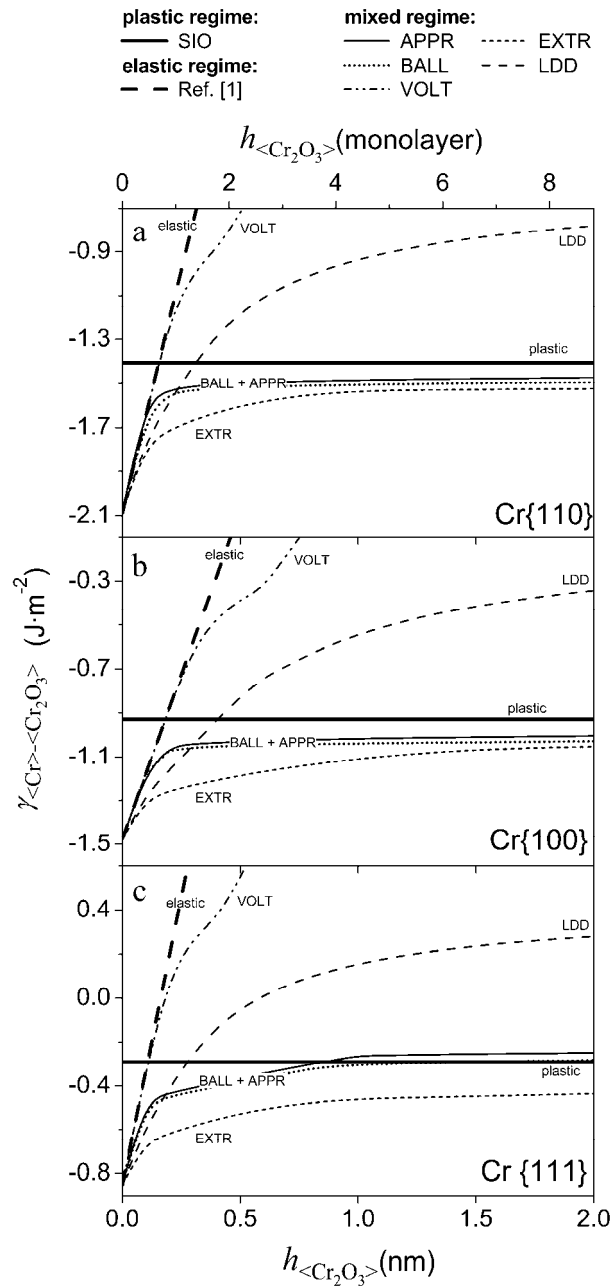


Figure 2.5. Crystalline-crystalline interface energy, $\gamma_{\langle Cr \rangle - \langle Cr_2O_3 \rangle}$, as function of the oxide-film thickness $h_{\langle Cr_2O_3 \rangle}$ at $T_0 = 298$ K, for the $\langle Cr_2O_3 \rangle$ overgrowth on the (a) Cr{110}, (b) Cr{100} and (c) Cr{111} faces of the $\langle Cr \rangle$ substrate. The bold solid and bold dashed lines correspond to the two limiting cases that all lattice mismatch is fully accommodated by either elastic strain (fully elastic accommodation according to Ref. [1]) or misfit dislocations (fully plastic accommodation according to the SIO approach in Sec. 2.2.3A), respectively. All other data correspond to values of $\gamma_{\langle Cr \rangle - \langle Cr_2O_3 \rangle}$ in the mixed regime (Fig. 2.2), as obtained by employing the different indicated approaches for the estimation of the misfit-dislocation energy contribution, $i \gamma_{\langle Cr \rangle - \langle Cr_2O_3 \rangle}^{\text{dislocation}}$ (see Secs. 2.2.3A–F).

As follows from Fig. 2.5, both the VOLT approach and the LDD approach yield unrealistic results in the mixed and plastic regimes: interface energy values much larger than the limiting interfacial energy value for pure plastic accommodation. This is due to the large initial mismatch, f_1 , in direction 1 within the $\langle \text{Cr} \rangle - \langle \text{Cr}_2\text{O}_3 \rangle$ interface planes (see above) which results in a relatively small dislocation distance, d_1 , along this direction (even at the onset of growth). Consequently, the main assumption $c_i^2/d_i^2 \approx 0$ made in the LDD approach (see Sec. 2.2.2B) no longer holds. The VOLT approach does not account for a change of the chemical bond strength across the interface (Sec. 2.2.2F), as is required, in particular, for thin overgrowths with high dislocation densities (as considered here) [20, 24], and hence the results of the VOLT approach are unrealistic for the case considered.

The other approaches (i.e., the EXTR, BALL and APPR approaches) used to estimate the misfit-dislocation energy contribution result in a value of $\gamma_{\langle \text{Cr} \rangle - \langle \text{Cr}_2\text{O}_3 \rangle}$ that is generally lower than the corresponding limiting values for the elastic and plastic regimes (Fig. 2.5). Only for the $\langle \text{Cr}_2\text{O}_3 \rangle$ overgrowths with $h_{\langle \text{Cr}_2\text{O}_3 \rangle} > 1$ nm on the Cr {111} substrate (Fig. 2.5c), the $\langle \text{Cr} \rangle - \langle \text{Cr}_2\text{O}_3 \rangle$ interfacial energy as calculated using the BALL and (especially) the APPR approach slightly exceeds the corresponding limiting value for the plastic regime. This slight, 'apparent' overestimation of the value of $\gamma_{\langle \text{Cr} \rangle - \langle \text{Cr}_2\text{O}_3 \rangle}$ is due to the different interfacial potential energy density functions employed in the APPR and BALL approaches (as adopted for overgrowths of *finite* thickness; see Secs. 2.2.3D and E, respectively).

The interfacial energies as calculated using the EXTR approach are considerably lower than those calculated using the BALL and APPR approach (Fig. 2.5), which can be attributed to an underestimation of the effective dislocation strain field and the application of an inappropriate interfacial potential energy density function (as derived for infinitely thick overgrowths) within the thin-film regime. The EXTR approach is only valid for $\langle \text{Cr}_2\text{O}_3 \rangle$ overgrowths thicker than about ten oxide monolayers.

The values of $\gamma_{\langle \text{Cr} \rangle - \langle \text{Cr}_2\text{O}_3 \rangle}$ calculated according to the BALL and APPR approaches, are nearly equal over the entire thickness range considered (i.e., from 0 nm to 2 nm; see Fig. 2.5), with the interface energy as obtained using the BALL approach being systematically a little lower, presumably because the strain gradient perpendicular to the surface/interface plane is not accounted for in the BALL approach (which assumption is reasonable only in the monolayer-thickness regime; see Sec. 2.2.3E).

As outcome of the above discussion, the APPR approach will be employed further to assess the misfit-dislocation energy contribution, $\gamma_{\langle\text{Cr}\rangle-\langle\text{Cr}_2\text{O}_3\rangle}^{\text{dislocation}, i}$, in the current model calculations (recognizing that the other approaches can be applicable for larger film thicknesses and/or metal/oxide systems with small initial lattice-mismatch values). The resulting value of $\gamma_{\langle\text{Cr}\rangle-\langle\text{Cr}_2\text{O}_3\rangle}$ (i.e., as calculated using the APPR approach) increases with increasing thickness, $h_{\langle\text{Cr}_2\text{O}_3\rangle}$, initially very fast and approximately linearly within the submonolayer thickness regime, and then increases more gradually within the mixed regime (Fig. 2.5). Upon approaching the plastic regime (i.e., for thicknesses $h_{\langle\text{Cr}_2\text{O}_3\rangle} > 2$ nm), the interface energy becomes nearly independent of the film thickness, because practically all mismatch strain becomes fully accommodated by misfit dislocations at the $\langle\text{Cr}\rangle-\langle\text{Cr}_2\text{O}_3\rangle$ interface.

Values of the interaction, $\gamma_{\langle\text{Cr}\rangle-\langle\text{Cr}_2\text{O}_3\rangle}^{\text{interaction}}$, and mismatch, $\gamma_{\langle\text{Cr}\rangle-\langle\text{Cr}_2\text{O}_3\rangle}^{\text{mismatch}}$, energy contributions, as calculated using the APPR approach, and the resultant value of the $\langle\text{Cr}\rangle-\langle\text{Cr}_2\text{O}_3\rangle$ interfacial energy, $\gamma_{\langle\text{Cr}\rangle-\langle\text{Cr}_2\text{O}_3\rangle}$, have been gathered in Table 2.7 for crystalline oxide overgrowth on the differently oriented $\langle\text{Cr}\rangle$ substrates at various growth temperatures and for various film thicknesses, $h_{\langle\text{Cr}_2\text{O}_3\rangle}$. The corresponding residual homogeneous strains in the $\langle\text{Cr}_2\text{O}_3\rangle$ overgrowth (i.e., $\bar{\epsilon}_{11}$ and $\bar{\epsilon}_{22}$ along the defined directions 1 and 2 within the $\langle\text{Cr}\rangle-\langle\text{Cr}_2\text{O}_3\rangle$ interface plane, respectively; see Table 2.6) have been plotted in Figs. 2.6a-c as function of $h_{\langle\text{Cr}_2\text{O}_3\rangle}$ at $T_0 = 298$ K. Finally, the energy contributions $\gamma_{\langle\text{Cr}\rangle-\langle\text{Cr}_2\text{O}_3\rangle}^{\text{interaction}}$, $\gamma_{\langle\text{Cr}\rangle-\langle\text{Cr}_2\text{O}_3\rangle}^{\text{strain}}$ and $\gamma_{\langle\text{Cr}\rangle-\langle\text{Cr}_2\text{O}_3\rangle}^{\text{dislocation}, i}$ ($i = 1, 2$) to the resultant $\langle\text{Cr}\rangle-\langle\text{Cr}_2\text{O}_3\rangle$ interfacial energy, $\gamma_{\langle\text{Cr}\rangle-\langle\text{Cr}_2\text{O}_3\rangle}$, are shown in Figs. 2.7a-c as function of $h_{\langle\text{Cr}_2\text{O}_3\rangle}$ at $T_0 = 298$ K.

Table 2.7. Values of the interaction, $\gamma_{\langle\text{Cr}\rangle-\langle\text{Cr}_2\text{O}_3\rangle}^{\text{interaction}}$, and mismatch, $\gamma_{\langle\text{Cr}\rangle-\langle\text{Cr}_2\text{O}_3\rangle}^{\text{mismatch}}$, energy contributions to the resultant $\langle\text{Cr}\rangle-\langle\text{Cr}_2\text{O}_3\rangle$ interfacial energy, $\gamma_{\langle\text{Cr}\rangle-\langle\text{Cr}_2\text{O}_3\rangle}$, for the overgrowth of the crystalline $\langle\text{Cr}_2\text{O}_3\rangle$ cell (see Fig. 2.1b) on the differently oriented $\langle\text{Cr}\rangle$ substrates for various growth temperatures, T , and film thicknesses, $h_{\langle\text{Cr}_2\text{O}_3\rangle}$, (see Sec. 2.2.2). All data have been calculated according to the numerical procedure outlined in Sec. 2.2.4, employing Eqs. (2.4c) to (2.4e) and (2.5b) and the data reported in Tables 2.2, 2.3, 2.5, 2.6 and Refs. [1, 27]. In the calculations, the APPR approach (Sec. 2.2.3D) has been employed to estimate the misfit-dislocation energy contributions, ${}^i\gamma_{\langle\text{Cr}\rangle-\langle\text{Cr}_2\text{O}_3\rangle}^{\text{dislocation}}$. See also Fig. 2.7.

T (K)	$h_{\langle\text{Cr}_2\text{O}_3\rangle}$ (nm)	$\gamma_{\langle\text{Cr}\rangle-\langle\text{Cr}_2\text{O}_3\rangle}^{\text{interaction}}$ ($\text{J}\cdot\text{m}^{-2}$)			$\gamma_{\langle\text{Cr}\rangle-\langle\text{Cr}_2\text{O}_3\rangle}^{\text{mismatch}}$ ($\text{J}\cdot\text{m}^{-2}$)			$\gamma_{\langle\text{Cr}\rangle-\langle\text{Cr}_2\text{O}_3\rangle}$ ($\text{J}\cdot\text{m}^{-2}$)		
		{110}	{100}	{111}	{110}	{100}	{111}	{110}	{100}	{111}
298	1	-1.73	-1.28	-0.68	0.25	0.26	0.42	-1.49	-1.02	-0.26
	3	-1.72	-1.27	-0.68	0.26	0.28	0.44	-1.46	-1.00	-0.24
	5	-1.72	-1.27	-0.68	0.28	0.29	0.45	-1.45	-0.98	-0.23
500	1	-1.71	-1.26	-0.68	0.24	0.25	0.42	-1.47	-1.01	-0.26
	3	-1.70	-1.26	-0.67	0.26	0.27	0.43	-1.45	-0.98	-0.24
	5	-1.70	-1.25	-0.67	0.27	0.29	0.44	-1.43	-0.97	-0.23
1000	1	-1.55	-1.14	-0.62	0.22	0.24	0.39	-1.33	-0.90	-0.23
	3	-1.54	-1.14	-0.61	0.26	0.27	0.41	-1.29	-0.87	-0.20
	5	-1.55	-1.14	-0.61	0.29	0.30	0.42	-1.26	-0.84	-0.20

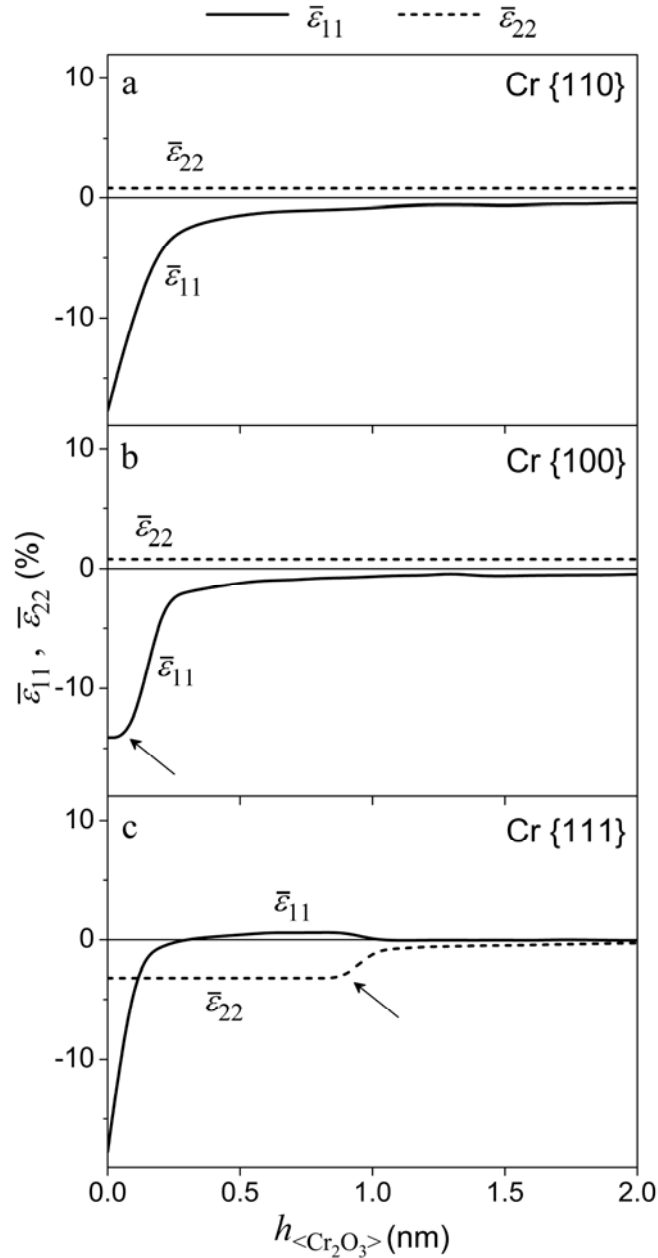


Figure 2.6. Residual homogeneous strains ($\bar{\varepsilon}_{11}$ and $\bar{\varepsilon}_{22}$) in the $\langle\text{Cr}_2\text{O}_3\rangle$ overgrowth (along the defined directions 1 and 2 parallel to the $\langle\text{Cr}\rangle$ - $\langle\text{Cr}_2\text{O}_3\rangle$ interface plane; see Table 2.6) as function of the crystalline oxide-film thickness, $h_{\langle\text{Cr}_2\text{O}_3\rangle}$, for the overgrowth on the (a) Cr{110}, (b) Cr{100} and (c) Cr{111} faces of the $\langle\text{Cr}\rangle$ substrate at $T_0 = 298$ K, as calculated (Sec. 2.2.4) using the APPR approach (Sec. 2.2.3D).

The film thickness beyond which misfit dislocations are introduced at the $\langle\text{Cr}\rangle$ - $\langle\text{Cr}_2\text{O}_3\rangle$ interface, where upon the homogeneous strain within the $\langle\text{Cr}_2\text{O}_3\rangle$ overgrowth is reduced significantly (see arrows in Figs. 2.6b and c), strongly depends on the initial lattice mismatch values f_1 and f_2 at the onset of growth (compare Figs. 2.6, 2.7 and Table 2.6). For the $\langle\text{Cr}_2\text{O}_3\rangle$

overgrowths on the Cr{110} and Cr{111} substrates, a large initial lattice mismatch is present along direction 1 (i.e., $f_1 = -17.7\%$; see Table 2.6) and, consequently, misfit dislocations are introduced already at the onset of growth along this direction (note the decrease of the *absolute* value of $\bar{\epsilon}_{11}$ with increasing thickness for $h_{\langle \text{Cr}_2\text{O}_3 \rangle} > 0$ nm; see Figs. 2.6a and c). For the $\langle \text{Cr}_2\text{O}_3 \rangle$ overgrowth on the Cr{100} substrate with $f_1 = -14.1\%$, misfit dislocations are introduced in the submonolayer thickness regime (i.e., $h_{\langle \text{Cr}_2\text{O}_3 \rangle} < 0.2$ nm; see Fig. 2.6b). For the $\langle \text{Cr}_2\text{O}_3 \rangle$ overgrowths on the Cr{110}, Cr{111} and Cr{100} substrates in the plastic regime (i.e., if all lattice mismatch is fully accommodated by only misfit dislocations), dislocation distances along direction 1 of five, five and seven lattice spacings \bar{c}_1 have been obtained from the model calculations, respectively.

For the $\langle \text{Cr}_2\text{O}_3 \rangle$ overgrowth on the Cr{111} substrate, an additional, considerable (compressive) initial strain of $\epsilon_{22} = f_2 = -3.2\%$ exists along direction 2 and, consequently, for $h_{\langle \text{Cr}_2\text{O}_3 \rangle} > 1$ nm (see Fig. 6c), misfit dislocations are also introduced along direction 2 (Thereby for this case a network of perpendicular misfit dislocations develops); the dislocation distance along direction 2 slightly decreases from 34 lattice spacings \bar{c}_2 at $T_0 = 298$ K to 29 lattice spacings \bar{c}_2 at $T = 1000$ K. For the $\langle \text{Cr}_2\text{O}_3 \rangle$ overgrowths on the Cr{110} and Cr{100} substrates the initial lattice mismatch along direction 2 is small (see Table 2.6) and all lattice mismatch along direction 2 is fully compensated by only elastic deformation even for thicknesses up to 5 nm.

The interaction contribution, $\gamma_{\langle \text{Cr} \rangle - \langle \text{Cr}_2\text{O}_3 \rangle}^{\text{interaction}}$, is most negative for the $\langle \text{Cr}_2\text{O}_3 \rangle$ overgrowth on the most densely packed Cr{110} substrate (with the highest density of metal-oxygen bonds across the interface). The (partial) relaxation of the compressive growth strain in the $\langle \text{Cr}_2\text{O}_3 \rangle$ film upon introduction of misfit dislocations at the $\langle \text{Cr} \rangle - \langle \text{Cr}_2\text{O}_3 \rangle$ interface results in a decrease of the number of metal-oxygen bonds across the $\langle \text{Cr} \rangle - \langle \text{Cr}_2\text{O}_3 \rangle$ interface per unit interface area (especially in direction 1; see above). Consequently, the aforementioned decrease of the strain contribution, $\gamma_{\langle \text{Cr} \rangle - \langle \text{Cr}_2\text{O}_3 \rangle}^{\text{strain}}$, and concurrent increase of the misfit-dislocation energy contribution, $\gamma_{\langle \text{Cr} \rangle - \langle \text{Cr}_2\text{O}_3 \rangle}^{\text{dislocation}}$, upon introduction of misfit dislocations at the $\langle \text{Cr} \rangle - \langle \text{Cr}_2\text{O}_3 \rangle$ interface are accompanied by a decrease of the absolute value of the

(dominating) negative interaction contribution, $\gamma_{\langle\text{Cr}\rangle-\langle\text{Cr}_2\text{O}_3\rangle}^{\text{interaction}}$, [see Eq. (2.4c) in Sec. 2.2.2 and see Fig. 2.7]. Upon approaching the plastic regime, the value of $\gamma_{\langle\text{Cr}\rangle-\langle\text{Cr}_2\text{O}_3\rangle}^{\text{interaction}}$ becomes independent of $h_{\langle\text{Cr}_2\text{O}_3\rangle}$ (Fig. 2.7).

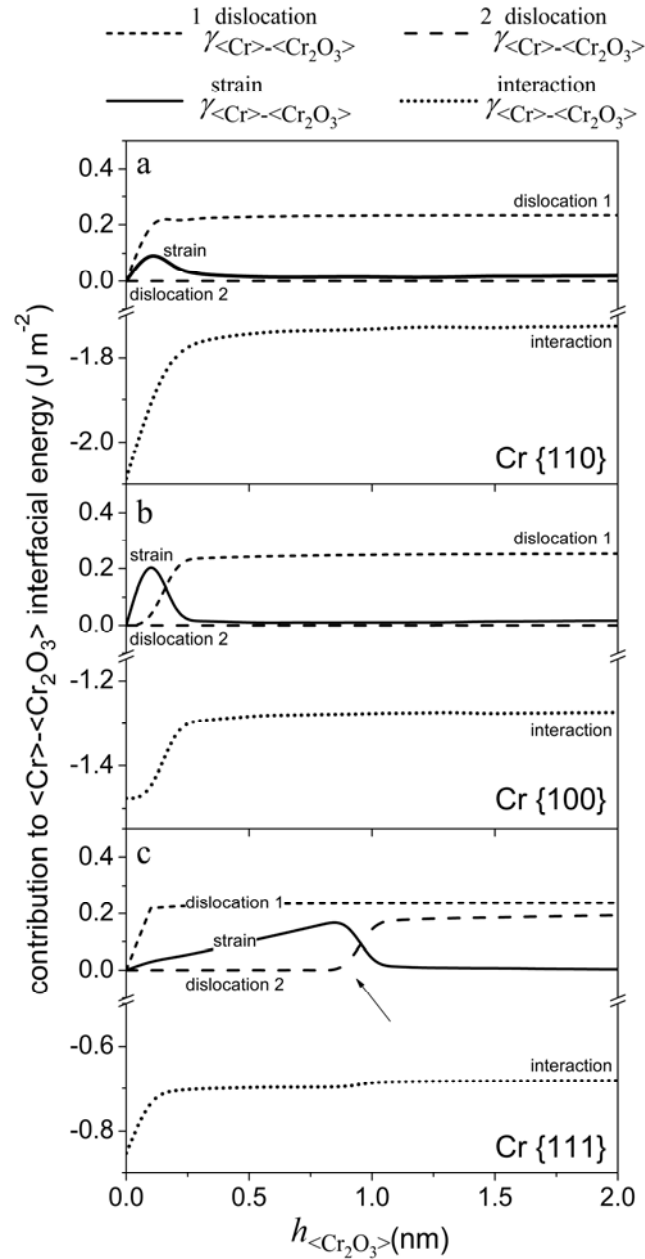


Figure 2.7. Interaction, $\gamma_{\langle\text{Cr}\rangle-\langle\text{Cr}_2\text{O}_3\rangle}^{\text{interaction}}$, residual strain, $\gamma_{\langle\text{Cr}\rangle-\langle\text{Cr}_2\text{O}_3\rangle}^{\text{strain}}$, and misfit dislocation, $\gamma_{\langle\text{Cr}\rangle-\langle\text{Cr}_2\text{O}_3\rangle}^{\text{dislocation } i}$ (in directions $i = 1$ and 2 ; see Table 2.6), energy contributions to the resultant $\langle\text{Cr}\rangle-\langle\text{Cr}_2\text{O}_3\rangle$ interfacial energy, $\gamma_{\langle\text{Cr}\rangle-\langle\text{Cr}_2\text{O}_3\rangle}$, for the overgrowth on the (a) Cr{110}, (b) Cr{100} and (c) Cr{111} faces of the $\langle\text{Cr}\rangle$ substrate as function of the crystalline oxide-film thickness $h_{\langle\text{Cr}_2\text{O}_3\rangle}$ at $T_0 = 298$ K, as calculated (Sec. 2.2.4) using the APPR approach (Sec. 2.2.3D).

It is concluded that the $\langle \text{Cr} \rangle$ - $\langle \text{Cr}_2\text{O}_3 \rangle$ interfacial energy, $\gamma_{\langle \text{Cr} \rangle - \langle \text{Cr}_2\text{O}_3 \rangle}$, increases with increasing oxide-film thickness (Fig. 2.5) mainly as a result of the associated increase of the (positive) mismatch contribution, $\gamma_{\langle \text{Cr} \rangle - \langle \text{Cr}_2\text{O}_3 \rangle}^{\text{mismatch}}$. The increase of $\gamma_{\langle \text{Cr} \rangle - \langle \text{Cr}_2\text{O}_3 \rangle}$ with increasing growth temperature is mainly due to the increase of the negative interaction contribution, $\gamma_{\langle \text{Cr} \rangle - \langle \text{Cr}_2\text{O}_3 \rangle}^{\text{interaction}}$. It is interesting to note that this last result contrasts with the case for the temperature dependence of the $\langle \text{Al} \rangle$ - $\langle \gamma\text{-Al}_2\text{O}_3 \rangle$ interfacial energy, $\gamma_{\langle \text{Al} \rangle - \langle \gamma\text{-Al}_2\text{O}_3 \rangle}$ (as calculated for the Al-Al₂O₃ system in Ref. [1] see also Chapter 3), where the increase of $\gamma_{\langle \text{Al} \rangle - \langle \gamma\text{-Al}_2\text{O}_3 \rangle}$ with also increasing T is dominated by the associated increase of the corresponding mismatch contribution, $\gamma_{\langle \text{Al} \rangle - \langle \gamma\text{-Al}_2\text{O}_3 \rangle}^{\text{mismatch}}$ (due to the large difference in thermal expansion coefficients of the Al substrate and $\langle \gamma\text{-Al}_2\text{O}_3 \rangle$ overgrowth).

C) Difference in interface energy of the crystalline and amorphous overgrowths

The calculated difference in interfacial energy, $\gamma_{\langle \text{Cr} \rangle - \langle \text{Cr}_2\text{O}_3 \rangle} - \chi \cdot \gamma_{\langle \text{Cr} \rangle - \langle \text{Cr}_2\text{O}_3 \rangle}$, for the competing cells (per unit area of the $\langle \text{Cr} \rangle - \langle \text{Cr}_2\text{O}_3 \rangle$ interface and for $h_{\langle \text{Cr}_2\text{O}_3 \rangle} = 2$ nm) has been plotted in Fig. 2.8 as function of the growth temperature for the differently oriented $\langle \text{Cr} \rangle$ substrates. It follows that the interfacial energy difference is around zero for the overgrowths on the most densely packed Cr{110} substrate and negative for the other substrate orientations. Hence, the interface energy contributes to possible stabilization of an amorphous oxide film on the Cr{100} and Cr{111} substrates. The interfacial energy difference is most negative for the overgrowths on the Cr{111} substrate.

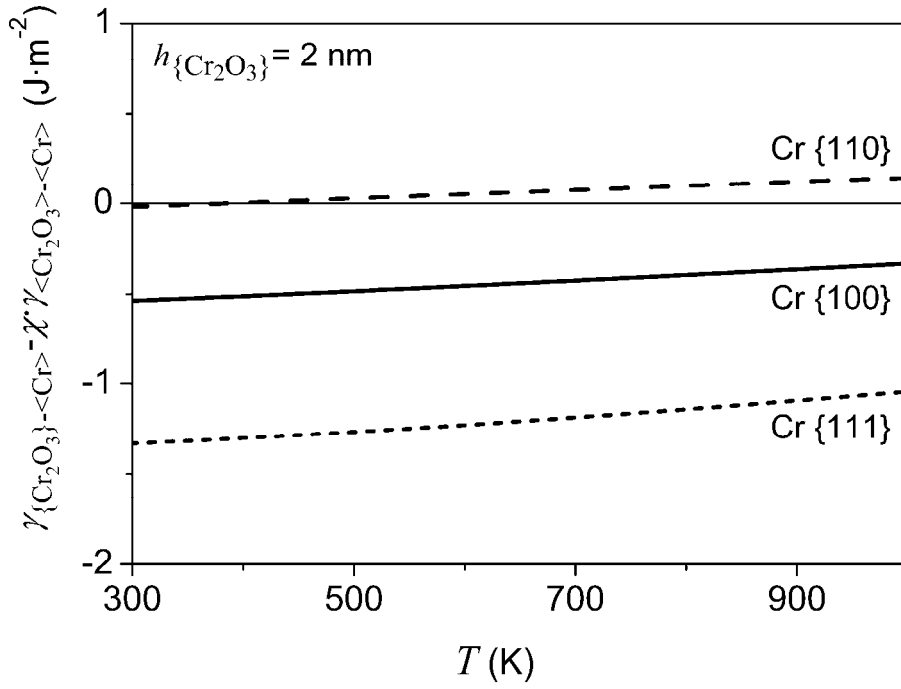


Figure 2.8. Interfacial energy difference, $\gamma_{\{Cr_2O_3\}-\langle Cr \rangle} - \chi \cdot \gamma_{\langle Cr \rangle-\{Cr_2O_3\}}$, [per unit area of the $\langle Cr \rangle-\{Cr_2O_3\}$ interface; see Eq. (2.1)] as function of the growth temperature, T , for the competing amorphous $\{Cr_2O_3\}$ and crystalline $\langle Cr_2O_3 \rangle$ cells on the $\{110\}$, $\{100\}$ and $\{111\}$ faces of the $\langle Cr \rangle$ substrate within the plastic regime (i.e., for a thickness of the $\{Cr_2O_3\}$ overgrowth of $h_{\{Cr_2O_3\}} = 2$ nm). The $\langle Cr \rangle-\langle Cr_2O_3 \rangle$ interfacial energy has been calculated according to the numerical procedure outlined in Sec. 2.2.4, while employing the APPR approach for the estimation of the misfit-dislocation energy contribution, $\gamma_{\langle Cr \rangle-\langle Cr_2O_3 \rangle}^{dislocation}$ (see Sec. 2.2.3D).

The interfacial energy difference slightly increases with increasing temperature (i.e., the crystalline $\langle Cr_2O_3 \rangle$ cell becomes relatively more stable with increasing T) as a result of a relatively faster increase with temperature of the $\langle Cr \rangle-\{Cr_2O_3\}$ interfacial energy. The thickness-dependence of the interfacial energy difference (not shown here) is governed by the thickness-dependence of the $\langle Cr \rangle-\langle Cr_2O_3 \rangle$ interfacial energy, as discussed in Sec. 2.3.3B, thereby stabilizing the $\{Cr_2O_3\}$ cell with increasing thickness in the elastic and mixed regime (in the plastic regime, the interfacial energy difference is independent of the film thickness; see Sec. 2.3.3B and Fig. 2.7).

The thus obtained values of the interface energy can only be compared with corresponding theoretical values as obtained by e.g., atomistic static lattice simulation or molecular dynamics, as has been done by the present authors in Ref. [1] of the revised manuscript. Here it is noted that the outcome of the model calculations is only sensitive to

relative interface energy differences (between amorphous and crystalline oxide overgrowth) and the outcome of the model calculations is therefore less sensitive on systematic errors in the absolute values of the corresponding interface energies.

2.4. Relative stabilities of amorphous and crystalline oxide films

2.4.1. Model predictions

An amorphous nature for the oxide film is preferred over a crystalline modification if $\Delta G = G_{\langle \text{Cr}_2\text{O}_3 \rangle} - G_{\langle \text{Cr}_2\text{O}_3 \rangle} < 0$ (see Sec. 2.2). Defining the critical thickness, $h_{\langle \text{Cr}_2\text{O}_3 \rangle}^{\text{critical}}$, as the thickness of the amorphous cell for which $\Delta G = 0$ (i.e., $G_{\langle \text{Cr}_2\text{O}_3 \rangle} = G_{\langle \text{Cr}_2\text{O}_3 \rangle}$), then for $h_{\langle \text{Cr}_2\text{O}_3 \rangle} < h_{\langle \text{Cr}_2\text{O}_3 \rangle}^{\text{critical}}$ the thermodynamically most stable substrate/overgrowth configuration is the amorphous one, whereas for $h_{\langle \text{Cr}_2\text{O}_3 \rangle} > h_{\langle \text{Cr}_2\text{O}_3 \rangle}^{\text{critical}}$ the crystalline $\langle \text{Cr}_2\text{O}_3 \rangle$ cell is thermodynamically preferred. The value of $h_{\langle \text{Cr}_2\text{O}_3 \rangle}^{\text{critical}}$ has been calculated as function of the growth temperature and the $\langle \text{Cr} \rangle$ substrate orientation by application of Eq. (1) and using the results for the bulk, surface and interfacial energies presented in Sec. 2.3. These final results are shown in Fig. 2.9. Because of the minimization procedure implemented to calculate the $\langle \text{Cr} \rangle - \langle \text{Cr}_2\text{O}_3 \rangle$ interfacial energy [see Eq. (2.13) in Sec. 2.2.4], an analytical expression for the critical thickness, $h_{\langle \text{Cr}_2\text{O}_3 \rangle}^{\text{critical}}$, (as presented in Ref. [1] for the elastic regime) cannot be given here.

It is concluded that (see Fig. 2.9) the onset of oxidation on the bare Cr{100} and Cr{111} substrates is predicted to proceed by the direct formation and growth of an *amorphous* $\{\text{Cr}_2\text{O}_3\}$ oxide film up to a critical thickness of about 0.5 nm and 0.8 nm at $T_0 = 298$ K, and up to a critical thickness of about 0.6 nm and 1 nm at $T = 1000$ K, respectively. Thus the amorphous $\{\text{Cr}_2\text{O}_3\}$ film is most stable on the *least* densely-packed Cr{111} surface. The amorphous $\{\text{Cr}_2\text{O}_3\}$ film on the Cr{100} and Cr{111} substrates is stabilized, as compared to the crystalline modification, by the lower sum of the surface and interfacial energies for the amorphous configuration, with the relative contribution of the surface energy difference predominating for the overgrowth on the Cr{100} substrate, whereas the surface and interfacial energy differences are about equal for the overgrowth on the Cr{111} substrate (compare Figs. 2.4 and 2.8).

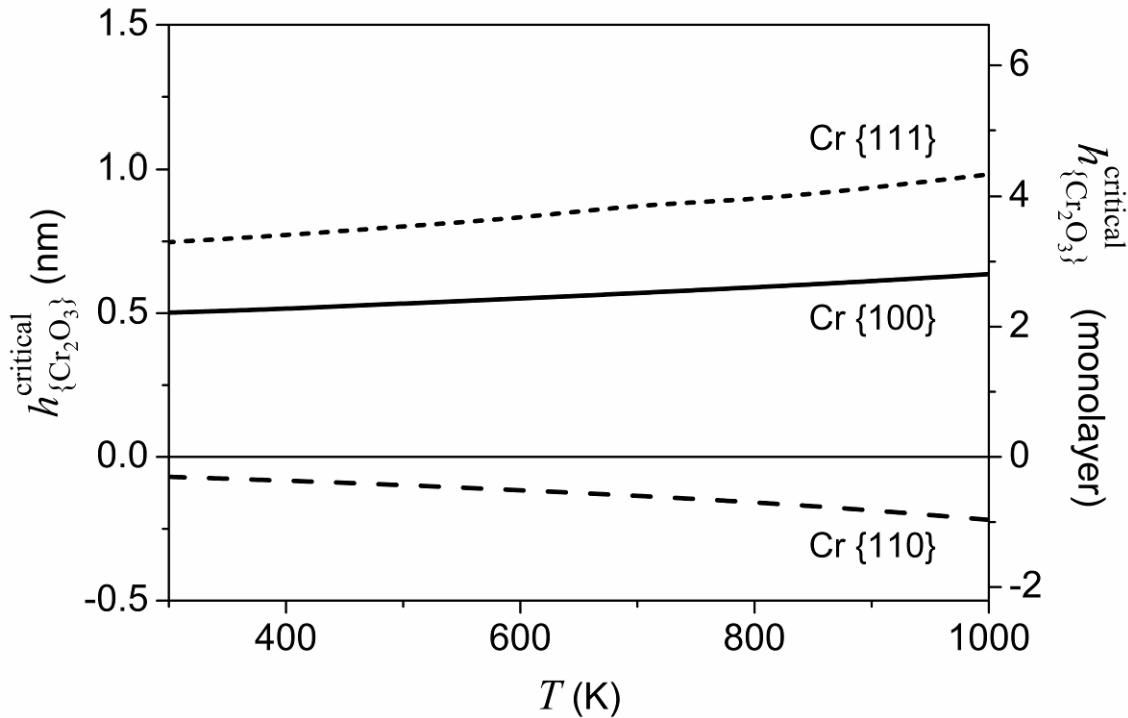


Figure 2.9. The critical oxide-film thickness, $h_{\{\text{Cr}_2\text{O}_3\}}^{\text{critical}}$, up to which an amorphous $\{\text{Cr}_2\text{O}_3\}$ overgrowth instead of a crystalline $\langle\text{Cr}_2\text{O}_3\rangle$ overgrowth is thermodynamically preferred on the $\{110\}$, $\{100\}$ and $\{111\}$ faces of a single-crystalline $\langle\text{Cr}\rangle$ substrate as function of the growth temperature, T .

A negative critical thickness, $h_{\{\text{Cr}_2\text{O}_3\}}^{\text{critical}}$, is obtained for the overgrowth on the bare Cr $\{110\}$ substrate, which implies that the onset of oxidation on the *most* densely-packed Cr surface is predicted to proceed by the direct formation and growth of a semi-coherent crystalline $\langle\text{Cr}_2\text{O}_3\rangle$ oxide. In this case the positive bulk Gibbs energy difference between the amorphous and crystalline cells (see Fig. 2.3) cannot be compensated solely by the relatively lower surface energy of the amorphous $\{\text{Cr}_2\text{O}_3\}$ cell on the Cr $\{110\}$ substrate (see Fig. 2.4).

The critical thickness increases more strongly with temperature T for the Al-Al $_2$ O $_3$ system (see Fig. 6 in Ref. [1]), which is due to the relative large difference in thermal expansion coefficient between the Al substrate and the Al $_2$ O $_3$ overgrowth (which results in a strong increase of the initial lattice mismatch with increasing T ; cf. the end of Sec. 2.3.3B).

2.4.2. Experimental observations versus model predictions

For the thermal oxidation of a bare, single-crystalline Cr $\{111\}$ substrate at room temperature, the development of an amorphous Cr-oxide (of thickness 0.9 nm) has been reported, as deduced from the shape of valence band spectra of the oxidized metal as recorded using UPS

and XPS [13]. For the corresponding oxidations at an elevated temperature of 773 K, instead an epitaxial crystalline Cr_2O_3 film of thickness ~ 4.1 nm has been reported [13]. Both these observations are in full agreement with the present model predictions (Fig. 2.9).

The available microstructural observations of the initial oxide developing on the bare $\text{Cr}\{100\}$ substrate are very ambiguous [7, 9, 11]: Whereas the formation of an initial amorphous oxide film at 1073 K is suggested by LEED [9], corresponding observations by RHEED are indicative of the formation of a polycrystalline oxide film at $T = 773$ K [7] and $T > 873$ K [11].

In full agreement with the model predictions, the direct formation of a semi-coherent crystalline oxide film has been observed for the bare $\text{Cr}\{110\}$ surface by X-ray scattering [12], LEED [7, 8] and RHEED [10] upon thermal oxidation at various temperatures (in the range of 463 K – 1173 K) and for various oxide-film thicknesses (in the range of 2 – 5 nm). Also, the coherent Cr_2O_3 film grown at $T = 1173$ K showed LEED spots characteristic of the $\text{Cr}_2\text{O}_3\{0001\}$ surface (as employed in the current model calculations; see Sec. 2.3.2) [7]. Moreover, a layer-by-layer growth mode has been indicated on the basis of reflectivity measurements for the 4.4 nm thick, epitaxial oxide film grown at 603 K [12].

2.5. Conclusion

A conclusive description of the thermodynamics of initial oxide-film growth on a bare, single-crystalline metal substrate, $\langle M \rangle$, is only obtained if the role of interface and surface energies is accounted for. On such a basis a meaningful comparison of the relative stabilities of amorphous and crystalline modifications of the oxide overgrowth, $\{M_xO_y\}$ and $\langle M_xO_y \rangle$, respectively, can be made.

For the assessment of the $\langle M \rangle - \langle M_xO_y \rangle$ interface energy, the relaxation of elastic growth strain in the crystalline overgrowth by introduction of misfit dislocations at the $\langle M \rangle - \langle M_xO_y \rangle$ interface (i.e. by plastic deformation) has now been accounted for in the thermodynamic modelling. The total interface energy of the $\langle M \rangle - \langle M_xO_y \rangle$ interface can be conceived as the resultant of three additive energy contributions due to (i) the chemical bonding between the oxide overgrowth and the metal substrate across the $\langle M \rangle - \langle M_xO_y \rangle$ interface, (ii) the residual homogeneous strain in the semi-coherent, crystalline oxide film, and (iii) the misfit dislocations at the $\langle M \rangle - \langle M_xO_y \rangle$ interface. The misfit dislocation

configuration of and the residual strain in the developing crystalline oxide film follow from the minimum value of the $\langle M \rangle - \langle M_x O_y \rangle$ interface energy, as determined iteratively.

Comparing and evaluating various models for crystalline misfit accommodation, the 'First Approximation' approach was found to be most suitable model for estimation of the energy of an array network of misfit dislocations in the oxide overgrowth for a wide range of initial lattice-mismatch values in both the monolayer and nanometer thickness regimes. Application of the corresponding 'Semi-infinite Overgrowth', 'Large Dislocation Distance', 'Extrapolation' and 'Volterra' approaches is restricted to metal-substrate/oxide-film systems with small initial lattice mismatches and/or to thick overgrowths within the plastic regime, whereas application of the 'Ball' approach is confined to the monolayer thickness regime.

Evaluation of the thermodynamic model on this basis for an oxide film growing on a metal substrate shows that the relatively high bulk Gibbs energy for the amorphous oxide film can be more than compensated by its relatively low sum of surface and interface energies.

For the case of crystalline oxide overgrowths on the $\{111\}$, $\{110\}$ and $\{100\}$ crystallographic faces of a bare single-crystalline Cr substrate, misfit dislocations are introduced at already the onset of the growth along the direction (in the interface plane) of high initial lattice mismatch (i.e. $|f| > 14\%$). Only for the crystalline oxide overgrowth on the Cr $\{111\}$ substrate, a second array of misfit dislocations is introduced in the corresponding perpendicular direction of low initial lattice mismatch (i.e. $|f| > 3\%$) for film thicknesses > 1 nm, whereas for the Cr $\{110\}$ and Cr $\{100\}$ substrates, the relatively small lattice mismatch (i.e. 0.8%) in the second direction is accommodated fully elastically up to film thicknesses of at least 5 nm.

The thermodynamic model applied to the onset of oxide-film growth on the relatively less-densely packed Cr $\{111\}$ and Cr $\{100\}$ substrates predicts the direct formation and growth of an amorphous $\{\text{Cr}_2\text{O}_3\}$ film up to a critical thickness of about 3 to 5 oxide monolayers (i.e. 0.5 – 1 nm) in the temperature range of 398 – 1000 K; beyond the critical thickness the crystalline modification is more stable than the amorphous one. Similarly it is predicted that oxide-film growth on the most-densely packed Cr $\{110\}$ substrate starts with the formation and growth of a semi-coherent crystalline oxide film that exhibits a strong anisotropic, elastic growth strain. These predicted energetics of the oxide films grown on the differently oriented Cr substrates provide a thermodynamic (rather than kinetic) explanation of the experimental observations.

References

- [1] L. P. H. Jeurgens, W. G. Sloof, F. D. Tichelaar and E. J. Mittemeijer, *Phys. Rev. B* **62** (2000) 4707.
- [2] F. P. Fehlner, *Low-temperature Oxidation: The Role of Vitreous Oxides* (Wiley-Interscience, New York, 1986).
- [3] I. E. Wachs, *Catal. Today* **100** (2005)79.
- [4] A. Johansson, G. Sambandamurthy, D. Shahar, N. Jacobson and R. Tenne, *Phys. Rev. Lett.* **95** (2005) 116805.
- [5] C. J. Först, K. Schwarz and P. E. Blöchl, *Phys. Rev. Letters* **95** (2005) 137602.
- [6] A. Tschöpe, *J. Electroceramics* **14** (2005) 5.
- [7] P. Michel and Ch. Jardin, *Surf. Sci.* **36** (1973) 478.
- [8] H. Ma, Y. Berthier and P. Marcus, *Appl. Surf. Sci.* **153** (1999) 40.
- [9] C. A. Haque and H. E. Farnsworth, *Surf. Sci.* **1** (1964) 378.
- [10] H. M. Kennett and A. E. Lee, *Surf. Sci.* **33** (1972) 377.
- [11] J. S. Arlow, D. F. Mitchell and M. J. Graham, *J. Vac. Sci. Techn. A* **5** (1987) 572.
- [12] A. Stierle, P. Bödeker and H. Zabel, *Surf. Sci.* **327** (1995) 9.
- [13] G. Gewinner, J. C. Peruchetti, A. Jaéglé and A. Kalt, *Surf. Sci.* **78** (1978) 439.
- [14] F. R. de Boer, R. Boom, W. C. M. Mattens, A. R. Miedema and A. K. Niessen, *Cohesion in Metals: Transition Metal Alloys* (North-Holland, Amsterdam, 1989), Chaps. 2 and 4.
- [15] S. H. Oh, Y. Kauffmann, C. Scheu, W. D. Kaplan and M. Rühle, *Science* **310** (2005) 661.
- [16] C. A. B. Ball, *Phys. Status Solidi* **42** (1970) 357.
- [17] J. H. van der Merwe, *Surf. Sci.* **31** (1972) 198.
- [18] J. H. van der Merwe, *J. Appl. Phys.* **34** (1963) 117; **34** (1963) 123; **34** (1963) 3420(E).
- [19] J. H. van der Merwe, in *Single Crystal Films*, edited by M. H. Francombe and H. Sato (Pergamon Press, Oxford, 1964), p.139.
- [20] J. H. van der Merwe and W. A. Jesser, *J. Appl. Phys.* **64** (1988) 4968.
- [21] J. H. van der Merwe and N. G. van der Berg, *Surf. Sci.* **32** (1972) 1.
- [22] J. H. van der Merwe, *J. Appl. Phys.* **41** (1970) 4725.
- [23] J. W. Matthews, *J. Vac. Sci. Techn.* **12** (1975) 126.

- [24] J. W. Matthews, in *Dislocation in Solids*, edited by F. R. N. Nabarro (North-Holland, Amsterdam, 1979), Vol. 2, Chap. 7, p.461.
- [25] MATLAB version 6.1.0.450, Release 12.1 (The MathWorks Inc., Natick, 2001).
- [26] Powder Diffraction Files, Cards 89-4055 and 82-1484 from JCPDS-International Centre for Diffraction Data (2001).
- [27] M. W. Chase, Jr., NIST-JANAF Thermochemical Tables Part II, Cr-Zr, 4th edition (J. Phys. Chem. Ref. Data, 1998), p.959.
- [28] C. Jardin and P. Michel, *Surf. Sci.* **71** (1978) 575.
- [29] F. Reichel, L. P. H. Jeurgens and E. J. Mittemeijer, submitted (2007).
- [30] N. Zouvelou, D. Skarmoutsos and P. Nikolopoulos, *Key Engineering Mater.* **264-268** (2004) 679.
- [31] D. T. Livey and P. Murray, *J. Am. Ceram. Soc.* **39** (1956) 363.
- [32] P. J. Lawrence, S. C. Parker and P. W. Tasker, *J. Am. Ceram. Soc.* **71** (1988) C-389.
- [33] R. G. Linford, *Chem. Soc. Rev.* **1** (1972) 445.
- [34] Y. S. Touloukian, R. K. Kirby, R. E. Taylor and T. Y. R. Lee, *Thermophysical Properties of Matter: Thermal Expansion; Elements and Alloy* (IFI/Plenum, New York, 1977), Vol. 12, p.61.
- [35] Y. S. Touloukian, R. K. Kirby, R. E. Taylor and T. Y. R. Lee, *Thermophysical Properties of Matter: Thermal Expansion; Nonmetallic Solids* (IFI/Plenum, New York, 1977), Vol. 13, p.217.
- [36] L. Vitos, A. V. Ruban, H. L. Skriver and J. Kollár, *Surf. Sci.* **411** (1998) 186.
- [37] J.-M. Zhang, F. Ma and K.-W. Xu, *Surf. Interface Anal.* **35** (2003) 662.
- [38] B.-J. Lee, M. I. Baskes, H. Kim and Y. K. Cho, *Phys. Rev. B* **64** (2001) 184102.
- [39] H. Wawra, *Z. Metallkd.* **66**, 395 (1975).
- [40] H. L. Alberts and J. C. A. Boeyens, *J. Magn. Magn. Mater* **2** (1976) 327.
- [41] G. Simmons, *Single Crystal Elastic Constants and Calculated Aggregate Properties: A Handbook*, 2nd edition (M.I.T. Press, Cambridge, Massachusetts, 1971), p.20.

Chapter 3

The thermodynamic stability of amorphous oxide overgrowths on metals

F. Reichel, L. P. H. Jeurgens and E. J. Mittemeijer

Abstract

On a thermodynamic foundation, for in particular interface energetics, the initial oxide overgrowth on a bare metal surface can be predicted to be either amorphous or (semi-) coherent, crystalline as function of the oxidation temperature and substrate orientation. Model calculations were performed for a range of metal/oxide systems (oxidation of Al, Ni, Cu, Cr, Fe, Mg, Zr and Ti) on the basis of the sum of the surface, interfacial and bulk energy differences between the competing amorphous and crystalline oxide overgrowths on the same metal substrate. It follows that an amorphous state for the initial oxide overgrowth can be thermodynamically (instead of kinetically) preferred as long as the higher bulk Gibbs energy of the amorphous oxide overgrowth is overcompensated by its low sum of surface and interface energies. The dominating factors, which thermodynamically favour the formation of an amorphous oxide overgrowth, are exposed and discussed.

3.1. Introduction

Until now the research on the development of initial oxide overgrowths on bare metal surfaces (ultra-thin oxide films < 5 nm) has been focussed on the growth kinetics (cf. Refs. [1-4] and references therein). The thermodynamics of the initial oxide overgrowth, which provides the conditions, as temperature, pressure, oxide-film thickness, chemical composition, and parent metal-substrate orientation, under which a given oxide phase can form on its bare metal surface, have received only little attention. This can be understood recognizing that the resulting oxide-film microstructures often differ from those known and as predicted by *bulk* thermodynamics. Such (microstructural) differences may be ascribed to the relatively large contributions of the interface and surface energies to the total energy of the metal-substrate/oxide-film systems. Hence, valid theoretical predictions on the thermodynamically

preferred microstructure for such thin oxide films require knowledge of the surface and interface energies of the studied metal-substrate/oxide-film system. Unfortunately, such knowledge is not available, in particular for amorphous oxide overgrowths.

Very recent work has shown indeed that interfacial and/or surface energies of very thin oxide films, or nano-particle systems, may stabilize phases that are unstable as bulk solids (cf. Ref. [5], Chapter 4 and references therein). Although it has been acknowledged that such nano-size-related phenomena are of utmost importance for many areas of application, such as microelectronics, solid-state devices, surface coatings and catalysis, it has been only recently demonstrated, on the basis of thermodynamic model calculations, that e.g. an *amorphous* phase for the initial oxide overgrowth on a metal can be thermodynamically stable up to a certain critical thickness, as long as the higher bulk energy of the amorphous oxide phase (as compared to that of the competing crystalline oxide phase) can be overcompensated by the lower sum of surface and interface energies for the amorphous oxide-film configuration [6, 7]. Similarly, very recently it has been theoretically demonstrated and experimentally confirmed that for the growth of a very thin, *crystalline* oxide film on a metal substrate, a crystallographic orientation relationship (COR) of very high mismatch with its metal substrate can be thermodynamically preferred (as compared to the crystalline overgrowth with a COR of the lowest mismatch, see Chapter 4). Such thermodynamic model predictions oppose many previous statements in the literature (e.g. see Refs. [8-10]) that the observed occurrence of an amorphous or pseudomorphic oxide phase on bare metal substrates upon oxidation at low temperatures (of, say, $T < 600$ K) would be due to kinetical obstructions of the formation of the stable crystalline modification.

In this contribution, employing the thermodynamic model developed in Refs. [6, 7] and Chapter 2 (briefly summarized in Sec. 3.2.1), theoretical predictions of the thermodynamically preferred microstructure of thin oxide overgrowths on their metal substrates are presented for a range of metal/oxide systems (oxidation of Ni, Cu, Cr, Fe, Mg, Zr, Ti and Si¹) as function of growth temperature and the orientation of the parent metal substrate. Thereby, fundamental, comprehensive knowledge is obtained on the material parameters which thermodynamically favour the development of amorphous or (semi-) coherent crystalline oxide phases on metal substrates. A thermodynamically stable amorphous or a coherent, single-crystalline oxide film on a metal surface is often desired, because of the

¹ The semiconductor Si will here further be denoted as metal.

absence of grain boundaries in both types of oxide films, which reduces both ionic and electronic migration through the oxide, thereby improving properties as the electrical resistivity, corrosion resistance and catalytic activity [1, 11-13]. In particular in the field of microelectronics, thin amorphous oxide films are required, because of their uniform thickness and specific microstructure and related properties (e.g., passivating oxide-film growth kinetics, low leakage current, high dielectric constant, high corrosion resistance) [1, 12, 13].

The thermodynamic model predictions obtained in this work for the various metal-substrate/oxide-film systems are compared with the available experimental observations reported in the literature and obtained by e.g. high-resolution transmission electron microscopy (HRTEM) or low energy electron diffraction (LEED). Unfortunately, the *microstructure* of the initial oxide overgrowth on a bare metal surface and, in particular, its dependence on the substrate orientation and the growth temperature is often unknown. Moreover, many contradictory observations of the developing oxide-film microstructure on 'identical' bare metal surfaces have been reported: for example, both amorphous and crystalline oxide overgrowths are observed on Cr{100} [14, 15], different crystallographic orientation relationships (CORs) between the crystalline oxide overgrowth and the parent substrate are reported for Mg and Ni single-crystals [16-19] and different crystalline oxide phases were observed for the oxide overgrowths on Fe [20, 21]. Apparently, only a few experiments have been carried out under sufficiently clean conditions, with proper microstructural characterization of the thin oxide overgrowth and its parent metal surface, as well as with accurate control of the growth conditions, to serve as an adequate tool for verification of thermodynamic model predictions as presented in this chapter.

3.2. Theory and calculation

3.2.1. Basics of the model

To investigate, on a thermodynamic basis, the preferred formation of either an amorphous or a crystalline oxide overgrowth, M_xO_y , on a bare (i.e. without a native oxide) single-crystalline metal substrate, the energetics of the amorphous oxide film, $\{M_xO_y\}$, with thickness $h_{\{M_xO_y\}}$ on $\langle M \rangle$ can be compared to those of the corresponding crystalline oxide film, $\langle M_xO_y \rangle$, with

equivalent thickness $h_{\langle M \rangle}$ on $\langle M \rangle$.² To this end, cells of volumes $h_{\{M_xO_y\}} \times l_{\{M_xO_y\}}^2$ and $h_{\langle M_xO_y \rangle} \times l_{\langle M_xO_y \rangle}^2$ are defined for the amorphous oxide-film configuration and the corresponding crystalline one, respectively, such that both cells contain the same molar quantity of oxygen (and thus the same molar quantity of oxide provided that $\{M_xO_y\}$ and $\langle M_xO_y \rangle$ cells have the same composition) [6]. The difference in total Gibbs energy between the cell in the amorphous and the cell in the crystalline oxide-film configuration, i.e. $\Delta G^{\text{total}} = G_{\{M_xO_y\}}^{\text{total}} - G_{\langle M_xO_y \rangle}^{\text{total}}$, for the corresponding oxide overgrowths on the same crystallographic surface of the metal substrate at growth temperature, T , can then be given as [6]:

$$\Delta G^{\text{total}} = h_{\{M_xO_y\}} \cdot \left(\frac{\Delta G_{\{M_xO_y\}}^{\text{f}} - \Delta G_{\langle M_xO_y \rangle}^{\text{f}}}{V_{\{M_xO_y\}}} \right) + \gamma_{\{M_xO_y\}\text{-vac}} + \gamma_{\langle M \rangle\text{-}\{M_xO_y\}} - \chi \cdot \left(\gamma_{\langle M_xO_y \rangle\text{-vac}} + \gamma_{\langle M \rangle\text{-}\langle M_xO_y \rangle} \right), \quad (3.1)$$

where $\Delta G_{\{M_xO_y\}}^{\text{f}}$ and $\Delta G_{\langle M_xO_y \rangle}^{\text{f}}$ are the Gibbs energies of formation of the amorphous and the crystalline oxide phase; $V_{\{M_xO_y\}}$ is the molar volume of the amorphous oxide; $\gamma_{\{M_xO_y\}\text{-vac}}$ and $\gamma_{\langle M_xO_y \rangle\text{-vac}}$ are the surface energies of the amorphous oxide and the crystalline oxide in contact with the ambient (*here*: vacuum); $\gamma_{\langle M \rangle\text{-}\{M_xO_y\}}$ and $\gamma_{\langle M \rangle\text{-}\langle M_xO_y \rangle}$ are the interfacial energies of the interface between the metal substrate and the amorphous and crystalline oxide overgrowth, respectively. The ratio χ corresponds to the surface area ratio of the unstrained amorphous cell and the (strained) crystalline cell at the growth temperature [6].

Evidently, for thick oxide overgrowths, bulk thermodynamics will always tend to stabilize the crystalline oxide overgrowth (i.e. $\Delta G_{\langle M_xO_y \rangle}^{\text{f}}$ of a crystalline oxide phase will always be lower than $\Delta G_{\{M_xO_y\}}^{\text{f}}$ of the corresponding amorphous oxide phase). However, for very thin oxide overgrowths it is possible that, the higher bulk Gibbs energy of the amorphous oxide phase can be overcompensated by its lower sum of surface and interface energies (as

² The braces $\{ \}$ and the brackets $\langle \rangle$ refer to the amorphous state and the crystalline state, respectively. Further it is noted that the stoichiometry of the oxide phase is denoted here with M_xO_y (with x and y being the number of cations and anions per oxide molecule, respectively) instead of MO_x as in Refs. [6, 7], since in the present calculations the number of metal ions per oxide unit (“molecule”) becomes relevant (see Appendix 3.B).

compared to the corresponding crystalline oxide configuration), thereby stabilizing the amorphous oxide overgrowth up to a certain critical thickness, $h_{\{M_xO_y\}}^{\text{critical}}$ [i.e. $\Delta G^{\text{total}} < 0$; cf. Eq. (3.1), Refs. [6, 7] and Chapter 2]. A theoretical prediction of the critical thickness, up to which the amorphous oxide overgrowth on the bare metal is thermodynamically (instead kinetically) preferred, is obtained by solving $h_{\{M_xO_y\}}$ in Eq. (3.1) for $\Delta G^{\text{total}} = 0$. The amorphous oxide overgrowth may even be stabilized up to thicknesses beyond $h_{\{M_xO_y\}}^{\text{critical}}$, if a high activation-energy barrier occurs for the amorphous-to-crystalline transition (i.e. the amorphous-to-crystalline transformation might become kinetically hindered). On the other hand, a negative value of $h_{\{M_xO_y\}}^{\text{critical}} < 0$, as obtained from the energy balance of Eq. (3.1), has no physical meaning and simply implies that the oxide overgrowth on the bare metal substrate is predicted to proceed by the direct formation and growth of a (semi-)coherent crystalline oxide phase.

To resolve the critical oxide-film thickness, $h_{\{M_xO_y\}}^{\text{critical}}$, from Eq. (3.1) for $\Delta G^{\text{total}} = 0$, at various growth temperatures T and for various metal-substrate orientations, knowledge is required on the values (or the relative differences) of the bulk, surface and interface energy terms of the amorphous and crystalline oxide cells, as function of the oxide-film thickness, growth temperature and substrate orientation. Experimental values for the surface and interfacial energies are generally not available (in particular not for the amorphous oxide overgrowth). Therefore, approximate expressions have been derived [6, 7] to estimate these energy contributions on the basis of the macroscopic atom approach (see Ref. [22] and Secs. 3.2.2 - 3.2.4), in combination with the Frank-van der Merwe approach [23] and/or empirical relationships established from corresponding data reported in the literature (see Appendices 3.A to 3.C).

3.2.2. Bulk energy differences

The difference in the bulk Gibbs energies of formation of the amorphous and the crystalline oxide overgrowths on the metal per unit area, i.e. the energy term $h_{\{M_xO_y\}} \cdot \left(\Delta G_{\{M_xO_y\}}^{\text{f}} - \Delta G_{\langle M_xO_y \rangle}^{\text{f}} \right) / V_{\{M_xO_y\}}$ in Eq. (3.1), is always positive, thereby stabilizing the crystalline oxide cell with increasing oxide-film thickness, $h_{\{M_xO_y\}}$. Since the bulk Gibbs energy difference decreases with increasing T (and eventually becomes zero at the melting

point of the oxide), the bulk amorphous oxide phase becomes relatively more stable (less unstable) at higher T . The absolute difference in bulk Gibbs energy between the amorphous and corresponding crystalline oxide will strongly depend on the metal/oxide system considered: thus $\left| \Delta G_{\{M_xO_y\}}^f - \Delta G_{\langle M_xO_y \rangle}^f \right|$ is relatively small for e.g. SiO_2 and Al_2O_3 , but relatively large for e.g. NiO and MgO (see Sec. 3.3.1).

The values for the enthalpies and entropies of oxide formation to determine the corresponding bulk Gibbs energies of oxide formation (as required for the calculation of the bulk energy difference term, and as also needed for other calculations performed in this study; cf. Sec. 3.2.4) were taken from the NIST-JANAF Thermochemical Tables [24] (only for NiO these values were taken from Refs. [25, 26]), while considering the amorphous oxide as a configurationally frozen liquid below the glass transition. The molar volumes of the crystalline oxides, $V_{\langle M_xO_y \rangle}$, were calculated from their corresponding lattice parameter(s) as reported in Ref. [27]. The molar volumes of the amorphous oxides, $V_{\{M_xO_y\}}$, were taken from the literature [28-32] or estimated using Eq. (3.5) (for details, see Appendix 3.A). The temperature dependence of $V_{\{M_xO_y\}}$ for the amorphous oxide phases (cf. Ref. [6]) is taken to be the same as that of the corresponding crystalline oxide, as obtained from the corresponding thermal expansion coefficient(s) [33-35]. Thermal expansion coefficients of the corresponding metals were taken from Ref. [36].

3.2.3. Surface energy differences

The surface energy difference of the amorphous and the crystalline oxide overgrowths on the metal per unit area, i.e. the energy term $\gamma_{\{M_xO_y\}\text{-vac}} - \chi \cdot \gamma_{\langle M_xO_y \rangle\text{-vac}}$ in Eq. (3.1) is generally negative, because the amorphous oxide generally has a lower surface energy than the corresponding crystalline oxide phase (see Appendix 3.B). The surface energy difference, which only has a slight temperature dependence, in some cases may be the dominating energy term responsible for the stabilization of the amorphous oxide overgrowth (see Refs. [5-7] and Sec. 3.3.1). Values of the surface energies for the amorphous oxide phases, as well as for the corresponding low index faces of the corresponding crystalline oxide phases, were taken from the literature [37-60] or estimated using the corresponding approximate expressions given in Appendix 3.B.

3.2.4. Interface energy differences

Approximate expressions for the solid-solid interfacial energies in Eq. (3.1) have been derived on the basis of the macroscopic atom approach [6, 7, 22] and adopting the Frank-van der Merwe approach [23] for the estimation of the energy of the induced misfit dislocations in the crystalline oxide overgrowths (Chapter 2), as outlined in the following.

A) The crystalline-amorphous interface energy

The energy of the crystalline-*amorphous* interface $\langle M \rangle - \{M_xO_y\}$, $\gamma_{\langle M \rangle - \{M_xO_y\}}$, can be expressed as the resultant of three additive energy contributions (for details, see Ref. [6]): (i) the negative interaction contribution, $\gamma_{\langle M \rangle - \{M_xO_y\}}^{\text{interaction}}$, resulting from the chemical bonding between the amorphous oxide and the metal substrate across the interface, (ii) the positive entropy contribution, $\gamma_{\langle M \rangle - \{M_xO_y\}}^{\text{entropy}}$, due to the ordering (i.e. the decrease of configurational entropy) of the amorphous oxide *near* the interface with the crystalline metal substrate, and (iii) the positive enthalpy contribution, $\gamma_{\langle M \rangle - \{M_xO_y\}}^{\text{enthalpy}}$, arising from the relative increase in enthalpy of the metal substrate atoms *at* the interface (as compared to the bulk) due to the liquid-type of bonding with the amorphous oxide at the interface [6]:

$$\gamma_{\langle M \rangle - \{M_xO_y\}} = \gamma_{\langle M \rangle - \{M_xO_y\}}^{\text{interaction}} + \gamma_{\langle M \rangle - \{M_xO_y\}}^{\text{entropy}} + \gamma_{\langle M \rangle - \{M_xO_y\}}^{\text{enthalpy}} = \frac{1/3 \Delta H_{O \text{ in } \langle M \rangle}^{\infty}}{A_{\{O\}}} - \frac{T \Delta S_{M_xO_y}}{A_{\{O\}}} + \frac{1/3 H_{\langle M \rangle}^{\text{fuse}}}{A_{\langle M \rangle}}, \quad (3.2)$$

where $\Delta H_{O \text{ in } \langle M \rangle}^{\infty}$ is the enthalpy of mixing 1 mol O(g) atoms at infinite dilution in $\langle M \rangle$ (as taken from the literature [61-65] or estimated using Eq. (3.9) in Appendix 3.C); $\Delta S_{M_xO_y}$ denotes the entropy difference between crystalline and amorphous M_xO_y per mol oxygen and $H_{\langle M \rangle}^{\text{fuse}}$ represents the molar enthalpy of fusion of $\langle M \rangle$; the fraction $1/3$ is a geometric factor assuming a shape of the Wigner-Seitz cell of oxygen in the oxide intermediate of a cube and a sphere [22]; $A_{\{O\}}$ and $A_{\langle M \rangle}$ are the molar interface areas of oxygen in the oxide and of metal atoms in the substrate *at* the crystalline-amorphous interface, respectively. It follows that the value of $A_{\langle M \rangle}$ depends on the metal substrate crystal orientation. The value of $A_{\{O\}}$ at the corresponding $\langle M \rangle - \{M_xO_y\}$ interface is approximated by the corresponding molar interface area for the most densely packed plane of the corresponding (unstrained) crystalline oxide

phase at the interface, because a dense packing of oxygen at the $\langle M \rangle - \{M_xO_y\}$ interface will be thermodynamically preferred [5, 6]. It is assumed that, at the oxide growth temperature, no strain resides in the amorphous oxide overgrowth [6].

Calculated values for the *negative* interaction energy contribution, $\gamma_{\langle M \rangle - \{M_xO_y\}}^{\text{interaction}}$, to the resultant $\langle M \rangle - \{M_xO_y\}$ interfacial energy, $\gamma_{\langle M \rangle - \{M_xO_y\}}$, range between $-4.6 \text{ J}\cdot\text{m}^{-2}$ (for oxidized Zr) and $-0.16 \text{ J}\cdot\text{m}^{-2}$ (for oxidized Cu) at $T_0 = 298 \text{ K}$; its value become less negative with increasing temperature as governed by the slight increase in $A_{\{O\}}$ with increasing T . For the corresponding *positive* entropy contribution, $\gamma_{\langle M \rangle - \{M_xO_y\}}^{\text{entropy}}$, values in the range of $0.005 \text{ J}\cdot\text{m}^{-2}$ (for oxidized Si) to $0.15 \text{ J}\cdot\text{m}^{-2}$ (for oxidized Ni) at T_0 are found; its value increases approximately linearly with increasing T [see Eq. (3.2)]. Finally, the *positive* enthalpy contribution, $\gamma_{\langle M \rangle - \{M_xO_y\}}^{\text{enthalpy}}$, varies between $0.03 \text{ J}\cdot\text{m}^{-2}$ (oxidized Mg) and $0.25 \text{ J}\cdot\text{m}^{-2}$ (oxidized Cr) at T_0 ; its value depends on the growth temperature and, to a much lesser extent, on the metal-substrate orientation (as governed by the associated changes in $A_{\langle M \rangle}$ [6]). It follows that, for most metal/amorphous oxide interfaces, the resultant value of the $\langle M \rangle - \{M_xO_y\}$ interfacial energy, $\gamma_{\langle M \rangle - \{M_xO_y\}}$, and its corresponding temperature dependence are governed by $\gamma_{\langle M \rangle - \{M_xO_y\}}^{\text{interaction}}$ (only for Cu_2O on Cu the entropy contribution is dominant; see Ref. [66] and Sec. 3.3.1C) and $\gamma_{\langle M \rangle - \{M_xO_y\}}^{\text{entropy}}$, respectively.

B) The crystalline-crystalline interface energy

The energy, $\gamma_{\langle M \rangle - \langle M_xO_y \rangle}$, of the crystalline-crystalline interface, $\langle M \rangle - \langle M_xO_y \rangle$ is expressed as the resultant of a negative interaction contribution, $\gamma_{\langle M \rangle - \langle M_xO_y \rangle}^{\text{interaction}}$ (cf. Sec. 3.2.4A), and two positive energy contributions originating from the initial lattice mismatch between the metal substrate and the crystalline oxide overgrowth: i.e. the strain contribution, $\gamma_{\langle M \rangle - \langle M_xO_y \rangle}^{\text{strain}}$, due to the residual homogeneous strain within the oxide overgrowth and the dislocation contribution, $\gamma_{\langle M \rangle - \langle M_xO_y \rangle}^{\text{dislocation}}$, due to the periodic, inhomogeneous strain field associated with misfit dislocations at the $\langle M \rangle - \langle M_xO_y \rangle$ interface [7]:

$$\begin{aligned}
\gamma_{\langle M \rangle - \langle M_x O_y \rangle} &= \gamma_{\langle M \rangle - \langle M_x O_y \rangle}^{\text{interaction}} + \gamma_{\langle M \rangle - \langle M_x O_y \rangle}^{\text{strain}} + \gamma_{\langle M \rangle - \langle M_x O_y \rangle}^{\text{dislocation}} \\
&= \frac{1/3 \Delta H_{\text{O in } \langle M \rangle}^{\infty}}{A_{\langle O \rangle}^{\text{unstr}}} \cdot (1 + \bar{\epsilon}_{11}) \cdot (1 + \bar{\epsilon}_{22}) - h_{\langle M_x O_y \rangle} \cdot C_{ijkl} \cdot \bar{\epsilon}_{ij} \cdot \bar{\epsilon}_{kl} + {}^1\gamma_{\langle M \rangle - \langle M_x O_y \rangle}^{\text{dislocation}} + {}^2\gamma_{\langle M \rangle - \langle M_x O_y \rangle}^{\text{dislocation}}, \quad (3.3)
\end{aligned}$$

where $A_{\langle O \rangle}^{\text{unstr}}$ equals the molar interface area of oxygen at the $\langle M \rangle - \langle M_x O_y \rangle$ interface for the concerned crystallographic plane of the (unstrained) crystalline oxide phase at the interface; C_{ijkl} is the fourth-rank stiffness tensor of $\langle M_x O_y \rangle$; $\bar{\epsilon}_{11}$ and $\bar{\epsilon}_{22}$ are components of the residual homogeneous strain tensor $\bar{\epsilon}_{ij}$ of $\langle M_x O_y \rangle$ in two perpendicular directions 1 and 2 within the concerned $\langle M \rangle - \langle M_x O_y \rangle$ interface plane (as determined by the COR between the metal substrate and the oxide overgrowth; see Sec. 3.3.1); the dislocation energy contribution, $\gamma_{\langle M \rangle - \langle M_x O_y \rangle}^{\text{dislocation}}$, equals the sum of energies, ${}^1\gamma_{\langle M \rangle - \langle M_x O_y \rangle}^{\text{dislocation}}$ and ${}^2\gamma_{\langle M \rangle - \langle M_x O_y \rangle}^{\text{dislocation}}$, of two perpendicular, regularly spaced arrays of misfit dislocations with Burgers vectors parallel to the two corresponding perpendicular directions 1 and 2 in $\langle M_x O_y \rangle$. Values for the elastic constants of the considered metals and crystalline oxides, as required for the calculation of $\gamma_{\langle M \rangle - \langle M_x O_y \rangle}$, were taken from Refs. [67-78].

Different approaches for crystalline misfit accommodation (as reported in the literature) have been compared and evaluated in Chapter 2 to assess the misfit-energy contribution ${}^i\gamma_{\langle M \rangle - \langle M_x O_y \rangle}^{\text{dislocation}}$. It was found that the 'First Approximation' approach (APPR) of Frank and van der Merwe (for details, see Chapter 2 and references therein) has the greatest overall accuracy for the estimation of the ${}^i\gamma_{\langle M \rangle - \langle M_x O_y \rangle}^{\text{dislocation}}$ for a wide range of initial lattice-mismatch values in both the monolayer and nanometer thickness regimes (up to about ten oxide monolayers (ML); 1 ML \sim 0.2 – 0.3 nm). Only for the Si/SiO₂ system, instead the extrapolation approach (EXTR) of Frank and van der Merwe (for details, see Chapter 2 and references therein) was adopted in the calculation of $\gamma_{\langle M \rangle - \langle M_x O_y \rangle}$, because the thickness regime for the corresponding amorphous-to-crystalline transition exceeds 10 MLs.

Since the energy contributions due to residual homogeneous strain and misfit dislocations in the crystalline oxide film are assigned here to the interface energy and not to the bulk energy of the film [see Eqs. (3.1) and (3.3)], it follows that a minimum in the total Gibbs energy of the crystalline oxide cell (thermodynamic equilibrium) is attained if

$\gamma_{\langle M \rangle - \langle M_x O_y \rangle}$ is at its minimum value (Chapter 2). Due to the thickness dependence of both $\bar{\epsilon}_{ii}$ and $\gamma_{\langle M \rangle - \langle M_x O_y \rangle}^{\text{dislocation}}$ [see Eq. (3.3)], the minimization of $\gamma_{\langle M \rangle - \langle M_x O_y \rangle}$ can only be performed numerically (Chapter 2).

For metal/oxide systems, such as $\text{TiO}_2\{100\}$ on $\text{Ti}\{10\bar{1}0\}$, with a low initial lattice mismatch of only +3% and -0.3% along two perpendicular directions parallel to the metal/oxide interface plane (Sec. 3.3.1H), the growth strain due to the initial lattice mismatch is completely accommodated elastically by the thin oxide overgrowth (i.e. no misfit dislocations are built in at the metal/oxide interface at the onset of growth). Consequently, the strain energy contribution in such a case increases linearly with increasing oxide-film thickness (cf. Figs. 3.1a and b) until an array of misfit dislocations is introduced in the overgrowth at the metal/oxide interface along the highest mismatch direction (parallel to the interface plane) for $h_{\langle \text{TiO}_2 \rangle} > 0.8$ nm. Only for $h_{\langle \text{TiO}_2 \rangle} > 5$ nm, a full, square grid of misfit dislocations is formed in the oxide overgrowth by the introduction of an additional array of misfit dislocations along the low mismatch direction.

On the other hand, for metal/oxide systems, such as $\text{NiO}\{100\}$ on $\text{Ni}\{111\}$, with initial lattice mismatch values of +19% and +3% (Sec. 3.3.1B), the resulting (anisotropic and tensile) elastic growth strain in the oxide overgrowth becomes relaxed by the introduction of misfit dislocations at the metal/oxide interface already at the onset of growth along the high mismatch direction, but subsequently also along the low mismatch direction (after attaining an oxide-film thickness of about 0.5 nm; compare Figs. 3.1a and b). The release of tensile growth strain leads to an increase of the absolute value of the interaction energy contribution due to the associated increase of the density of oxygen-metal bonds across the interface (see Fig. 3.1c).

Analogously, if an initially compressive growth strain resides in the oxide overgrowth, as for $\text{ZrO}_2\{1\bar{1}1\}$ on $\text{Zr}\{0001\}$ (with a corresponding near-isotropic initial lattice mismatch of -5%; see Sec. 3.3.1G), the release of the elastic growth strain with increasing oxide thickness, by the introduction of misfit dislocations, is associated with an unfavourable decrease of the absolute value of the interaction energy contribution (see Fig. 3.1c). It follows that, for compressively strained crystalline oxide overgrowths, a relatively larger part of the initial lattice mismatch can be accommodated elastically, as compared to tensilely strained crystalline oxide overgrowths. Further, since the misfit-dislocation energy contribution

$\gamma_{\langle M \rangle - \langle M_x O_y \rangle}^{\text{dislocation}}$ will be larger for a stronger bonding between the metal substrate and the oxide overgrowth across the interface (Chapter 2), it follows that more elastic growth strain can be stored in the crystalline oxide overgrowth for metal/oxide systems with more negative interaction energy contribution, $\gamma_{\langle M \rangle - \langle M_x O_y \rangle}^{\text{interaction}}$ [i.e. a more negative value of $\Delta H_{\text{O in } \langle M \rangle}^{\infty}$; cf. Eq. (3.9) and Appendix 3.C]. For all metal/oxide systems studied (see Sec. 3.3), the calculated sum of strain and dislocation energy contributions does not exceed the value of $0.5 \text{ J}\cdot\text{m}^{-2}$.

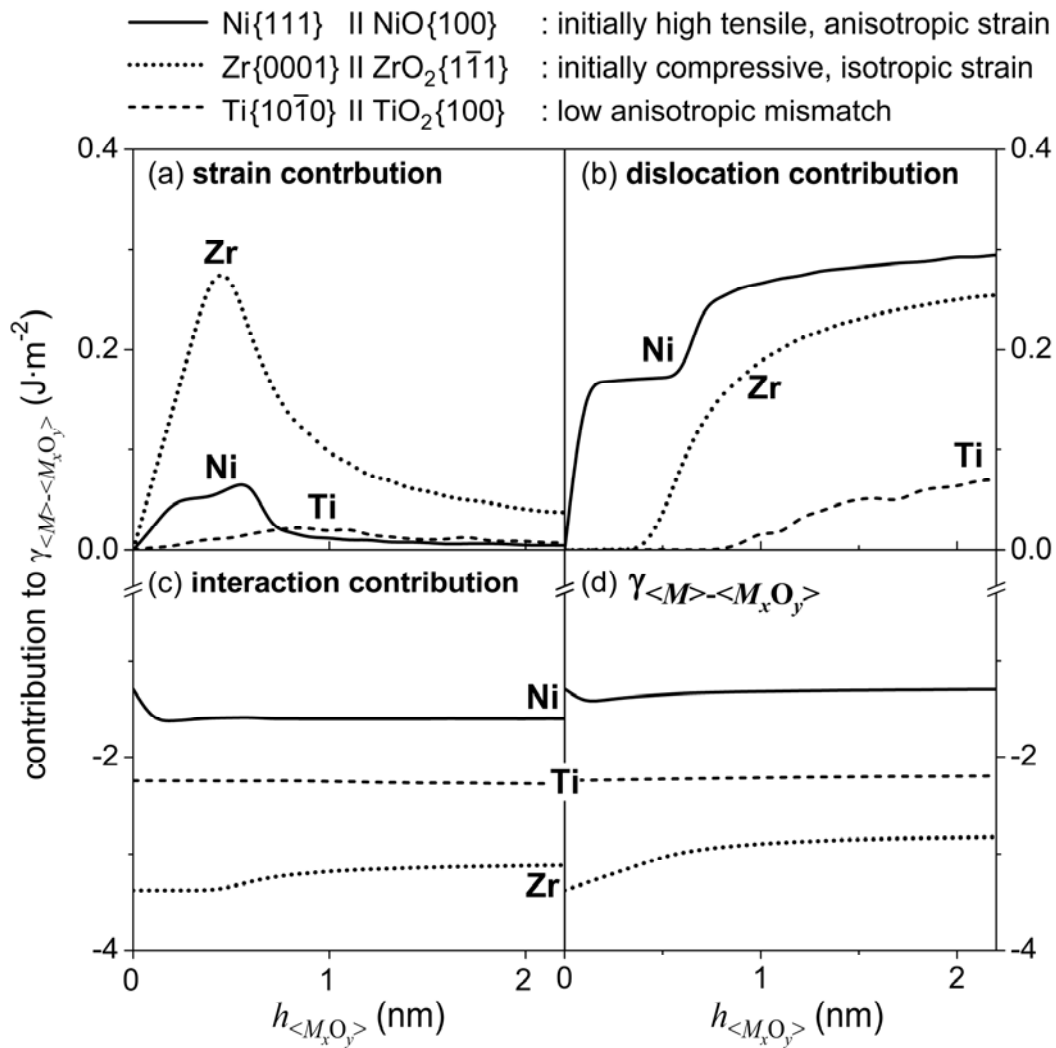


Figure 3.1. (a) Strain energy contribution ($\gamma_{\langle M \rangle - \langle M_x O_y \rangle}^{\text{strain}}$), (b) misfit-dislocation energy contribution ($\gamma_{\langle M \rangle - \langle M_x O_y \rangle}^{\text{dislocation}}$), (c) interaction energy contribution ($\gamma_{\langle M \rangle - \langle M_x O_y \rangle}^{\text{interaction}}$) and (d) resultant interfacial energy of the $\langle M \rangle - \langle M_x O_y \rangle$ interface ($\gamma_{\langle M \rangle - \langle M_x O_y \rangle}$) as function of the oxide-film thickness ($h_{\langle M_x O_y \rangle}$) for the Ni{111}||NiO{100}, the Zr{0001}||ZrO₂{111} and the Ti{1010}||TiO₂{100} interface (see Secs. 3.3.1B, 3.3.1G and 3.3.1H, respectively)

As for the crystalline-amorphous interfacial energy (Sec. 3.2.4A), the crystalline-*crystalline* interfacial energy $\gamma_{\langle M \rangle - \langle M_x O_y \rangle}$ is generally governed by the interaction energy contribution (except for crystalline oxide overgrowths on Cu; see also Sec. 3.2.4A); the value of $\gamma_{\langle M \rangle - \langle M_x O_y \rangle}^{\text{interaction}}$ is of the same magnitude as the corresponding value of $\gamma_{\langle M \rangle - \{M_x O_y\}}^{\text{interaction}}$ [differences between $\gamma_{\langle M \rangle - \langle M_x O_y \rangle}^{\text{interaction}}$ and $\gamma_{\langle M \rangle - \{M_x O_y\}}^{\text{interaction}}$ only arise from differences in the adopted values of $A_{\langle O \rangle}$ and $A_{\{O\}}$; compare Eqs. (3.2) and (3.3)]. For a large difference of the thermal expansion coefficients of the metal substrate and the crystalline oxide, the value of $\gamma_{\langle M \rangle - \langle M_x O_y \rangle}$ exhibits a pronounced temperature dependence due to the associated temperature dependence of the initial lattice mismatch. For example, the thermal expansion coefficient of Al is much larger than that of γ -Al₂O₃, resulting in an increase of the tensile growth strain (due to an increase of the initial lattice mismatch) and thus an increase of $\gamma_{\langle \text{Al} \rangle - \langle \gamma\text{-Al}_2\text{O}_3 \rangle}$ with increasing T [6].

3.3. Model predictions

3.3.1. System specific details and results

A) Al/Al₂O₃

For oxide overgrowths on bare Al{111}, Al{100} and Al{110} substrates, the amorphous oxide overgrowth competes with crystalline γ -Al₂O₃ [5, 79]. A low-mismatch COR relationship exists for the γ (-like)-Al₂O₃ overgrowths on both Al{111} and Al{110} according to: Al(111)[1 $\bar{1}$ 0] || γ -Al₂O₃(111)[1 $\bar{1}$ 0], which induces an isotropic, tensile growth strain in the $\langle \gamma\text{-Al}_2\text{O}_3 \rangle$ cell with an initial lattice mismatch of about +2% (at T_0) (see Chapter 4 and Ref. [6]). For the γ (-like)-Al₂O₃ overgrowth on Al{100}, a high-mismatch COR relationship was found according to Al(100)[01 $\bar{1}$] || γ -Al₂O₃(111)[01 $\bar{1}$], which induces an anisotropic tensile growth strain in the $\langle \gamma\text{-Al}_2\text{O}_3 \rangle$ cell with initial lattice mismatches of about +18% and +2% along the Al[011] and Al[01 $\bar{1}$] directions parallel to the Al(100)|| γ -Al₂O₃(111) interface plane (see Chapter 4).

It follows that the γ -Al₂O₃{111} crystallographic plane, which corresponds to the γ -Al₂O₃ surface with the lowest energy [5, 6, 37], constitutes the surfaces of the $\langle \gamma\text{-Al}_2\text{O}_3 \rangle$ overgrowths on Al{111} and Al{100} (see Chapter 4). As shown by molecular dynamics

simulations of relaxed γ - Al_2O_3 surfaces in contact with vacuum, the simulated γ - $\text{Al}_2\text{O}_3\{111\}$ surfaces become highly disordered (i.e. ‘amorphous’) as a result of surface reconstruction [37]. Therefore, in the present model calculations, the surface energies of the γ - $\text{Al}_2\text{O}_3\{111\}$ -surfaces for the $\langle\gamma\text{-Al}_2\text{O}_3\rangle$ overgrowths on $\text{Al}\{111\}$ and $\text{Al}\{100\}$ have been taken equal to the surface energy of the corresponding *am*- $\{\text{Al}_2\text{O}_3\}$ overgrowths: i.e. $\gamma_{\langle\text{Al}_2\text{O}_3(111)\rangle\text{-vac}} = \gamma_{\{\text{Al}_2\text{O}_3\}\text{-vac}}$, the value of which is about $0.8 \text{ J}\cdot\text{m}^{-2}$ lower than the corresponding energy of the γ - $\text{Al}_2\text{O}_3\{110\}$ surface which holds for the $\langle\gamma\text{-Al}_2\text{O}_3\rangle$ overgrowth on $\text{Al}\{110\}$ (see Table 3.2 in Appendix 3.B).

For the high-mismatch $\langle\gamma\text{-Al}_2\text{O}_3\rangle$ overgrowth on $\text{Al}\{100\}$, as well as for the low-mismatch overgrowths on $\text{Al}\{111\}$ and $\text{Al}\{110\}$, most (but not all) of the elastic growth strain due to the lattice mismatch will be relaxed by the built in of misfit dislocations at the $\langle\text{Al}\rangle$ - $\langle\gamma\text{-Al}_2\text{O}_3\rangle$ interface. The resulting sum of the strain and dislocation energy contributions to the $\langle\text{Al}\rangle$ - $\langle\gamma\text{-Al}_2\text{O}_3\rangle$ interfacial energy ($\gamma_{\langle\text{Al}\rangle\text{-}\langle\gamma\text{-Al}_2\text{O}_3\rangle}$) does never exceed the value of $0.5 \text{ J}\cdot\text{m}^{-2}$ (see Sec. 3.2.4B). Moreover, the O-Al bond strength is relatively high (i.e. the O-Al bond formation energy is highly exothermic; see Appendix 3.C). Consequently, the value of the $\langle\text{Al}\rangle$ - $\langle\gamma\text{-Al}_2\text{O}_3\rangle$ interfacial energy, $\gamma_{\langle\text{Al}\rangle\text{-}\langle\gamma\text{-Al}_2\text{O}_3\rangle}$, is dominated by the interaction energy contribution, $\gamma_{\langle\text{Al}\rangle\text{-}\langle\gamma\text{-Al}_2\text{O}_3\rangle}^{\text{interaction}}$ [see Eq. (3.3)]. Similarly, the $\langle\text{Al}\rangle$ - $\{\text{Al}_2\text{O}_3\}$ interface energy, $\gamma_{\langle\text{Al}\rangle\text{-}\{\text{Al}_2\text{O}_3\}}$, is dominated by the negative interaction energy contribution $\gamma_{\langle\text{Al}\rangle\text{-}\{\text{Al}_2\text{O}_3\}}^{\text{interaction}}$ [i.e. the corresponding positive energy contributions $\gamma_{\langle\text{Al}\rangle\text{-}\{\text{Al}_2\text{O}_3\}}^{\text{entropy}}$ and $\gamma_{\langle\text{Al}\rangle\text{-}\{\text{Al}_2\text{O}_3\}}^{\text{enthalpy}}$ are relatively small; cf. Eq.(3.2)].

For the $\{\text{Al}_2\text{O}_3\}$ overgrowths and the $\langle\gamma\text{-Al}_2\text{O}_3(111)\rangle$ overgrowths on $\text{Al}\{111\}$ and $\text{Al}\{100\}$, a similar dense packing of oxygen occurs at the metal/oxide interface (i.e. $A_{\{\text{O}\}} \cong A_{\langle\text{O}\rangle}$; see Sec. 3.2.4) and, consequently, the corresponding interaction energy contributions are about equal. Due to the resulting small surface and interface energy differences for the $\{\text{Al}_2\text{O}_3\}$ and $\langle\gamma\text{-Al}_2\text{O}_3\rangle$ overgrowths on $\text{Al}\{111\}$ and $\text{Al}\{100\}$, the critical oxide-film thicknesses up to which the $\{\text{Al}_2\text{O}_3\}$ overgrowth is thermodynamically preferred are only about 0.6 nm and 0.7 nm at T_0 , respectively (see Figs. 3.2 and 3.3; in spite of the relatively small bulk Gibbs energy difference of $+1 \text{ J}\cdot\text{m}^{-2}$ between $\{\text{Al}_2\text{O}_3\}$ and $\langle\gamma\text{-Al}_2\text{O}_3\rangle$)

cells at T_0 for $h_{\{\text{Al}_2\text{O}_3\}} = 1$ nm). Hence, for oxide overgrowths on Al{111} and Al{100}, the predicted value of $h_{\{\text{Al}_2\text{O}_3\}}^{\text{critical}}$ lies in the range of 2 - 4 oxide MLs in the considered temperature range of $T = 298 - 900$ K, which is in good agreement with experimental observations (see Chapter 5). For oxide overgrowth on Al{110}, the relatively low density of metal-oxygen bonds across the interface for the $\langle \gamma\text{-Al}_2\text{O}_3 \rangle$ overgrowth in combination with the unfavourably high $\gamma\text{-Al}_2\text{O}_3\{110\}$ surface energy (see above) results in a calculated critical oxide-film thickness of $h_{\{\text{Al}_2\text{O}_3\}}^{\text{critical}} = 3.6$ nm at T_0 (see Fig. 3.3). This model prediction of $h_{\{\text{Al}_2\text{O}_3\}}^{\text{critical}}$ on Al{110} needs careful experimental verification, because a reconstruction of the very open Al{110} surface and/or the occurrence of a faceted crystalline oxide surface (due to the high energy of the $\gamma\text{-Al}_2\text{O}_3\{110\}$ surface energy, see Chapter 5) may occur (which is not considered in the present model calculations).

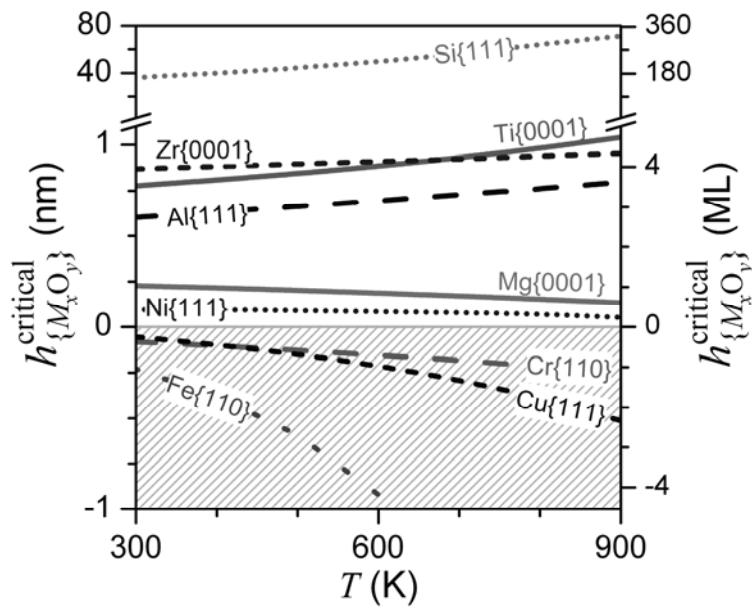


Figure 3.2. Critical thickness ($h_{\{M_xO_y\}}^{\text{critical}}$) up to which an amorphous oxide overgrowth (instead of the corresponding crystalline oxide overgrowth) is thermodynamically preferred on the most densely packed face of the corresponding bare metal substrate as function of the growth temperature (T) for various metal/oxide systems. The right ordinate indicates the corresponding critical thickness in oxide monolayers (MLs) as obtained by taking 1 oxide ML \cong 0.22 nm.

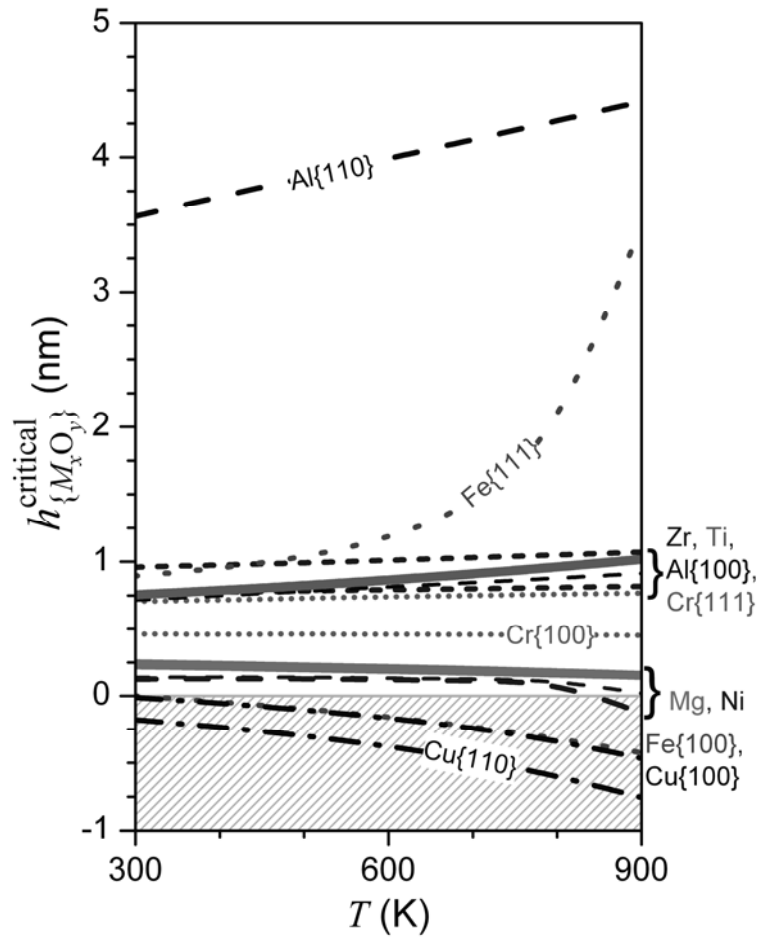


Figure 3.3. Critical thickness ($h_{\{M_xO_y\}}^{\text{critical}}$) up to which an amorphous oxide overgrowth (instead of the corresponding crystalline oxide overgrowth) is thermodynamically preferred on less densely packed faces of the corresponding bare metal substrate (i.e. Al{100}, Al{110}, Ni{100}, Ni{110}, Cu{100}, Cu{110}, Cr{100}, Cr{111}, Fe{100}, Fe{111}, Mg {1 $\bar{1}$ 00}, Mg {1 $\bar{1}$ 01}, Zr {10 $\bar{1}$ 0}, Zr {11 $\bar{2}$ 0}, Ti {10 $\bar{1}$ 0} and Ti {11 $\bar{2}$ 0}) as function of the growth temperature (T) for various metal/oxide systems.

B) Ni/NiO

For the crystalline $\langle \text{NiO} \rangle$ overgrowths on Ni{111}, Ni{100} and Ni{110}, the following CORs were found: Ni(111)[01 $\bar{1}$] \parallel NiO(100)[010], Ni(100)[01 $\bar{1}$] \parallel NiO(100)[01 $\bar{1}$] and Ni(110)[1 $\bar{1}$ 0] \parallel NiO(100)[010], respectively [16]. Clearly, the occurring CORs are governed by the relatively low surface energy of the non-polar NiO{100} surface (as compared to the much higher surface energy of the polar {111} surface; this holds for all other oxides

exhibiting the NaCl-type crystal structure, such as MgO; see Sec. 3.3.1F and Appendix 3.B).³ For the $\langle \text{NiO} \rangle$ overgrowth on Ni{100}, a (isotropic) compressive growth strain resides in the $\langle \text{NiO} \rangle$ cell with an initial lattice mismatch of about -16% (at T_0). On Ni{111} an anisotropic, tensile growth strain prevails with initial lattice mismatches of about +19% and +3% along the Ni[01 $\bar{1}$] and Ni[$\bar{2}$ 11] directions parallel to the Ni(111)||NiO(100) interface plane (see Fig. 3.1). Finally, on Ni{110} the growth strain in the $\langle \text{NiO} \rangle$ cell is highly anisotropic due to a compression along the Ni[001] direction (with -16% initial lattice mismatch) and an elongation along the Ni[1 $\bar{1}$ 0] direction (with +19% initial lattice mismatch) within the Ni(110)||NiO(100) interface plane.

Due to the relatively low energy of the nonpolar NiO{100} surface, the resulting surface energy differences between the {NiO} and $\langle \text{NiO} \rangle$ overgrowths are relatively small (i.e. about $-0.27 \text{ J}\cdot\text{m}^{-2}$). The corresponding interfacial energy differences are also relatively small, because (i) the sum of the entropy and enthalpy energy contributions to $\gamma_{\langle \text{Ni} \rangle\text{-}\{\text{NiO}\}}$ are about equal to the sum of the corresponding strain and dislocation energy contributions to $\gamma_{\langle \text{Ni} \rangle\text{-}\langle \text{NiO} \rangle}$ and (ii) the absolute differences in the interaction energy contributions (due to differences in the density of Ni-O bonds across the interfaces) are relatively small as a result of the low Ni-O bond strength (as compared to the M -O bond strengths for $M = \text{Al}, \text{Zr}$ and Ti ; see Appendix 3.C). Only the bulk energy difference between the {NiO} and $\langle \text{NiO} \rangle$ cells is relatively large (i.e. about four times larger than the corresponding bulk energy difference between the {Al₂O₃} and $\langle \gamma\text{-Al}_2\text{O}_3 \rangle$ cells; Sec. 3.3.1A). As a result, for all Ni substrate orientations and growth temperatures, the resolved critical oxide-film thickness, $h_{\{\text{NiO}\}}^{\text{critical}}$, is less than one oxide ML (cf. Figs. 3.2 and 3.3). Indeed, initial oxide overgrowth on bare Ni single crystals has been observed to proceed by the formation and growth of a crystalline NiO [16, 17].

³ On Ni{111} another COR, according to Ni{111}||NiO{111}, was also found [17]. However, as an outcome of the present model calculations, the Ni{111}||NiO{100} COR is thermodynamically preferred due to the relatively low energy of the NiO{100} surface (Appendix 3.B), in spite of its higher crystalline-crystalline interface energy. The Ni{111}||NiO{111} COR might become more likely if a growth mode deviating from layer-by-layer growth (e.g. islands or islands-by-layer growth) occurs [7].

C) Cu/CuO₂

For the crystalline $\langle \text{Cu}_2\text{O} \rangle$ overgrowths on Cu{111} and Cu{110}, a COR according to Cu(111)[1 $\bar{1}$ 0]||Cu₂O(111)[1 $\bar{1}$ 0] was adopted [81], resulting in an isotropic, compressive growth strain with an initial lattice mismatch (at T_0) of about -15%. A different COR according to Cu(100)[01 $\bar{1}$]||Cu₂O(111)[01 $\bar{1}$] was found for $\langle \text{Cu}_2\text{O} \rangle$ on Cu{100} [81, 82], resulting in an anisotropic, compressive growth strain with initial lattice mismatches of -15% along the Cu[01 $\bar{1}$] direction and -2% along the Cu[011] direction parallel to the Cu{100}||Cu₂O{111} interface plane.

Among all metal/oxide systems studied here, the Cu/Cu₂O system has the smallest metal-oxygen bond strength (cf. Appendix 3.C) and thereby the least negative interaction energy contribution. Hence, the calculated values of the $\langle \text{Cu} \rangle$ -{Cu₂O} interface energies ($\gamma_{\langle \text{Cu} \rangle\text{-}\{\text{Cu}_2\text{O}\}}$) are, instead, dominated by the entropy contribution (with $\gamma_{\langle \text{Cu} \rangle\text{-}\{\text{Cu}_2\text{O}\}}^{\text{entropy}} \sim 0.14 \text{ J}\cdot\text{m}^{-2}$ at T_0), which results in a slightly positive interfacial energy difference of the {Cu₂O} and $\langle \text{Cu}_2\text{O} \rangle$ overgrowths (i.e. $\gamma_{\langle \text{Cu} \rangle\text{-}\{\text{Cu}_2\text{O}\}} < \gamma_{\langle \text{Cu}_2\text{O} \rangle\text{-}\{\text{Cu}_2\text{O}\}}$) in the submonolayer thickness regime. In addition, the (negative) surface energy difference of the {Cu₂O} and $\langle \text{Cu}_2\text{O} \rangle$ overgrowths is relatively small. Consequently, the (positive) bulk energy difference (in combination with the positive interface energy difference within the monolayer thickness regime) results in a negative value of $h_{\{\text{Cu}_2\text{O}\}}^{\text{critical}}$ for all growth temperatures and Cu substrate orientations considered (see Figs. 3.2, 3.3 and Ref. [66]). Indeed, initial oxide overgrowth on bare Cu single-crystals is observed to proceed by the direct formation and growth of crystalline Cu₂O [80, 81].

D) Cr/Cr₂O₃

Details on the model calculations for the Cr/Cr₂O₃ system (i.e. CORs, calculated surface and interface energy differences and critical thicknesses) are given in Chapter 2. Summarizing, a highly anisotropic, overall compressive growth strain resides in the $\langle \text{Cr}_2\text{O}_3 \rangle$ overgrowths with initial lattice mismatches (at T_0) of -18% and +1% along the Cr[1 $\bar{1}$ 0] and Cr[001] directions for Cr{110}; -14% and +1% along Cr[010] and Cr[001] for Cr{100}; and -18% and -3% along Cr[1 $\bar{1}$ 0] and Cr[$\bar{1}$ $\bar{1}$ 2] for Cr{111}.

The very high (anisotropic) compressive strain in crystalline oxide overgrowth on Cr{110} leads to a higher density of metal/oxygen bonds across the $\langle \text{Cr} \rangle$ - $\langle \text{Cr}_2\text{O}_3 \rangle$ interface

(as compared to the corresponding $\langle \text{Cr} \rangle$ - $\{\text{Cr}_2\text{O}_3\}$ interface) and thereby to a positive interfacial energy difference (i.e. $\gamma_{\langle \text{Cr} \rangle - \langle \text{Cr}_2\text{O}_3 \rangle} < \gamma_{\langle \text{Cr} \rangle - \{\text{Cr}_2\text{O}_3\}}$). In combination with the relatively low surface energy difference, this results in a negative value for $h_{\{\text{Cr}_2\text{O}_3\}}^{\text{critical}}$ on $\text{Cr}\{110\}$ (see Fig. 3.2 and Chapter 2). On the other hand, the relatively high surface energy of the high-indexed oxide surfaces of the $\langle \text{Cr}_2\text{O}_3 \rangle$ overgrowths on $\text{Cr}\{100\}$ and $\text{Cr}\{111\}$ results in positive values of $h_{\{\text{Cr}_2\text{O}_3\}}^{\text{critical}} = 0.5$ nm and $h_{\{\text{Cr}_2\text{O}_3\}}^{\text{critical}} = 0.7$ nm at T_0 , respectively (see Fig. 3.3), in agreement with the experimental observations of amorphous oxide overgrowths on $\text{Cr}\{100\}$ and $\text{Cr}\{111\}$ (for more details, see Chapter 2).

E) Fe/FeO and Fe/Fe₃O₄

For the crystalline overgrowths on $\alpha\text{-Fe}\{110\}$, $\alpha\text{-Fe}\{100\}$ and $\alpha\text{-Fe}\{111\}$, various oxide phases with similar bulk Gibbs energies of formation, $\Delta G_{\langle \text{Fe}_x\text{O}_y \rangle}^{\text{f}}$, can be considered: FeO with $\Delta G_{\langle \text{FeO} \rangle}^{\text{f}} = -272$ kJ/(mole O), Fe₃O₄ with $\Delta G_{\langle \text{Fe}_3\text{O}_4 \rangle}^{\text{f}} = -280$ kJ/(mole O) and $\alpha\text{-Fe}_2\text{O}_3$ with $\Delta G_{\langle \alpha\text{-Fe}_2\text{O}_3 \rangle}^{\text{f}} = -275$ kJ/(mole O). For the thermal oxidation of bare Fe single-crystal surfaces, depending on the oxidation conditions, the initial oxide *film* is generally constituted of either FeO (with a NaCl-type crystal structure) [20, 82, 83] or Fe₃O₄ (with a spinel-type crystal structure) [21, 84].⁴

For $\langle \text{FeO} \rangle$ overgrowths on $\text{Fe}\{100\}$ and $\text{Fe}\{110\}$, the following CORs were established: $\text{Fe}(100)[01\bar{1}]||\text{FeO}(100)[010]$ [20, 83] and $\text{Fe}(110)[001]||\text{FeO}(111)[1\bar{1}0]$ [20], respectively. For $\langle \text{Fe}_3\text{O}_4 \rangle$ overgrowths on $\text{Fe}\{110\}$, $\text{Fe}\{100\}$ and $\text{Fe}\{111\}$, CORs according to $\text{Fe}(110)[001]||\text{Fe}_3\text{O}_4(111)[1\bar{1}0]$, $\text{Fe}(100)[010]||\text{Fe}_3\text{O}_4(100)[011]$ and $\text{Fe}(111)[0\bar{1}1]||\text{Fe}_3\text{O}_4(210)[001]$, respectively [21], were found. It follows that, on $\text{Fe}\{100\}$, isotropic growth strains reside in the $\langle \text{Fe}_3\text{O}_4 \rangle$ and $\langle \text{FeO} \rangle$ overgrowths with initial lattice mismatches (at T_0) of +0.2% and -6%, respectively. For the $\langle \text{Fe}_3\text{O}_4 \rangle$ and $\langle \text{FeO} \rangle$ overgrowths on $\text{Fe}\{110\}$, initial

⁴ For the thermal oxidation of bare Fe single-crystals at relatively low temperatures ($T < 450$ K), the initial oxide film can also be constituted of either FeO or Fe₃O₄ in combination with $\gamma\text{-Fe}_2\text{O}_3$ and/or $\alpha\text{-Fe}_2\text{O}_3$ (predominantly located at the oxide surface) [82-84]. However, upon annealing of these oxide films at higher temperatures, a single-phase oxide film consisting of either FeO or Fe₃O₄ results.

lattice mismatches of -18% and +0.2% and of -24% and -6% occur along the $\text{Fe}[1\bar{1}0]$ and $\text{Fe}[001]$ directions parallel to the interface plane, respectively. Finally, for the $\langle\text{Fe}_3\text{O}_4\rangle$ overgrowth on $\text{Fe}\{111\}$, initial lattice mismatches of -22% and +0.2% arise along the $\text{Fe}[11\bar{2}]$ and $\text{Fe}[1\bar{1}0]$ directions, respectively (*note*: an $\langle\text{FeO}\rangle$ overgrowth on $\text{Fe}\{111\}$ is not considered; see above).

The model calculations show that the $\langle\text{FeO}\rangle$ and $\langle\text{Fe}_3\text{O}_4\rangle$ overgrowths on $\text{Fe}\{100\}$ and $\text{Fe}\{110\}$ (employing the aforementioned CORs) are indeed about equally stable (i.e. in agreement with the experimental observation of the occurrence of both these oxide phases on $\text{Fe}\{100\}$ and $\text{Fe}\{110\}$; see above). The $\langle\text{FeO}\rangle$ overgrowth is slightly preferred on $\text{Fe}\{100\}$ due to its relatively low surface energy (and in spite of the relatively large initial lattice mismatch; see above). Similarly (i.e. due to its relatively low surface energy), the $\langle\text{Fe}_3\text{O}_4\rangle$ overgrowth is slightly preferred on $\text{Fe}\{110\}$.

As for the Cu/CuO_2 system (Sec. 3.3.1C), the interfacial energy differences of the $\{\text{Fe}_x\text{O}_y\}$ and $\langle\text{Fe}_x\text{O}_y\rangle$ oxide overgrowths on $\text{Fe}\{100\}$ and $\text{Fe}\{110\}$ are positive (i.e. $\gamma_{\langle\text{Fe}\rangle-\langle\text{Fe}_x\text{O}_y\rangle} < \gamma_{\langle\text{Fe}\rangle-\{\text{Fe}_x\text{O}_y\}}$) for small oxide-film thicknesses due to the relatively large enthalpy and entropy energy contributions in combination with a relatively low Fe-O bond strength (cf. Appendix 3.C). Additionally, the surface energy differences between the $\{\text{Fe}_x\text{O}_y\}$ and $\langle\text{Fe}_x\text{O}_y\rangle$ oxide overgrowths are relatively small. Consequently, the positive bulk energy difference, $h_{\{\text{Fe}_x\text{O}_y\}} \cdot \left(\Delta G_{\{\text{Fe}_x\text{O}_y\}}^f - \Delta G_{\langle\text{Fe}_x\text{O}_y\rangle}^f \right) / V_{\{\text{Fe}_x\text{O}_y\}}$ [cf. Eq. (3.1)], cannot be overcompensated by a larger negative sum of the corresponding surface and interfacial energies differences, resulting in a negative value of $h_{\{\text{Fe}_x\text{O}_y\}}^{\text{critical}}$ for the $\langle\text{FeO}\rangle$ and $\langle\text{Fe}_3\text{O}_4\rangle$ overgrowths on $\text{Fe}\{100\}$ and $\text{Fe}\{110\}$ (see Figs. 3.2, 3.3 and 3.4a), which agrees with experimental investigations showing only crystalline oxide films on $\text{Fe}\{110\}$ and $\text{Fe}\{100\}$ [20, 21]. Strikingly, for the $\langle\text{Fe}_3\text{O}_4\rangle$ overgrowth on $\text{Fe}\{111\}$, the lower Fe-O bond density across the $\langle\text{Fe}\rangle-\langle\text{Fe}_3\text{O}_4\rangle$ interface (as compared to the Fe-O bond density across the corresponding $\langle\text{Fe}\rangle-\{\text{Fe}_3\text{O}_4\}$ interface), as well as the relatively high energy of the $\langle\text{Fe}_3\text{O}_4\rangle(210)$ surface, stabilizes the $am\text{-}\{\text{Fe}_3\text{O}_4\}$ overgrowth up to a critical thickness of $h_{\{\text{Fe}_3\text{O}_4\}}^{\text{critical}} = 0.9$ nm at T_0 (see Figs. 3.3 and 3.4a). This model prediction of $h_{\{\text{Fe}_3\text{O}_4\}}^{\text{critical}}$ on $\text{Fe}\{111\}$ still needs careful experimental

verification (cf. discussion of $h_{\{\text{Al}_2\text{O}_3\}}^{\text{critical}}$ on Al{110}; Sec. 3.3.1A), because a reconstruction of the very open Fe{111} surface and/or the occurrence of a faceted crystalline oxide surface (due to the high energy of the $\langle\text{Fe}_3\text{O}_4\rangle(210)$ surface) may occur (which is are not considered in the present model calculations).

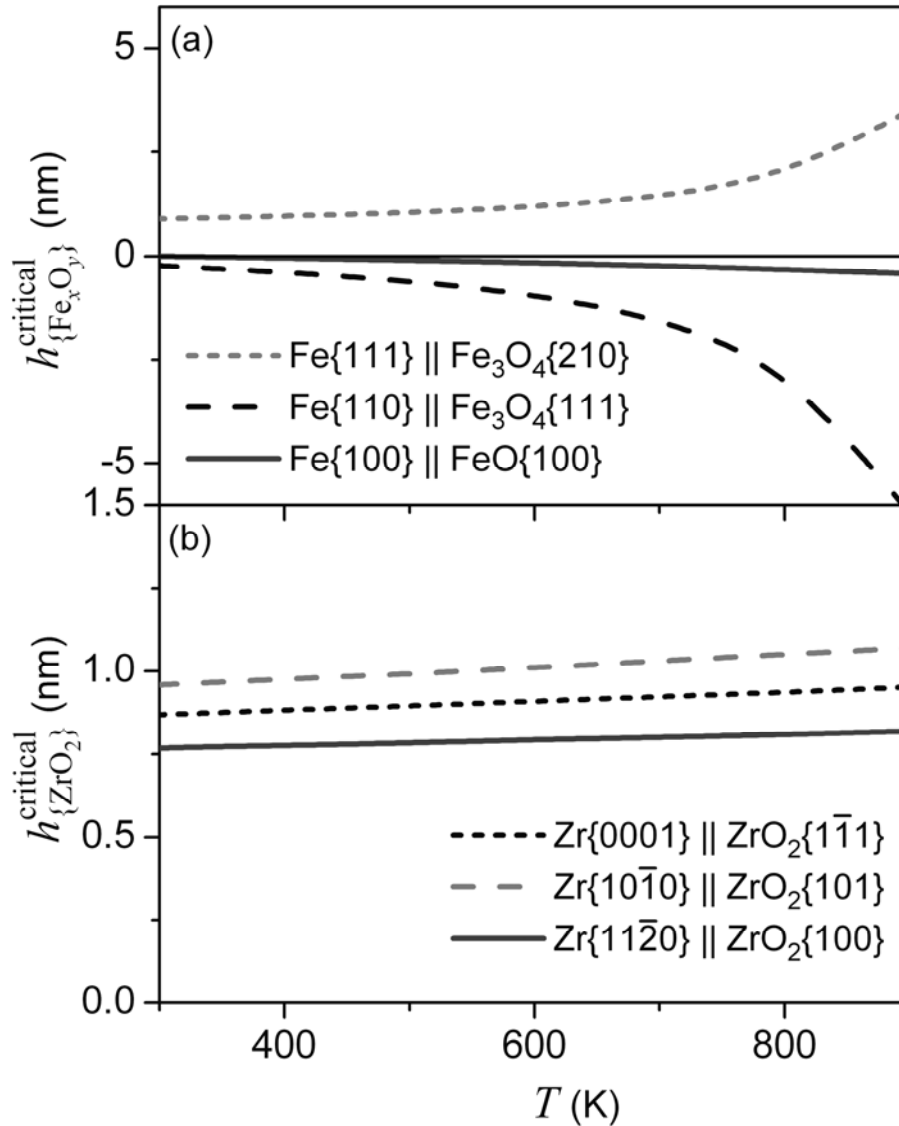


Figure 3.4. Critical thickness ($h_{\{M_xO_y\}}^{\text{critical}}$) up to which an amorphous oxide overgrowth (instead of the corresponding crystalline oxide overgrowth) is thermodynamically preferred on the different surfaces of bare (a) Fe (see Sec. 3.3.1E) and (b) Zr (see Sec. 3.3.1G) substrates as function of the growth temperature (T).

F) Mg/MgO

For the crystalline overgrowths on Mg{0001} and Mg{110} substrates, CORs according to Mg(0001)[1120]||MgO(100)[011] and Mg(110)[1120]||MgO(100)[011], respectively,

were established [18, 19]. As for the $\langle \text{NiO} \rangle$ overgrowths on Ni (see Sec. 3.3.1B and footnote 3; $\langle \text{NiO} \rangle$ and $\langle \text{MgO} \rangle$ both have the NaCl-type crystal structure), the thermodynamically preferred CORs for the $\langle \text{MgO} \rangle$ overgrowths on $\text{Mg}\{0001\}$ and $\text{Mg}\{1\bar{1}00\}$ are governed by the relatively low energy of the $\text{MgO}\{100\}$ surface. Therefore, a COR according to $\text{Mg}(1\bar{1}01)[11\bar{2}0]||\text{MgO}(100)[01\bar{1}]$ was chosen for the $\langle \text{MgO} \rangle$ overgrowth on $\text{Mg}\{1\bar{1}01\}$ in the model calculations.

It follows that an anisotropic growth strain resides in the crystalline oxide overgrowths with an initial lattice mismatch (at T_0) of +8% along the $\text{Mg}[11\bar{2}0]$ direction on all three considered Mg substrates in combination with a corresponding lattice mismatch of -7% along the $[1\bar{1}00]$ direction for $\text{Mg}\{0001\}$, -13% along $[0001]$ direction for $\text{Mg}\{1\bar{1}00\}$ and -1% along the $[\bar{1}102]$ direction for $\text{Mg}\{1\bar{1}01\}$.

The Mg-O bond strength is the highest among all metal/oxide systems studied here (cf. Fig. 3.11 in Appendix 3.C). Therefore, a slightly higher Mg-O bond density across the $\langle \text{Mg} \rangle$ - $\{\text{MgO}\}$ interface (as compared to the corresponding $\langle \text{Mg} \rangle$ - $\langle \text{MgO} \rangle$ interfaces) already results in a relatively large (negative) interfacial energy difference (i.e. $\gamma_{\langle \text{Mg} \rangle - \{\text{MgO}\}} \ll \gamma_{\langle \text{Mg} \rangle - \langle \text{MgO} \rangle}$, as compared to e.g. the Al/ Al_2O_3 and Zr/ ZrO_2 systems; see Secs. 3.3.1A and 3.3.1G). However, the relatively large bulk energy difference (at T_0) of about $5 \text{ J}\cdot\text{m}^{-2}$ of 1 nm thick $\{\text{MgO}\}$ and $\langle \text{MgO} \rangle$ overgrowths (which can be compared to a corresponding bulk energy difference of $1 \text{ J}\cdot\text{m}^{-2}$ for the Al/ Al_2O_3 system; see Sec. 3.3.1A) suppresses the critical oxide-film thickness, up to which the *am*- $\{\text{MgO}\}$ overgrowth is thermodynamically preferred, to below 1 ML (i.e. $h_{\{\text{MgO}\}}^{\text{critical}} \lesssim 1 \text{ ML}$; see Figs. 3.2, 3.3 and 3.5a) for all Mg substrate orientations considered.

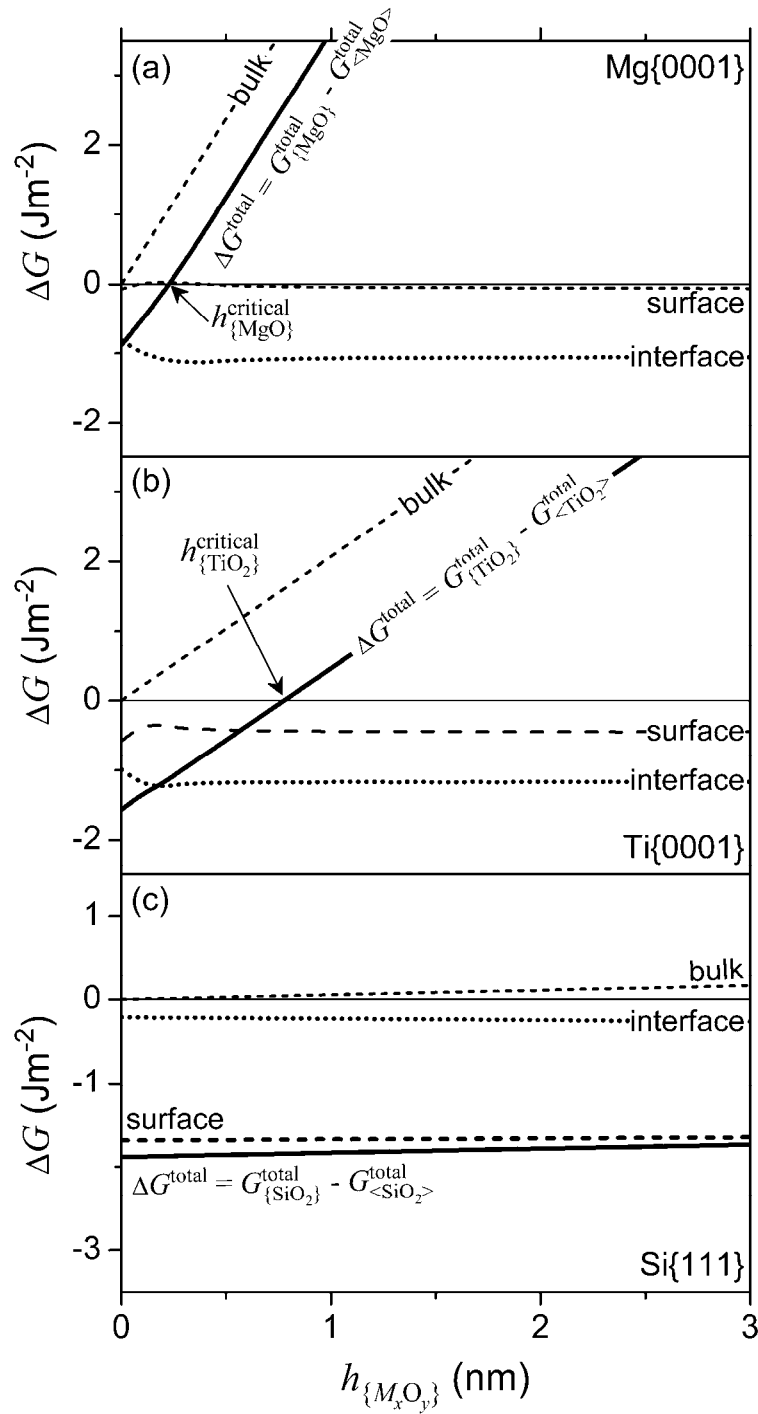


Figure 3.5. Bulk, interfacial and surface energy differences, as well as the corresponding total Gibbs energy difference ($\Delta G^{\text{total}} = G_{\{M_xO_y\}}^{\text{total}} - G_{\langle M_xO_y \rangle}^{\text{total}}$), of the amorphous oxide overgrowth and the corresponding crystalline oxide overgrowth on the bare (a) Mg{0001}, (b) Ti{0001} and (c) Si{111} substrates as function of oxide-film thickness ($h_{\{M_xO_y\}}$) at a growth temperature of $T_0 = 298$ K.

G) Zr/ZrO₂

For crystalline monoclinic $\langle \text{ZrO}_2 \rangle$ oxide overgrowths on Zr{0001}, Zr{10 $\bar{1}$ 0} and Zr{11 $\bar{2}$ 0} substrates, the following CORs were found: Zr(0001)[11 $\bar{2}$ 0]||ZrO₂(1 $\bar{1}$ 1)[10 $\bar{1}$], Zr(10 $\bar{1}$ 0)[0001]||ZrO₂(101)[010] and Zr(11 $\bar{2}$ 0)[0001]||ZrO₂(100)[001], respectively [85-87]. It follows that for $\langle \text{ZrO}_2 \rangle$ on Zr{0001} an isotropic initial lattice mismatch of -5% occurs (Fig. 3.1), whereas anisotropic mismatches occur for $\langle \text{ZrO}_2 \rangle$ on Zr{10 $\bar{1}$ 0} and Zr{11 $\bar{2}$ 0}: initial lattice mismatches of -5% and -1% along the Zr[$\bar{1}$ 2 $\bar{1}$ 0] and Zr[0001] directions within the Zr(10 $\bar{1}$ 0)||ZrO₂(101) interface plane and initial lattice mismatches of 0% and +7% along the Zr[0001] and Zr[1 $\bar{1}$ 00] directions within the Zr(11 $\bar{2}$ 0)||ZrO₂(100) interface plane, respectively.

Since the Zr-O bond strength is relatively large (cf. Appendix 3.C), a slightly higher Zr-O bond density across the $\langle \text{Zr} \rangle$ - $\{\text{ZrO}_2\}$ interface (as compared to the $\langle \text{Zr} \rangle$ - $\langle \text{ZrO}_2 \rangle$ interfaces) already leads to a relatively large (negative) interfacial energy difference (as compared to e.g. the Mg/MgO, Al/Al₂O₃ and Zr/ZrO₂ systems). In spite of the large negative sum of the surface and interfacial energy differences for the $\{\text{ZrO}_2\}$ and $\langle \text{ZrO}_2 \rangle$ overgrowths (i.e. $\gamma_{\langle \text{Zr} \rangle - \{\text{ZrO}_2\}} \ll \gamma_{\langle \text{Zr} \rangle - \langle \text{ZrO}_2 \rangle}$ and $\gamma_{\{\text{ZrO}_2\} - \text{vac}} \ll \gamma_{\langle \text{ZrO}_2 \rangle - \text{vac}}$), the relatively large bulk Gibbs energy difference of the $\{\text{ZrO}_2\}$ and $\langle \text{ZrO}_2 \rangle$ overgrowths ($\sim 2.8 \text{ J}\cdot\text{m}^{-2}$ at T_0 for $h_{\{\text{ZrO}_2\}} = 1 \text{ nm}$) restrains the calculated critical thickness to about 4 - 5 MLs; i.e. $h_{\{\text{ZrO}_2\}}^{\text{critical}} \sim 0.9 \pm 0.2 \text{ nm}$ for all Zr substrate orientations and growth temperatures considered (see Figs. 3.2 – 3.4b). Indeed, a TEM investigation on the oxidation of Zr metal indicates an initial overgrowth of *am*- $\{\text{ZrO}_2\}$ on Zr single-crystals [88].

H) Ti/TiO₂

For the crystalline overgrowths on Ti{0001}, Ti{10 $\bar{1}$ 0} and Ti{11 $\bar{2}$ 0} the following CORs have been established: Ti(0001)[11 $\bar{2}$ 0]||TiO₂(010)[001], Ti(10 $\bar{1}$ 0)[0001]||TiO₂(100)[010] and Ti(11 $\bar{2}$ 0)[0001]||TiO₂(001)[100], respectively [89]. It follows that the growth strain for the rutile $\langle \text{TiO}_2 \rangle$ overgrowth on Ti{0001} is predominantly tensile with initial lattice mismatches (at T_0) of +11% and -0.3% along the Ti[1 $\bar{1}$ 00] and Ti[11 $\bar{2}$ 0] directions, respectively, within

the Ti(0001)||TiO₂(010) interface plane. For $\langle \text{TiO}_2 \rangle$ on Ti{10 $\bar{1}$ 0} very low initial mismatch values occur of +2% and -0.3% along the Ti[0001] and Ti[11 $\bar{2}$ 0] directions, respectively, within the Ti(10 $\bar{1}$ 0)||TiO₂(100) interface plane (Fig. 3.1). Finally, on Ti{11 $\bar{2}$ 0} a tensile growth strain resides in the $\langle \text{TiO}_2 \rangle$ overgrowth with initial mismatches of +11% and +2% along the Ti[1 $\bar{1}$ 00] and Ti[0001] directions, respectively, within the Ti(11 $\bar{2}$ 0)||TiO₂(001) interface plane.

As for the Zr/ZrO₂ system, in spite of the relatively high Ti-O bond strength in combination with a relatively high density of Ti-O bonds across the $\langle \text{Ti} \rangle$ - $\langle \text{TiO}_2 \rangle$ interface (as compared to the $\langle \text{Ti} \rangle$ - $\langle \text{TiO}_2 \rangle$ interfaces), the bulk Gibbs energy difference of about 2 J·m⁻² (at T_0 for $h_{\{\text{TiO}_2\}} = 1$ nm) results in a calculated critical thickness of $h_{\{\text{TiO}_2\}}^{\text{critical}} = 0.75 \pm 0.05$ nm for all Ti substrates considered (see Figs. 3.2, 3.3 and 3.5b). Unfortunately, for the Ti/TiO₂ system, no detailed literature study was found on the initial microstructural evolution of such thin oxide overgrowths (i.e. < 1 nm) on bare Ti single-crystalline surfaces.

l) Si/SiO₂

The overgrowth of SiO₂ on Si substrates presents an exceptional case, because the bulk Gibbs energy difference of the amorphous and corresponding crystalline oxide overgrowths is very small [the term $h_{\{\text{SiO}_2\}} \cdot (\Delta G_{\{\text{SiO}_2\}}^f - \Delta G_{\langle \text{SiO}_2 \rangle}^f) / V_{\{\text{SiO}_2\}}$ in Eq. (3.1) is only 0.05 J·m⁻² at T_0 for $h_{\{\text{SiO}_2\}} = 1$ nm].

To our knowledge, no observations of CORs between crystalline $\langle \text{SiO}_2 \rangle$ overgrowths and $\langle \text{Si} \rangle$ have been reported in the literature (only *am*- $\langle \text{SiO}_2 \rangle$ overgrowths on $\langle \text{Si} \rangle$ have been observed). Therefore, CORs between $\langle \text{SiO}_2 \rangle$ and $\langle \text{Si} \rangle$ (for the model calculations) were adopted recognizing the low energy of the SiO₂{0001} surface in combination with the possibly lowest initial lattice mismatch values along two perpendicular directions parallel to the interface plane concerned: i.e. Si(111)[0 $\bar{1}$ 1]||SiO₂(0001)[11 $\bar{2}$ 0], Si(110)[001]||SiO₂(0001)[11 $\bar{2}$ 0] and Si(100)[001]||SiO₂(0001)[11 $\bar{2}$ 0] for $\langle \text{SiO}_2 \rangle$ overgrowths on Si{111}, Si{110} and Si{100}, respectively. It follows that only a small (isotropic) lattice mismatch of +3% (at T_0) occurs for $\langle \text{SiO}_2 \rangle$ overgrowth on Si{111}, whereas highly anisotropic initial lattice mismatches of -10% and +10% along the Si[1 $\bar{1}$ 0] and Si[001]

directions, respectively, parallel to the Si(110)||SiO₂(0001) interface plane, and of +27% and +10% along the Si[010] and Si[001] directions, respectively, parallel to the Si(100)||SiO₂(0001) interface plane, occur for $\langle \text{SiO}_2 \rangle$ overgrowths on Si{100} and Si{110}, respectively.

Although the Si-O bond strength (and thereby the interfacial energy difference of the {SiO₂} and $\langle \text{SiO}_2 \rangle$ overgrowths) is relatively small (cf. Fig. 3.11 in Appendix 3.C), the calculated critical thickness on Si substrates is very high (i.e. in the range of about 40 – 80 nm between $T = 298$ K and $T = 900$ K; see Fig. 3.2) due to the exceptionally small bulk energy difference contribution in combination with the considerably lower surface energy of the *am*-{SiO₂} overgrowth (see Fig. 3.5c). Indeed, in practice amorphous {SiO₂} oxide films are observed [1]. The micrometer thick *am*-{SiO₂} layers on Si are found to be stable up to temperatures even as high as 1400 K, which may be attributed to a high activation energy for the amorphous-to-crystalline transition [1].

3.3.2. Thermodynamic stability of amorphous oxide film on various metals

The calculated critical oxide thickness up to which an amorphous oxide overgrowth is thermodynamically preferred over the corresponding crystalline modification has been plotted for the most densely packed surface and for less densely packed surfaces of various metals as function of the growth temperature in Figs. 3.2 and 3.3, respectively. The corresponding surface, interfacial and bulk energy differences of the amorphous and crystalline oxide overgrowths on Mg{0001}, Ti{0001} and Si{111} are shown as function of the growth temperature in Figs. 3.5a, b and c, respectively. Further, the dependence of the critical oxide thickness on the metal-substrate orientation is illustrated in Figs. 3.4a and b for oxide overgrowths on different low-index crystallographic surfaces of Fe and Zr, respectively.

The stabilization of an amorphous oxide phase on Si is governed by the low surface energy of the *am*-SiO₂ in combination with the exceptionally small bulk energy difference between amorphous and crystalline SiO₂ (see Sec. 3.3.1I and Fig. 3.5c). For oxide overgrowths on Zr{0001} and Ti{0001}, in spite of the relatively low surface and interfacial energy for the amorphous oxide-film configuration, the relatively large difference in bulk energy between the amorphous and crystalline oxide hinders a stabilization of the amorphous oxide phase beyond a thickness of 1 nm (~ 5 oxide MLs; see Fig. 3.5b and Secs. 3.3.1G and 3.3.1H). For oxide overgrowths on Al{111} the amorphous oxide phase is thermodynamically preferred up to a critical thickness of about 3 to 4 MLs mainly due to the slightly lower

energy of the $\langle \text{Al}(111) \rangle$ - $\{\text{Al}_2\text{O}_3\}$ interface (because the corresponding $\langle \gamma\text{-Al}_2\text{O}_3 \rangle$ overgrowth is tensilely strained; see Sec. 3.2.4B) in combination with a relatively small bulk energy difference between *am*- Al_2O_3 and $\gamma\text{-Al}_2\text{O}_3$ (see Sec. 3.3.1A and Fig. 3.5c).

For oxide overgrowths on $\text{Mg}\{0001\}$ and $\text{Ni}\{111\}$ the calculated critical oxide-film thickness is less than 1 oxide ML (Figs. 3.2), which indicates that the development of a thermodynamically stable, amorphous oxide *film* on these metal surfaces is unlikely. Despite the relatively low energy of the $\langle \text{Mg}(0001) \rangle$ - $\{\text{MgO}\}$ interface, the critical thickness of the amorphous overgrowth on $\text{Mg}\{0001\}$ is suppressed by the large difference in bulk energy difference between amorphous and crystalline MgO (see Fig. 3.5a and Sec. 3.3.1F). For the overgrowth on $\text{Ni}\{111\}$ the (negative) surface and interface energy differences between amorphous and crystalline NiO are too small to compensate the corresponding (positive) bulk energy difference (see Sec. 3.3.1B).

Oxide overgrowth on $\text{Cr}\{110\}$, $\text{Cu}\{111\}$ and $\text{Fe}\{110\}$ is predicted to proceed by the direct formation and growth of a (semi-)coherent crystalline oxide phase (i.e. $h_{\{M_xO_y\}}^{\text{critical}} < 0$), in accordance with the limited number of experimental observations reported in the literature (see Sec. 3.3.1D, 3.3.1C and 3.3.1E). In these cases the (negative) sum of the surface and interfacial energy differences of the amorphous and crystalline oxide overgrowths are too small (*note*: the interfacial energy difference may even be positive, as for overgrowths on $\text{Cu}\{111\}$ and $\text{Cr}\{110\}$) to overcompensate the corresponding (positive) bulk energy difference (see Sec. 3.3.1D, 3.3.1C and 3.3.1E).

The temperature dependence of $h_{\{M_xO_y\}}^{\text{critical}} (> 0)$ is generally small (Figs. 3.2 and 3.3) and mainly governed by the decrease of the bulk Gibbs energy difference of the amorphous and crystalline oxide phases with increasing growth temperature, possibly in combination with a change of the initial lattice mismatch for the crystalline overgrowth due to a significant difference in thermal expansion coefficient between the metal and crystalline oxide phase (as for the $\text{Al}/\gamma\text{-Al}_2\text{O}_3$ system [6]). The dependence of $h_{\{M_xO_y\}}^{\text{critical}}$ on the metal-substrate orientation arises from the differences in oxide surface energy and *M*-O bond density across the metal/oxide interface for the differently orientated crystalline oxide overgrowths (as imposed by the COR between the crystalline oxide overgrowth and the parent metal substrate). The substrate-orientation dependence of $h_{\{M_xO_y\}}^{\text{critical}}$ is small for e.g. Zr (see Fig. 3.4b), Ni, Cu, Cr, Mg and Ti, but distinct for Al (see Refs. [5, 6]), Fe (see Fig. 3.4a) and Si.

It would be very elucidative if a simple, general expression could be given as a prediction for thermodynamic stability of an amorphous oxide overgrowth on its parent metal substrate (i.e. without performing detailed model calculations such as presented in this chapter; Secs. 3.2 and 3.3.1). To this end, one may propose to ignore the (positive) contributions to the interfacial energies (i.e. the entropy and the enthalpy contributions to the $\langle M \rangle$ - $\{M_xO_y\}$ interface energy and the strain and dislocation contribution to the $\langle M \rangle$ - $\langle M_xO_y \rangle$ interfacial energy), because they often approximately cancel each other out (see Sec. 3.3.1). The resulting interfacial energy difference is then only determined by the difference in the average molar interface areas $A_{\langle O \rangle}$ and $A_{\{O\}}$ of oxygen at the $\langle M \rangle$ - $\{M_xO_y\}$ and $\langle M \rangle$ - $\langle M_xO_y \rangle$ interfaces, respectively (see Sec. 3.2.4), and the M -O bond strength (as estimated from the enthalpy of mixing of O(g) atoms at infinite dilution in $\langle M \rangle$, $\Delta H_{O \text{ in } \langle M \rangle}^\infty$; see Sec. 3.2.4 and Appendix 3.C). Then, if the difference in molar volume between the amorphous and crystalline oxide is also neglected [i.e. $\chi = 1$ in Eq. (3.1)], the following simple, consequently (very) approximate expression can be given to estimate the critical thickness up to which an amorphous oxide (instead of the corresponding crystalline oxide overgrowth) is thermodynamically preferred on its parent metal substrate:

$$h_{\{M_xO_y\}}^{\text{critical,est}} = \frac{V_{\{M_xO_y\}} \left[\gamma_{\langle M_xO_y \rangle\text{-vac}} - \gamma_{\{M_xO_y\}\text{-vac}} + p \Delta H_{O \text{ in } \langle M \rangle}^\infty \cdot \left(A_{\langle O \rangle}^{-1} - A_{\{O\}}^{-1} \right) \right]}{\Delta G_{\{M_xO_y\}}^f - \Delta G_{\langle M_xO_y \rangle}^f}. \quad (3.4)$$

Application of Eq. (3.4) to the various metal/oxide systems studied in this work gives a qualitative agreement with the results of the more detailed theoretical analysis in Sec. 3.3 for oxidation at $T_0 = 298$ K (see Fig. 3.6). Same trends are also observed for the stability of an amorphous oxide overgrowth on the various metals as function of the growth temperature and substrate orientation. However, the quantitative values for $h_{\{M_xO_y\}}^{\text{critical}}$ can differ significantly (e.g. for Cu{111} $h_{\text{Cu}_2\text{O}}^{\text{critical}} < 0$, whereas $h_{\text{Cu}_2\text{O}}^{\text{critical,est}} > 0$; see Fig. 3.6).

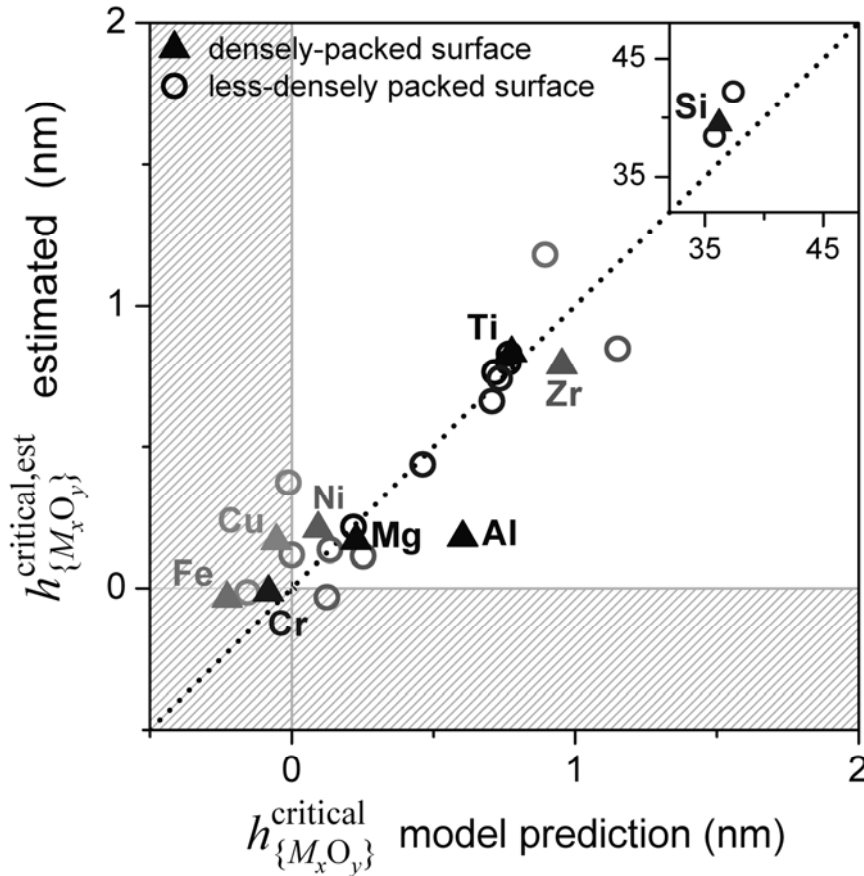


Figure 3.6. Estimated critical oxide-film thickness [i.e. $h_{\{M_xO_y\}}^{\text{critical,est}}$ as obtained from the approximate expression:

Eq. (3.4) in Sec. 3.3.2] versus the corresponding theoretical critical oxide-film thickness (i.e. $h_{\{M_xO_y\}}^{\text{critical}}$, as obtained on the basis of the thermodynamic model presented in Sec. 3.2) at T_0 for oxide overgrowths on the most-densely packed (*solid triangles*) and on less-densely packed (*open circles*) metal surfaces for various metal/oxide systems. Note that indication of the metal substrate has only been printed for the data points corresponding to the most densely packed metal surfaces. The dashed line indicates the ideal correlation:

$$h_{\{M_xO_y\}}^{\text{critical,est}} = h_{\{M_xO_y\}}^{\text{critical}}.$$

3.4. Conclusions

An amorphous phase for the oxide overgrowth on its metal substrate can be thermodynamically stable up to a certain critical thickness, as long as the positive bulk Gibbs energy difference of the competing amorphous and crystalline oxide phases can be overcompensated by a negative difference of the sum of the surface and interfacial energies of the amorphous and crystalline oxide overgrowths. Evidently, beyond a certain critical oxide-film thickness, bulk thermodynamics will always strive to stabilize the crystalline modification of the oxide overgrowth, although a large activation energy for the amorphous-

to-crystalline transition may (to some extent) preserve the initially-grown amorphous oxide phase upon further oxide growth.

As demonstrated by thermodynamic model calculations of the total, surface, interfacial and bulk energy differences of the amorphous and corresponding crystalline oxide overgrowths on the bare metal substrate, applied to a range of metal/oxide systems, the development of an amorphous oxide phase can have various principle reasons:

- (i) A small difference in the bulk Gibbs energy of formation of the amorphous and crystalline modification of the oxide phase (as for e.g. SiO₂ and Al₂O₃).
- (ii) A considerably lower surface energy for the amorphous oxide overgrowth (as for e.g. SiO₂).
- (iii) A relatively large metal-oxygen bond strength across the metal/oxide interface (as for e.g. Mg-O, Zr-O, Al-O and Ti-O).
- (iv) A relatively low density of metal-oxygen bonds across the crystalline-crystalline metal/oxide interface, indicating that a tensile strain in the competing (semi-)coherent crystalline oxide overgrowth (e.g. Al/ γ -Al₂O₃, Ti/TiO₂) and/or a lesser densely-packed crystalline oxide plane parallel to metal/oxide interface (e.g. γ -Al₂O₃{110}, Fe₃O₄{210}) favour the amorphous modification.

The aforementioned factors (ii) and (iv) are dependent on the crystallographic orientation relationship of the competing crystalline oxide overgrowth with respect to the parent metal substrate.

The model calculations show that the critical thickness, $h_{\{M_xO_y\}}^{\text{critical}}$, up to which an amorphous oxide overgrowth is thermodynamically preferred on the densely-packed Si{111}, Zr{0001}, Ti{0001}, Al{111} metal surfaces is in the range of 40 - 80 nm, 0.9 - 1 nm, 0.7 - 1 nm and 0.6 - 0.7 nm, respectively, between $T = 298$ K and $T = 900$ K (in agreement with the scarce experimental observations reported in the literature). For the densely-packed Cr{110}, Cu{111} and Fe{110} metal surfaces, oxide overgrowth is predicted to proceed by the direct formation and growth of a (semi-)coherent oxide phase (i.e. $h_{\{M_xO_y\}}^{\text{critical}} < 0$). On Mg{0001} and Ni{111} metal surfaces, the initial development of an amorphous oxide phase is unlikely, because the calculated critical oxide-film thickness is less than 1 oxide ML.

Finally, a simplified analytical expression for the approximation of $h_{\{M_xO_y\}}^{\text{critical}}$ on the various metals as function of the growth temperature and substrate orientation has been derived by neglecting the generally relatively small entropy, enthalpy and mismatch energy

contributions to the interfacial energies of the competing amorphous and crystalline oxide overgrowths, as well as their difference in density.

Appendix 3.A. Estimation of the density of an amorphous oxide

The following empirical relationship between the density, $\rho_{\{M_xO_y\}}^0$, of an amorphous oxide phase and the density, $\rho_{\langle M_xO_y \rangle}^0$, of the corresponding (thermodynamically most stable) crystalline *bulk* modification at the reference temperature $T_0 = 298$ K was obtained from the corresponding data in Refs. [27-32, 90, 91] (see Fig. 3.7):

$$\rho_{\{M_xO_y\}}^0 = 1.0466 \cdot \rho_{\langle M_xO_y \rangle}^0 - 0.6728 \quad (10^3 \text{ kg} \cdot \text{m}^{-3}). \quad (3.5)$$

Note that the thermodynamically most stable crystalline *bulk* modification at T_0 may differ from the crystalline oxide phase competing with the amorphous oxide phase for the ultra-thin oxide overgrowths considered here (e.g. $\gamma\text{-Al}_2\text{O}_3$ instead of $\alpha\text{-Al}_2\text{O}_3$; cf. Ref. [6]).

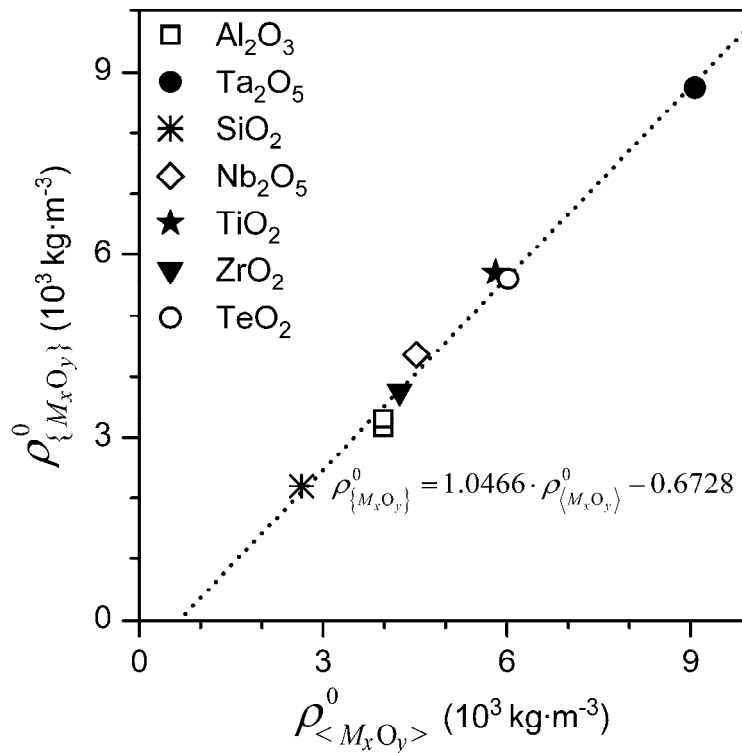


Figure 3.7. Density, $\rho_{\{M_xO_y\}}^0$, of the amorphous oxide phase versus the density, $\rho_{\langle M_xO_y \rangle}^0$, of the corresponding (thermodynamically most stable) crystalline bulk oxide phase at $T_0 = 298$ K. The dashed line represents a linear fit through the data points (with the indicated linear relationship), as obtained from the data in Refs. [27-32, 90, 91]

Appendix 3.B. Estimation of the surface energies of the oxide overgrowths

Often neither experimental nor theoretical values are available for the surface energies (and their temperature dependencies) of amorphous oxide phases, as well as of the low-index crystallographic faces of the corresponding crystalline oxide phases. In the following, empirical expressions will be derived to estimate these surface energies (and their temperature dependencies).

3.B.1. Amorphous oxides

A value for the surface energy of an amorphous oxide, $\gamma_{\{M_xO_y\}\text{-vac}}^0$, at T_0 can be approximated by extrapolation from the corresponding surface energy (which equals in the case of liquids the surface tension), $\gamma_{\{M_xO_y\}\text{-vac}}^m$, of the liquid oxide at its melting point, T_m . If required, an estimate of $\gamma_{\{M_xO_y\}\text{-vac}}^m$ is obtained from the empirical relationship between $\gamma_{\{M_xO_y\}\text{-vac}}^m$ and the molar volume, $V_{\langle M_xO_y \rangle}^0$, of the corresponding crystalline oxide at $T_0 = 298$ K, as established from the data in Refs. [92-94] (see Fig. 3.8), i.e.

$$\gamma_{\{M_xO_y\}\text{-vac}}^m \cong 1.764 \cdot k_B \cdot T_m \left(\frac{V_{\langle M_xO_y \rangle}^0}{N_A \cdot x} \right)^{-2/3} - 0.0372 \quad (\text{J} \cdot \text{m}^{-2}), \quad (3.6)$$

where x is the number of metal ions per M_xO_y unit “molecule” (k_B and N_A denote Boltzmann’s constant and Avogadro’s constant, respectively).

As argued in Ref. [95], a value of $\gamma_{\{M_xO_y\}\text{-vac}}^m$ may also be approximated by taking it to be equal to $3/4$ of the energy of the crystallographic surface plane of the corresponding crystalline oxide having the lowest energy (while neglecting the temperature dependence of the surface energy). Whereas the estimates for $\gamma_{\{M_xO_y\}\text{-vac}}^m$ as obtained using the different approaches are in good agreement for oxides like Cr_2O_3 , MgO , TiO_2 , FeO and BaO , the approach according to Ref. [95] results in lower $\gamma_{\{M_xO_y\}\text{-vac}}^m$ values for oxides like CaO and MnO and a higher $\gamma_{\{M_xO_y\}\text{-vac}}^m$ value for $\alpha\text{-Al}_2\text{O}_3$. The approach on the basis of Eq. (3.6) is used here for the estimation of $\gamma_{\{M_xO_y\}\text{-vac}}^m$.

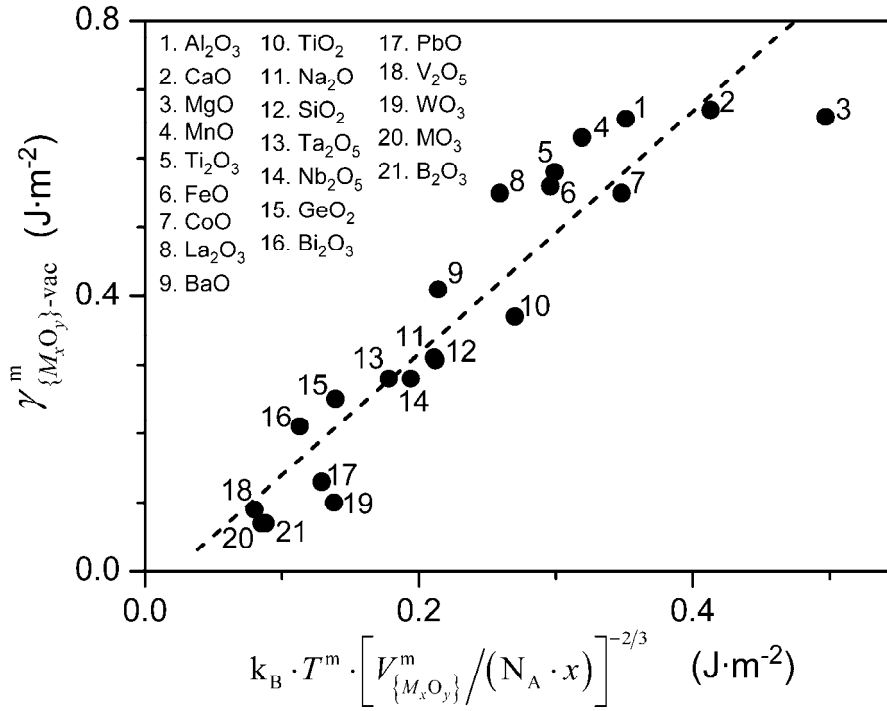


Figure 3.8. Surface energy, $\gamma_{\{M_xO_y\}\text{-vac}}^m$, of liquid oxides at their melting point, T^m , versus the corresponding energy term, $k_B \cdot T^m \cdot \left[V_{\{M_xO_y\}}^m / (N_A \cdot x) \right]^{-2/3}$, using the data in Refs. [92, 93, 96]. Here, $V_{\{M_xO_y\}}^0$ denotes the molar volume of the corresponding crystalline oxide at $T_0 = 298$ K, x is the number of metal atoms per M_xO_y molecule (k_B and N_A denote Boltzmann's constant and Avogadro's constant, respectively). The dashed line represents a linear fit through the data points according to Eq. (3.6).

Some reported literature values on the temperature dependence of the surface energy of liquid oxides have been given in Table 3.1 [93, 96]. It follows that the corresponding temperature coefficient, $\partial \gamma_{\{M_xO_y\}\text{-vac}}^{\text{liq}} / \partial T$, for most liquid oxides is negative with an average value of $-0.07(\pm 0.05) \times 10^{-3} \text{ J} \cdot \text{m}^{-2} \cdot \text{K}^{-1}$, whereas for some network-forming oxides (e.g. GeO_2 , B_2O_3 and V_2O_5 ; SiO_2 also belongs to this group) a positive temperature coefficient is found with an average value of $+0.04(\pm 0.03) \times 10^{-3} \text{ J} \cdot \text{m}^{-2} \cdot \text{K}^{-1}$.

Now, as verification, adopting Eq. (3.6) in combination with the appropriate estimate for $\partial \gamma_{\{M_xO_y\}\text{-vac}}^{\text{liq}} / \partial T$, surface energies at T_0 of, for example, $\gamma_{\{\text{Al}_2\text{O}_3\}\text{-vac}}^0 = 0.90 \text{ J} \cdot \text{m}^{-2}$ (taking $\partial \gamma_{\{\text{Al}_2\text{O}_3\}\text{-vac}}^{\text{liq}} / \partial T = -0.187 \times 10^{-3} \text{ J} \cdot \text{m}^{-2} \cdot \text{K}^{-1}$) and $\gamma_{\{\text{SiO}_2\}\text{-vac}}^0 = 0.21 \text{ J} \cdot \text{m}^{-2}$ (taking $\partial \gamma_{\{\text{SiO}_2\}\text{-vac}}^{\text{liq}} / \partial T \cong \partial \gamma_{\{\text{GeO}_2\}\text{-vac}}^{\text{liq}} / \partial T = +0.056 \times 10^{-3} \text{ J} \cdot \text{m}^{-2} \cdot \text{K}^{-1}$) have been obtained for amorphous Al_2O_3 and SiO_2 ,

respectively, which are consistent with corresponding experimental values of $\gamma_{\{\text{Al}_2\text{O}_3\}\text{-vac}}^0 = 0.88 \text{ J}\cdot\text{m}^{-2}$ [37] and $\gamma_{\{\text{SiO}_2\}\text{-vac}}^0 = 0.26 \text{ J}\cdot\text{m}^{-2}$ [38], respectively.

Table 3.1. Temperature coefficient of the surface energy, $\partial\gamma_{\{M_xO_y\}\text{-vac}}^{\text{liq}}/\partial T$, (in $[10^{-3} \text{ J}\cdot\text{m}^{-2}\cdot\text{K}^{-1}]$) of molten oxides.

Oxide	$\frac{\partial\gamma_{\{M_xO_y\}\text{-vac}}^{\text{liq}}}{\partial T}$ ($10^{-3} \text{ J}\cdot\text{m}^{-2}\cdot\text{K}^{-1}$)	References
Al_2O_3	-0.187	[93]
Bi_2O_3	-0.027	[96]
Nb_2O_5	-0.0596	[93]
P_2O_5	-0.033	[93]
TiO_2	-0.174	[96]
Ti_2O_3	-0.0744	[93]
B_2O_3	+0.055	[96]
GeO_2	+0.056	[96]
V_2O_5	+0.0111	[93]

3.B.1. Crystalline oxides

Numerous literature values of the surface energies, $\gamma_{\langle M_xO_y \rangle\text{-vac}}^{\text{relaxed}}$, of various (relaxed) low-index crystallographic faces of crystalline oxides with different structures have been gathered in Table 3.2. Only for MgO, experimental literature values for the clean single-crystalline {100} surface were found [39, 40]. All other surface energies in Table 3.2 pertain to theoretical values as obtained from molecular dynamics simulations for the relaxed oxide surfaces at (or extrapolated to) $T = 0 \text{ K}$ [37, 41-59, 96-102]. If several values of $\gamma_{\langle M_xO_y \rangle\text{-vac}}^{\text{relaxed}}$ have been reported in the literature, only the averaged value of $\gamma_{\langle M_xO_y \rangle\text{-vac}}^{\text{relaxed}}$ has been given here.

On the basis of a systematic investigation of the relationships between the surface energy of a given crystallographic plane and its corresponding oxide crystal structure (using the data in Table 3.2), the following empirical expression has been established to approximate the surface energy at $T = 0 \text{ K}$ of any given crystallographic oxide surface (see Fig. 3.9):

$$\gamma_{\langle M_xO_y \rangle\text{-vac}}^{\text{relaxed}} \cong -0.0105 \cdot N_{M-O}^{\text{NN}} \cdot E_{\langle M_xO_y \rangle}^{\text{lattice}} \cdot y^{-1} \quad (\text{J} \cdot \text{m}^{-2}), \quad (3.7)$$

where N_{M-O}^{NN} denotes the molar number of broken, near-neighbouring bonds at the oxide surface per unit surface area (which depends on the crystallographic surface plane considered), $E_{\langle M_xO_y \rangle}^{\text{lattice}}$ is the lattice energy (i.e. the Gibbs energy to form the oxide from its respective ions at $T = 0$ K) and y is the number of oxygen ions per M_xO_y unit.

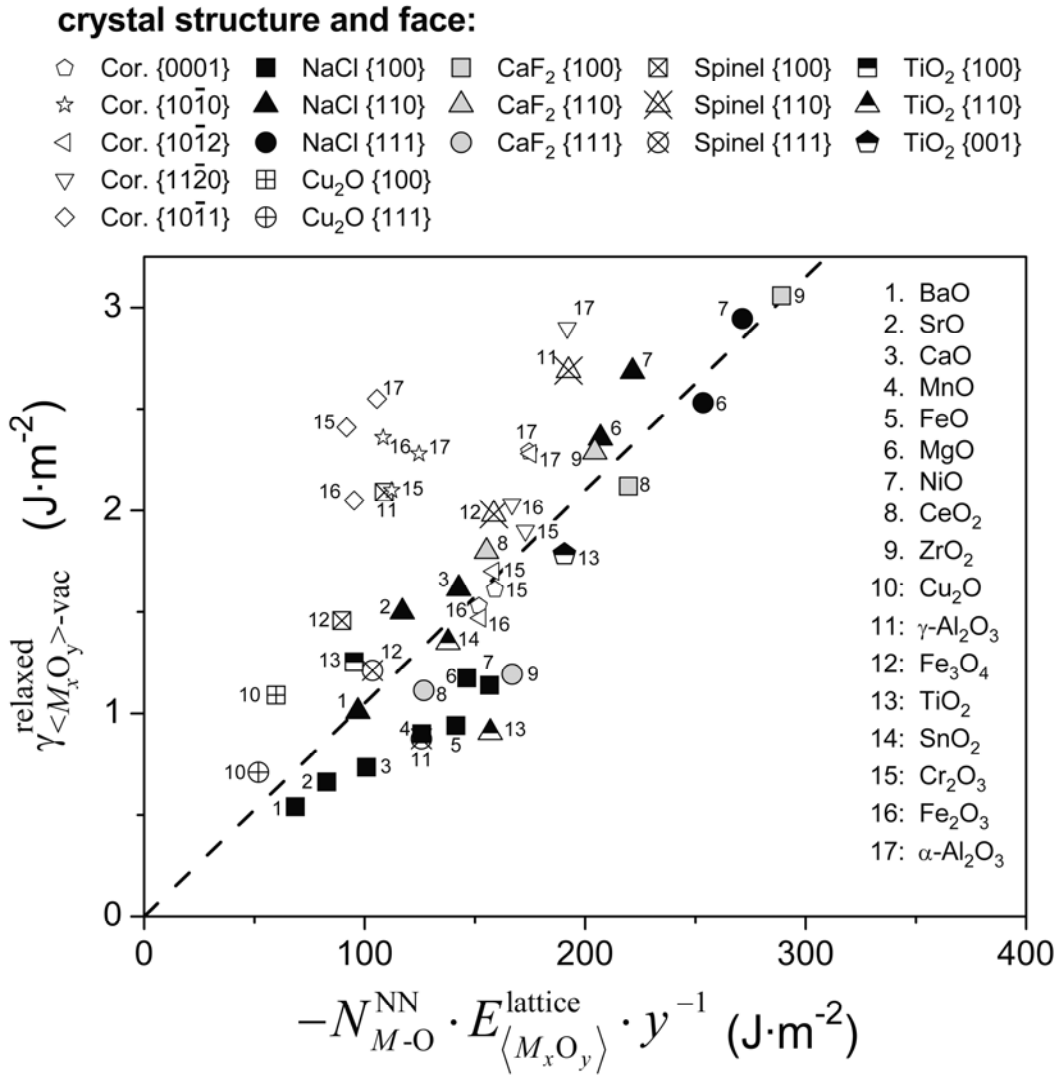


Figure 3.9. Surface energies, $\gamma_{\langle M_xO_y \rangle\text{-vac}}^{\text{relaxed}}$, of different crystallographic oxide surfaces at 0 K versus the corresponding energy term $N_{M-O}^{\text{NN}} \cdot E_{\langle M_xO_y \rangle}^{\text{lattice}} \cdot y^{-1}$, using the data in Table 3.2. Here N_{M-O}^{NN} denotes the molar number of broken, near-neighbouring bonds at the oxide surface per unit surface area, $E_{\langle M_xO_y \rangle}^{\text{lattice}}$ is the lattice energy and y is the number of oxygen ions per M_xO_y unit. The dashed line represents a linear fit through the data points according to Eq. (3.7).

Table 3.2. Surface energies, $\gamma_{\langle M_xO_y \rangle\text{-vac}}^{\text{relaxed}}$, of (relaxed) low-index crystallographic faces of (solid) crystalline oxide phases with a cubic, tetragonal and hexagonal structure, as obtained from the literature or by employing the empirical relationships as given in Appendix 3.B.2 (*small italic*). Only for MgO, an experimental literature value for the clean single-crystalline {100} surface was found [39, 40]; all other surface energies from the literature pertain to theoretical values for the relaxed oxide surfaces as obtained from molecular dynamics simulations at 0 K or 300 K (only $\gamma\text{-Al}_2\text{O}_3$ and $\alpha\text{-Al}_2\text{O}_3$). If several values of $\gamma_{\langle M_xO_y \rangle\text{-vac}}^{\text{relaxed}}$ have been reported, the here determined averaged value has been given. All listed $\gamma_{\langle M_xO_y \rangle\text{-vac}}^{\text{relaxed}}$ values pertain to a temperature of 0 K (if required literature values were extrapolated to 0 K).

Oxide	Structure	$\gamma_{\langle M_xO_y \rangle\text{-vac}}^{\text{relaxed}}$ ($\text{J}\cdot\text{m}^{-2}$) at $T = 0$ K					References
		{100}	{110}	{111}			
Cubic phase →		{100}	{110}	{111}			
BaO	rock salt	0.54	1.01	<i>1.16</i>			[41, 97]
SrO	rock salt	0.66	1.50	<i>1.40</i>			[41, 42]
CaO	rock salt	0.74	1.62	<i>1.79</i>			[41, 42, 96]
MnO	rock salt	0.90	<i>2.02</i>	<i>2.17</i>			[43]
FeO	rock salt	0.94	<i>2.24</i>	<i>2.42</i>			[43]
MgO	rock salt	1.18	2.36	2.53			[39-47]
NiO	rock salt	1.14	2.69	2.95			[43, 48, 49]
CeO ₂	fluorspar	2.12	1.80	1.11			[98, 99]
ZrO ₂	fluorspar	3.06	2.29	1.19			[50, 98]
Cu ₂ O	cuprite	1.09	<i>0.44</i>	0.71			[51, 52]
$\gamma\text{-Al}_2\text{O}_3$	spinel-like	2.09	2.69	0.94			[37]
Fe ₃ O ₄	spinel-like	1.46	1.98	1.21			[43, 53, 54]
Tetragonal phase →		{100}	{110}	{001}			
TiO ₂	rutile	1.25	0.91	1.78			[55-58]
SnO ₂	rutile	<i>0.92</i>	1.35	<i>1.83</i>			[100]
Hexagonal phase →		{0001}	{10 $\bar{1}$ 0}	{10 $\bar{1}$ 2}	{11 $\bar{2}$ 0}	{10 $\bar{1}$ 1}	
Cr ₂ O ₃	corundum	1.61	2.10	1.70	1.90	2.05	[59]
Fe ₂ O ₃	corundum	1.53	2.36	1.47	2.03	2.41	[101]
$\alpha\text{-Al}_2\text{O}_3$	corundum	2.29	2.28	2.28	2.90	2.55	[37, 101, 102]

Most literature values for $\gamma_{\langle M_xO_y \rangle\text{-vac}}^{\text{relaxed}}$ pertain to the various crystallographic surfaces of oxides with a rock salt structure (further denoted as $\langle MO \rangle$), since both x and y are equal to one

for oxides with a rock salt structure). Therefore, a specific (more accurate) empirical relationship could be established for approximation of in particular the surface energies at $T = 0$ K of the $\{100\}$, $\{110\}$ and $\{111\}$ crystallographic faces of the oxide phases with a rock salt structure (see Fig. 3.10), i.e.

$$\gamma_{\langle MO \rangle \{100\}\text{-vac}}^{\text{relaxed}} \cong -0.012 \cdot E_{\langle MO \rangle}^{\text{lattice}} \cdot V_{\langle MO \rangle}^0{}^{-2/3} \cdot N_A^{-1/3} \quad (\text{J} \cdot \text{m}^{-2}), \quad (3.8a)$$

$$\gamma_{\langle MO \rangle \{110\}\text{-vac}}^{\text{relaxed}} \cong -0.026 \cdot E_{\langle MO \rangle}^{\text{lattice}} \cdot V_{\langle MO \rangle}^0{}^{-2/3} \cdot N_A^{-1/3} \quad (\text{J} \cdot \text{m}^{-2}), \quad (3.8b)$$

$$\gamma_{\langle MO \rangle \{111\}\text{-vac}}^{\text{relaxed}} \cong -0.028 \cdot E_{\langle MO \rangle}^{\text{lattice}} \cdot V_{\langle MO \rangle}^0{}^{-2/3} \cdot N_A^{-1/3} \quad (\text{J} \cdot \text{m}^{-2}), \quad (3.8c)$$

where $V_{\langle MO \rangle}$ denotes the molar volume of the oxide phase.

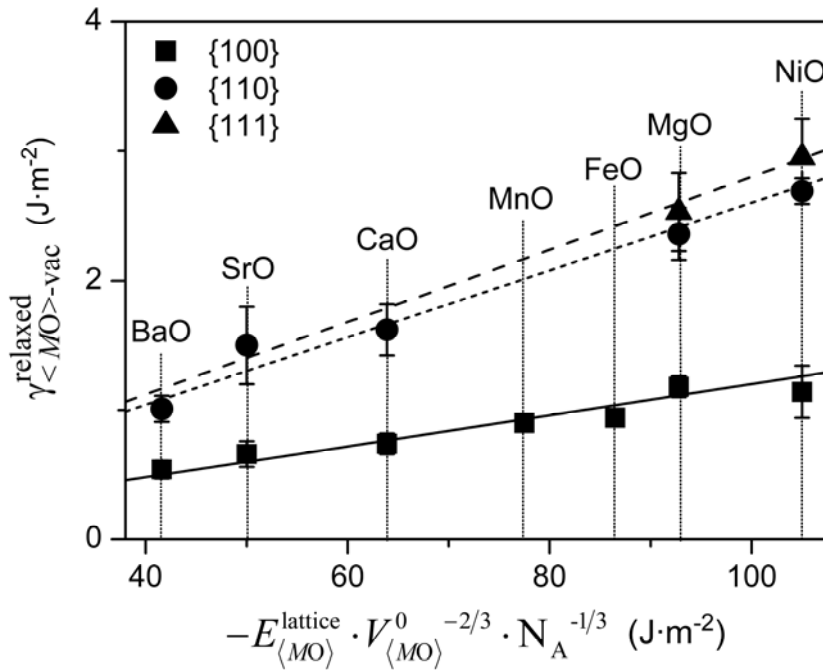


Figure 3.10. Surface energies, $\gamma_{\langle MO \rangle \text{-vac}}^{\text{relaxed}}$, of the low-index crystallographic faces of crystalline oxides with a rock-salt structure at $T = 0$ K versus the energy term, $-E_{\langle MO \rangle}^{\text{lattice}} \cdot V_{\langle MO \rangle}^0{}^{-2/3} \cdot N_A^{-1/3}$, using the data in Table 3.2. Here, $V_{\langle MO \rangle}$ and $E_{\langle MO \rangle}^{\text{lattice}}$ denote the molar volume and the lattice energy, respectively (N_A is Avogadro's constant). The lines represent linear fits through the concerned data points according to Eqs. (3.8a) – (3.8c).

Now, adopting Eqs. (3.8b) and (3.8c), as an example the following estimates have been obtained for the (missing) surface energies of $\text{FeO}\{110\}$ and $\text{FeO}\{111\}$ faces at $T = 0$ K:

$\gamma_{\langle \text{FeO} \rangle \{110\}\text{-vac}}^{\text{relaxed}} = 2.2 \text{ J} \cdot \text{m}^{-2}$ and $\gamma_{\langle \text{FeO} \rangle \{111\}\text{-vac}}^{\text{relaxed}} = 2.4 \text{ J} \cdot \text{m}^{-2}$, respectively. All unknown surface energies as required in the model calculations have been estimated from either Eq. (3.7) or

(3.8) (as listed with a smaller italic font size in Table 3.2). The surface energy at $T = 0$ K of the corresponding high indexed oxide surfaces can be estimated using a “surface step” model (i.e. by assuming that the surface consists of stepped terraces of the corresponding low-indexed surfaces [103]).

Some reported literature values on the temperature dependence, $\partial\gamma_{\langle M_xO_y \rangle\text{-vac}}^{\text{relaxed}}/\partial T$, of the surface energy of (solid) crystalline oxides have been gathered in Table 3.3. It follows that the temperature coefficient, $\partial\gamma_{\langle M_xO_y \rangle\text{-vac}}^{\text{relaxed}}/\partial T$, is negative and of the order of $10^{-4} - 10^{-3} \text{ J}\cdot\text{m}^{-2}\cdot\text{K}^{-1}$ with an average value of $-0.4\cdot 10^{-3} \text{ J} \times \text{m}^{-2}\cdot\text{K}^{-1}$ (this average value is used in the model calculations if the corresponding specific literature value is lacking).

Table 3.3. Temperature coefficient of the surface energy, $\partial\gamma_{\langle M_xO_y \rangle\text{-vac}}^{\text{relaxed}}/\partial T$, (in [$10^{-3} \text{ J}\cdot\text{m}^{-2}\cdot\text{K}^{-1}$]) of some (solid) crystalline oxides.

Oxide	$\frac{\partial\gamma_{\langle M_xO_y \rangle\text{-vac}}}{\partial T}$ ($10^{-3} \text{ J}\cdot\text{m}^{-2}\cdot\text{K}^{-1}$)	Reference
$\alpha\text{-Al}_2\text{O}_3$	-0.784	[104]
BeO	-0.359	[104]
MgO	-0.476	[104]
CaO	-0.381	[104]
ThO ₂	-0.24	[104]
UO ₂	-0.346	[104]
TiO ₂	-0.167	[104]

Appendix 3.C. Enthalpy of mixing O in $\langle M \rangle$

The enthalpy of mixing, $\Delta H_{\text{O in } \langle M \rangle}^{\infty}$, at infinite dilution of 1 mol oxygen atoms (in gaseous state) in a solid metal, $\langle M \rangle$, can be estimated from an empirical relationship between $\Delta H_{\text{O in } \langle M \rangle}^{\infty}$ and the enthalpy of oxide formation, $\Delta H_{\langle M_xO_y \rangle}^{\text{f}}$, per mol O, as obtained from the data in Refs. [24, 61-65] (see Fig. 3.11 and Ref. [6]),

$$\Delta H_{\text{O in } \langle M \rangle}^{\infty} \cong 1.2\Delta H_{\langle M_xO_y \rangle}^{\text{f}} + 1 \times 10^5 \quad (\text{J}\cdot\text{mol}^{-1}). \quad (3.9)$$

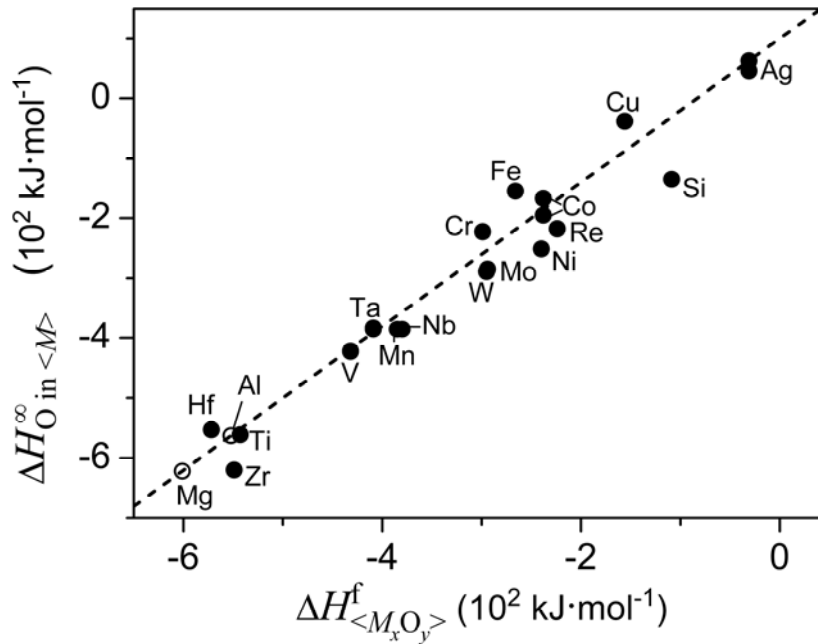


Figure 3.11. The enthalpy of mixing, $\Delta H_{O \text{ in } \langle M \rangle}^{\infty}$, at infinite dilution of 1 mol oxygen atoms (in gaseous state) in a solid metal, $\langle M \rangle$, as function of the enthalpy of formation, $\Delta H_{\langle M_x O_y \rangle}^f$, per mol O. The data (filled markers) have been taken from Refs. [24, 61-65], leading to a relationship (line) according to: $\Delta H_{O \text{ in } \langle M \rangle}^{\infty} \cong 1.2 \cdot \Delta H_{\langle M_x O_y \rangle}^f + 1 \times 10^5 \text{ J mol}^{-1}$. The open markers for Al and Mg indicate calculated values according to the aforementioned equation.

References

- [1] F. P. Fehlner, *Low-Temperature Oxidation: The Role of Vitreous Oxides*. (John Wiley & Sons, New York, 1986).
- [2] K. R. Lawless, *Rep. Prog. Phys.* **37** (1974) 231.
- [3] L. P. H. Jeurgens, W. G. Sloof, F. D. Tichelaar and E. J. Mittemeijer, *J. Appl. Phys.* **92** (2002) 1649.
- [4] L. P. H. Jeurgens, A. Lyapin and E. J. Mittemeijer, *Acta Mater.* **53** (2005) 4871.
- [5] F. Reichel, L. P. H. Jeurgens, G. Richter, P. A. van Aken and E. J. Mittemeijer, *Acta Mater.* **55** (2007) 6027.
- [6] L. P. H. Jeurgens, W. G. Sloof, F. D. Tichelaar and E. J. Mittemeijer, *Phys. Rev. B* **62** (2000) 4707.
- [7] F. Reichel, L. P. H. Jeurgens and E. J. Mittemeijer, *Phys. Rev. B* **74** (2006) 144103.
- [8] F. P. Fehlner and N. F. Mott, *Oxid. Met.* **2** (1970) 59.

- [9] N. Cabrera and N. F. Mott, Rep. Prog. Phys. **12** (1949) 163.
- [10] A. G. Revesz and F. P. Fehlner, Oxid. Met. **15** (1981) 297.
- [11] H.-J. Freund, Surf. Sci. **601** (2007) 1438.
- [12] A. Johansson, G. Sambandamurthy, D. Shahar, N. Jacobson and R. Tenne, Phys. Rev. Lett. **95** (2005) 116805.
- [13] C. J. Först, K. Schwarz and P. E. Blöchl, Phys. Rev. Lett. **95** (2005) 137602.
- [14] P. Michel and Ch. Jardin, Surf. Sci. **36** (1973) 478.
- [15] C. A. Haque and H. E. Farnsworth, Surf. Sci. **1** (1964) 378.
- [16] M. A. Muñoz-Márquez, R. E. Tanner and D. P. Woodruff, Surf. Sci. **565** (2004) 1.
- [17] T. M. Christensen, C. Raoul and J. M. Blakely, Appl. Surf. Sci. **26** (1986) 408.
- [18] B. Hayden, E. Schweizer, R. Kötz and A. M. Bradshaw, Surf. Sci. **111** (1981) 26.
- [19] S. A. Flodström and C. W. B. Martinson, Surf. Sci. **118** (1982) 513.
- [20] C. Leygraf and S. Ekelund, Surf. Sci. **40** (1973) 609.
- [21] J. B. Wagner Jr., K. R. Lawless and A. T. Gwathmey, Trans. Metall. Soc. AIME **221** (1961) 257.
- [22] F. R. de Boer, R. Boom, W. C. M. Mattens, A. R. Miedema and A. K. Niessen, *Cohesion in Metals: Transition Metal Alloys* (North-Holland, Amsterdam, 1989) Chapters 2 and 4.
- [23] J. H. van der Merwe, Surf. Sci. **31** (1972) 198.
- [24] M. W. Chase Jr., *NIST-JANAF Thermochemical Tables, 4th edition*. J. Phys. Chem. Ref. Data (1998).
- [25] E. G. King and A. U. Christensen Jr., J. Am. Chem. Soc. **80** (1958) 1800.
- [26] G. V. Samsonov, *The Oxide Handbook*. (IFI/Plenum, New York, 1973).
- [27] Powder Diffraction Files, JCPDS-International Centre for Diffraction Data (2007).
- [28] W. J. Bernard and J. W. Cook, J. Electrochem. Soc. **106** (1959) 643.
- [29] K. Fukuda, T. Hanada, S. Tanabe and T. Yao, J. Am. Ceram. Soc. **85** (2002) 915.
- [30] L. Young, *Anodic Oxide Films* (Academic Press, London, 1961).
- [31] D. B. Dingwell, J. Am. Ceram. Soc. **74** (1991) 2718.
- [32] O. Pilla, L. Angelani, A. Fontana, J. R. Gonçalves and G. Ruocco, J. Phys.: Condens. Matter **15** (2003) S995.

- [33] Y. S. Touloukian, R. K. Kirby, R. E. Taylor and T. Y. R. Lee, *Thermal Expansion. Nonmetallic Solids*, Vol. 13 (IFI/Plenum, New York, 1977).
- [34] H. Yanagida and G. Yamaguchi, *Bull. Chem. Soc. Jpn.* **37** (1964) 1229.
- [35] A. L. Pranatis, *J. Am. Ceram. Soc.* **51** (1968) 182.
- [36] Y. S. Touloukian, R. K. Kirby, R. E. Taylor and T. Y. R. Lee, *Thermal Expansion. Elements and Alloys*, Vol. 12 (IFI/Plenum, New York, 1977).
- [37] S. Blonski and S. H. Garofalini, *Surf. Sci.* **295** (1993) 263.
- [38] R. K. Iler, *The Chemistry of Silica* (John Wiley & Sons, New York, 1979). p. 645.
- [39] J. J. Gilman, *J. Appl. Phys.* **31** (1960) 2208.
- [40] G. Jura and C. W. Garland, *J. Am. Chem. Soc.* **74** (1952) 6033
- [41] P. Broquist, H. Grönbeck and I. Panas, *Surf. Sci.* **554** (2004) 262.
- [42] J. Goniakowski and C. Noguera, *Surf. Sci.* **319** (1994) 68.
- [43] J. Robertson and M. I. Manning, *Mater. Sci. Technol.* **6** (1990) 81.
- [44] A. R. C. Westwood and D. L. Goldheim, *J. Appl. Phys.* **34** (1963) 3335.
- [45] A. Wander, I. J. Bush and N. M. Harrison, *Phys. Rev. B* **68** (2003) 233405.
- [46] D. Wolf, *Solid State Ionics* **75** (1995) 3.
- [47] J. H. Harding, D. J. Harris and S. C. Parker, *Surf. Sci.* **422** (1999) L183.
- [48] C. A. J. Fisher, *Scripta Mater.* **50** (2004) 1045.
- [49] P. M. Oliver, G. W. Watson and S. C. Parker, *Phys. Rev. B* **52** (1995) 5323.
- [50] A. Christensen and E. A. Carter, *Phys. Rev. B* **58** (1998) 8050.
- [51] M. A. Nygren, L. G. M. Pettersson, A. Freitag, V. Staemmler, D. H. Gay and A. L. Rohl, *J. Phys. Chem.* **100** (1996) 294.
- [52] A. Soon, T. Söhnell and H. Idriss, *Surf. Sci.* **579** (2005) 131.
- [53] J. R. Rustad, E. Wasserman and A. R. Felmy, *Surf. Sci.* **432** (1999) L583.
- [54] R. K. Mishra and G. Thomas, *J. Appl. Phys.* **48** (1977) 4576.
- [55] V. Swamy, J. Muscat, J. D. Gale and N. M. Harrison, *Surf. Sci.* **504** (2002) 115.
- [56] J. Purton, D. W. Bullett, P. M. Oliver and S. C. Parker, *Surf. Sci.* **336** (1995) 166.
- [57] S. P. Bates, G. Kresse and M. J. Gillan, *Surf. Sci.* **385** (1997) 386.
- [58] J. Muscat and N. M. Harrison, *Surf. Sci.* **446** (2000) 119.
- [59] P. J. Lawrence, S. C. Parker and P. W. Tasker, *J. Am. Ceram. Soc.* **71** (1988) C-389.

- [60] I. Molodetsky, A. Navrotsky, M. J. Paskowitz, V. J. Leppert and S. H. Risbud, *J. Non-Cryst. Solids* **262** (2000) 106.
- [61] O. Kubaschewski, C. B. Alcock and P. J. Spencer, *Materials Thermochemistry*, 6th ed. (Pergamon Press, Oxford, 1993) p.47.
- [62] E. Fromm, O. Mayer and W. Nickerson, *Surf. Sci.* **57** (1976) 775.
- [63] E. Fromm, E. Gebhardt (ed.), *Gase und Kohlenstoffe in Metallen* (Springer, Berlin, 1976).
- [64] T. Tokuda and H. Harada, in: S. Takeuchi (ed.), *Proceedings of the 2nd International Conference on the Properties of Liquid Metals, Tokyo 1972* (Taylor & Francis, London, 1973) p. 583.
- [65] R. C. Newman, M. J. Binns, W. P. Brown, F. M. Livingston, S. Messoloras, R. J. Stewart and J. G. Wilkes, *Physica B* **116** (1983) 264.
- [66] F. Reichel, L. P. H. Jeurgens and E. J. Mittemeijer, *Thin Solid Films* (2007) in press.
- [67] G. Simmons and H. Wang, *Single Crystal Elastic Constants and Calculated Aggregate Properties: A Handbook*, 2nd ed. (The M.I.T. Press, Cambridge, Massachusetts, 1971).
- [68] M. R. Gallas and G. J. Piermarini, *J. Am. Ceram. Soc.* **77** (1994) 2917.
- [69] H. L. Alberts and J. C. A. Boeyens, *J. Magnetism Magnetic Mater.* **2** (1976) 327
- [70] M. M. Beg and S. M. Shapiro, *Phys. Rev. B* **13** (1976) 1728.
- [71] J. Hallberg and R. C. Hanson, *Phys. Status Solidi* **42** (1970) 305.
- [72] M. H. Manghnani, W. S. Brower and H. S. Parker, *Phys. Status Solidi a* **25** (1974) 69.
- [73] P. de V. Du Plessis, S. J. van Tonder and L. Alberts, *J. Phys. C: Solid State Phys.* **4** (1971) 1983.
- [74] S.-K. Chan, Y. Fang, M. Grimsditch, Z. Li, M. V. Nevitt, W. M. Robertson and E. S. Zouboulis, *J. Am. Ceram. Soc.* **74** (1991) 1742.
- [75] S. V. Sinogeikin, J. M. Jackson, B. O'Neill, J. W. Palko and J. D. Bass, *Rev. Sci. Instrum.* **71** (2000) 201.
- [76] K. Marklund and S. A. Mahmoud, *Physica Scripta* **3** (1971) 75.
- [77] J. V. Atanasoff and P. J. Hart, *Phys. Rev.* **59** (1941) 85.
- [78] H. Kimizuka and H. Kaburaki, *Phys. Status Solidi b* **242** (2005) 607.
- [79] J. I. Eldridge, R. J. Hussey, D. F. Mitchell and M. J. Graham, *Oxid. Met.* **30** (1988) 301.
- [80] K. R. Lawless and A. T. Gwathmey, *Acta Metall.* **4** (1956) 153.
- [81] A. T. Fromhold, Jr. and M. H. Anderson, Jr., *Oxid. Met.* **62** (2004) 237.

- [82] S. J. Roosendaal, B. van Asselen, J. W. Elsenaar, A. M. Vredenberg and F. H. P. M. Habraken, *Surf. Sci.* **442** (1999) 329.
- [83] P. B. Sewell, D. F. Mitchell and M. Cohen, *Surf. Sci.* **33** (1972) 535.
- [84] F. Qin, N. P. Magtoto, M. Garza and J. A. Kelber, *Thin Solid Films* **444** (2003) 179.
- [85] R. A. Ploc, *J. Nucl. Mater.* **110** (1982) 59.
- [86] R. A. Ploc, *J. Nucl. Mater.* **113** (1983) 75.
- [87] R. A. Ploc, *J. Nucl. Mater.* **115** (1983) 110.
- [88] D. L. Douglass and J. van Landuyt, *Acta Metall.* **13** (1965) 1069.
- [89] H. M. Flower and P. R. Swann, *Acta Metall.* **22** (1974) 1339.
- [90] F. Holtzberg, A. Reisman, M. Berry and M. Berkenblit, *J. Am. Chem. Soc.* **79** (1957) 2039.
- [91] R. Nayak, V. Gupta, A. L. Dawar and K. Sreenivas, *Thin Solid Films* **445** (2003) 118.
- [92] T. Tanaka, K. Hack, T. Iida and S. Hara, *Z. Metallkd.* **87** (1996) 380.
- [93] N. Ikemiya, J. Umemoto, S. Hara and K. Ogino, *ISIJ Int.* **33** (1993) 156.
- [94] N. Eustarhopoulos, M. G. Nicholas and B. Drevet, *Wettability at High Temperatures* (Pergamon, Amsterdam, 1999) Chap. 4, p. 148.
- [95] J. W. Taylor, *J. Inst. Met.* **86** (1957-58) 456.
- [96] S. H. Overbury, P. A. Bertrand and G. A. Somorjai, *Chem. Rev.* **75** (1975) 547.
- [97] D. T. Livey and P. Murray, *J. Am. Ceram. Soc.* **39** (1956) 363.
- [98] S. Gennard, F. Cora and C. R. A. Catlow, *J. Phys. Chem. B* **103** (1999) 10158.
- [99] M. Nolan, S. Grigoleit, D. C. Sayle, S. C. Parker and G. W. Watson, *Surf. Sci.* **576** (2005) 217.
- [100] I. Manassidis, J. Goniakowski, L. N. Kantorovich and M. J. Gillan, *Surf. Sci.* **339** (1995) 258.
- [101] W. C. Mackrodt, R. J. Davey, S. N. Black and R. Docherty, *J. Crystal Growth* **80** (1987) 441.
- [102] I. Manassidis and M. J. Gillan, *J. Am. Ceram. Soc.* **77** (1994) 335.
- [103] P. G. Shewmon and W. M. Robertson, in: *Metal Surfaces: Structure, Energetics and Kinetics* (American Society for Metals, Metals Park, Ohio, 1963) Chap. 3, p. 67.
- [104] N. Zouvelou, D. Skarmoutsos and P. Nikolopoulos, *Key Eng. Mater.* **264-268** (2004) 679.

Chapter 4

The origin of high mismatch orientation relationships for ultra-thin oxide overgrowths

F. Reichel, L. P. H. Jeurgens, G. Richter, P. A. van Aken and E. J. Mittemeijer

Abstract

A crystallographic orientation relationship (COR) of unusual high lattice mismatch ($> 15\%$) between an Al{100} substrate and its ultra-thin (< 1 nm) oxide overgrowth is reported. This striking observation is in contrast with the general assumption that a COR with the lowest mismatch is preferred. However, as shown by thermodynamic model calculations, despite the relatively large energy contributions due to residual strain and misfit dislocations, the high-mismatch overgrowth can be stabilized by a relatively low surface energy and a relatively high density of metal-oxygen bonds across the interface.

4.1. Introduction

Controlled preparation of ultra-thin (< 5 nm) oxide films and nano-sized oxide particles in application areas such as microelectronics, solid-state devices, surface coatings and catalysis, can result in stable oxide microstructures different from those predicted by *bulk* thermodynamics. For example, for the overgrowth of ultra-thin oxide films on metal substrates (e.g., by thermal or plasma oxidation), an amorphous oxide phase instead of the corresponding crystalline modification can be thermodynamically preferred, because of the lower sum of surface and interface energies for the amorphous oxide configuration [1, 2]. The obvious absence of lattice defects and grain boundaries in these amorphous films reduces both ionic and electronic migration through the oxide, thereby improving their properties such as the electrical resistivity, corrosion resistance or catalytic activity [3, 4]. Similarly, for nano-sized oxide particles, a crystalline oxide phase unstable as bulk material can be thermodynamically preferred due to its relatively low surface energy: e.g., γ -Al₂O₃ [5] or θ -Al₂O₃ [6] instead of α -Al₂O₃, γ -Y₂O₃ instead of α -Y₂O₃ [7] or tetragonal ZrO₂ instead of monoclinic ZrO₂ [8]. Only above some critical oxide-film thickness or particle size, a

transformation into an, according to bulk thermodynamics, more stable oxide phase can be realized [1].

The present contribution addresses another, up to date unrecognized, nano-size-related phenomenon occurring for ultra-thin oxide overgrowths on their metal substrates: i.e., the occurrence of a crystallographic orientation relationship (COR) of *exceptionally high lattice mismatch* (i.e. $> 15\%$) between a metal substrate and its oxide overgrowth. This striking observation, as found here using Low Energy Electron Diffraction (LEED) and High-Resolution Transmission Electron Microscopy (HR-TEM) for the overgrowth of ultra-thin oxide films on single-crystalline Al{100} substrates grown by thermal oxidation, is in contrast with the general assumption that, for the overgrowth of a crystalline film on a parent substrate, a COR corresponding with the lowest possible lattice mismatch is preferred [9, 10]. However, as demonstrated by calculations using a new thermodynamic model [2] for the observed high-mismatch COR between the oxide overgrowth and its parent Al{100} substrate, the large energy contributions due to residual growth strain and misfit dislocations in such thin overgrowths can be overcompensated by a relatively low surface energy contribution (as compared to the low-mismatch COR) in combination with a relatively high density of metal-oxygen bonds across the metal/oxide interface (and thus a more negative chemical interaction contribution to the resultant interface energy; see Sec. 4.5). Therefore, ignoring the role of the surface energy and/or the interface energy contributions, as e.g. in the commonly applied Bollmann's method [9], can lead to wrong theoretical predictions of CORs for ultra-thin overgrowths.

Several HR-TEM investigations have been reported on the microstructure of metal/oxide interfaces, which give information to an atomic level on the composition and atomic arrangements at and adjacent to the interface (e.g. Refs. [11, 12]). However, the microstructure of *ultra-thin* oxide overgrowths on *bare* metal surfaces, as well as their COR with the parent metal substrate, have only scarcely been addressed until the present day (cf. Refs. [13, 14]). Most HR-TEM studies on the oxidation of metal surfaces [15-19] have been performed in the presence of a native oxide on the metal surface at the onset of oxidation and for elevated oxidation temperatures (> 600 K), where much thicker oxide films are grown. In this contribution, a combined experimental approach by HR-TEM, LEED and Angle-Resolved X-ray Photoelectron Spectroscopy (AR-XPS) is employed to investigate the microstructure and composition, as well as the COR with respect to the parent metal substrate, of *ultra-thin* (0.4 – 1 nm thick) Al₂O₃ films grown on *bare* Al{111} and Al{100} substrates by thermal oxidation.

4.2. Experimental

4.2.1. Material and surface preparation

Disc-shaped Al{111} and Al{100} single-crystals (10 mm diameter, 1 mm thick, purity better than 5N, orientation alignment better than 0.5°) were supplied and their surfaces polished by 'Surface Preparation Laboratory' (Zaandam, The Netherlands). Prior to each oxidation experiment, performed in a UHV processing and analysis system (base pressure $< 5 \times 10^{-8}$ Pa), the Al single-crystals were outgassed, cleaned and their crystal order restored by a cyclic treatment of sputter-cleaning with 1 keV Ar⁺ ions while applying sample rotation at a speed of about 6 °/s (to avoid roughening of the sample surface) and subsequent annealing in UHV at 723 K (to restore the crystal order at the ion-bombarded surface). This cyclic treatment was repeated until no contamination of C, O, Ar or other impurities were detected by Angle-Resolved X-Ray Photoelectron Spectroscopy (for details, see Sec. 4.2.3). Next, in-situ LEED (Specs 4-grid ER-LEED system using primary electron energies in the range of 30 – 200 eV) was applied to verify that the crystal order of the metal surface was restored after the final annealing step. The thus obtained single-crystal surfaces will be further designated as *bare* metal substrates. As verified by atomic force microscopic analysis, the root mean square surface roughness of the bare metal substrates after repetitive cycles of sputter-cleaning, annealing and oxidation is still as low as 9.1 ± 0.1 nm.

4.2.2. Oxidation

Next, ultra-thin (thickness < 1 nm) oxide films were grown in the temperature (T) range of 350 – 650 K by exposure of a bare Al{111} or Al{100} substrate for 6000 s to pure oxygen gas (purity: 99.997 vol.%) at a partial oxygen pressure (p_{O_2}) of 1×10^{-4} Pa (as measured with a Bayerd-Alpert nude pressure gauge). All oxidations were carried out in the UHV reaction chamber (base pressure $< 3 \times 10^{-8}$ Pa), which is directly coupled to UHV chambers for AR-XPS analysis (base pressure $< 5 \times 10^{-8}$ Pa) and thin film deposition by Molecular Beam Epitaxy (MBE) (base pressure $< 2 \times 10^{-8}$ Pa). Sample heating was performed by focusing the light emitted by a halogen light bulb on the backside of the specimen using a gold-coated, elliptical mirror. A uniform temperature profile across the sample surface was obtained (i.e. temperature gradients along the sample surface were minimal) by optimizing the position of the focus point of the light beam below the backside of the sample. The surface temperature was controlled using a Eurotherm 2404 control unit by employing feed back of the surface temperature, as measured by a type K (NiAl / NiCr) thermocouple wire mechanically pressed

onto the sample surface, to the output power of the halogen light bulb. As verified by in-situ melting of small pieces of pure metals of very low vapour pressure (i.e. In, Bi, Pb, Sn) on a polycrystalline Al sample surface, the error in the measurement of the 'real' surface temperature lies within the range of approximately 5 K to 8 K (the error slightly increases with increasing temperature). Next, first in-situ AR-XPS analysis of the oxidized substrate was performed to determine the oxide-film thickness and composition (Sec. 4.2.3). Finally, in-situ LEED analysis (Sec. 4.2.1) was applied to determine the crystal structure of the oxide overgrowth.

4.2.3. AR-XPS analysis and quantification

X-ray Photoelectron Spectroscopic (XPS) analysis of the specimen surface before and after oxidation was performed with a Thermo VG Thetaprobe system employing monochromatic Al K α radiation ($h\nu = 1486.68$ eV; spot size 400 μm). XPS survey spectra, covering a binding energy (BE) range of 0 eV to 1200 eV, were recorded with a step size of 0.2 eV at constant pass energy of 200 eV. Further, detailed *angle-resolved* XPS (AR-XPS) spectra of the Al 2p and O 1s regions were recorded in so-called data acquisition mode by detecting the photoelectrons simultaneously over the angular detection range of 23° to 83° in eight ranges of 7.5° each (for details, see Ref. [20]) with a step size and a constant pass energy of 0.05 eV and 50 eV, respectively. The AR-XPS measurements were performed at 9 defined locations on the surface (spot size 400 μm) equally distributed over an entire analysis area of 3 \times 3 mm². For the quantification of the measured AR-XPS spectra, the recorded spectra were first averaged over all measured positions of the sample surface for each angular range of photoelectron detection employed. Next, the thus obtained spectra were corrected for the electron kinetic energy dependent transmission of the spectrometer analyzer by adopting the corresponding correction factor as provided by the manufacturer. Then, for each detection angle, the Al 2p primary zero loss (PZL) intensities [21] of the corresponding asymmetrically shaped metallic main peaks (i.e. including the tail towards higher BE values, but excluding the intrinsic plasmon intensity [21]) and the symmetrically shaped oxidic Al 2p and O 1s main peaks were resolved from the measured AR-XPS spectra of the bare and the oxidized substrate according to the procedure described in detail in Refs. [21, 22].

The average thicknesses and compositions (and corresponding standard deviations) of the grown oxide films were calculated from the thus resolved metallic Al 2p, oxidic Al 2p and O1s total PZL intensities of the oxidized metal (for various detection angle sets), analogously

to the iterative calculation scheme presented in Ref. [22] for the quantification of oxide films grown on MgAl alloys.

4.2.4. HR-TEM sample preparation and analysis

For the preparation of the HR-TEM metal/oxide cross sections, bare single-crystalline substrates were oxidized for 6000 s (at $p_{\text{O}_2} = 1 \times 10^{-4}$ Pa) and employing an oxidation temperature of 373 K or 550 K for Al{111} and of 550 K for Al{100} (Sec. 4.2.2). After subsequent AR-XPS analysis, the grown films were sealed *in-situ* by deposition of a dense ~150 nm thick Al capping layer in the UHV MBE chamber. The seal deposition was performed by evaporation of ultra-pure Al metal (purity better than 6N) from a boron-nitride crucible using a cold-lip effusion cell operating at a temperature of 1050°C (deposition rate ~ 2 nm/min). During the deposition the specimen (holder) was cooled with liquid nitrogen to prevent any microstructural changes of the oxide film by a local heating up of the oxidized sample surface by heat irradiation from the evaporation source, as well as to minimize the chemical interaction of the Al capping layer with the oxide-film surface. Next, the oxidized specimens with capping layer were removed from the UHV system and, subsequently, a TEM-lamella was cut from the specimens using a dual Focused Ion Beam (FIB Nova Nanolab 600 from FEI company) with Ga⁺ ions accelerated at 30 keV and employing an ion current that decreased from 7 nA to 30 pA with increasing operation time. Prior to the FIB cutting procedure, the specimen surface was protected with a Pt capping layer deposited on top of the Al capping layer. The thus obtained lamella has a size of 3 μm × 4 μm and a thickness of about 80 nm to 100 nm. An overview of the thus obtained cross-sectional TEM lamella is shown in the bright-field TEM micrograph of Fig. 4.1.

The HR-TEM analysis was performed using a JEOL JEM-ARM1250 electron microscope with a very high acceleration voltage of 1250 kV and a point-to-point resolution with the side entry lens of 0.12 nm (for instrumental details, see Ref. [23]). To retard the occurrence of microstructural changes in the irradiated area of specimen, as inflicted by the high-energy electron beam, the lamellae were cooled with liquid nitrogen during the HR-TEM analysis. Despite the liquid nitrogen cooling, irreversible microstructural changes were induced by the electron irradiation within the thin oxide films after more prolonged HR-TEM analysis at a single position (see Appendix 4.A). Therefore, it was ensured that all microstructural characterization of the oxide overgrowths by HR-TEM, as presented in this study (see Sec. 4.4), only pertains to micrographs of ‘fresh’ (i.e. not previously irradiated) cross-sectional areas, as recorded within irradiation times of at most 2 minutes. The negatives

of the recorded micrographs were digitized for further quantitative evaluation. Internal calibration of the length scale was performed on the micrographs using the known lattice constant of the Al metal (0.40494 nm [24]).

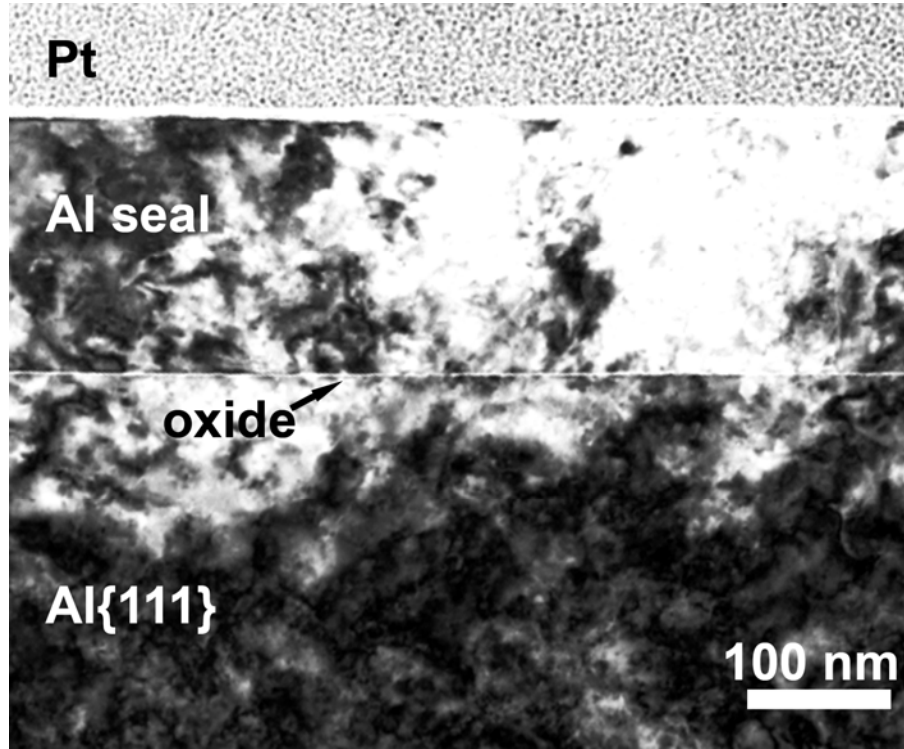


Figure 4.1. Bright field transmission electron micrograph of the cross-sectional TEM lamella obtained from the oxidized and sealed Al{111} substrate (see text).

4.3. Thermodynamics of oxide overgrowths on metals; summary of theoretical background

Consider a homogeneous oxide film, M_xO_y , with thickness $h_{M_xO_y}$, on a single-crystalline metal substrate, M . The difference in total Gibbs energy per unit area between oxide overgrowths of different microstructure (i.e., amorphous versus crystalline or low-mismatch versus high-mismatch) on the same substrate, ΔG , can be given as the sum of the differences in bulk, surface, $\gamma_{M_xO_y-vac}$, and interface, $\gamma_{M-M_xO_y}$, energy contributions (see Refs. [1, 2] and Chapter 2).

Approximate expressions for the solid-solid interfacial energies in Eq. (4.1) (see below) have been derived on the basis of the macroscopic atom approach [1, 2, 25]. To this end, the energy, $\gamma_{\langle M \rangle - \langle M_xO_y \rangle}$ of a coherent or semi-coherent crystalline-crystalline interface, is expressed (for details, see Ref. [2]) as the resultant of the negative chemical interaction contribution

($\gamma_{\langle M \rangle - \langle M_x O_y \rangle}^{\text{interaction}}$) and two positive energy contributions originating from the initial lattice mismatch between the metal substrate and the crystalline oxide film: i.e. the strain contribution ($\gamma_{\langle M \rangle - \langle M_x O_y \rangle}^{\text{strain}}$) due to residual homogeneous strain within the oxide overgrowth and the dislocation contribution ($\gamma_{\langle M \rangle - \langle M_x O_y \rangle}^{\text{dislocation}}$) due to the periodic, inhomogeneous strain field associated with misfit dislocations at the metal/oxide interface:

$$\gamma_{\langle M \rangle - \langle M_x O_y \rangle} = \gamma_{\langle M \rangle - \langle M_x O_y \rangle}^{\text{interaction}} + \gamma_{\langle M \rangle - \langle M_x O_y \rangle}^{\text{strain}} + \gamma_{\langle M \rangle - \langle M_x O_y \rangle}^{\text{dislocation}}. \quad (4.1)$$

The dislocation energy contribution ($\gamma_{\langle M \rangle - \langle M_x O_y \rangle}^{\text{dislocation}}$) equals the sum of the energies of two perpendicular, regularly spaced arrays of misfit dislocations with Burgers vectors parallel to two corresponding perpendicular directions within the metal/oxide interface plane and is calculated here using a first approximation approach of Frank and van der Merwe (for details, see Refs. [2,26]). Because the *total* growth strain at the $\langle M \rangle - \langle M_x O_y \rangle$ interface equals the sum of the residual homogeneous strain and the superimposed periodic, inhomogeneous strain associated with the grid of misfit dislocations [26], a decrease of the residual homogeneous strain energy contribution, $\gamma_{\langle M \rangle - \langle M_x O_y \rangle}^{\text{strain}}$, by the introduction of misfit dislocations at the $\langle M \rangle - \langle M_x O_y \rangle$ interface is always accompanied by a increase of the dislocation energy contribution, $\gamma_{\langle M \rangle - \langle M_x O_y \rangle}^{\text{dislocation}}$. It is further noted that the interaction energy contribution, $\gamma_{\langle M \rangle - \langle M_x O_y \rangle}^{\text{interaction}}$, is also affected by the introduction of misfit dislocations due to the associated change of the density of metal-oxygen bonds across the interface [2]. The energy contributions due to the residual homogeneous, possible anisotropic strain and the misfit dislocations in the crystalline oxide film are attributed here to the interface energy instead of to the bulk energy of the film, and hence it follows that a minimum in the total Gibbs energy of the crystalline cell (thermodynamic equilibrium) is attained if $\gamma_{\langle M \rangle - \langle M_x O_y \rangle}$ is at its minimum value [2]. To determine the minimum value of $\gamma_{\langle M \rangle - \langle M_x O_y \rangle}$, the residual-strain-affected lattice spacings of the crystalline film in two mutually perpendicular directions within the interface plane are solved simultaneously by minimization of $\gamma_{\langle M \rangle - \langle M_x O_y \rangle}$ with respect to the residual, possibly anisotropic, homogeneous strain in the film for a given oxide-film thickness, $h_{\langle M_x O_y \rangle}$, and growth temperature, T , i.e. [2]

$$\frac{\partial \gamma_{\langle M \rangle - \langle M_x O_y \rangle}}{\partial \bar{\epsilon}_{ij}} = 0, \quad (4.2)$$

where $\bar{\epsilon}_{ij}$ is the residual strain tensor. The minimization has been performed by adopting the Nelder-Mead simplex method as implemented in Matlab [27] (see Chapter 2).

4.4. Experimental results and discussion

4.4.1. The oxidized Al{111} substrate

Oxidation of the bare Al{111} substrates for 6000 s in the oxidation temperature regime between 350 K and 600 K resulted in the formation of oxide films with ‘limiting’ thicknesses (cf. Ref. [28]) in the range of 0.4 nm to 1 nm. As confirmed by the HR-TEM analysis (e.g. Figs. 4.1 – 4.3), the thicknesses of the grown oxide films are very uniform. The oxide-film thickness values as obtained from the HR-TEM analysis are in good agreement with those determined by AR-XPS. The average oxygen-to-aluminium ratio of the grown oxide films of 1.5 ± 0.1 , as determined by quantitative AR-XPS analysis (Sec. 4.2.3 and Chapter 5), indicates that *overall* stoichiometric oxide films are formed (although local deviations from the stoichiometric composition might exist *at* the metal/oxide interface and/or oxide surface; cf. Ref. [29]).

For oxidation temperatures $T \leq 450$ K, no diffraction spots are observed by the LEED analysis and, indeed, oxide films formed at these relatively low temperatures were found to be amorphous by the HR-TEM analysis as well (Fig. 4.2). However, for the oxide films grown at $T = 475$ K and $t = 6000$ s, a first weak LEED diffraction pattern with a six-fold symmetry is observed (Fig. 4.4a). The diffraction spots become more pronounced with increasing temperature due to the gradual replacement of the amorphous phase by the crystalline phase in the thickening oxide film [30]. The six-fold symmetry as observed in the LEED patterns is typical for the {111} surface of an oxide with an fcc-type oxygen sublattice, such as γ -Al₂O₃. Indeed, the value for the lattice parameter for the fcc O sublattice of the crystalline oxide overgrowth, as determined in the present study (see below and Sec. 4.4.2), matches (within the estimated accuracy) with the corresponding lattice parameter values of γ -Al₂O₃ and a similar fcc transition oxide phase designated as γ' -Al₂O₃ in the literature [31, 32]. However, no LEED spots corresponding to Al cation periodicities in the oxide could be detected in the recorded LEED patterns of the oxidized Al{111} substrates and also the HR-TEM images provide no direct information on the Al cation distribution in the oxide phase. The cation

distribution in the O sublattice of γ - Al_2O_3 and the transition oxides strongly depends on the growth conditions [33] with the ratio of tetrahedrally-to-octahedrally coordinated Al cations decreasing in the order amorphous- $\text{Al}_2\text{O}_3 \rightarrow \gamma'$ - $\text{Al}_2\text{O}_3 \rightarrow \gamma$ - $\text{Al}_2\text{O}_3 \rightarrow \alpha$ - Al_2O_3 [31, 34, 35]. It follows that, because of the *gradual* amorphous-to-crystalline transformation [30] and the lack of knowledge on the precise atomic arrangement of the Al cations in the interstices of the oxygen sublattice, the crystalline Al_2O_3 (transition) oxide phase need not be identical to and cannot not be uniquely identified as γ - Al_2O_3 , which is known to be the thermodynamically most stable crystalline modification for thin Al_2O_3 films (e.g., Refs. [1, 5]). Therefore, the here observed fcc transition Al_2O_3 phase will be further denoted as γ'' - Al_2O_3 . For $T > 550$ K, some additional LEED spots appear (more pronounced at the lower primary electron energies) due to the development of a $(2\sqrt{3} \times 2\sqrt{3})\text{R}30^\circ$ surface periodicity of the $\{111\}$ plane of the γ'' - Al_2O_3 phase (Figs. 4.4b and c, respectively).

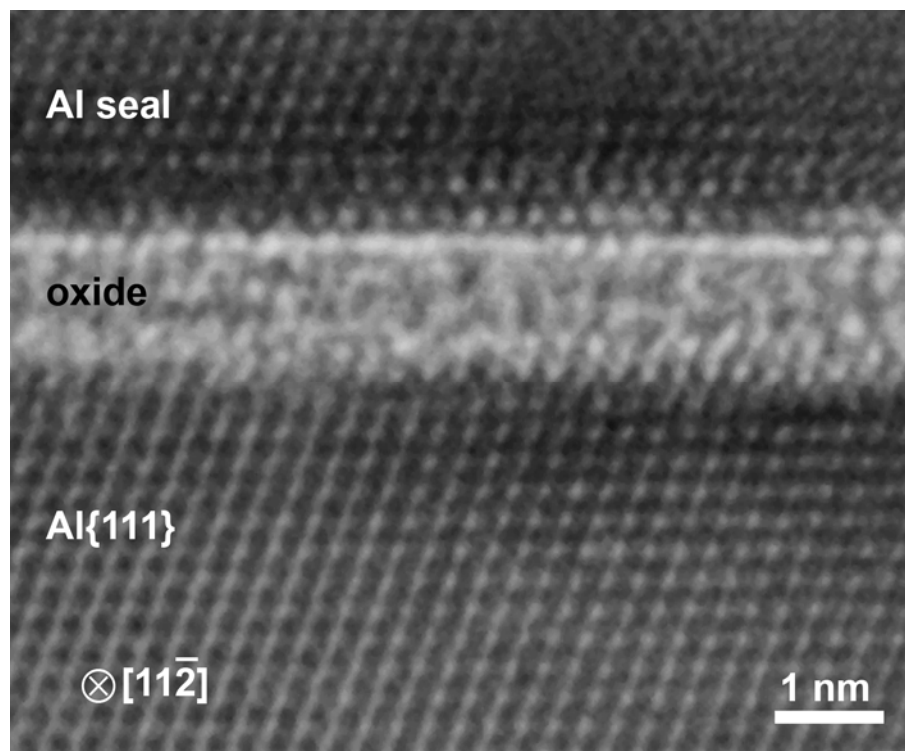


Figure 4.2. High-resolution transmission electron micrograph of the amorphous Al_2O_3 overgrowth on $\text{Al}\{111\}$ after oxidation at $T = 373$ K and $p_{\text{O}_2} = 1 \times 10^{-4}$ Pa for $t = 6000$ s (and subsequent in-situ deposition of a MBE-grown Al seal; see Sec. 4.2.4). The direction of the primary electron beam was along the zone axis $[11\bar{2}]$ of the $\text{Al}\{111\}$ substrate (with the $[111]$ direction perpendicular to the substrate-oxide interface).

HR-TEM analysis of a metal/oxide cross-section of an oxide film grown on $\text{Al}\{111\}$ at $T = 550$ K and $t = 6000$ s (Fig. 4.3) shows that the interface between the γ'' - Al_2O_3 overgrowth

and the Al{111} substrate is *coherent*. Consequently, the corresponding crystalline oxide overgrowth on the Al{111} substrate gives rise to only a single LEED diffraction pattern originating from both the metal substrate and the oxide overgrowth. Both the HR-TEM and LEED observations indicate the existence of a COR between the oxide overgrowth and the Al{111} substrate according to: Al(111)[110]|| γ "-Al₂O₃(111)[110], which is the expected COR with lowest possible mismatch between the Al{111} substrate and a γ (-like)-Al₂O₃ overgrowth (i.e. an Al₂O₃ phase with an fcc-type of oxygen sublattice). These observations of the low-mismatch COR for γ (-like)-Al₂O₃ oxide overgrowths on bare Al{111} substrates are in accordance with previous studies reported in the literature [1, 15-18]. Also the interface between the single-crystalline Al capping layer as grown by MBE (which contains some subgrain boundaries) and the γ "-Al₂O₃ overgrowth is coherent, with the {111} plane of the Al capping layer parallel to the metal/oxide interface (Fig. 4.3).

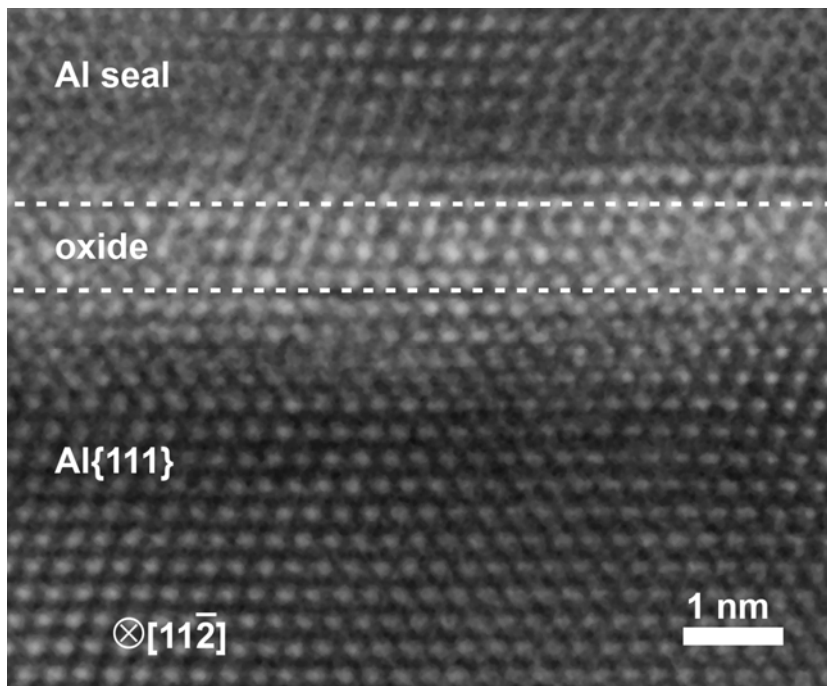


Figure 4.3. High-resolution transmission electron micrograph of the crystalline Al₂O₃ overgrowth on Al{111} after oxidation at 550 K and $p_{\text{O}_2} = 1 \times 10^{-4}$ Pa for $t = 6000$ s. The direction of the primary electron beam was along the zone axis $[11\bar{2}]$ of the Al{111} substrate (with the [111] direction perpendicular to the substrate-oxide interface). The dashed lines roughly indicate the boundaries between the oxide and the Al{111} substrate and the oxide and the Al seal, respectively.

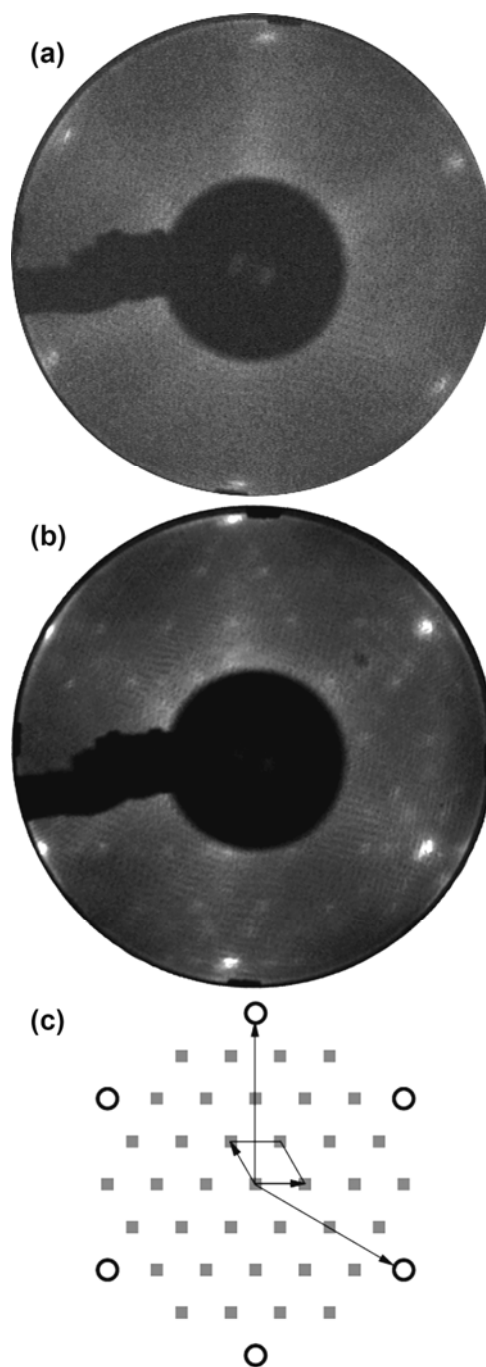


Figure 4.4. LEED patterns as recorded (with a primary electron energy of 53 eV) from the $\text{Al}\{111\}$ substrate after oxidation and $p_{\text{O}_2} = 1 \times 10^{-4}$ Pa for $t = 6000$ s at (a) $T = 475$ K, showing the six spots [see open circles in (c)] typical for the $\{111\}$ surface of an oxide with fcc O sublattice, and (b) $T = 600$ K, showing additionally the spots [see squares in (c)] due to the surface periodicity. (c) Schematic diffraction pattern corresponding to the $(2\sqrt{3} \times 2\sqrt{3})R30^\circ$ surface periodicity of the $\gamma\text{-Al}_2\text{O}_3\{111\}$ surface.

The existence of a coherent interface between the $\text{Al}\{111\}$ substrate and the $\gamma''\text{-Al}_2\text{O}_3$ overgrowth implies that the *residual* lattice parameter of the fcc O sublattice for the $\gamma''\text{-Al}_2\text{O}_3$ overgrowth (which differs from the corresponding ‘hypothetical’ *unstrained* lattice parameter

due to the presence of misfit dislocations and residual strain within the grown oxide film; cf. Ref. [2]) matches that of the (fcc) unit cell of Al (= 0.405 nm at room temperature). This value of 0.405 nm for the *residual* lattice parameter of the oxide overgrowth on Al{111} is only slightly larger than the corresponding value of 0.397 nm which holds for the *unstrained* lattice parameter of the oxygen sublattice of γ -Al₂O₃ (i.e. the thermodynamically most stable oxide phase for thin oxide films [1, 5]).¹ This suggests that a small residual, isotropic, in-plane tensile growth strain resides within the epitaxial γ' -Al₂O₃ overgrowth on Al{111} consistent with an initial lattice mismatch between substrate and oxide of about +2.0% at room temperature (i.e. the Al lattice parameter is 2.0% larger than the unstrained lattice parameter of the fcc O sublattice of γ -Al₂O₃ [1]). The mismatch increases with increasing temperature up to +2.6% at 600 K due to the higher thermal expansion of Al as compared to γ -Al₂O₃ [1, 37, 38].

4.4.2. The oxidized Al{100} substrate

As for the Al{111} substrate (Sec. 4.4.1), an overall stoichiometric Al₂O₃ film of uniform thickness develops on the bare Al{100} substrate after oxidation for 6000 s in the temperature range of 350 K – 600 K (as verified by AR-XPS and HR-TEM analysis; cf. Figs. 4.5 – 4.7). For oxidation temperatures $T < 450$ K, the oxide films were found to be amorphous by LEED. The first (weak) LEED diffraction patterns were observed for $T \geq 450$ K. They consist of separate diffraction spots originating from the Al{100} substrate (exhibiting a four-fold symmetry) and the crystalline oxide overgrowth (exhibiting a twelve-fold symmetry with spots located in rings) (Figs. 4.8a–c), which suggest the existence of a semi-coherent (or incoherent) metal/oxide interface.² The diffraction spots from the crystalline oxide overgrowth become more pronounced with increasing T (compare Figs. 4.8a and b) and can be interpreted in terms of two γ' -Al₂O₃ domains with their {111} plane parallel to the surface

¹ Due to the defect-spinel structure of γ -Al₂O₃, the lattice parameter of the γ -Al₂O₃ unit cell of 0.794 nm [36] equals twice the lattice parameter of its fcc oxygen sublattice.

² Note that, due to the existence of a *coherent* Al(111)[110]|| γ' -Al₂O₃(111)[110] interface, the corresponding crystalline oxide overgrowth on the Al{111} substrate gives rise to only a *single* LEED diffraction pattern originating from both the metal substrate and the oxide overgrowth (see Fig. 4.4 and Sec. 4.4.1).

and rotated with respect to each other by 90° around the surface normal.³ As for the γ'' - Al_2O_3 overgrowth on $\text{Al}\{111\}$, some additional spots become visible for $T > 550$ K due to an $(2\sqrt{3} \times 2\sqrt{3})\text{R}30^\circ$ overlayer periodicity on the γ'' - Al_2O_3 domains (see Fig. 4.8b).

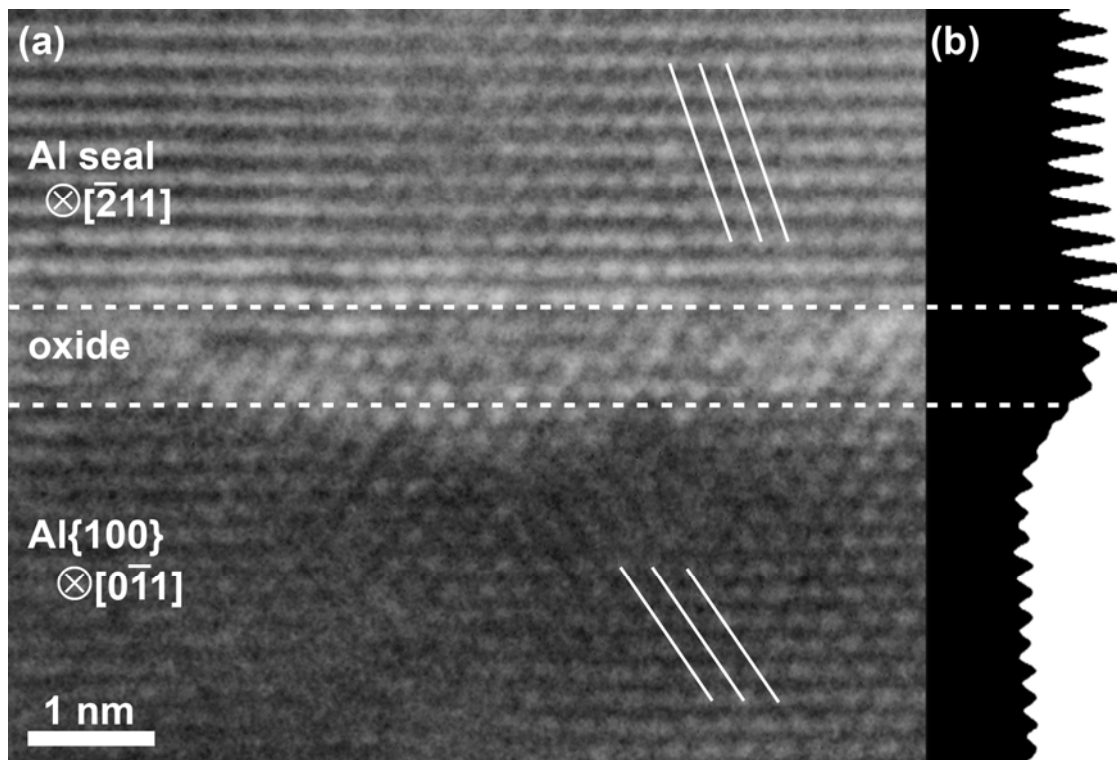


Figure 4.5. (a) High-resolution transmission electron micrograph of the Al_2O_3 overgrowth on $\text{Al}\{100\}$ after oxidation at $T = 550$ K and $p_{\text{O}_2} = 1 \times 10^{-4}$ Pa for $t = 6000$ s. The direction of the primary electron beam was along the zone axis $[0\bar{1}1]$ of the $\text{Al}\{100\}$ substrate. (b) Average line profile perpendicular to the metal/oxide interface, as obtained by integration of the pixel intensities of micrograph (a) parallel to the metal/oxide interface. The sets of parallel lines, as indicated in the Al substrate and Al capping layer, correspond with the $[2\bar{1}\bar{1}]$ direction in the Al substrate and $[213]$ direction in the Al capping layer, respectively.

The LEED results indicate that the $\{111\}$ plane of the oxide film is parallel to the $\{100\}$ plane of the substrate and hence parallel to the surface. The positions of the diffraction spots of the γ'' - Al_2O_3 overgrowth relative to those of the $\text{Al}\{100\}$ substrate in the recorded LEED patterns (Fig. 4.8), indicate the existence of a COR according to: $\text{Al}(100)[011] \parallel \gamma''$ -

³ For any given COR between an overlayer with hexagonal surface symmetry (e.g. the $\{111\}$ surface of the γ'' - Al_2O_3 overgrowth) on a substrate surface with four-fold symmetry (e.g. the $\text{Al}\{100\}$ substrate), an additional COR of identical energy exists which is rotated by 90° around the surface normal (with respect to the first COR). Hence, a two-domain structure for the γ'' - Al_2O_3 overgrowth on the $\text{Al}\{100\}$ substrate is likely to occur.

$\text{Al}_2\text{O}_3(111)[01\bar{1}]$, which differs from the expected COR as observed for $\gamma''\text{-Al}_2\text{O}_3$ overgrowths on $\text{Al}\{111\}$ (see Sec. 4.4.1). The existence of this unexpected COR for the $\gamma''\text{-Al}_2\text{O}_3$ overgrowths on $\text{Al}\{100\}$ is confirmed by the HR-TEM analysis performed in this study (see below).

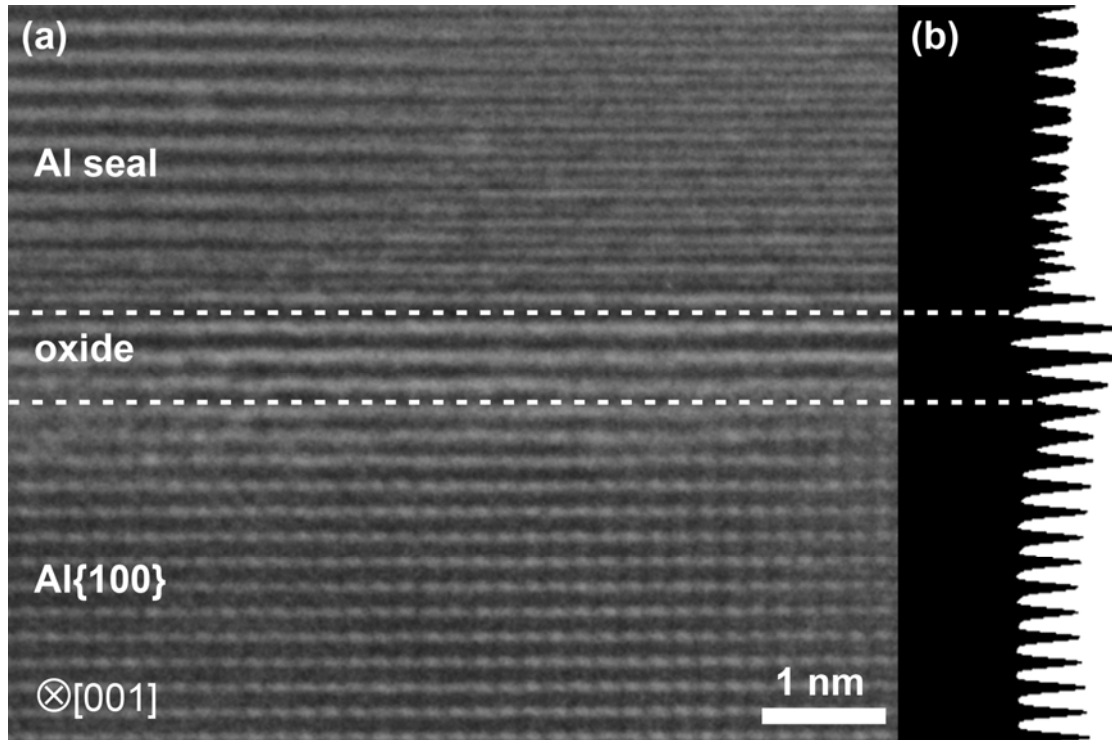


Figure 4.6. (a) High-resolution transmission electron micrograph of the Al_2O_3 overgrowth on $\text{Al}\{100\}$ after oxidation at $T = 550$ K and $p_{\text{O}_2} = 1 \times 10^{-4}$ Pa for $t = 6000$ s. The direction of the primary electron beam was along the $[001]$ zone axis of the $\text{Al}\{100\}$ substrate. (b) Average line profile perpendicular to the metal/oxide interface, as obtained by integration of the pixel intensities of micrograph (a) parallel to the metal/oxide interface.

HR-TEM micrographs of the oxide film grown on $\text{Al}\{100\}$ at 550 K, as recorded along the $[0\bar{1}1]$ and $[001]$ zone axes of the substrate, are shown in Figs. 4.5a and 4.6a, respectively. From the HR-TEM analysis (which also includes the analysis of the diffraction patterns obtained by Fourier transformation of the recorded micrographs), it follows that the Al capping layer has its (111) plane parallel to the metal/oxide interface (as for the capping layers on the oxide films grown on $\text{Al}\{111\}$; see Sec. 4.4.1). Moreover, as follows from the quantitative analysis of a total of ten average “line profiles”, as obtained by integration of the intensity in each micrograph along the direction parallel to the metal/oxide interface (see, for example, Figs. 4.5b and 4.6b), the thus obtained lattice spacing within the oxide film

perpendicular to the metal/oxide interface of 0.228 ± 0.018 nm corresponds (within the experimental accuracy, taken equal to the standard deviation of the “line profile” analysis) with both (i) the lattice spacing in the Al seal perpendicular to the metal/oxide interface of 0.234 ± 0.007 nm, and (ii) the unstrained $\{111\}$ lattice spacing in $\gamma\text{-Al}_2\text{O}_3$ of $a_{\text{fcc-}\gamma\text{-Al}_2\text{O}_3} / \sqrt{3} = 0.229$ nm (where $a_{\text{fcc-}\gamma\text{-Al}_2\text{O}_3} = 0.397$ nm is the unstrained lattice parameter of the fcc oxygen sublattice of $\gamma\text{-Al}_2\text{O}_3$ [36]). Also these results indicate that the (111) plane of the $\gamma''\text{-Al}_2\text{O}_3$ overgrowth is parallel to the metal/oxide interface.

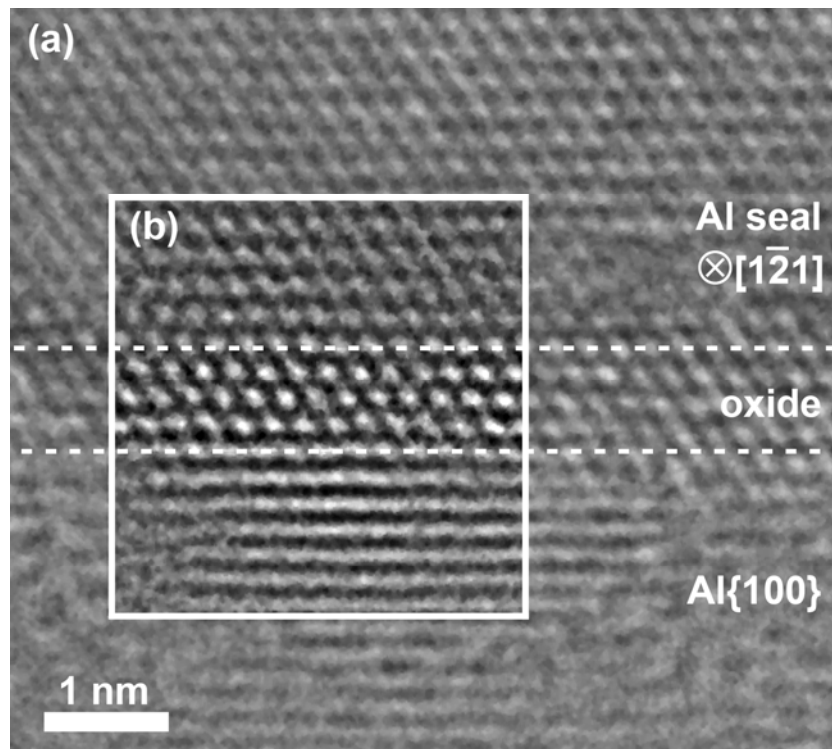


Figure 4.7. (a) High-resolution transmission electron micrograph of the Al_2O_3 overgrowth on $\text{Al}\{100\}$ after oxidation at $T = 550$ K and $p_{\text{O}_2} = 1 \times 10^{-4}$ Pa for $t = 6000$ s. The direction of the primary electron beam was along the zone axis $[\bar{1}21]$ of the Al capping layer. (b) Fourier-filtered region of the original micrograph in (a), as obtained after inverse Fourier transformation of the 2D Fourier transform of the square area after removing the noise around the primary beam spot.

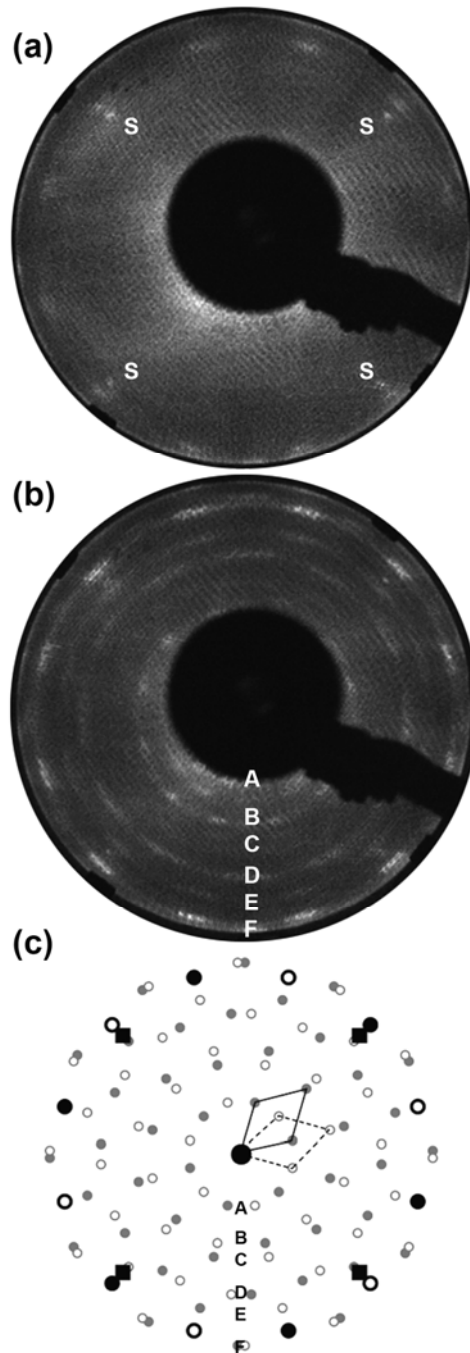


Figure 4.8. LEED patterns as recorded (with a primary electron of energy 55eV) from the Al{100} substrate after oxidation and $p_{\text{O}_2} = 1 \times 10^{-4}$ Pa for $t = 6000$ s at (a) $T = 450$ K, showing the twelve spots [see large circles in (c)] typical for two types of domains of the {111} surface of an oxide with fcc O sublattice and four spots from the Al{100} substrate [see letter S in (a) squares in (c)], and (b) $T = 650$ K, showing additionally the spots [see small circles in (c)] due to the surface periodicity. (c) Schematic diffraction pattern resulting from the Al{100} substrate [black squares in (c), letter S in (a)], from two $\gamma\text{-Al}_2\text{O}_3\{111\}$ oxide domains rotated by 90° around the surface normal (open and filled large black circles) and from their corresponding $(2\sqrt{3} \times 2\sqrt{3})R30^\circ$ surface periodicity [open and filled small gray circles, letters A to F in (b) and (c)].

As follows from the matching and parallelism of identical lattice planes in the Al seal and the γ'' -Al₂O₃ overgrowth across their interface (see, for example, Fig. 4.7), the Al seal and oxide overgrowth have identical orientations with respect to the Al{100} substrate. The quantitative analysis of the lattice spacings and corresponding relative atom row directions of the Al seal with respect to those of the Al{100} substrate (see, for example, Fig. 4.5), indicates a COR between the Al{100} substrate and the Al seal according to: Al(100)[011]||Al-seal(111)[01 $\bar{1}$]. Therefore, the COR between the γ'' -Al₂O₃ overgrowth and Al{100} substrate corresponds to Al(100)[011]|| γ'' -Al₂O₃(111)[01 $\bar{1}$], in accordance with the COR as determined from the LEED analysis (see above).

To a first approximation, the lattice parameter of the *unstrained* γ'' -Al₂O₃ phase can be taken equal to that of the fcc oxygen sublattice of γ -Al₂O₃ (see Sec. 4.4.1). It then follows that an initial lattice mismatch between substrate and oxide of about +18% (increasing from 17.9% at room temperature to 18.5% at 600 K)⁴ exists within the oxide film in one direction parallel to the metal/oxide interface; a much lower initial lattice mismatch of about +2.0% (as for the overgrowth on Al{111}; Sec. 4.4.1) exists in the perpendicular direction. Consequently, the γ'' -Al₂O₃ overgrowth on Al{100} exhibits a large anisotropic tensile growth strain, part of which has most probably been relaxed by the formation of defects at the metal/oxide interface (presumably misfit dislocations [2], which could not be resolved by the HR-TEM analysis). Further, as evidenced by the apparent smearing out in rings of the LEED spots originating from the γ'' -Al₂O₃ domains (Fig. 4.8b), strain relaxation has also occurred by slight, in-plane rotations of the γ'' -Al₂O₃ domains (of about $\pm 4^\circ$) with respect to the aforementioned high-mismatch COR. If (still) any residual *elastic* in-plane growth strain resides within the γ'' -Al₂O₃ overgrowth on Al{100}, then the residual lattice spacings of the fcc O sublattice of the γ'' -Al₂O₃ overgrowth *parallel* and *perpendicular* to the metal/oxide interface should differ. The residual lattice spacings of the fcc O sublattice of the γ'' -Al₂O₃ overgrowth on Al{100} *perpendicular* and *parallel* to the metal/oxide interface can be determined from the aforementioned HR-TEM “line profile” and LEED analysis, respectively. The residual lattice parameter of the fcc O sublattice of the γ'' -Al₂O₃ of $0.39 \pm$

⁴ Here the initial lattice mismatch is determined (cf. Refs. [1, 2]) from the unstrained lattice spacing along the [01 $\bar{1}$] direction in the (100) Al substrate plane and the unstrained lattice spacing along the [2 $\bar{1}\bar{1}$] direction in the (111) γ -Al₂O₃ plane at the growth temperature concerned (i.e. 0.573 nm and 0.486 nm at 298 K, respectively).

0.03 nm *perpendicular* to the metal/oxide interface (from the HR-TEM line profile analysis; cf. Figs. 4.5b and 4.6b) corresponds (within the experimental accuracy) to the lattice parameter of 0.37 ± 0.01 nm *parallel* to the interface (from the LEED analysis; cf. Fig. 4.8). So no significant state of residual tensile stress appears to exist in the oxide. The above values for the lattice parameter for the fcc O sublattice of the γ'' -Al₂O₃ on Al{100} are, on average, somewhat smaller than the corresponding Al fcc lattice constant of 0.405 nm, but lie within the range of corresponding lattice parameter values of 0.354 nm, 0.396 nm and 0.397 nm, as reported for another Al₂O₃ fcc-type transition oxide [35], for the transition oxide γ' -Al₂O₃ [31, 32] and for γ -Al₂O₃ [36], respectively.

4.5. Experiment versus model predictions

To explain the observed occurrence of a high lattice-mismatch COR between the γ'' -Al₂O₃ overgrowth and its parent Al{100} substrate (Sec. 4.4.2) on a thermodynamic basis, the various energy contributions to the total Gibbs energy of the crystalline overgrowth have to be considered. To this end, the surface energy and the interface energy contributions for a γ -Al₂O₃ oxide overgrowth (which represents the thermodynamically most stable oxide phase for thin overgrowths [1, 5]) on Al{100} were calculated on the basis of the general thermodynamic model presented in Sec. 4.3 (Refs. [1, 2]) for both the *observed case of high-mismatch* COR between the overgrowth and Al{100}, and for the *originally expected case of low-mismatch* COR between the overgrowth and Al{100} (Table 4.1, Fig. 4.9). The corresponding energy contributions as calculated for the low-mismatch oxide overgrowth on Al{111} have also been given for comparison (Table 4.1, Fig. 4.9).

It follows from these model calculations that, for all substrate orientations and COR's considered, the built-up elastic growth strain (Fig. 4.9a) within the oxide overgrowth already gets released by the introduction of misfit dislocations at the metal/oxide interface (Fig. 4.9b) within the monolayer thickness regime (1 oxide ML in γ -Al₂O₃ \sim 0.2 nm). With increasing thickness, the residual elastic growth strain decreases continuously by the concurrent generation of new misfit dislocations at the metal/oxide interface (as reflected in Fig. 4.9b by an increasing misfit dislocation energy contribution). Thus, the strain field at the metal/oxide interface for the 1 nm γ -Al₂O₃ thick overgrowth is dominated by the periodic, inhomogeneous strain field, resulting from the sum of strain fields associated with each of the misfit dislocations. The ongoing relaxation of tensile growth strain in the oxide overgrowth by the successive formation of misfit dislocations leads to an overall increase in density of metal-oxygen bonds across the metal/oxide interface within the monolayer thickness regime, as

reflected in Fig. 4.9c by a decrease of the (negative) interfacial energy contribution with increasing thickness. Since the metal-oxygen interaction energy is the dominant contribution to the resultant interface energy, the calculated growth strain in the overgrowth can even be slightly compressive to maximize the density of metal-oxygen bonds across the metal/oxide interface (cf. Ref. [1]). The elastic strain, misfit dislocation and interaction energy contributions to the resultant interface energy (Fig. 4.9d) all attain approximately constant values at a thickness of about 1 nm (*note*: the oxide films grown in this study have uniform thicknesses in the range of 0.4 nm to 1 nm; see Sec. 4.4).

As expected, the energy contribution due to the sum of the *residual* growth strain and misfit dislocations in the oxide overgrowth (i.e. the two interfacial energy contributions originating from the initial lattice mismatch at the metal/oxide interface) is largest (i.e. most positive) for the *high-mismatch* COR between the γ -Al₂O₃ overgrowth and Al{100}, i.e. for the resultant interface energy $\gamma_{\text{Al}\{100\}\|\gamma\text{-Al}_2\text{O}_3\{111\}}$ (Table 4.1 and Fig. 4.9). The corresponding anisotropic elastic growth strains due to initial lattice mismatches of about +18% and +2.0% (in two perpendicular directions parallel to the interface plane; see Sec. 4.4.2) becomes largely compensated (for 1 nm thick oxide films) by a rectangular grid of misfit dislocations. The calculated dislocation distance in the high-mismatch direction (i.e., the $[2\bar{1}\bar{1}]$ direction in the (111) γ -Al₂O₃ plane, which runs parallel to the $[01\bar{1}]$ direction in the (100) Al substrate plane; see Sec. 4.4.2) of 5 to 6 lattice spacings (one misfit dislocation for every 5 to 6 oxygen ions at the interface) is much smaller than the corresponding calculated dislocation distance of 30 to 40 lattice spacings in the perpendicular low-mismatch direction. For the *low-mismatch* overgrowths on Al{100} and Al{111}, on the other hand, the corresponding isotropic elastic growth strain due to an initial lattice mismatch of about +2.0% (in all directions parallel to the interface plane) becomes practically fully compensated (for 1 nm thick oxide films) by a square grid of misfit dislocations with a calculated dislocation distance of about 30 to 40 lattice spacings.

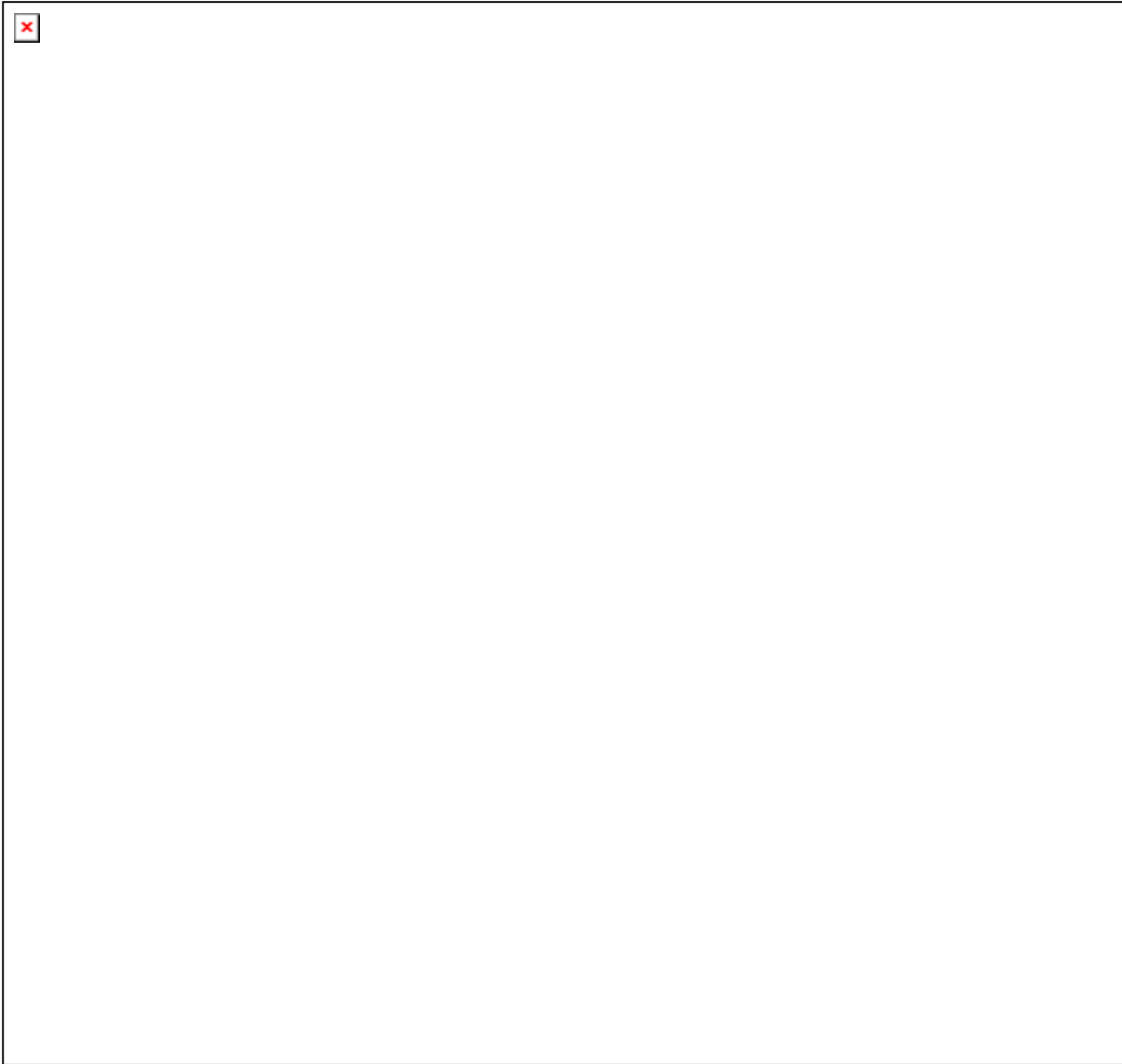


Figure 4.9. Calculated (a) residual strain energy, (b) misfit dislocation energy and (c) chemical interaction energy contributions to (d) the resultant Al- γ -Al₂O₃ interface energy, $\gamma_{\langle \text{Al} \rangle - \langle \gamma\text{-Al}_2\text{O}_3 \rangle}$, as function of the oxide-film thickness, for γ -Al₂O₃ overgrowth on bare Al{100} and Al{111} substrates at $T = 298$ K. The calculations were performed on the basis of the general thermodynamic model presented in Chapters 2 and 3 and adopting either the low-mismatch (i.e., Al{100}|| γ -Al₂O₃{100}) or the high-mismatch (i.e., Al{100}|| γ -Al₂O₃{111}) crystallographic orientation relationship between the oxide overgrowth and the Al{100} substrate. The corresponding energies for the overgrowth of low-mismatch (i.e., Al{111}|| γ -Al₂O₃{111}) on the Al{111} substrate are also shown for comparison.

Table 4.1. Residual strain, misfit dislocation and chemical interaction contributions to the resultant Al-Al₂O₃ interface energy [all in (J·m⁻²)] for the case of a 0.6 nm thick γ -Al₂O₃ overgrowth on the Al{100} and Al{111} substrates at 298 K. The calculations were performed on the basis of the general thermodynamic model presented in Chapter 2 and adopting either the low-mismatch (i.e., Al{100}|| γ -Al₂O₃{100}) or the high-mismatch (i.e., Al{100}|| γ -Al₂O₃{111}) crystallographic orientation relationship between the oxide overgrowth and the Al{100} substrate. The corresponding energies as calculated for the overgrowth of low-mismatch (i.e., Al{111}|| γ -Al₂O₃{111}) on the Al{111} substrate have also been given for comparison. The corresponding surface energies [in (J·m⁻²)] of the oxide overgrowths at 300 K were obtained by molecular dynamic calculations for the relaxed γ -Al₂O₃ surfaces in Ref. [39].

	interface energy (J·m ⁻²)				surface energy (J·m ⁻²)
	strain contribution	dislocation contribution	interaction contribution	total	
high mismatch Al{100} γ -Al ₂ O ₃ {111}	0.07	0.3	-4.7	-4.4	0.9
low mismatch Al{100} γ -Al ₂ O ₃ {100}	0.01	0.2	-4.0	-3.8	1.9
low mismatch Al{111} γ -Al ₂ O ₃ {111}	0.03	0.2	-4.7	-4.5	0.9

Although the interfacial energy contributions due to elastic strain and misfit dislocations are relatively high for the high-mismatch overgrowth on Al{100} (as compared to the low-mismatch overgrowths), the corresponding interaction energy contribution is much more negative due to a higher density of metal-oxygen bonds across the Al{100}|| γ -Al₂O₃{111} interface (see Table 4.1 and Fig. 4.9). Since the (negative) interaction energy is the dominant energy contribution to the interface energy, the larger sum of the residual strain and misfit dislocations contributions to the resultant interface energy, $\gamma_{\text{Al}\{100\}||\gamma\text{-Al}_2\text{O}_3\{111\}}$, is overcompensated by the more negative interaction energy contribution.

In addition, the energy of the γ -Al₂O₃{111} surface is much lower than that of the γ -Al₂O₃{100} surface, due to a much more pronounced relaxation (reconstruction) of the γ -Al₂O₃{111} surface [39] (see Table 4.1). It follows that the observed high-mismatch COR for the initial oxide overgrowth on Al{100} is thermodynamically preferred (instead of the low-mismatch COR), because of the lower sum of the surface and interface energy contributions.

4.6. Conclusions

Al oxide films grown on bare Al{111} and Al{100} substrates after exposure for 6000 s to pure oxygen gas in the temperature range of 350 K to 600 K at $p_{\text{O}_2} = 1 \times 10^{-4}$ Pa are overall stoichiometric and of uniform thickness in the range of 0.4 nm to 1 nm. Up to oxidation temperatures of about 450 K, the oxide films are amorphous, whereas at higher temperatures a crystalline oxide occurs on both substrate orientations. The resulting crystalline oxide, designated here as $\gamma''\text{-Al}_2\text{O}_3$, possesses an fcc oxygen sublattice structure with a lattice parameter similar to that of $\gamma\text{-Al}_2\text{O}_3$, but with an unknown defect structure and Al cation distribution.

For the oxide overgrowth on Al{111}, the expected crystallographic orientation relationship (COR) of lowest possible mismatch between the Al{111} substrate and the $\gamma''\text{-Al}_2\text{O}_3$ overgrowth occurs in reality: Al(111)[110]|| $\gamma''\text{-Al}_2\text{O}_3$ (111)[110], with a coherent metal/oxide interface.

For the oxide overgrowth on Al{100} an unexpected COR of exceptionally high mismatch occurs: Al(100)[011]|| $\gamma''\text{-Al}_2\text{O}_3$ (111)[01 $\bar{1}$], with a semi-coherent metal/oxide interface. In the last case the oxide overgrowth structure consists of two types of $\gamma''\text{-Al}_2\text{O}_3$ domains with their {111} plane parallel to the surface, but rotated with respect to each other by 90° around the surface normal. As evidenced by the smearing out in rings of the LEED spots originating from the $\gamma''\text{-Al}_2\text{O}_3$ domains, relaxation of the anisotropic, tensile, elastic growth strain in the oxide overgrowth does not only occur by the formation of defects at the metal/oxide interface (presumably misfit dislocations), but also by slight, in-plane rotations of the $\gamma''\text{-Al}_2\text{O}_3$ domains (of about $\pm 4^\circ$) with respect to the aforementioned high-mismatch COR.

As demonstrated by thermodynamic model calculations, the high-mismatch COR between the $\gamma''\text{-Al}_2\text{O}_3$ overgrowth and the parent Al{100} substrate (instead of the corresponding low-mismatch COR) is preferred due to the lower sum of the surface and interface energy contributions, in spite of the higher energy contributions due to residual strain and misfit dislocations in the oxide overgrowth. The relatively lower interface energy for the $\gamma''\text{-Al}_2\text{O}_3$ overgrowth of high-mismatch on Al{100} (as compared to the corresponding low-mismatch overgrowth) is due to a higher density of oxygen-metal bonds across the metal/oxide interface and hence a more negative chemical interaction contribution to the interface energy. The generally adopted assumption, that the COR corresponding with the lowest possible lattice mismatch (i.e. the 'best fit' COR) is energetically preferred, need not hold for ultra-thin

overgrowths: the role of surface and interface energies can be dominant for the thermodynamic stability of the oxide film.

Acknowledgements

The authors are grateful to Mrs. U. Eigenthaler for the FIB preparation of the TEM lamellae.

Appendix 4.A. Electron-radiation-induced changes of the oxide-film microstructure

To retard the occurrence of microstructural changes in the irradiated area of specimen, as inflicted by the high-energy electron beam, the cross-sectional lamellae (Sec. 4.2.4) were cooled with liquid nitrogen during the HR-TEM analysis. Despite the liquid nitrogen cooling, irreversible microstructural changes were induced by the 1250 keV electron irradiation within the thin oxide films after more prolonged HR-TEM analysis at a single position (as traced by live video recording). For example, after irradiation times of about 5 minutes, the amorphous Al_2O_3 films (as grown at 373 K in this study; see Sec. 4.4.1 and Fig. 4.10a) were found to gradually crystallize under influence of the electron beam (in accordance with Ref. [40]). Distinct ordering phenomena at the interfaces of the amorphous oxide film in contact with the Al substrate and the Al seal were sometimes already observed for even shorter irradiation times. After 10 minutes of oxidation almost the complete oxide film was crystallized (see Fig. 4.10b). For irradiation times longer than about 10 minutes, the onset of oxide dissociation for both the amorphous and the crystalline oxide films was observed, which eventually led to a complete disappearance of the oxide film in the irradiated area, ending up with a pure Al grain boundary between the Al substrate and the Al capping layer after an irradiation time of about 20 min (see Fig. 4.10c). Therefore, it was ensured that all microstructural characterization of the oxide overgrowths by HR-TEM, as presented in this study (see Sec. 4.4), only pertains to micrographs of ‘fresh’ (i.e. not previously irradiated) cross-sectional areas, as recorded within irradiation times of at most 2 minutes.

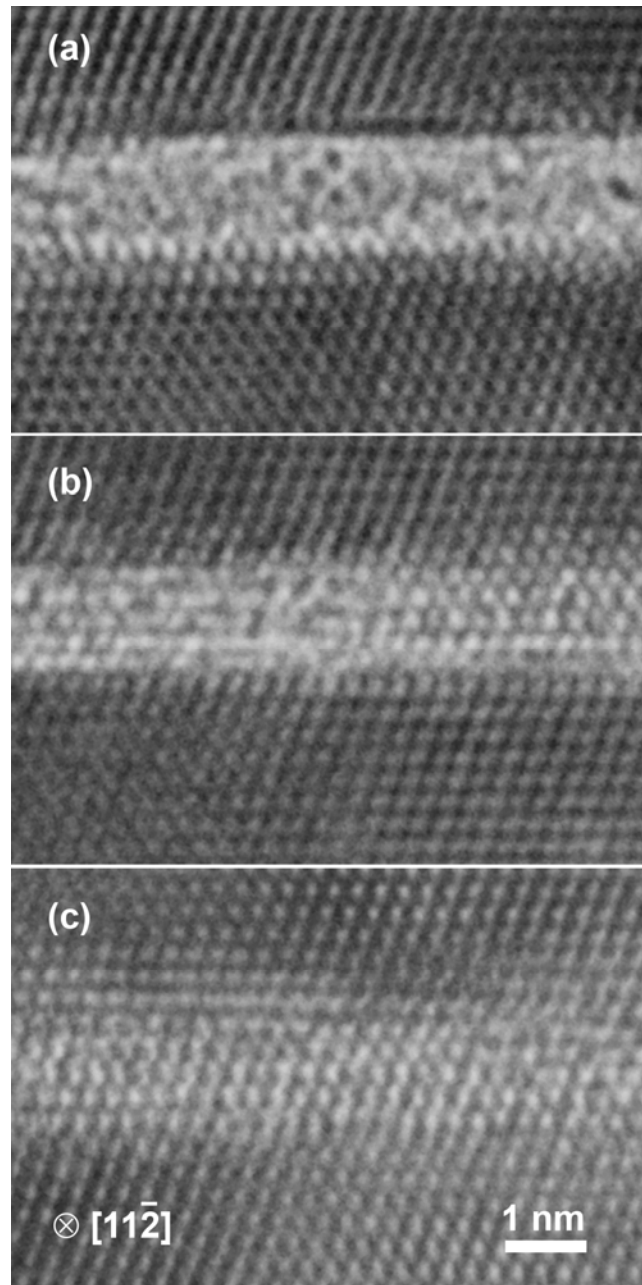


Figure 4.10. High-resolution transmission electron micrographs of the Al_2O_3 overgrowth on $\text{Al}\{111\}$ after oxidation at 373 K (and subsequent in-situ deposition of a MBE-grown Al seal; see Sec. 4.2.4) and for various electron irradiation times of the same HR-TEM analysis area by the 1250 keV primary electron beam. Corresponding electron micrographs as recorded: (a) at the onset of the HR-TEM analysis (the oxide film is amorphous and clearly distinguishable from the Al substrate and the Al seal), (b) after 10 minutes of electron radiation (the initial amorphous oxide film has completely crystallized under influence of the incident electron beam) (c) after 15 minutes of analysis (the oxide dissociates under influence of the electron irradiation and oxygen diffuses out of the TEM lamella and into the adjacent Al substrate and Al seal). The direction of the primary electron beam was along the zone axis $[11\bar{2}]$ of the $\text{Al}\{111\}$ substrate.

References

- [1] L. P. H. Jeurgens, W. G. Sloof, F. D. Tichelaar and E. J. Mittemeijer, *Phys. Rev. B* **62** (2000) 4707.
- [2] F. Reichel, L. P. H. Jeurgens and E. J. Mittemeijer, *Phys. Rev. B* **74** (2006) 144103.
- [3] F. P. Fehlner, *Low-temperature Oxidation: The Role of Vitreous Oxides* (Wiley-Interscience, New York, 1986).
- [4] I. E. Wachs, *Catal. Today* **100** (2005) 79.
- [5] J. M. McHale, A. Auroux, A. J. Perrotta and A. Navrotsky, *Science* **277** (1997) 788.
- [6] A. Stierle, V. Formoso, F. Comin and R. Franchy, *Surf. Sci.* **467** (2000) 85.
- [7] G. Skandan, C. M. Foster, H. Frase, M. N. Ali, J. C. Parker and H. Hahn, *Nanostructured Mater.* **1** (1992) 313.
- [8] R. C. Garvie, *J. Phys. Chem.* **82** (1978) 218.
- [9] W. Bollmann, *Crystal Defects and Crystalline Interfaces*, (Springer, Berlin, 1970), p. 143.
- [10] I. Salles-Desvignes, T. Montesin, C. Valot, J. Favergeon, G. Bertrand and A. Vadon, *Acta Mater.* **48** (2000) 1505.
- [11] M. Rühle, *J. Eur. Ceram. Soc.* **16** (1996) 353.
- [12] H. B. Groen, B. J. Kooi, W. P. Vellinga and J. T. M. De Hosson, *Mater. Sci. Forum* **294-296** (1999) 107.
- [13] G. Zhou and J. C. Yang, *J. Mater. Res.* **20** (2005) 1684.
- [14] L. P. H. Jeurgens, W. G. Sloof, F. D. Tichelaar and E. J. Mittemeijer, *Thin Solid Films* **418** (2002) 89.
- [15] P. E. Doherty and R. S. Davis, *J. Appl. Phys.* **34** (1963) 619.
- [16] K. Shinohara, T. Seo and H. Kyogoku, *Z. Metallkde.* **73** (1982) 774.
- [17] J. I. Eldridge, R. J. Hussey, D. F. Mitchell and M. J. Graham, *Oxid. Met.* **30** (1988) 301.
- [18] K. Hart and J. K. Maurin, *Surf. Sci.* **20** (1970) 285.
- [19] H. M. Flower and P. R. Swann, *Acta Metall.* **22** (1974) 1339.
- [20] M. S. Vinodh and L. P. H. Jeurgens, *Surf. Interface Anal.* **36** (2004) 1629.
- [21] L. P. H. Jeurgens, W. G. Sloof, C. G. Borsboom, F. D. Tichelaar and E. J. Mittemeijer, *Appl. Surf. Sci.* **161** (2000) 139.
- [22] L. P. H. Jeurgens, M. S. Vinodh and E. J. Mittemeijer, *Appl. Surf. Sci.* **253** (2006) 627.

- [23] F. Phillipp, R. Höschen, M. Osaki, G. Möbus and M. Rühle, *Ultramicroscopy* **56** (1994) 1.
- [24] Powder Diffraction Files, Card 00-004-0787 from JCPDS-International Centre for Diffraction Data (2007).
- [25] F. R. de Boer, R. Boom, W. C. M. Mattens, A. R. Miedema and A. K. Niessen, *Cohesion in Metals: Transition Metals Alloys*, (North-Holland, Amsterdam, 1989), Chaps. 2 and 4.
- [26] J. H. van der Merwe, *Surf. Sci.* **31** (1972) 198.
- [27] MATLAB version 6.1.0.450, Release 12.1 (The MathWorks Inc., Natick, 2001).
- [28] L. P. H. Jeurgens, A. Lyapin and E. J. Mittemeijer, *Acta Mater.* **53** (2005) 4871.
- [29] L. P. H. Jeurgens, W. G. Sloof, F. D. Tichelaar and E. J. Mittemeijer, *Surf. Sci.* **506** (2002) 313.
- [30] P. C. Snijders, L. P. H. Jeurgens and W. G. Sloof, *Surf. Sci.* **589** (2005) 98.
- [31] U. Bardi, A. Atrei, and G. Rovida, *Surf. Sci.* **268** (1992) 87.
- [32] R. S. Alwitt, C. K. Dyer and B. Noble, *J. Electrochem. Soc.* **129** (1982) 711.
- [33] F. H. Streitz and J. W. Mintmire, *Phys. Rev. B* **60** (1999) 773.
- [34] G. Gutiérrez and B. Johansson, *Phys. Rev. B* **65** (2002) 104202.
- [35] H. J. Van Beek and E. J. Mittemeijer, *Thin Solid Films* **122** (1984) 131.
- [36] Powder Diffraction Files, Card 00-050-0741 from JCPDS-International Centre for Diffraction Data (2007).
- [37] Y. S. Touloukian, R. K. Kirby, R. E. Taylor and T. Y. R. Lee, *Thermal Expansion. Elements and Alloys. Thermophysical Properties of Matter*, Vol. **12**. (New York, IFI/Plenum, 1977).
- [38] H. Yanagida and G. Yamaguchi, *Bull. Chem. Soc. Jpn.* **37** (1964) 1229.
- [39] S. Blonski and S. H. Garofalini, *Surf. Sci.* **295** (1993) 263.
- [40] B. J. H. Stadler, M. Oliveria and L. O. Bouthillette, *J. Am. Ceram. Soc.* **78** (1995) 3336.

Chapter 5

The amorphous-to-crystalline transition for oxide overgrowths on Al substrates

F. Reichel, L. P. H. Jeurgens, G. Richter and E. J. Mittemeijer

Abstract

The thermodynamic and kinetic background of the stability of ultra-thin (< 2 nm) amorphous Al_2O_3 overgrowths on Al substrates was investigated for ultra-thin oxide films grown on bare Al{111}, Al{100} and Al{110} substrates by thermal oxidation in pure oxygen gas for oxidation times up to 6000 s in the temperature range of $T = 350 - 650$ K. The microstructural evolutions of the developing oxide films were analysed by angle-resolved X-ray photoelectron spectroscopy, low energy electron diffraction and high-resolution transmission electron microscopy. On Al{111} for $T \leq 450$ K, amorphous Al_2O_3 films with uniform thicknesses up to 0.9 nm are formed, which are stable upon in-situ UHV annealing for 3600 s at 700 K. On Al{100} for $T \leq 400$ K, amorphous Al_2O_3 films with uniform thicknesses up to 0.6 nm are formed, which are only stable upon in-situ UHV annealing at 700 K up to a critical oxide-film thickness of about 0.45 ± 0.15 nm. On Al{110} for $T \leq 550$ K, amorphous Al_2O_3 films with uniform thicknesses up to 1.2 nm are formed, which are stable upon in-situ UHV annealing at 700 K in agreement with thermodynamic model predictions. At more elevated temperatures, crystalline Al_2O_3 films develop on Al{111} and Al{100} due to a change in oxide growth mode and a reduction of the activation-energy barrier for nucleation of crystallization. On Al{110} for $T > 550$ K, a thermodynamically-preferred reconstruction (i.e. a {111}-faceting) of the original Al{110} surface occurs during oxidation and then the amorphous-to-crystalline transition can be kinetically hindered.

5.1. Introduction

Recent thermodynamic model calculations (see Chapters 2, 3 and Refs. [1, 2]) have shown that an amorphous state for the initial oxide overgrowth on a bare Al substrate can be thermodynamically, instead of kinetically, preferred up to a certain critical oxide-film

thickness, because of its lower sum of surface and interface energies (as compared to the corresponding crystalline modification). Beyond this critical oxide-film thickness, which is calculated to be about 0.7 ± 0.1 nm, 0.8 ± 0.1 nm and 4.0 ± 0.5 nm for oxide overgrowths on Al{111}, Al{100} and Al{110}, respectively, (as calculated according to the model given in Chapter 3; see Fig. 5.1), bulk thermodynamics favour the occurrence of the competing crystalline oxide phase γ -Al₂O₃.

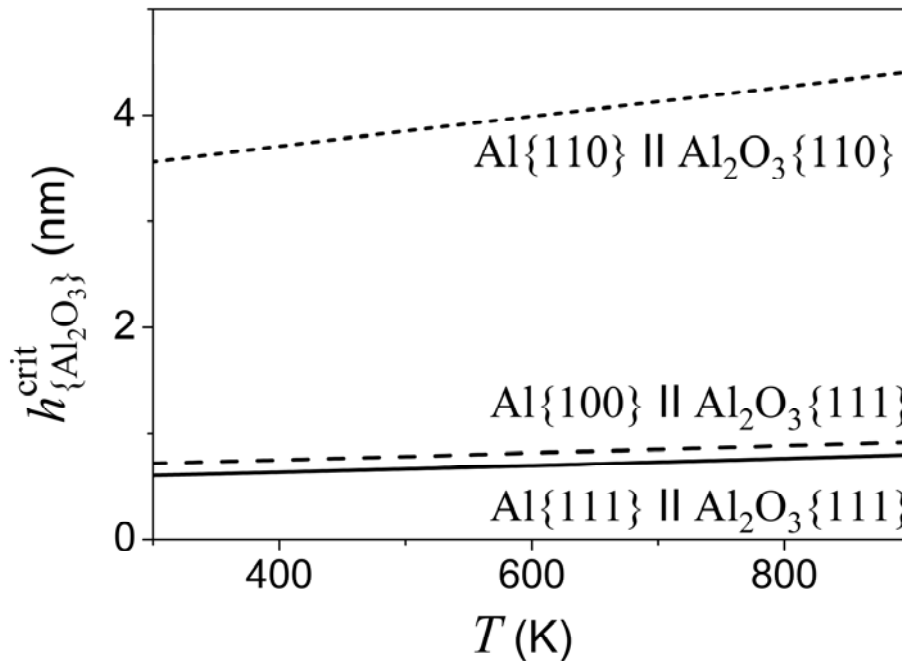


Figure 5.1. Calculated critical thickness ($h_{\text{Al}_2\text{O}_3}^{\text{critical}}$) up to which an amorphous oxide overgrowth (in instead of the corresponding crystalline γ -Al₂O₃ overgrowth with indicated orientation relationship) is thermodynamically preferred on the {111}, {100} and {110} surfaces of bare Al substrates, as function of the growth temperature (T). Calculated according to the model given in Chapter 3.

Straightforward experimental verification of the thermodynamic model predictions of the critical oxide-film thicknesses on Al{111}, Al{100} and Al{110} (Fig. 5.1) is hindered by the kinetics of the oxide-film growth process: Initial oxide-film growth on bare Al substrates by thermal oxidation at low temperatures (say, $T < 600$ K) generally proceeds by an initial, *very fast* growth stage and a subsequent, very slow growth stage ending with an oxide film of (near-)limiting thickness [3, 4]. Therefore, it is very difficult to produce a series of Al₂O₃ films with various uniform thicknesses in the predicted critical thickness range from 0.6 nm to 5 nm (Fig. 5.1). Furthermore, because of kinetic constraints, the initial oxide films can possess/maintain an amorphous state even beyond the critical thickness.

The present work is intended to provide an experimental verification of the model predictions on the thermodynamic stability of thin amorphous oxide films on their metal substrates as expressed by critical oxide-film thickness (Chapter 3). To this, *bare* Al single-crystal {111}, {100} and {110} surfaces were exposed to pure oxygen gas in the temperature range 350 – 650 K. The microstructure of the oxide films was investigated by angle-resolved X-ray photoelectron spectroscopy (AR-XPS), low energy electron diffraction (LEED) and high-resolution transmission electron microscopy (HR-TEM). The results obtained were discussed in terms of thermodynamic and kinetic parameters influencing the stability of either an amorphous state or a crystalline state for the oxide overgrowth.

5.2. Experimental details

Disc-shaped Al{111}, Al{100} and Al{110} single-crystals (10 mm diameter, 1 mm thick, purity better than 5N, orientation alignment better than 0.5°) were supplied and their surfaces polished by 'Surface Preparation Laboratory' (Zaandam, The Netherlands). Prior to each oxidation experiment, the Al single-crystals were outgassed, cleaned and their crystal order restored by a cyclic treatment of sputter-cleaning with 1 keV Ar⁺ ions (employing sample rotation) and subsequent annealing in ultra high vacuum (UHV) at 723 K. In-situ LEED (Specs 4-grid ER-LEED system using primary electron energies in the range of 30 – 200 eV) was applied to verify that the crystal order of the metal surface was restored after the final annealing step. The cleanness of the thus obtained *bare* single-crystalline Al substrates was verified by AR-XPS (see below). Next, the *bare* single-crystalline Al substrates were oxidized in an UHV reaction chamber (base pressure < 3×10⁻⁸ Pa) in the temperature (*T*) range of 350 – 650 K by exposure for an oxidation time (*t*) of up to 6000 s to pure oxygen gas at a pressure (*p*_{O₂}) of 1×10⁻⁴ Pa. Some of the oxidized Al substrates (after the AR-XPS and LEED analysis; see below) were subjected to an additional annealing for 3600 – 6000 s at 700 K in UHV and then again analysed by AR-XPS and LEED (see below). For additional details on sample preparation, cleaning and oxidation, see Chapter 4 of this thesis.

During the oxidation experiments real-time in-situ spectroscopic ellipsometry (RISE) measurements were performed, using a J. A. Woollam M-2000L spectroscopic ellipsometer equipped with a Xe light source and mounted directly to the flanges of the UHV reaction chamber, so that the angles of incidence and reflection were 70° relative to the sample surface normal (for details on the RISE analysis and data evaluation, see Chapter 6 of this thesis and references therein).

AR-XPS analysis of the specimen surface before and after oxidation, as well as after the additional annealing treatment in UHV (see above), was performed with a Thermo VG Thetaprobe system employing monochromatic Al K α radiation ($h\nu = 1486.68$ eV; spot size 400 μm). Detailed AR-XPS spectra of the Al 2p and O 1s binding-energy regions were recorded in so-called parallel data acquisition mode by detecting the photoelectrons simultaneously over the angular detection range α (with respect to the sample surface normal) of 23° to 83° in eight ranges of 7.5° each (for details, see Ref. [5]) with a step size and a constant pass energy of 0.05 eV and 50 eV, respectively. The AR-XPS measurements were performed at 9 defined locations on the surface (spot size 400 μm) equally distributed over an entire analysis area of 3 \times 3 mm².

For the preparation of the HR-TEM metal/oxide cross sections, the oxidized single-crystalline substrates were sealed *in-situ* by molecular beam epitaxy (MBE) deposition of a dense \sim 150 nm thick Al capping layer in the same UHV system, where the oxidation was performed, to protect the grown oxide films from further growth under atmospheric conditions after their removal from the UHV system. During the deposition of the Al capping layer, the sample holder containing the oxidized single crystal was cooled with liquid nitrogen to suppress microstructural changes at the oxide-film surface due to possible chemical interactions with the Al capping layer. Next, a TEM-lamella was cut from the sealed oxidized specimens using a dual Focused Ion Beam (FIB; Nova Nanolab 600, FEI Co.) with Ga⁺ ions accelerated at 30 keV and employing an ion current that decreased from 7 nA to 30 pA with increasing operation time. Prior to the FIB cutting procedure, the specimen surface was protected with a Pt capping layer deposited on top of the Al capping layer. The thus obtained cross-sectional HR-TEM lamella has a size of 3 $\mu\text{m} \times$ 4 μm and a thickness of about 80 nm to 100 nm. An overview of the thus obtained cross-sectional TEM lamellae for the oxidized Al{111} and Al{110} substrates are provided by the bright-field TEM micrographs shown in Figs. 5.2a and b, respectively.

The HR-TEM analysis was performed using a JEOL JEM-ARM1250 electron microscope with a very high acceleration voltage of 1250 kV and a point-to-point resolution with the side entry lens of 0.12 nm (for instrumental details, see Ref. [6]). To retard the occurrence of microstructural changes in the irradiated area of the specimen, as inflicted by the high-energy electron beam, the lamellae were cooled with liquid nitrogen during the HR-TEM analysis. Further, all microstructural characterization of the oxide overgrowths by HR-TEM, as presented in this study, only pertains to ‘fresh’ (i.e. not previously irradiated) cross-sectional areas, as recorded within irradiation times of at most 2 minutes. For details on

electron-irradiation-induced microstructural changes of the oxide film for longer HR-TEM analysis at the same position, see Appendix 4.A in Chapter 4 of this thesis. The negatives of the recorded micrographs were digitized for quantitative evaluation. Internal calibration of the length scale of the micrographs was performed using the known lattice constant of the Al metal (0.40494 nm [7]).

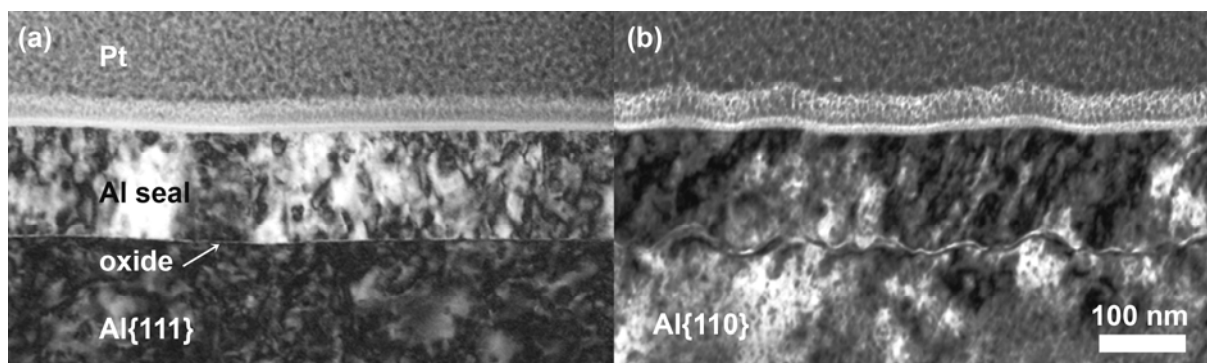


Figure 5.2. Bright field transmission electron micrographs of the cross-sectional TEM lamella obtained from (a) the Al{111} substrate oxidized at $T = 550$ K and (b) the Al{110} substrate oxidized at $T = 640$ K (note the faceting of the substrate, see Sec. 5.4.3). Both oxidized single-crystalline substrates were sealed with an Al capping layer (prior to removal from UHV) and a double-layered Pt seal (prior to the cutting of the FIB lamellae) (see Sec. 5.2).

5.3. AR-XPS spectral reconstruction and quantification

The angle-resolved Al 2p and O 1s spectra, as measured at 9 points homogeneously distributed over a 3×3 mm² central area of the sample surface (Sec. 5.2), were averaged for each angular range of photoelectron detection employed and then corrected for the electron-kinetic-energy-dependent transmission of the spectrometer analyzer by adopting the corresponding correction factor as provided by the manufacturer. Next, for each photoelectron detection angle (as taken equal to the centre of each angular detection range; see Sec. 5.2), the total primary zero loss (PZL) intensities [8] of the asymmetrically shaped metallic Al 2p main peak and the symmetrically shaped oxidic Al 2p and O 1s main peaks were resolved from the corresponding AR-XPS spectra recorded from the bare and the oxidized substrate, as follows (see also the procedures as described in [8, 9]).

5.3.1. Resolving the metallic Al 2p PZL intensity of the bare metal

To determine the total metallic Al 2p PZL intensity [8] of the *bare Al substrate* for each angular detection range, first the lower binding energy (BE) side of the metallic main peak was set to zero (background) intensity by subtraction of a constant background, the value of

which was taken equal to the averaged minimum intensity at the lower BE side of the Al 2p main peak (Fig. 5.3a). Next, a background of inelastically scattered photoelectrons was subtracted from the thus obtained Al 2p spectrum over the BE range from 69.2 eV to 79.8 eV, using Tougaard's formalism [10] for a homogeneous substrate and adopting a three-parameter universal cross-section for inelastic-electron scattering with $B = 16.5 \text{ eV}^2$, $C = 230 \text{ eV}^2$ and $D = 4.5 \text{ eV}^2$ (cf. Eq. (6) in Ref. [11]). Subsequently, the shape of the *intrinsic* metallic Al 2p main peak was determined by linear-least squares (LLS) fitting of the background-corrected part of the metallic Al 2p main over the BE from 69.2 eV to 79.8 eV with the sum of two Doniach-Šunjić line shape functions [12] of identical shape representing the Al $2p^{3/2} - Al2p^{1/2}$ spin-orbit doublet [i.e. the same full-width-at-half-maximum (FWHM) and singularity index were used in combination with a known spin-orbit splitting and relative intensity ratio of 0.417 eV and 0.5, respectively] after their convolution with a Gauss function to account for instrumental broadening. The LLS fitting was performed simultaneously for the entire set of AR-XPS spectra recorded at different detection angles from the bare Al substrate using the Nelder-Mead simplex search method as implemented in Matlab [13]). The position, height, FWHM and singularity index of the Al $2p^{3/2}$ Doniach-Šunjić line shape function, as well as the instrumental broadening factor, were adopted as fit parameters, while allowing only the position and height of the Al $2p^{3/2}$ Doniach-Šunjić line shape to vary with detection angle (i.e. single values of FWHM and the singularity index were fitted for all detection angles). Now, the PZL intensity of the metallic Al 2p main peak was obtained for each detection angle by integrating the intrinsic metallic Al 2p main peak over the BE range of 69.2 eV to 79.8 eV and adding to this intensity the integrated intensity of the excluded intrinsic tail-part of the metallic main peak extending below the plasmon structure from 79.8 eV towards higher BE values (Fig. 5.3a). This excluded tail-part was constructed by extrapolation of the previously optimized Doniach-Šunjić line shape function of the metallic Al 2p main peak over the BE range from 79.8 eV to 87.05 eV (Fig. 5.3a). Finally, the *total* metallic Al 2p PZL intensity of the bare metal substrate (i.e. the PZL intensity of the resolved metallic main peak (see above) *plus* its associated intrinsic plasmon intensity) was determined by adopting the estimated value of $P_{BP} = 0.11$ [8] for the intrinsic bulk plasmon excitation probability of the Al 2p photoelectron emission process in the alloy.

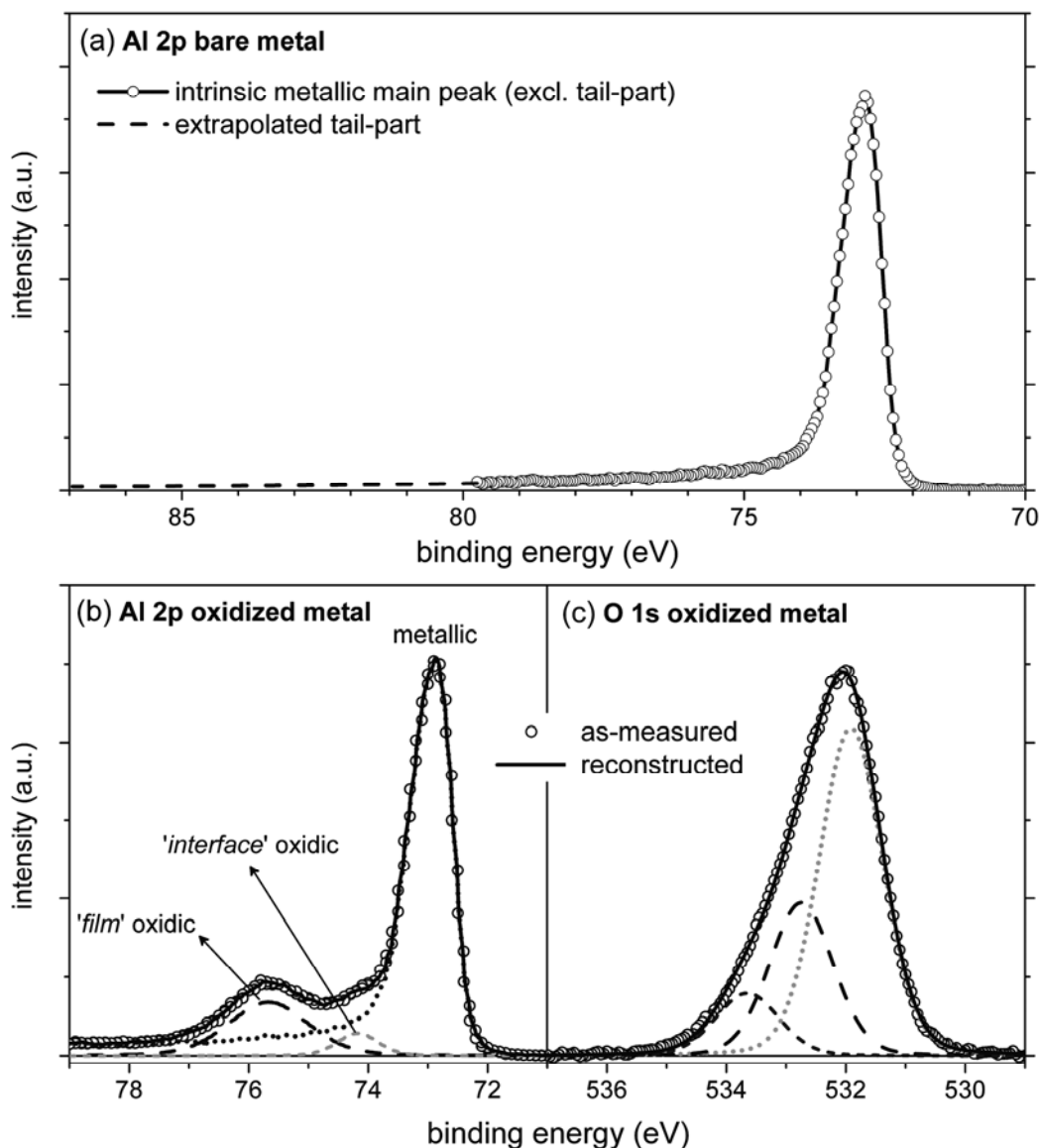


Figure 5.3. Spectral reconstruction of (a) the intrinsic metallic Al 2p main peak for the background corrected Al 2p XPS spectrum of the bare Al{100} substrate (Sec. 5.3.1), (b) the metallic Al 2p main peak and the two oxidic Al 2p main peaks (all peaks plus their individual inelastic backgrounds) for the as-measured Al 2p XPS spectrum of the oxidized Al{100} substrate after zero-background offset (Sec. 5.3.2) and (c) the three O 1s main peaks of the background-corrected O 1s XPS spectrum of the oxidized Al{100} substrate (Sec. 5.3.3). The bare and oxidized spectra were recorded at a detection angle of $\alpha = 41.75^\circ$ and pertain to the bare Al{100} substrate before and after oxidation for $t = 6000$ s at $T = 500$ K and $p_{\text{O}_2} = 1 \times 10^{-4}$ Pa. The resulting, resolved oxidic Al 2p and O 1s peaks are indicated by the dashed and dotted lines in (b) and (c), respectively.

5.3.2. Resolving the metallic and oxidic Al 2p PZL intensities of the oxidized metal

For the case of the *oxidized Al substrates*, the total PZL intensities of the metallic and oxidic Al 2p main peaks were determined from the as-measured Al 2p XPS spectra, as follows [8, 9] (see Fig. 5.3b). First, the lower BE side of the Al 2p peak envelop was set to zero

(background) intensity by subtraction of a constant background (see Sec. 5.3.1). Next, the PZL metallic Al 2p main peak (due to Al in the metal substrate) plus its associated inelastic background was constructed from the shape and position of the metallic Al 2p main peak as resolved from the corresponding spectrum of the bare metal substrate (Sec. 5.3.1). For the calculation of the corresponding inelastic background, Tougaard's formalism [10] for the case of the metal substrate covered with a thin Al₂O₃ film of uniform thickness was adopted, while taking different (three-parameter) universal cross-sections for inelastic-electron scattering [11] in the Al metal substrate (with $B = 16.5 \text{ eV}^2$, $C = 230 \text{ eV}^2$ and $D = 4.5 \text{ eV}^2$) and in the oxide film (taken non-zero for energy losses larger than the band gap energy of 5.7 eV for γ -Al₂O₃ with $B = 3.8 \text{ eV}^2$, $C = 99 \text{ eV}^2$ and $D = 23.5 \text{ eV}^2$; see Eq. (7) in Ref. [11]). As in Refs. [8, 9], one predominant and one weak oxidic Al 2p main peak (plus their associated inelastic backgrounds) were constructed at the higher- and lower BE sides of the oxidic Al 2p peak envelop (further designated as '*film*' and '*interface*' component; see Sec. 5.4) using two symmetric, mixed Gaussian-Lorentzian line shape functions (with the same Gauss fraction, but each with a different position, height and FWHM; see Fig. 5.3b). LLS fitting of the total reconstructed to the zero-background-corrected Al 2p spectra was performed simultaneously for the entire set of AR-XPS spectra recorded at different detection angles from a single oxidized Al substrate (over the BE range from 69.2 eV to 79.8 eV). To account for a possible small energy shift of the metallic main peak in the measured spectra of the oxidized metal with respect to the BE position of the corresponding metallic main peak in the spectrum from the bare metal (e.g. as a result of charging of the thin oxide film during XPS analysis), the BE range of the oxidized metal spectrum was allowed to shift up to $\pm 0.05 \text{ eV}$ during the fitting. Thus, the position, height, FWHM and Gaussian fraction of the oxidic Al 2p main peaks, the height of the metallic Al 2p main peak, and the BE shift of the oxidized alloy spectrum, were employed as fit parameters, while only allowing the position and height of the '*film*' oxidic main peak, the height of the '*interface*' oxidic main peak and the height of the metallic main peak to vary with detection angle. During each iteration step of the LSS fitting, an averaged value of the oxide-film thickness, as required in the calculation of the Tougaard backgrounds of the reconstructed metallic and oxidic main peaks, was estimated from the intensity ratios of the reconstructed metallic and oxidic main peaks for each angular detection range [employing Eqs. (5.2) and (5.3a) in Appendix 5.A]. Finally, the PZL intensity of the metallic Al 2p main peak was obtained, after subtraction of its associated inelastic background, as described in Sec. 5.3.1. The corresponding PZL intensity of each oxidic Al 2p main peak was obtained by integration after subtraction of its associated inelastic background.

5.3.3. Resolving the O 1s PZL intensities of the oxidized metal

For the case of the oxidized Al substrate, the PZL intensities of the identified O 1s main peaks were determined from the as-measured O 1s XPS spectra, as follows (see Fig. 5.3c) [9]. First, a Shirley-type background was subtracted from the as-measured O 1s spectra over the BE range from 528 eV to 538.5 eV. Next, the background-corrected O 1s spectra was fitted with three symmetric, mixed Gaussian-Lorentzian line shape functions, representing the identified O 1s main peaks. Thus, a minimum of three O 1s main peaks are required to accurately describe the background-corrected O 1s peak envelop: a predominant peak at the low BE side, a distinct peak at an intermediate BE position and a minor peak at the high BE side (see Fig. 5.3c). LLS fitting of the total reconstructed O 1s spectrum to the background-corrected O 1s spectrum of the oxidized alloy over the BE range from 528 eV to 538.5 eV was performed simultaneously for the entire set of AR-XPS spectra recorded at different detection angles from a single oxidized alloy substrate. The positions, heights, FWHM's and the Gaussian fraction of the fitted O 1s main peaks were employed as fit parameters, while allowing only the positions and heights of the peaks to vary with detection angle (i.e. the same Gaussian fraction and FWHM were adopted for the three main peaks). Finally, the PZL intensity of each of the fitted O 1s main peaks was obtained by integration of the three mixed Gaussian-Lorentzian peaks over the BE range from 528 eV to 538.5 eV.

5.3.4. Quantification

One metallic Al 2p main peak, two oxidic Al 2p main peaks (designated as 'film' and 'interface' component) and three O 1s main peaks were resolved from the as-measured Al 2p and O 1s AR-XPS spectra of the oxidized metal (Secs. 5.3.1 – 5.3.3 and Fig. 5.3). Next, the corresponding *effective depths* below the specimen surface (for definition and background of thin concept, see Ref. [9]) for the various identified oxidic Al 2p and O 1s species within the oxide film were calculated using Eq. (5.4b) in Appendix 5.B (and employing the corresponding PZL intensities as resolved for a set of more near-normal and more grazing detection angles, i.e. in the range of $\alpha = 30-46^\circ$ and $\alpha = 60-76^\circ$, respectively [9]). It follows that the oxidic 'interface' aluminium component with thickness L^{int} is located at an effective depth corresponding to the position of the metal/oxide interface, whereas the oxidic 'film' aluminium component with oxide-film thickness L^{ox} is concentrated at an effective depth in the interior of the oxide film (see also Sec. 5.4). The resolved oxygen components, on the other hand, *cannot* be uniquely assigned to specific effective depths within the oxide film, at the metal/oxide interface or at the outer oxide surface [although there is a slight tendency for

the oxygen corresponding to the pronounced low-BE and intermediate-BE O 1s main peaks (Fig. 5.3c) to be concentrated closer to the metal/oxide interface and the oxide surface, respectively].

Table 5.1. Physical constants used for the quantification of the AR-XPS spectra recorded from the oxidized Al substrates (see Sec. 5.3).

Material	Constant	Symbol	Value	Unit	Reference
Al metal	density	ρ_{Al}	$2.669 \cdot 10^3$	$\text{kg} \cdot \text{m}^{-3}$	[7]
	Al 2p intrinsic bulk plasmon probability	P_{BP}	0.11		[8]
Al_2O_3	density <i>am</i> - Al_2O_3	$\rho_{\text{am-Al}_2\text{O}_3}$	$3.17 \cdot 10^3$	$\text{kg} \cdot \text{m}^{-3}$	[15]
	density γ - Al_2O_3	$\rho_{\gamma\text{-Al}_2\text{O}_3}$	$3.630 \cdot 10^3$	$\text{kg} \cdot \text{m}^{-3}$	[7]
	band gap	E_{g}	5.7	eV	[16-18]
Al / Al_2O_3	ratio of photoionization cross-sections	$\sigma_{\text{O } 1s} / \sigma_{\text{Al } 2p}$	4.38		own work
	asymmetry factor	$\beta_{\text{Al } 2p}$	0.93		[19]
	asymmetry factor	$\beta_{\text{O } 1s}$	2.00		[19]

The average thicknesses ($L = L^{\text{ox}} + L^{\text{int}}$) and compositions (as expressed by the O:Al ratio) of the grown oxide films were calculated from the metallic Al 2p, oxidic Al 2p and O1s PZL intensities, as resolved from the spectra of the oxidized metal (for the various detection angles α), according to the iterative procedure described in the Appendix 5.A.2 (and adopting the physical constants reported in Table 5.1). Since the resolved O 1s components cannot be uniquely assigned to specific depths within the oxide film (see above), the PZL intensities of the resolved O 1s main peaks were summed, whereas the PZL intensities of the resolved 'film' and 'interface' oxidic Al 2p main peaks were treated separately in the quantification (with corresponding thicknesses of L^{ox} and L^{int} , respectively). Values for the effective attenuation lengths (EALs) and asymmetry factors, as required in the calculations were determined according to Refs. [5, 14] and using the physical constants as reported in Table 5.1. Note that

the effects of the anisotropy of the photo-ionization cross-section and elastic scattering of the emitted photoelectrons in the solid were accounted for in the quantification by employing the asymmetry factor and the EAL (instead of the inelastic mean free path) in the calculations, respectively (see Refs. [5, 14]).

5.4. Oxide-film microstructure before and after annealing

The measured Al 2p photoelectron spectra recorded from the oxidized Al substrates could all be accurately fitted with one metallic main peak, one predominant higher-BE oxidic main peak ('film') and one weaker, lower-BE suboxidic main peak ('interface') (see Fig. 5.3 and Sec. 5.3.2). Evidently, the metallic Al 2p main peak corresponds to Al in the metal substrate (as also follows from the effective depth value). The relation of the resolved oxidic 'film' and 'interface' Al 2p main peaks with the oxide-film microstructure can be deduced on the basis of the corresponding relative BE positions in combination with their relative effective depths within the oxide film (calculated as described in Sec. 5.3.4, and see Appendix 5.B). The effective depth analysis of the resolved oxidic 'film' and 'interface' main peaks showed that the 'interface' main peak is due to aluminium located at the metal/oxide interface, whereas the 'film' main peak is concentrated at an effective depth between the metal/oxide interface and the outer oxide surface. The average oxygen-to-aluminium ratio of 1.5 ± 0.1 for the grown oxide films (as obtained from the quantitative AR-XPS analysis; see Sec. 5.3.4) indicates that *overall* stoichiometric oxide films are formed. It is thus concluded that the oxidic 'film' contribution is associated with the stoichiometric Al₂O₃ oxide phase in the interior of the film, whereas the suboxidic 'interface' contribution arises from the deficient coordination of Al cations by nearest-neighbour O anions *at* the metal/oxide interface. This interpretation of the 'interface' component is compatible with the relatively lower BE position of the 'interface' main peak, as well as with the submonolayer thickness of the 'interface' oxide component: The average thickness of the 'interface' oxide of $L^{\text{int}} \cong 0.1 \pm 0.05$ nm (independent of T and the substrate orientation), as determined by AR-XPS (see Appendix 5.A), equals about half of an oxide monolayer (1 ML $\cong 0.2$ nm), in good agreement with the corresponding thickness values obtained independently by the RISE analysis (Chapter 6 of this thesis).

Oxidation of the bare Al{111}, Al{100} and Al{110} substrates for $t = 6000$ s in the oxidation temperature range of $T = 350$ K – 600 K at $p_{\text{O}_2} = 1 \times 10^{-4}$ Pa resulted in the formation of oxide films with total thicknesses ($L = L^{\text{ox}} + L^{\text{int}}$) in the range of 0.5 nm to 2.1 nm (as determined by AR-XPS; see Fig. 5.4 and Sec. 5.3.4).

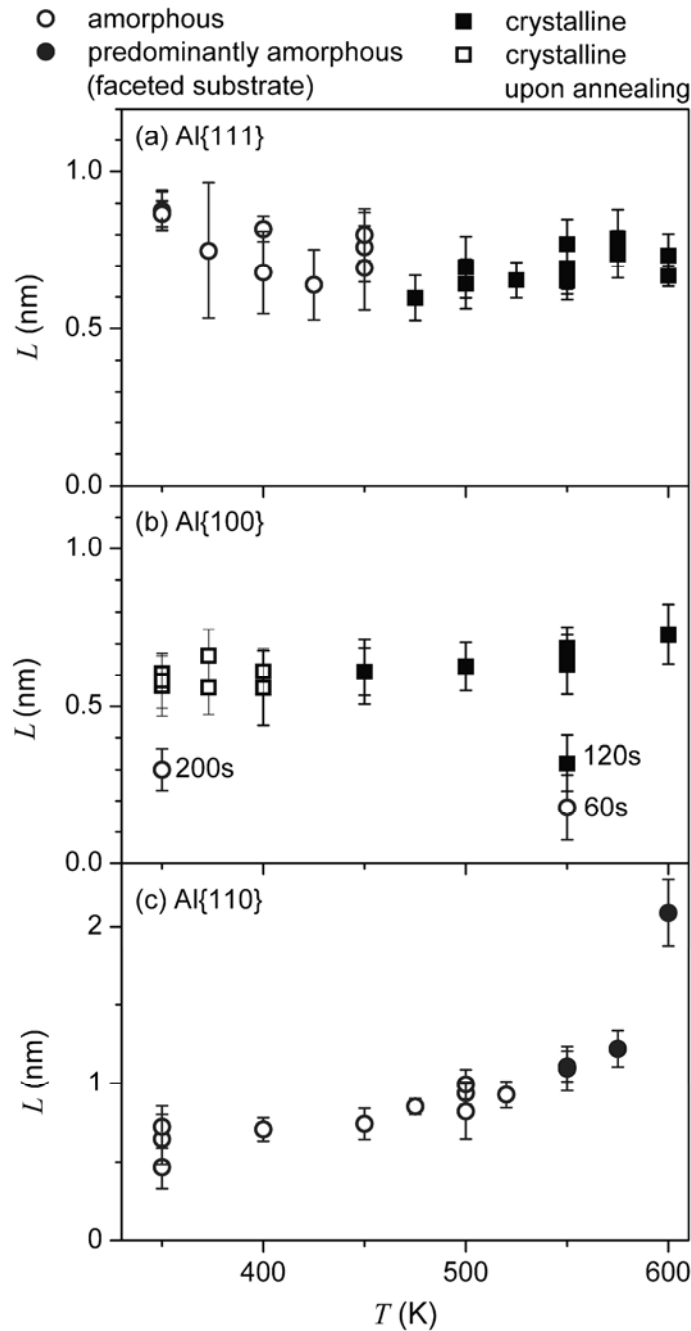


Figure 5.4. Oxide-film thickness (as determined by AR-XPS; Sec. 5.3.4) versus oxidation temperature for the oxidation of the bare (a) Al{111}, (b) Al{100} and (c) Al{110} substrates for different oxidation times in the range of $t = 60 - 6000$ s at $p_{\text{O}_2} = 1 \times 10^{-4}$ Pa (the oxidation times of the short-time experiments with $t < 6000$ s are indicated). Resulting amorphous oxide films, which remain in the amorphous state even after in-situ UHV annealing at 700 K, are indicated by the markers \circ . Resulting amorphous oxide films, which transform into a crystalline oxide film upon in-situ UHV annealing at 700 K, are indicated by the markers \square . Resulting crystalline oxide films are indicated by the markers \blacksquare . The development of a {111} faceted Al metal surface upon oxidation in association with a predominantly amorphous oxide overgrowth (which is stable upon in-situ UHV annealing at 700 K) is indicated by the markers \bullet .

5.4.2. Oxide films on Al{111}

The thickness of the oxide films grown on Al{111} after $t = 6000$ s of oxidation at $p_{\text{O}_2} = 1 \times 10^{-4}$ Pa is in the range of $L = 0.6$ nm to 0.9 nm (Fig. 5.4a). The oxide films are of uniform thickness and the metal/oxide interface is atomically flat (as evidenced from the cross-sectional HR-TEM analysis; see Figs. 5.2, 5.5, 5.6 and Chapter 4).

For oxidation temperatures $T \leq 450$ K, the oxide films grown on Al{111} after $t = 6000$ s of oxidation are amorphous as indicated by both LEED and HR-TEM (Fig. 5.5). In the amorphous temperature regime (i.e. $T \leq 450$ K), the oxide-film thickness reached after $t = 6000$ s of oxidation is slightly decreasing with increasing T from $L = (0.88 \pm 0.06)$ nm at $T = 350$ K to $L = (0.60 \pm 0.07)$ nm at $T = 475$ K (as determined with AR-XPS, Sec. 5.3.4, and also evidenced from the RISE analysis; see Chapter 6). The amorphous state, and the thickness and composition (i.e. the microstructure) of the oxide films grown on Al{111} for $T \leq 450$ K and $t = 6000$ s is preserved after in-situ UHV annealing for 6000 s at 700 K (as evidenced by AR-XPS and LEED).

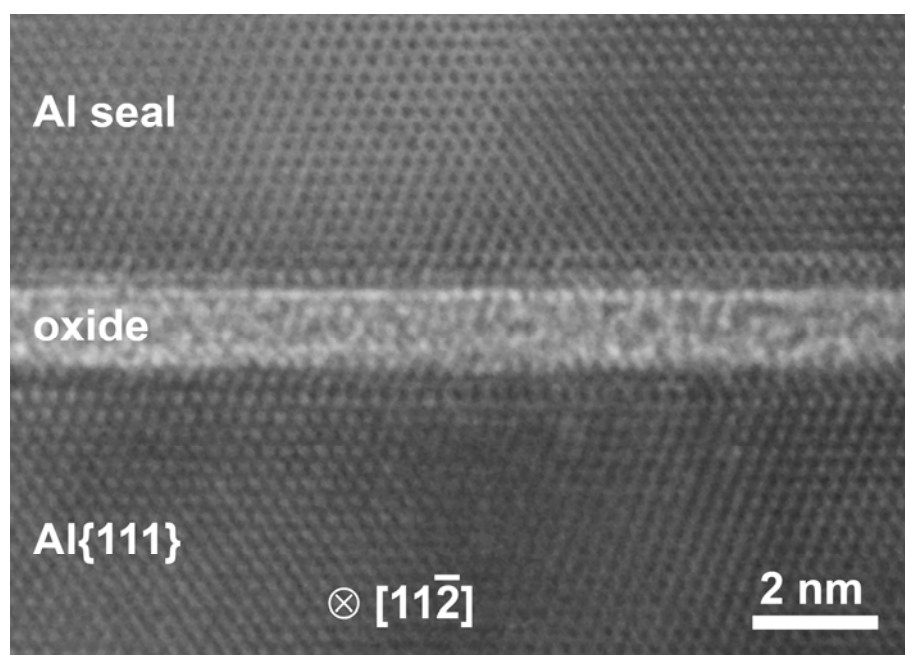


Figure 5.5. High-resolution transmission electron micrograph of the amorphous Al_2O_3 overgrowth on Al{111} after oxidation for $t = 6000$ s at $T = 373$ K and $p_{\text{O}_2} = 1 \times 10^{-4}$ Pa (and subsequent in-situ deposition of a MBE-grown Al seal; see Sec. 5.2). The direction of the primary electron beam was along the $[11\bar{2}]$ zone axis of the Al{111} substrate (with the $[111]$ direction perpendicular to the substrate-oxide interface).

For $T \geq 475$ K, the oxide-film thickness for $t = 6000$ s slowly increases with increasing temperature up to $L = (0.73 \pm 0.07)$ nm at $T = 600$ K (Fig. 5.4a) and, at the same time, diffraction spots are observed in the recorded LEED patterns, indicating the formation of a crystalline oxide phase (Fig. 5.6). As follows from the LEED and HR-TEM analysis of the crystalline oxide films grown on Al{111} for $T \geq 475$ K, an epitaxial γ (-like)-Al₂O₃ oxide film develops on the Al{111} substrate (designated as γ'' -Al₂O₃; see Chapter 4) with a resulting coherent metal/oxide interface (cf. Fig. 5.6). The crystallographic orientation relationship (COR) between the Al{111} metal substrate and the γ'' -Al₂O₃ overgrowth is: Al(111)[1 $\bar{1}$ 0] || γ'' -Al₂O₃(111)[1 $\bar{1}$ 0], which corresponds to the expected COR with lowest possible initial lattice mismatch (of about 2-3%) between the Al{111} substrate and the γ'' -Al₂O₃ overgrowth (see Chapter 4).

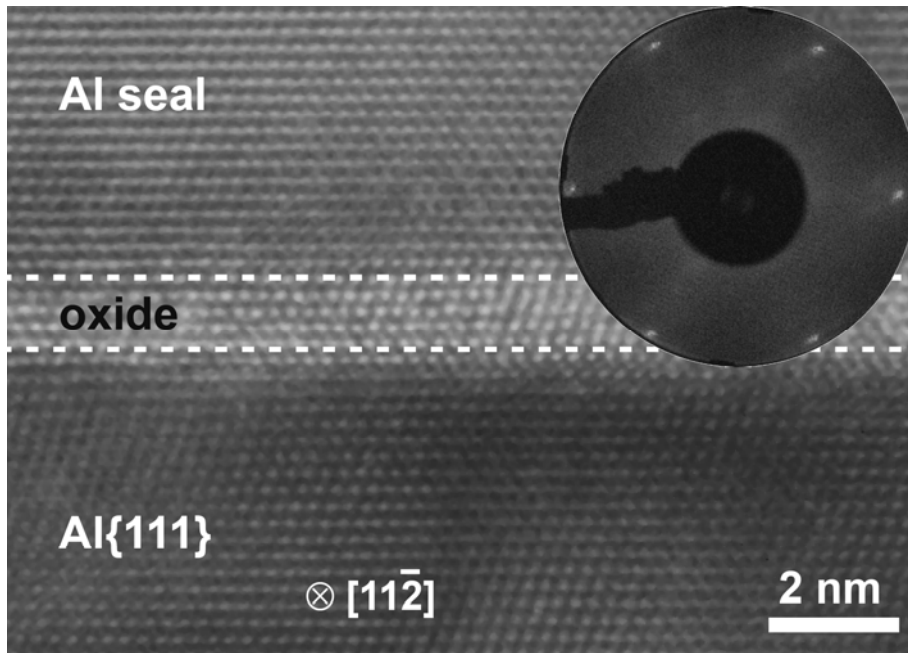


Figure 5.6. High-resolution transmission electron micrograph of the crystalline γ'' -Al₂O₃ overgrowth on Al{111} after oxidation for $t = 6000$ s at $T = 550$ K and $p_{\text{O}_2} = 1 \times 10^{-4}$ Pa. The direction of the primary electron beam was along the [11 $\bar{2}$] zone axis of the Al{111} substrate. The dashed lines roughly indicate the boundaries between the oxide and the Al{111} substrate and the oxide and the Al seal. The inset shows the corresponding LEED pattern as recorded (with a primary electron energy of 53 eV) directly after the oxidation (prior to in-situ deposition of the Al seal; Sec. 5.2); the six-fold symmetry observed in the LEED pattern is typical for the {111} surface of an oxide with an fcc-type oxygen sublattice, such as γ'' -Al₂O₃.

5.4.3. Oxide films on Al{100}

The thickness of the oxide films grown on Al{100} for $t = 6000$ s at $p_{\text{O}_2} = 1 \times 10^{-4}$ Pa gradually increases with increasing T from $L = (0.59 \pm 0.06)$ nm at $T = 350$ K to $L = (0.73 \pm 0.09)$ nm at $T = 600$ K (see Fig. 5.4b). The resulting oxide films are of uniform thickness and the metal/oxide interface is atomically flat (Fig. 5.7).

For $T \leq 400$ K, the oxide films grown on Al{100} up to $t = 6000$ s are amorphous as indicated by LEED. Upon in-situ UHV annealing for 3600 s at 700 K, the oxide films grown for $t = 200$ s at $T = 350$ K [with $L = (0.30 \pm 0.10)$ nm] maintain their amorphous state (and thickness and microstructure), whereas the thicker amorphous oxide films grown for $t = 6000$ s at $T = 350$ K [with $L = (0.59 \pm 0.06)$ nm] transform into crystalline $\gamma''\text{-Al}_2\text{O}_3$ (with their initial thickness and composition being preserved; as evidenced by AR-XPS and LEED).

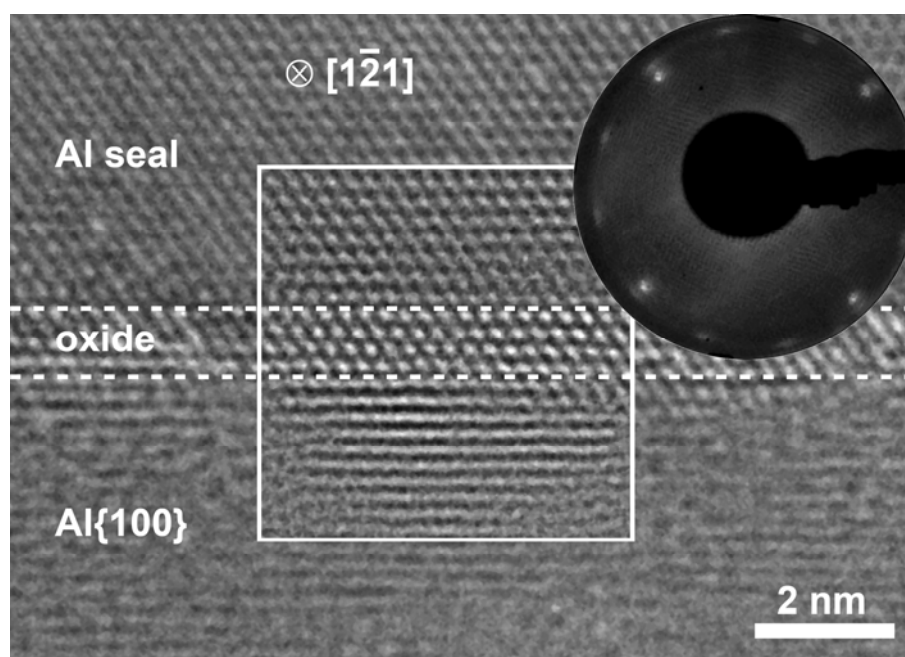


Figure 5.7. High-resolution transmission electron micrograph of the crystalline $\gamma''\text{-Al}_2\text{O}_3$ overgrowth on Al{100} after oxidation for $t = 6000$ s at $T = 550$ K and $p_{\text{O}_2} = 1 \times 10^{-4}$ Pa. The direction of the primary electron beam was along the $[1\bar{2}1]$ zone axis of the Al capping layer and the oxide film. The area of the micrograph within the square represents a Fourier-filtered region of the original micrograph as obtained after inverse Fourier transformation of the 2D Fourier transform of the original image after removing the noise around the primary beam spot. The corresponding LEED pattern as recorded (with a primary electron energy of 54 eV) directly after the oxidation shows separate diffraction spots originating from the Al{100} substrate (exhibiting a four-fold symmetry) and the crystalline oxide overgrowth (exhibiting a twelve-fold symmetry with spots located in rings; Chapter 4).

For $T > 400$ K, separate weak LEED spots originating from the oxide film and the Al substrate (Chapter 4) are observed for the oxidized Al{100} substrate after $t = 6000$ s at $T = 450$ K, corresponding to an oxide-film thickness of $L = (0.61 \pm 0.08)$ nm (Fig. 5.7). However, an additional short-time oxidation experiment performed for $t = 60$ s at $T = 550$ K showed that the resulting oxide film of thickness $L = (0.17 \pm 0.10)$ nm is still amorphous as indicated by LEED; a somewhat thicker oxide film grown for $t = 120$ s at $T = 550$ K [with $L = (0.28 \pm 0.10)$ nm] is crystalline, as indicated by LEED. Thus, the diffraction spots in the recorded LEED patterns become more pronounced with increasing temperature and oxide-film thickness due to the gradual replacement of the amorphous Al_2O_3 phase by the crystalline γ'' - Al_2O_3 phase in the thickening oxide film (see Chapters 4 and 6).

As follows from the LEED and HR-TEM analysis of the crystalline oxide films grown on Al{100} for $T > 400$ K (Chapter 4), the COR between the Al{100} substrate and the γ'' - Al_2O_3 overgrowth is: $\text{Al}(100)[011] \parallel \gamma''\text{-Al}_2\text{O}_3(111)[01\bar{1}]$ and, consequently, a very high initial lattice mismatch of nearly 18% resides with the crystalline oxide overgrowth in one direction parallel to the metal/oxide interface (the initial lattice mismatch in the perpendicular direction is only about +2.0%, as for the overgrowth on Al{111}; see Sec. 5.4.1). Thus, the γ'' - Al_2O_3 overgrowths on Al{100} exhibit a large anisotropic tensile growth strain, the largest part of which has been relaxed by the formation of defects at the metal/oxide interface, as well as by slight, in-plane rotations of two γ'' - Al_2O_3 domains with respect to the aforementioned high-mismatch COR (see Chapter 4 and Ref. [20] for details). As shown by thermodynamic model calculations in Chapter 4 of this thesis, the experimentally observed high-mismatch COR is thermodynamically preferred with respect to the expected low-mismatch COR due to the relatively higher density of metal-oxygen bonds across the metal/oxide interface and the relatively lower surface energy (which are overcompensating the unfavourable energy contributions due to residual strain and misfit dislocations).

5.4.4. Oxide films on Al{110}

The thickness of the oxide films grown on Al{110} after $t = 6000$ s of oxidation at $p_{\text{O}_2} = 1 \times 10^{-4}$ Pa increases with increasing T from $L = (0.68 \pm 0.14)$ nm at $T = 350$ K to $L = (2.75 \pm 0.3)$ nm at $T = 640$ K (see Fig. 5.4c).

For $T \leq 550$ K, no LEED spots are observed from the oxidized Al{110} substrates, indicating that amorphous oxide films have formed. The thickness and microstructure of the

amorphous oxide films grown at $T \leq 550$ K is preserved after in-situ UHV annealing for 3600 s at 700 K (as evidenced by AR-XPS and LEED).

For $T > 550$ K, LEED diffraction spots are observed for short oxidation times (e.g. after $t = 120$ s; Figs. 5.8a-c), which become *weaker* for longer oxidation times (at constant $T > 550$ K) and during subsequent annealing at 700 K. Only very weak LEED spots remain after prolonged oxidation at $T > 550$ K, in accordance with the predominantly amorphous state of the corresponding oxide films according to the HR-TEM analysis (Fig. 5.8d).

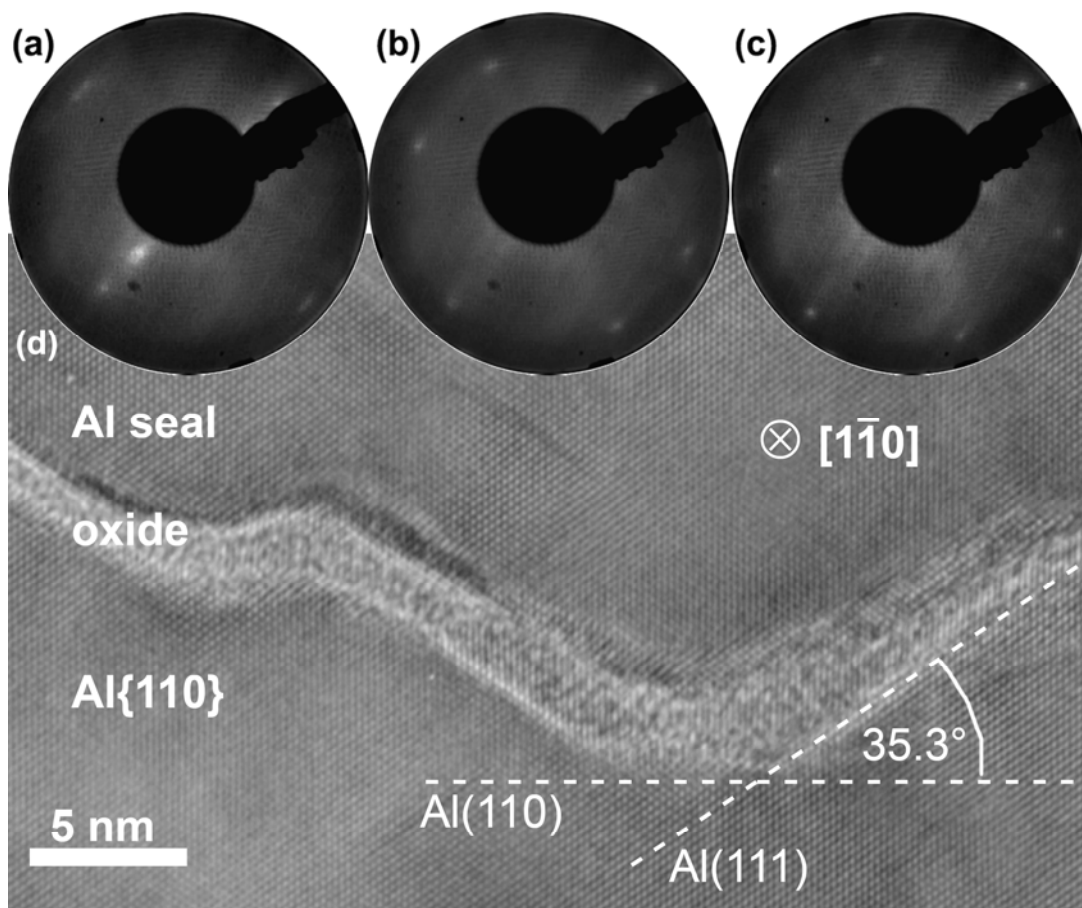


Figure 5.8. LEED patterns as recorded with a primary electron energy of (a) 54 eV, (b) 70 eV and (c) 80 eV, from the Al{110} substrate after oxidation for $t = 120$ s at $T = 650$ K and $p_{\text{O}_2} = 1 \times 10^{-4}$ Pa, indicative for the existence of a {111} faceted oxidized metal surface. (d) High-resolution transmission electron micrograph of the Al_2O_3 overgrowth on Al{110} after oxidation for $t = 6000$ s at $T = 640$ K and $p_{\text{O}_2} = 1 \times 10^{-4}$ Pa showing that {111} faceting of the Al{110} substrate had indeed occurred. The direction of the primary electron beam in (d) was along the $[1\bar{1}0]$ zone axis of both the Al substrate and the Al capping layer.

Detailed analysis of the *shifts* of the diffraction spots in the recorded LEED patterns with increasing energy of the primary electron beam from 20 eV to 200 eV (as performed for the short time oxidation experiments at $t = 120$ s; see Figs. 5.8a-c) indicates the existence of

$\{111\}$ facets at the oxidized Al $\{110\}$ surface for short time oxidations at $T > 550$ K. Indeed, the cross-sectional HR-TEM analysis of an oxide film grown on Al $\{110\}$ for $t = 6000$ s at $T = 640$ K clearly shows that $\{111\}$ facets had developed at the oxidized metal surface (Figs. 5.2 and 5.8d). The angle between the original (110) surface plane of the bare Al $\{110\}$ substrate and the (111) and $(11\bar{1})$ planes of the faceted metal surface is 35.3° . The $\{111\}$ facets often contain smaller steps and are rounded off at their trenches and crests (see Fig. 5.8d). The width between two trenches or crests of the $\{111\}$ facets, as observed for the oxidized Al $\{110\}$ surface at $T = 640$ K, is in the range of (6 – 200) nm with an average height (i.e. distance between an adjacent trench and crest as measured perpendicular to the original Al $\{110\}$ surface plane) of about 25 nm. Furthermore, the diffusiveness of the metal/oxide interface in the HR-TEM analysis, in particular at the edges of the facets, suggests that oxygen dissolution and inward diffusion into the parent metal substrate had occurred (predominantly at the edges of the facets), which is in good agreement with similar findings for the oxidation of an Al $\{110\}$ substrate at 673 K [22]. As a result, the thicknesses of the oxide films grown on Al $\{110\}$ at $T > 550$ K are no longer uniform; for example, the thickness of the oxide film grown for $t = 6000$ s at $T = 640$ K, as observed in the HR-TEM micrographs (e.g. Figs. 5.2 and 5.8d), varies between $L = 0.8$ nm and 4.2 nm with an average thickness of about (2.4 ± 0.8) nm, which is in good agreement with the corresponding average thickness of $L = (2.75 \pm 0.3)$ nm as determined by AR-XPS (Sec. 5.3.4). Oxidation-induced faceting of the Al $\{110\}$ surface at elevated temperatures has also been reported in Ref. [23], whereas an amorphous oxide phase without a reconstruction of the parent Al $\{110\}$ metal surface has been found at room temperature [24]. It is noted that the original $\{110\}$ crystallographic surface of the *bare* Al substrate becomes fully restored after subsequent cleaning and annealing (Sec. 5.2) of the oxidized, reconstructed Al $\{110\}$ surface in UHV (as verified by LEED and in agreement with thermodynamic model predictions; see Sec. 5.5.3).

5.5. Discussion: the stability of amorphous oxide films

5.5.1. Amorphous oxide films on Al $\{111\}$

Upon oxidation of the Al $\{111\}$ substrate at $T \leq 450$ K, amorphous Al₂O₃ films with uniform thicknesses in the range of about $L = 0.6$ nm to 0.9 nm are formed (Sec. 5.4.1). These amorphous oxide films on Al $\{111\}$ are stable upon subsequent in-situ UHV annealing at 700 K. Thin amorphous alumina layers were even found to be stable at higher annealing temperatures of 1000 K [25] (i.e. above the melting point of Al of 933 K). The thicknesses

(i.e. 0.6 – 0.9 nm) of the evidently stable, amorphous oxide films grown on Al{111} in the present study comply well with the predicted critical thickness of $h_{\{\text{Al}_2\text{O}_3\}}^{\text{critical}} = (0.7 \pm 0.1)$ nm up to which an amorphous Al₂O₃ film is thermodynamically preferred on the Al{111} substrate (for $T = 350 - 900$ K; see Fig. 5.1 as calculated in Chapter 3).

Upon oxidation of the Al{111} substrate at $T \geq 475$ K, on the other hand, *crystalline* γ -Al₂O₃ oxide films with limiting thicknesses in the range of about $L = 0.6$ nm to 0.8 nm develop on Al{111}. The observation of, on the one hand, stable amorphous oxide films with thicknesses in the range of 0.6 nm to 0.9 nm for growth temperatures $T \leq 450$ K and, on the other hand, crystalline oxide films of similar thicknesses for growth temperatures $T > 450$ K is explained below by **(i)** a change in oxide growth-mode, and **(ii)** an enhanced rate of oxygen incorporation into the bare metal surface region (see what follows).

Ad (i): For $T \leq 473$ K, the mobility of oxygen species on the Al metal surface is very low, thus preferred oxide island formation is kinetically hindered, and consequently a layer-by-layer oxide growth mode occurs for $T \leq 473$ K (see Ref. [21] and references therein). With increasing oxidation temperature, the lateral diffusion over the bare Al substrate surface of mobile oxygen species is increased and then continued oxide growth proceeds in an island-by-layer growth mode for $T > 473$ K (see Ref. [21] and references therein). Since the tensile growth strain associated with the development of an epitaxial crystalline oxide phase on Al{111} (Sec. 5.4.1) can be more easily relaxed by lateral extension for an island-by-layer growth mode (than for a layer-by-layer growth mode, if at all), the formation of the crystalline oxide phase will be promoted at $T > 473$ K. It then follows that the 'actual' value of the critical oxide-film thickness for the amorphous-to-crystalline transition at $T \geq 475$ K will be lower than the predicted value of $h_{\{\text{Al}_2\text{O}_3\}}^{\text{critical}} \cong 0.7 \pm 0.1$ nm (for $T = 350 - 600$ K; see Fig. 5.1), as calculated for a tensilely strained oxide film of *uniform thickness* (i.e. with an infinite lateral extension parallel to the metal/oxide interface; see Chapter 3).

Ad (ii): For the initial stage of interaction of oxygen gas and the bare Al metal surface, oxygen incorporation into the bare metal subsurface competes with the on-top chemisorption of oxygen on the bare metal surface (Chapter 6). Oxygen incorporation is favoured over on-top chemisorption on the less-densely packed metal surfaces and for increasing oxidation temperature. As indicated by the RISE analysis (Chapter 6) on-top oxygen chemisorption prevails for the initial oxidation of the bare Al{111} substrate at $T \leq 450$ K, whereas oxygen incorporation predominates at $T \geq 475$ K. It is suggested that incorporated oxygen atoms in the metal-surface adjacent region at the onset of oxidation can act as nuclei for the initiation

of crystallization of the initially amorphous oxide films (i.e. oxygen incorporation reduces the activation-energy barrier for the nucleation of crystallization), which is consistent with the observation by HR-TEM that the nucleation of γ -Al₂O₃, for the thicker oxide films grown at higher temperatures, takes place preferentially at the interface between the initially amorphous oxide film and the parent Al metal substrate [21]. As a consequence, the transformation of the low- T amorphous oxide films into γ'' -Al₂O₃ beyond the critical thickness $h_{\{\text{Al}_2\text{O}_3\}}^{\text{critical}}$ can be kinetically hindered, because oxygen incorporation does not dominate over chemisorption at $T \leq 450$ K.

It is concluded that the stability of amorphous oxide films on bare Al{111} substrates is governed by *both* the thermodynamics and the kinetics of the oxide growth process. Governing thermodynamic factors are: the lower sum of interface and surface energies for the amorphous oxide-film configuration (Chapter 3) and the reduction of the critical thickness of the amorphous-to-crystalline transition due to a change in the oxide growth mode, allowing tensile growth strain relaxation for the crystalline modification. Prevailing kinetic factors are: the increased mobility of oxygen species on the bare metal surface with increasing temperature (promoting an island-by-layer growth mode) and the extent of initial oxygen incorporation into the metal subsurface region (which lowers the energy barrier for nucleation of the crystalline oxide; Chapter 6).

5.5.2. Amorphous oxide films on Al{100}

Upon oxidation of the Al{100} substrate at $T \leq 400$ K for $t = 6000$ s, amorphous Al₂O₃ films with uniform, limiting thicknesses of about $L = 0.6 \pm 0.1$ nm are formed (Sec. 5.4.2). These low- T amorphous oxide films on Al{100} are transformed into crystalline γ'' -Al₂O₃ films by in-situ UHV annealing at 700 K, which implies that the formation of a crystalline oxide phase for continued oxide-film growth beyond the critical thickness at $T \leq 400$ K is kinetically hindered (*note*: the calculated critical thickness on Al{100} is about independent of T ; see Fig. 5.1). The $L = 0.3 \pm 0.1$ nm thick amorphous oxide films grown on Al{100} at $T = 350$ K for $t = 200$ s do maintain their amorphous state upon in-situ UHV annealing. It is therefore concluded that the experimentally-observed critical thickness, up to which an amorphous state for the initial oxide film on Al{100} is thermodynamically preferred, is in the range of 0.3 nm to 0.6 nm (for $T = 350 - 400$ K), which is slightly lower than the theoretically-predicted critical thickness value of $h_{\{\text{Al}_2\text{O}_3\}}^{\text{critical}} \cong 0.8 \pm 0.1$ nm (Chapter 3).

In the case of the more open Al{100} surface, as compared to the Al{111} surface, at the onset of oxidation, oxygen incorporation predominates over on-top chemisorption, whereas on-top oxygen chemisorption prevails for the densely-packed Al{111} surface up to $T = 450$ K (see Sec. 5.5.1 and Chapter 6). As previously stated in Sec. 5.5.1, the incorporated oxygen atoms in the Al{100} subsurface act as nuclei for the initiation of crystallization of the amorphous oxide films of thicknesses larger than the critical thickness upon subsequent in-situ UHV annealing (*note*: the amorphous oxide films grown on Al{111} at $T \leq 450$ K did not transform into crystalline γ'' -Al₂O₃ during in-situ UHV annealing; see Sec. 5.5.1).

Upon oxidation of the Al{100} substrate at $T > 400$ K, the initial amorphous oxide has transformed into crystalline γ'' -Al₂O₃ at a thickness of about $L = 0.23 \pm 0.1$ nm (at $T = 550$ K; see Sec. 5.4.2). At these elevated temperatures, initial oxidation involves the formation and growth of oxide islands on the bare Al substrate, as evidenced in the present study by the distinct oxidic Al 2p main peak in combination with a metallic surface plasmon peak in the measured spectra of the oxidized Al{100} substrate for short oxidation times at $T = 550$ K (in agreement with similar findings in Ref. [21]; see also related discussion in Sec. 5.5.1).¹ It follows that (see Sec. 5.5.1) the theoretically-predicted critical thickness value of $h_{\text{Al}_2\text{O}_3}^{\text{critical}} \cong 0.8 \pm 0.1$ nm presents an overestimate of the 'actual' critical oxide-film thickness for the amorphous-to-crystalline transition Al{100} at $T = 550$ K. Furthermore, the actual value of the critical oxide-film thickness for the amorphous-to-crystalline transition Al{100} at $T = 550$ K (as given by the average height of the oxide islands) will be larger than the corresponding *average* thickness value of 0.23 ± 0.1 nm, as determined by AR-XPS.

5.5.3. Amorphous oxide films on Al{110}

Upon oxidation of the Al{110} substrate at $T \leq 550$ K, where the substrate does not develop facets, amorphous Al₂O₃ films of uniform thicknesses in the range of about 0.6 nm to 1.2 nm are formed (Sec. 5.4.1). These amorphous oxide films on Al{110} are stable upon subsequent in-situ UHV annealing at 700 K. The thicknesses (i.e. between 0.6 – 1.2 nm) of the *stable*, amorphous oxide films on the *non-faceted* Al{110} substrate are indeed below the calculated critical thickness of $h_{\text{Al}_2\text{O}_3}^{\text{critical}} = 4.0 \pm 0.5$ nm up to which an amorphous Al₂O₃ film is

¹ For the short-time oxidations at lower temperatures, no surface plasmon structure associated with the Al 2p metallic main peak was observed in the measured XPS spectra of the oxidised metal substrates, which indicates that the entire Al metal surface is covered with oxide already at the onset of oxidation and layer-by-layer growth occurs [21].

thermodynamically preferred on the non-faceted Al{110} substrate (for $T = 350 - 900$ K; see Fig. 5.1 as calculated in Chapter 3).

Oxidation-induced **faceting** of the Al{110} substrate occurs upon oxidation at $T > 550$ K (Sec. 5.4.3 and Fig. 5.8), which is associated with an increase in surface (and metal/oxide interface) area of about 22%. As verified by thermodynamic model calculations (see Chapters 2 to 4), the calculated interfacial energy ($\gamma_{\langle \text{Al}\{111\}\rangle - \{\text{Al}_2\text{O}_3\}}$) of the Al{111}/*am*-Al₂O₃ interface is lower (more negative) than the corresponding interfacial energy ($\gamma_{\langle \text{Al}\{110\}\rangle - \{\text{Al}_2\text{O}_3\}}$) of the Al{110}/*am*-Al₂O₃ interface due to the relatively higher density of metal-oxygen bonds across the Al{111}/*am*-Al₂O₃ interface (Chapter 3). It follows that the increase in surface energy by the increase of interfacial area of the amorphous oxide film (of approximately 22%) as a result of the development of the {111} facets at the parent metal surface is overcompensated by the concurrent decrease in the *total* metal/oxide interfacial energy. Thus, the oxidation-induced faceting of the Al{110} is thermodynamically preferred. It is apparently kinetically hindered at $T \leq 550$ K.

Neglecting the energetics of the (rounded-off) edges of the developed {111} facets, the calculated value of the critical thickness up to which an amorphous oxide film is thermodynamically preferred on the {111}-faceted Al substrate will be equal to the corresponding value for a flat Al{111} substrate: i.e. $h_{\{\text{Al}_2\text{O}_3\}}^{\text{critical}} = 0.7 \pm 0.1$ nm (see Fig. 5.1 as calculated in Chapter 3). Indeed, for the 2.75 ± 0.3 nm thick oxide films grown on the {111}-faceted Al substrate at $T = 640$ K very weak diffraction spots are observed in the recorded LEED patterns, which are indicative for a partial crystallinity of the oxide film. According to the corresponding HR-TEM analysis, the oxide films with thicknesses much larger than the predicted critical thickness (as formed after prolonged oxidation at $T > 550$ K) are still predominantly amorphous, which suggests that the crystallization of the amorphous oxide films on the {111}-faceted Al{110} substrate is kinetically hindered.

The observation of *more distinct* LEED patterns for *shorter* oxidation times at $T > 550$ K (see Sec. 5.4.3) can be explained on the basis of a change in the oxide growth mode from layer-by-layer to island-by-layer growth at around $T = 550$ K (see also Secs. 5.5.1 and 5.5.2). Indeed, for the short oxidation times at $T > 550$ K, the surface plasmon peak associated with the metallic Al 2p main peak (due to the metal substrate) is still visible in the measured XPS spectra of the oxidized Al{110} metal (see footnote 1). The diffraction spots in the recorded LEED patterns for short oxidation times at $T > 550$ K therefore most probably originate mainly from the patches of (still) bare metal surface (and not from an ordering at the oxide

surface), which is compatible with the observation of weaker LEED spots for longer oxidation times (see above).

After cleaning and annealing (Sec. 5.2) of the {111}-faceted metal surface in UHV, the original {110} crystallographic surface of the *bare* Al substrate is restored, in agreement with the relatively lower surface area of the non-faceted Al{110} substrate (in spite of the relatively lower surface energy *per unit area* of the Al{111} surface as compared to the Al{110} surface).

5.6. Conclusions

Oxidation of bare Al{111}, Al{100} and Al{110} substrates by exposure to pure oxygen gas for times up to $t = 6000$ s in the temperature regime of $T = 350 - 650$ K at a partial oxygen pressure of $p_{\text{O}_2} = 1 \times 10^{-4}$ Pa results in the formation of ultra-thin (< 3 nm) stoichiometric Al₂O₃ films. The resulting oxide films on Al{111} and Al{100} are of uniform thicknesses and have atomically flat metal/oxide interfaces, whereas a {111}-faceted metal surface develops upon oxidation of the bare Al{110} surface at $T > 550$ K.

On **Al{111}** for $t = 6000$ s at $T \leq 450$ K, amorphous oxide films with thicknesses in the range of 0.6 – 0.9 nm are formed, which are stable upon subsequent in-situ UHV annealing at 700 K. The stability of these, low- T amorphous Al₂O₃ films on Al{111} is in good agreement with the corresponding calculated critical thickness of $h_{\{\text{Al}_2\text{O}_3\}}^{\text{critical}} = 0.7 \pm 0.1$ nm up to which an amorphous Al₂O₃ film is thermodynamically preferred on the Al{111} substrate. At more elevated temperatures $T \geq 475$ K, an epitaxial crystalline γ (-like)-Al₂O₃ film develops on Al{111} instead, because the critical oxide-film thickness for the amorphous-to-crystalline transition has decreased (due to growth strain relaxation in the crystalline film) as a result of a change in oxide growth mode (from layer-by-layer to island-by-layer growth). Moreover, initial oxygen incorporation predominates over on-top oxygen chemisorption for $T \geq 475$ K, thereby facilitating nucleation of crystallization.

On **Al{100}** for $t \leq 6000$ s at $T \leq 400$ K, amorphous oxide films with thicknesses up to 0.6 ± 0.1 nm are formed, which are transformed into γ (-like)-Al₂O₃ upon in-situ UHV annealing at 700 K beyond a critical oxide-film thickness of about 0.45 ± 0.15 nm. The experimentally-determined critical thickness value for the amorphous-to-crystalline transition on Al{100} (i.e. 0.45 ± 0.15 nm) is somewhat lower than the corresponding calculated critical thickness of $h_{\{\text{Al}_2\text{O}_3\}}^{\text{critical}} = 0.8 \pm 0.1$ nm. For $T > 400$ K the initial amorphous oxide film transforms into a highly-defective, high-mismatch γ (-like)-Al₂O₃ film beyond a critical

thickness of about 0.2 ± 0.1 nm. The relatively low value of the critical oxide-film thickness for $T > 400$ K (as compared to the critical thickness value for $T \leq 400$ K) is due to a change in oxide growth mode (as for the Al{111} face).

On Al{110} for $t \leq 6000$ s at $T < 550$ K, amorphous oxide films with thicknesses up to 1.2 ± 0.1 nm are formed, which are stable upon subsequent in-situ UHV annealing at 700 K, in accordance with the relatively high value of the calculated critical oxide-film thickness on Al{110} of $h_{\text{Al}_2\text{O}_3}^{\text{critical}} = 4.0 \pm 0.5$ nm. For $T > 550$ K, an oxidation-induced reconstruction of the parent Al{110} surface is observed and then a full amorphous-to-crystalline transition appears kinetically hindered. The resulting {111}-faceted oxidized metal surface is thermodynamically preferred due to the relatively low energy of the Al{111}/am-Al₂O₃ interface (as compared to the Al{110}/am-Al₂O₃ interface).

Acknowledgements

The authors are grateful to Mrs. U. Eigenthaler for the FIB preparation of the TEM lamellae, Mr. R. Höschel for technical TEM support and to Dr. P. A. van Aken for TEM support and advice.

Appendix 5.A. Procedures for the AR-XPS quantification

5.A.1. Expressions for the PZL photoelectron intensities

The observed total PZL intensities (I_{AX_n}) of the photoelectrons ejected with a kinetic energy KE from the n^{th} subshell of core-level shell, X , of an element A distributed within a solid can be expressed by [5]:

$$I_{AX_n}(\alpha, \psi) = K \cdot \sigma_{AX_n} \cdot W_{AX_n}(\alpha, \psi) \cdot \int_{z=0}^{\infty} C_A(z) \cdot \exp \left[- \int_{z'=0}^z \frac{dz'}{\lambda_{AX_n}^{\text{eff}}(z', KE, \alpha, \psi) \cdot \cos \alpha} \right] dz, \quad (5.1)$$

where K is an instrumental factor; σ_{AX_n} is the total photoionization cross-sections for the concerned core level; $W_{AX_n}(\alpha, \psi)$ is an asymmetry factor describing the intrinsic asymmetry of the photoionization cross-section σ_{AX_n} ; α and ψ are the angles between the specimen surface normal and detected photoelectrons and between the incident X-rays and the detected photoelectrons, respectively; $C_A(z)$ is the molar density of A in the solid as function of depth z below the sample surface; $\lambda_{AX_n}^{\text{eff}}(z, KE, \alpha, \psi)$ is the effective attenuation length of the detected

photoelectrons traversing with kinetic energy KE through the solid as function of depth z below the sample surface.

The corresponding total *metallic* PZL intensity, $I_{Al,met}$, of the metallic Al 2p main peak, as resolved from a measured XPS spectrum recorded from the Al metal substrate covered with a thin Al_2O_3 film of uniform thickness, L , can then be expressed by [as follows from Eq. (5.1)]:

$$I_{Al,met}(\alpha, \psi) = K \cdot \sigma_{Al} \cdot W_{Al}(\alpha, \psi) \cdot C_{Al}^{sub} \cdot \lambda_{Al,met}^{sub}(\alpha, \psi) \cdot \cos \alpha \cdot \exp\left(-\frac{L}{\lambda_{Al,met}^{ovl}(\alpha, \psi) \cdot \cos \alpha}\right), \quad (5.2)$$

where C_{Al}^{sub} is the molar density of Al in the metal substrate; $\lambda_{Al,met}^{sub}(\alpha, \psi)$ and $\lambda_{Al,met}^{ovl}(\alpha, \psi)$ are the effective attenuation lengths of the concerned Al 2p photoelectrons originating from the metal substrate and traversing through the metal substrate and the oxide overlayer, respectively. The corresponding total *oxidic* PZL intensity, $I_{Al,ox}$, of the oxidic Al 2p main peak, as resolved from the same measured XPS spectrum recorded from the oxidized Al metal substrate is then given by:

$$I_{Al,ox}(\alpha, \psi) = K \cdot \sigma_{Al} \cdot W_{Al}(\alpha, \psi) \cdot C_{Al}^{ovl} \cdot \lambda_{Al,ox}^{ovl}(\alpha, \psi) \cdot \cos \alpha \cdot \left[1 - \exp\left(-\frac{L}{\lambda_{Al,ox}^{ovl}(\alpha, \psi) \cdot \cos \alpha}\right)\right], \quad (5.3a)$$

where C_{Al}^{ovl} is the molar density of Al cations in the oxide film and $\lambda_{Al,ox}^{ovl}(\alpha, \psi)$ is the effective attenuation length of the concerned Al 2p photoelectrons originating from and traversing through the oxide film. Analogously, the corresponding total *oxygen* PZL intensity, $I_{O,ox}$, of the O 1s main peak (as evaluated from the same XPS measurement of the oxidised metal) is given by:

$$I_{O,ox}(\alpha, \psi) = K \cdot \sigma_O \cdot W_O(\alpha, \psi) \cdot C_O^{ovl} \cdot \lambda_{O,ox}^{ovl}(\alpha, \psi) \cdot \cos \alpha \cdot \left[1 - \exp\left(-\frac{L}{\lambda_{O,ox}^{ovl}(\alpha, \psi) \cdot \cos \alpha}\right)\right], \quad (5.4)$$

where C_O^{ovl} is the molar density of O anions in the oxide film and $\lambda_{O,ox}^{ovl}(\alpha, \psi)$ is the effective attenuation length of the concerned O 1s photoelectrons originating from and traversing through the oxide film.

5.A.2. Calculation of oxide-film composition and thickness

The total *oxidic* PZL intensities of the 'film' and 'interface' oxidic Al 2p main peaks, as resolved from a single measured Al 2p spectrum of the oxidized Al metal substrate, can be expressed by

$$I_{\text{Al,ox}}(\alpha, \psi) = K \cdot \sigma_{\text{Al}} \cdot W_{\text{Al}}(\alpha, \psi) \cdot C_{\text{Al}}^{\text{ovl}} \cdot \lambda_{\text{Al,ox}}^{\text{ovl}}(\alpha, \psi) \cdot \cos \alpha \cdot \left[1 - \exp\left(-\frac{L^{\text{ox}}}{\lambda_{\text{Al,ox}}^{\text{ovl}}(\alpha, \psi) \cdot \cos \alpha}\right) \right] \quad (5.3b)$$

and

$$I_{\text{Al,int}}(\alpha, \psi) = K \cdot \sigma_{\text{Al}} \cdot W_{\text{Al}}(\alpha, \psi) \cdot C_{\text{Al}}^{\text{ovl}} \cdot \lambda_{\text{Al,ox}}^{\text{ovl}}(\alpha, \psi) \cdot \cos \alpha \times \left[1 - \exp\left(-\frac{L^{\text{int}}}{\lambda_{\text{Al,ox}}^{\text{ovl}}(\alpha, \psi) \cdot \cos \alpha}\right) \right] \times \exp\left(-\frac{L^{\text{ox}}}{\lambda_{\text{Al,ox}}^{\text{ovl}}(\alpha, \psi) \cdot \cos \alpha}\right), \quad (5.3c)$$

respectively, where L^{ox} and L^{int} denote the average layer thicknesses of the 'film' and 'interface' oxide component, respectively [and taken the same values of the cation molar density and the effective attenuation length in Eq. (5.3b) and (5.3c)]. The corresponding total *oxygen* PZL intensity, $I_{\text{O,ox}}(\alpha, \psi)$, of the O 1s main peak (as evaluated from the same XPS measurement of the oxidised metal) is given by Eq. (5.4) with $L = L^{\text{ox}} + L^{\text{int}}$.

Thus, employing Eqs. (5.2), (5.3b), (5.3c) and (5.4), a total number of six theoretical intensity ratios $(I_i/I_j)_{\text{calc}}$ with $(i \neq j)$ can be calculated for each angular detection range: i.e.

$$I_{\text{Al,ox}}^{\text{ox}}(\alpha, \psi)/I_{\text{Al,ox}}^{\text{int}}(\alpha, \psi), \quad I_{\text{Al,ox}}^{\text{ox}}(\alpha, \psi)/I_{\text{O,ox}}(\alpha, \psi), \quad I_{\text{Al,ox}}^{\text{ox}}(\alpha, \psi)/I_{\text{Al,met}}(\alpha, \psi), \quad I_{\text{Al,ox}}^{\text{int}}(\alpha, \psi)/I_{\text{O,ox}}(\alpha, \psi),$$

$$I_{\text{Al,ox}}^{\text{int}}(\alpha, \psi)/I_{\text{Al,met}}(\alpha, \psi) \quad \text{and} \quad I_{\text{O,ox}}(\alpha, \psi)/I_{\text{Al,met}}(\alpha, \psi).$$

Values for the EALs and asymmetry factors, as required in the calculations, were determined according to Refs. [5, 14] and using the physical constants for either *am*-Al₂O₃ or γ -Al₂O₃ (see Table 5.1 and discussion below). Further, as determined from the quantitative AR-XPS analyses of an α -Al₂O₃ reference sample (with $C_{\text{O}}^{\alpha\text{-Al}_2\text{O}_3}/C_{\text{Al}}^{\alpha\text{-Al}_2\text{O}_3} = 1.5$) in the present study, the value of $\sigma_{\text{O}}/\sigma_{\text{Al}} = 4.38$ (independent of the local chemical environment of the photo-ionized atom in the solid [5]).

Average values for the total thickness, $L = L^{\text{ox}} + L^{\text{int}}$, and the composition (expressed as the O:Al ratio, $C_{\text{O}}^{\text{ovl}}/C_{\text{Al}}^{\text{ovl}}$) of the grown oxide films were calculated by LLS fitting of the calculated intensity ratios, $(I_i/I_j)_{\text{calc}}$, to the corresponding experimental intensity ratios, $(I_i/I_j)_{\text{exp}}$, as resolved from the measured Al 2p and O 1s spectra of the oxidized Al metal for

each angular detection range (see Sec. 5.2). The LLS minimization was performed using the Nelder-Mead simplex method as implemented in Matlab [13]) and adopting L^{ox} and L^{int} in combination with *either* $C_{\text{Al}}^{\text{ovl}}$ or $C_{\text{O}}^{\text{ovl}}$ as fit parameters (see below and Fig. 5.9). Since only the O:Al ratio ($C_{\text{O}}^{\text{ovl}}/C_{\text{Al}}^{\text{ovl}}$) can be uniquely resolved (and not the independent values of $C_{\text{Al}}^{\text{ovl}}$ and $C_{\text{O}}^{\text{ovl}}$), L^{ox} , L^{int} and $C_{\text{O}}^{\text{ovl}}$ are introduced as fit parameters in a first iteration cycle (i.e. for $n = 1$, see Fig. 5.9), while fixing $C_{\text{Al}}^{\text{ovl}}$ at its corresponding value $C_{\text{Al}}^{\text{ref-ox}}$ for the chosen oxide reference state (either *am*-Al₂O₃ or γ -Al₂O₃). If the optimized value of $C_{\text{O}}^{\text{ovl}}$ after the first iteration cycle is larger than the corresponding reference value $C_{\text{O}}^{\text{ref-ox}}$ (thereby implying a larger anion molar density in the oxide film than in the oxide reference), the value of $C_{\text{O}}^{\text{ovl}}$ is fixed to its corresponding reference value ($C_{\text{O}}^{\text{ref-ox}}$) and instead $C_{\text{Al}}^{\text{ovl}}$ is introduced as a fit parameter in a second iteration cycle (i.e. $n = 2$, see Fig. 5.9). The iterative calculation procedure according to Fig. 5.9 was performed twice employing either *am*-Al₂O₃ or γ -Al₂O₃ as the oxide reference state. The thus obtained average thickness and composition values, as calculated for *am*-Al₂O₃ as the reference state, have been used in Fig. 5.4 and Secs. 5.4 and 5.5. The errors bars were deduced from the differences between the thickness and composition values, as calculated for either *am*-Al₂O₃ or γ -Al₂O₃ as the reference oxide state, as well as for the different angular detection ranges employed (Sec. 5.2).

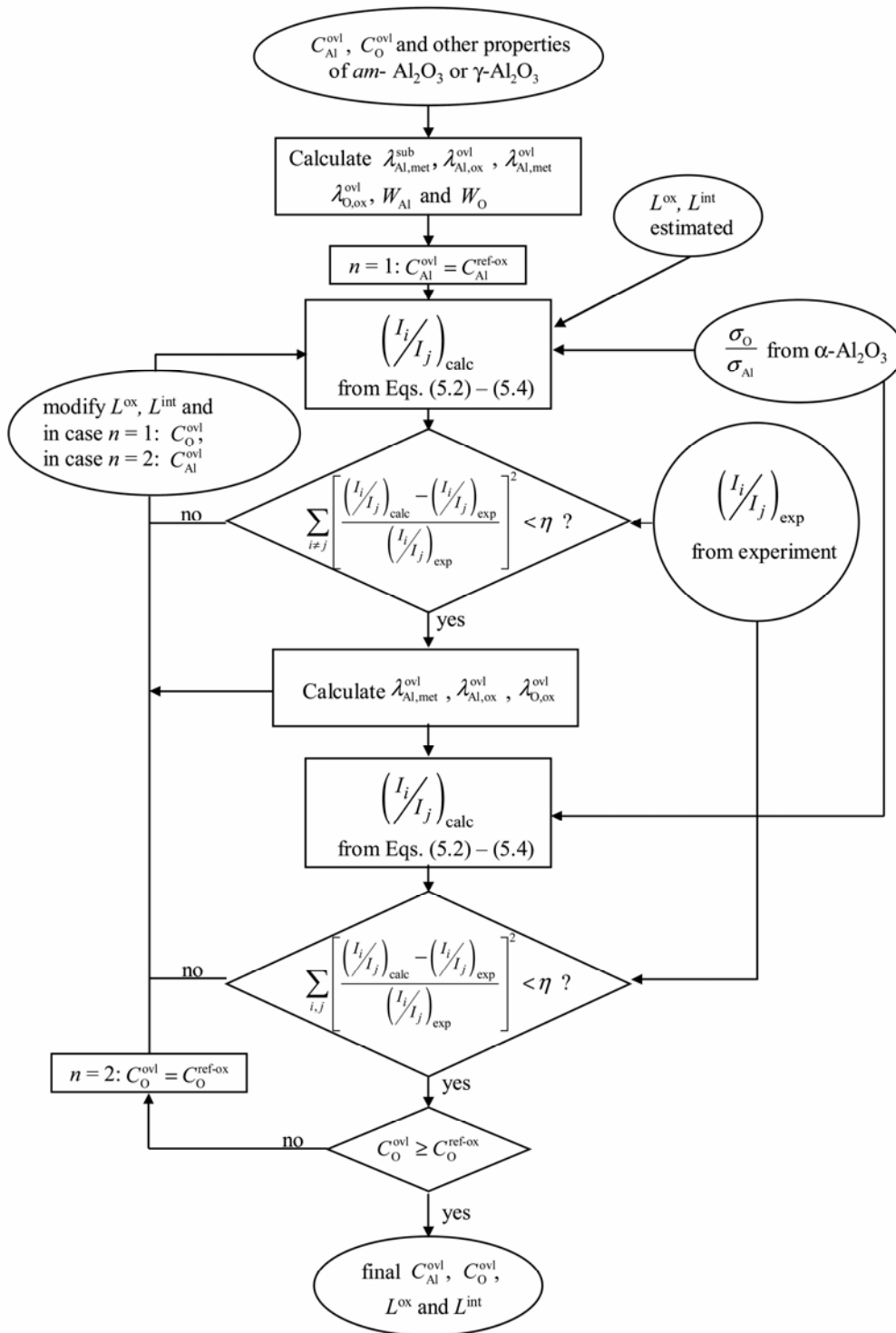


Figure 5.9. Schematic flow diagram of the iterative calculation procedure employed to calculate the oxide-film thickness ($L = L^{ox} + L^{int}$) and the molar densities of Al (C_{Al}^{ovl}) and O (C_O^{ovl}) in the grown oxide films. The annotations 'sub', 'ovl' and 'ref-ox' refer to the metal substrate, the oxide overlayer and the employed oxide reference (i.e. either $am\text{-Al}_2\text{O}_3$ or $\gamma\text{-Al}_2\text{O}_3$), respectively. The annotations 'exp' and 'calc' refer to experimental and calculated intensity ratios with $(i, j) = (\text{Al,met} ; \text{Al,ox} ; \text{Al,int} ; \text{O,ox})$, respectively. See Sec. 5.A.2 for details.

Appendix 5.B. Calculation of effective depths of resolved species

The effective depths below the specimen surface for the various identified oxidic Al 2p and O 1s species within the oxide film and in the subsurface region of the metal substrate (see Fig. 5.3) can be resolved by employing their corresponding PZL intensities as resolved for a set of near-normal and grazing detection angles in the range of $\alpha_1 = 30\text{-}46^\circ$ and $\alpha_2 = 60\text{-}76^\circ$, respectively [9].

The effective depth, z^{eff} , of a species A (here: Al or O) in the oxide film can be expressed by [see Ref. [9] and employing Eq. (5.1)]:

$$z_{A,\text{ox}}^{\text{eff}} = \ln \left(\frac{I_{A,\text{ox}}^\infty(\alpha_1, \psi_1) \cdot W_A(\alpha_2, \psi_2)}{I_{A,\text{ox}}^\infty(\alpha_2, \psi_2) \cdot W_A(\alpha_1, \psi_1)} \right) \times \left[\frac{1}{\lambda_{A,\text{ox}}^{\text{ovl}}(\alpha_2, \psi_2) \cdot \cos(\alpha_2, \psi_2)} - \frac{1}{\lambda_{A,\text{ox}}^{\text{ovl}}(\alpha_1, \psi_1) \cdot \cos(\alpha_1, \psi_1)} \right]^{-1}. \quad (5.4a)$$

Similarly, the effective depth (z^{eff}) of a species A (here: Al) in the subsurface region of the parent metal substrate covered with a thin oxide film of uniform thickness, L , can be estimated from [see Ref. [9] and Eq. (5.1)]:

$$z_{A,\text{met}}^{\text{eff}} = \ln \left(\frac{I_{A,\text{met}}^\infty(\alpha_1, \psi_1) \cdot W_A(\alpha_2, \psi_2)}{I_{A,\text{met}}^\infty(\alpha_2, \psi_2) \cdot W_A(\alpha_1, \psi_1)} \right) \times \left[\frac{1}{\lambda_{A,\text{met}}^{\text{sub}}(\alpha_2, \psi_2) \cos(\alpha_2, \psi_2)} - \frac{1}{\lambda_{A,\text{met}}^{\text{sub}}(\alpha_1, \psi_1) \cos(\alpha_1, \psi_1)} \right]^{-1} \times L \cdot \left(1 + \frac{\lambda_{A,\text{met}}^{\text{sub}}(\alpha_1, \psi_1) \cdot \lambda_{A,\text{met}}^{\text{sub}}(\alpha_2, \psi_2)}{\lambda_{A,\text{met}}^{\text{ovl}}(\alpha_1, \psi_1) \cdot \lambda_{A,\text{met}}^{\text{ovl}}(\alpha_2, \psi_2)} \times \frac{\lambda_{A,\text{met}}^{\text{ovl}}(\alpha_1, \psi_1) \cdot \cos(\alpha_1, \psi_1) - \lambda_{A,\text{met}}^{\text{ovl}}(\alpha_2, \psi_2) \cdot \cos(\alpha_2, \psi_2)}{\lambda_{A,\text{met}}^{\text{sub}}(\alpha_2, \psi_2) \cdot \cos(\alpha_2, \psi_2) - \lambda_{A,\text{met}}^{\text{sub}}(\alpha_1, \psi_1) \cdot \cos(\alpha_1, \psi_1)} \right). \quad (5.4b)$$

References

- [1] L. P. H. Jeurgens, W. G. Sloof, F. D. Tichelaar and E. J. Mittemeijer, Phys. Rev. B **62** (2000) 4707.
- [2] F. Reichel, L. P. H. Jeurgens and E. J. Mittemeijer, Phys. Rev. B **74** (2006) 144103.
- [3] K. R. Lawless, Rep. Prog. Phys. **37** (1974) 231.

- [4] L. P. H. Jeurgens, W. G. Sloof, F. D. Tichelaar and E. J. Mittemeijer, *J. Appl. Phys.* **92** (2002) 1649.
- [5] M. S. Vinodh and L. P. H. Jeurgens, *Surf. Interface Anal.* **36** (2004) 1629.
- [6] F. Phillipp, R. Höschen, M. Osaki, G. Möbus and M. Rühle, *Ultramicroscopy* **56** (1994) 1.
- [7] Powder Diffraction Files, Cards 00-004-0787 (Al) and 00-050-0741 (γ -Al₂O₃) from JCPDS-International Centre for Diffraction Data (2007).
- [8] L. P. H. Jeurgens, W. G. Sloof, C. G. Borsboom, F. D. Tichelaar and E. J. Mittemeijer, *Appl. Surf. Sci.* **161** (2000) 139.
- [9] L. P. H. Jeurgens, M. S. Vinodh and E. J. Mittemeijer, *Appl. Surf. Sci.* **253** (2006) 627.
- [10] S. Tougaard, *Solid State Commun.* **61** (1987) 547.
- [11] S. Tougaard, *Surf. Interface Anal.* **25** (1997) 137.
- [12] S. Doniach and M. Šunjić, *J. Phys. C* **3** (1970) 285.
- [13] Matlab version 6.1.0.450, Release 12.1: The MathWorks Inc, Natick; 2001.
- [14] A. Jablonski, C.J. Powell, *Surf. Sci. Rep.* **47** (2002) 33.
- [15] W. J. Bernard and J. W. Cook, *J. Electrochem. Soc.* **106** (1959) 643.
- [16] S. Miyazaki, *J. Vac. Sci. Technol. B* **19** (2001) 2212.
- [17] A. M. Goodman, *J. Appl. Phys.* **41** (1970) 2176.
- [18] M. Aguilar-Frutis, M. Garcia and C. Falcony, *Appl. Phys. Lett.* **72** (1998) 1700.
- [19] R. F. Reilman, A. Msezane and S. T. Manson, *J. Electron Spectrosc. Relat. Phenom.* **8** (1976) 389.
- [20] F. Reichel, L. P. H. Jeurgens, G. Richter, P. A. van Aken and E. J. Mittemeijer, *Acta Mater.* **55** (2007) 6027.
- [21] L. P. H. Jeurgens, W. G. Sloof, F. D. Tichelaar and E. J. Mittemeijer, *Thin Solid Films* **418** (2002) 89.
- [22] H. D. Castanjen, *Mater. Sci. Forum* **248-249** (1997) 459.
- [23] S. M. Bedair and H. P. Smith, Jr., *J. Appl. Phys.* **42** (1971) 3616.
- [24] C. W. B. Martinson and S. A. Flodström, *Surf. Sci.* **80** (1979) 306.
- [25] H. Momida, T. Hamada, Y. Takagi, T. Yamamoto, T. Uda and T. Ohno, *Phys. Rev. B* **73** (2006) 054108.

Chapter 6

The effect of substrate orientation on the kinetics of ultra-thin oxide-film growth on Al single-crystals

F. Reichel, L. P. H. Jeurgens and E. J. Mittemeijer

Abstract

The kinetics of ultra-thin (< 1.5 nm) oxide-film growth on bare Al{111}, Al{100} and Al{110} substrates in the temperature range of 350 – 600 K at $p_{\text{O}_2} = 1 \times 10^{-4}$ Pa was investigated by real-time in-situ spectroscopic ellipsometry. It follows that the oxide-film growth kinetics depends strongly on the parent metal-substrate orientation. On Al{100} and Al{110}, the growth kinetics can be subdivided into an initial, very fast oxidation stage and a subsequent very slow oxidation stage, which is characterized by the occurrence of a near-limiting oxide-film thickness that increases with increasing temperature. On Al{111}, the initial, very fast growth rate decreases more gradually with increasing oxidation time and an unexpected *decrease* of oxide-film thickness, for an oxidation time of 6000 s with *increasing* temperature up to 475 K is observed. The rate-limiting step(s) and mechanism(s) of the oxidation process were identified by a quantitative model description of the oxide-film growth kinetics on the basis of coupled currents of electrons (by both tunnelling and thermionic emission) and cations under influence of a surface-charge field. It followed that the unexpected decrease of the oxide-film thickness with increasing temperature on Al{111} is due to a slow increase of the (relatively low) activation-energy barrier for cation transport in combination with a constant kinetic potential due to the surface-charge field within the amorphous oxide-film regime (up to $T \leq 450$ K). For Al{100} and Al{110}, the energy barrier for cation transport, as well as the kinetic potential, increase with increasing temperature due to, as compared to Al{111}, a more gradual amorphous-to-crystalline transition, which already starts at lower temperatures $T < 400$ K.

6.1. Introduction

Upon oxidation of a bare metal substrate the initial formation of a closed oxide film covering the entire metal surface involves a series of concurrent steps, such as transport and subsequent physisorption of oxygen molecules to the metal surface, (dissociative) chemisorption, oxide nucleation and growth. Immediately after the oxide film covers the entire substrate surface, further oxide-film growth is decelerated, because the oxide film constitutes a diffusion barrier between the two reactants (i.e. parent metal substrate and oxygen gas). Continued oxide-film growth can only proceed if (charged) reactant species (as, possibly, cations, anions, electrons, holes and vacancies) are transported through the developing oxide film towards the reacting oxide/oxygen and/or metal/oxide interfaces [1-11].

To describe the observed oxidation rate as function of the oxidation conditions, the *rate-determining* steps of the oxidation process have to be known. If the intrinsic transport rate of one of the (charged) reactant species across the developing oxide film is much larger than those of all other reactant species, an electrostatic field develops across the growing oxide film, such that the transport of the less mobile (i.e., *rate-limiting*) charge species is enhanced. The resulting oxide-film growth under influence of both chemical (related to the concentration) and electrostatic potential (as indicated above) gradients is the basis of various models proposed to describe the initial oxide-film growth kinetics (up to thicknesses of, say, smaller than 10 nm) on bare metal and alloy surfaces at low temperatures (say, below 600 K) [1-4].

In the coupled-currents approach of Fromhold and Cook [3, 4], which provides a comprehensive treatment of the low temperature oxidation, at least one electronic current (by quantum-mechanical tunnelling and/or thermionic emission) and one ionic current (diffusion of cations and/or anions) are considered. These currents of charged species are coupled by the constraint that no net electric charge is transported through the film (so-called coupled-currents constraint). The principle of the coupled-currents model has been used successfully to describe the initial, low-temperature oxidation of bare Fe [8-10] and bare Zr [11] substrates. However, up to the present date, most other kinetic studies on the initial oxidation of bare metals surfaces did not identify the governing mechanism(s) and rate-limiting (or rate-determining) step(s) of the oxidation process as function of e.g. temperature, film-thickness regime and, in particular, the metal-substrate orientation. This is mostly due to lack of reliable quantitative experimental data on the initial oxide-film growth kinetics as function of the

oxidation conditions, whereas in the successful work [8-11] such data could be obtained in real-time by application of in-situ spectroscopic ellipsometry under UHV conditions [12, 13].

The effect of the microstructural evolution of the thickening oxide-film on its growth kinetics is generally unknown. For example, as demonstrated in the present work, the transformation of an initial amorphous oxide film into a crystalline oxide film for thickening oxide films grown at higher oxidation temperatures [14, 15] can influence the governing energy barriers for ion and/or electron transport across the oxide film, thereby causing, at first sight unexpected, changes of the oxide-film growth kinetics. The present study addresses, in particular, the effect of the metal-substrate orientation on the kinetics and mechanisms of ultra-thin (< 1.5 nm) oxide-film growth on bare Al single-crystalline surfaces at low temperatures.

To this end, bare single-crystalline Al{111}, Al{100} and Al{110} substrates were oxidized up to 6000 s by exposure to pure oxygen gas at a partial oxygen pressure of $p_{\text{O}_2} = 1 \times 10^{-4}$ Pa in the temperature range of $T = 350 - 600$ K. The corresponding oxide-film growth kinetics as function of the oxidation conditions have been established experimentally by real-time in-situ spectroscopic ellipsometry (RISE). The microstructural evolution of the developing oxide films, as investigated by a combined experimental approach of Low Energy Electron Diffraction (LEED), angle-resolved X-ray Photoelectron Spectroscopy (AR-XPS) and High-Resolution Transmission Electron Microscopy (HR-TEM), have been addressed in Chapters 4 and 5 (see Ref. [14]).

Thin alumina films combine several useful properties, including high dielectric strength, high resistivity, low refractive index, radiation resistance, high transparency, high hardness, wear resistance, thermal stability and chemical inertness. As such, they find numerous applications in optics, microelectronics, wear and corrosion resistant coatings, heat sinks or as sensor materials [16, 17]. Consequently, the initial low-temperature oxidation of *bare* (i.e. without a native oxide prior to oxidation) single-crystalline Al substrates has been investigated for various oxidation conditions (mostly at different T and p_{O_2}) and using a wide range of different surface analysis techniques (e.g. Refs. [18-29]). Most of these experimental [18-23] and theoretical (e.g. by first principle simulations; cf. Ref. [24]) studies have mainly focussed on the concurrent processes of physisorption, (dissociative) chemisorption and oxygen incorporation during the very initial stages of interaction of oxygen and the bare metal. Only a few experimental [25-28] and theoretical studies [29] were devoted to the successive stages of 3-dimensional oxide nucleation and continued oxide-film growth as

function of the oxidation conditions for the initial oxidation of *bare Al single-crystalline* substrates, but without considering the effects of substrate orientation and the developing oxide-film microstructure.

6.2. Experiment

Disc-shaped Al{111}, Al{100} and Al{110} single-crystals (10 mm diameter, 1 mm thick, purity better than 5N, orientation alignment better than 0.5°) were supplied and their surfaces polished by 'Surface Preparation Laboratory' (Zaandam, The Netherlands). Prior to each oxidation experiment, the Al single-crystals were cleaned and their crystal order in the surface region restored by a cyclic treatment of sputter-cleaning with 1 keV Ar⁺ ions and subsequent annealing in UHV at 723 K. The thus obtained *bare* single-crystal surfaces were oxidized in an ultra high vacuum (UHV) reaction chamber (base pressure $< 3 \times 10^{-8}$ Pa) in the temperature (T) range of 350 – 600 K (up to 640 K for Al{110}) by exposure for 6000 s to pure oxygen gas at a partial oxygen pressure (p_{O_2}) of 1×10^{-4} Pa. Additional details on sample preparation, cleaning and oxidation, have been given in Chapter 4 of this thesis [14].

During the oxidation experiments real-time in-situ spectroscopic ellipsometry (RISE) measurements were performed, using a J. A. Woollam M-2000L spectroscopic ellipsometer equipped with a Xe light source and mounted directly to the flanges of the UHV reaction chamber, so that the angles of incidence and reflection were 70° relative to the sample surface normal. The ellipsometric phase-shift and amplitude-ratio dependent parameters, $\Delta(\lambda)$ and $\Psi(\lambda)$, respectively, were recorded from the bare and oxidizing Al substrate in the wavelength (λ) range between 350 nm and 800 nm as function of the oxidation time (t), (for details see [12, 13, 30]).

6.3. Data evaluation

To obtain the oxide-film growth curves from the measured changes in the spectra of $\Delta(\lambda)$ and $\Psi(\lambda)$ as function of oxidation time (Sec. 6.2), a model description of $\Delta(\lambda, t)$ and $\Psi(\lambda, t)$ for the evolving substrate/film system has to be fitted to the measured RISE data. To this end, a model description was adopted, which considers the overgrowth of an Al₂O₃ film of uniform thickness, $L^{\text{ox}}(t)$, on top of the bare Al metal substrate in combination with a very thin (< 1 oxide monolayer (ML); 1 ML ~ 0.2 nm), non-stoichiometric Al-oxide layer of uniform thickness, $L^{\text{int}}(t)$, at the interface between the parent metal substrate and the thickening Al₂O₃ film (as described below).

The optical constants of the *bare* Al{111}, Al{100} and Al{110} substrates were in-situ measured prior to each of the oxidations by RISE analysis at the corresponding oxidation temperature in UHV (pressure $< 3 \times 10^{-8}$ mbar). Since Al₂O₃ is transparent over the considered wavelength range ($\lambda = 350 - 800$ nm), the extinction coefficient k of the thickening Al₂O₃ film $k(\lambda) \equiv 0$. The decrease of the refractive index, $n(\lambda)$, of the developing Al₂O₃ film with increasing wavelength, λ , can be expressed by a Cauchy-type function, according to

$$n(\lambda) = A^{\text{Cauchy}} + \frac{B^{\text{Cauchy}}}{\lambda^2} + \frac{C^{\text{Cauchy}}}{\lambda^4}, \quad (6.1)$$

with A^{Cauchy} , B^{Cauchy} and C^{Cauchy} as the Cauchy parameters [31]. The refractive index n is known to decrease in the order $\alpha\text{-Al}_2\text{O}_3 > \gamma\text{-Al}_2\text{O}_3 > am\text{-Al}_2\text{O}_3$ (mainly due to the associated decrease in density [16]). The $n(\lambda)$ -values for $am\text{-Al}_2\text{O}_3$ and $\gamma\text{-Al}_2\text{O}_3$ are about 97% and 94% of the corresponding $n(\lambda)$ -values of $\alpha\text{-Al}_2\text{O}_3$ with $A^{\text{Cauchy}} = 1.75$, $B^{\text{Cauchy}} = 7.15 \cdot 10^{-3} \mu\text{m}^2$ and $C^{\text{Cauchy}} = -2.06 \cdot 10^{-4} \mu\text{m}^4$ [32], respectively [16, 33, 34]. The Cauchy parameters B^{Cauchy} and C^{Cauchy} of the developing Al₂O₃ film, which describe the wavelength dependence of $n(\lambda)$, were taken equal to those of $\alpha\text{-Al}_2\text{O}_3$. The Cauchy parameter A^{Cauchy} of the developing Al₂O₃ film was determined separately for each oxidation experiment by fitting (see below).

To describe the absorption behaviour of the ultra-thin (< 1.5 nm) oxide overgrowths due to the presence of Al cations with a lower valence state (as compared to Al³⁺) in the oxide *at* the metal/oxide interface (as a result of the deficient coordination of Al cations by nearest-neighbour O anions *at* the metal/oxide interface; as evidenced by AR-XPS in the present project; cf. Chapter 5), a very thin (i.e. ≤ 1 ML; see Sec. 6.5.3) *non-stoichiometric* Al-oxide layer was adopted in-between the parent Al substrate and the thickening (stoichiometric) Al₂O₃ layer [as required for an accurate model description of $\Delta(\lambda, t)$ and, in particular, $\Psi(\lambda, t)$]. The optical constants of this intermediate layer of uniform thickness, $L^{\text{int}}(t) \leq 1$ ML (~ 0.2 nm), were estimated using an Effective Medium Approximation (EMA) based on the Maxwell-Garnett formulation and defining the stoichiometric Al₂O₃ top layer and the parent Al metal substrate as the matrix and the inclusion, respectively (see [12, 13, 30, 31, 35]; as calculated using the WVASE32 software package [31]). The EMA-fraction of metal inclusion is further denoted by f^{EMA} (with $0 \leq f^{\text{EMA}} \leq 1$). Only if the fitted value of $L^{\text{int}}(t)$ exceeded about $\frac{1}{2}$ ML (as only observed for the oxide overgrowth on Al{110} at elevated T ; see Sec. 6.5.3), an improved model description of $\Delta(\lambda)$ and $\Psi(\lambda)$ as function of t was achieved by linearly grading the EMA-fraction of the metal inclusion (f^{EMA}) from a value of $0 < f^{\text{EMA}} <$

1 at the bottom of the EMA layer (corresponding with the position of the metal/oxide interface) to a value of $f^{\text{EMA}} = 0$ at the top of the EMA layer (corresponding to the interface with the stoichiometric Al_2O_3 part of the oxide layer).

Since the oxide films grown in this study are very thin (< 1.5 nm), a strong correlation exists between the fit parameters $L^{\text{ox}}(t)$, $L^{\text{int}}(t)$, A^{Cauchy} and f^{EMA} in the fitting of $\Delta(\lambda)$ and $\Psi(\lambda)$ as function of t (see below) [31, 35]. Therefore, first individually optimized values of A^{Cauchy} and f^{EMA} were determined at the end of each oxide growth curve (i.e. after $t = 6000$ s) by fitting the calculated to the corresponding measured spectra of $\Delta(\lambda)$ and $\Psi(\lambda)$ for $t = 6000$ s, while fixing the total oxide-film thickness $L(t) = L^{\text{ox}}(t) + L^{\text{int}}(t)$ to the corresponding thickness value (at $t = 6000$ s) as determined by angle-resolved X-ray photoelectron spectroscopy (see Chapter 5) and adopting only A^{Cauchy} and f^{EMA} as fit parameters. The fitting was performed applying the WVASE32 software package [31] and by minimization of the mean-squared differences between the calculated and measured data (for details, see Refs. [13, 31]). As a result, it was found that the value of A^{Cauchy} for the stoichiometric Al_2O_3 top layer decreases with increasing T from $A^{\text{Cauchy}} = 1.66$ at 350 K (in agreement with corresponding literature data for thin *am*- Al_2O_3 and γ - Al_2O_3 films at room temperature [16, 33, 34]) to $A^{\text{Cauchy}} = 1.45$ at 600 K (no corresponding literature data exist for $T > 350$ K). Further, it was found that the value of f^{EMA} is about 0.84, 0.77 and 0.85 for oxide growth on $\text{Al}\{111\}$, $\text{Al}\{100\}$ and $\text{Al}\{110\}$, respectively (independent of T ; note that for $\text{Al}\{110\}$ the here given f^{EMA} value pertains to the EMA fraction at the bottom of the graded, non-stoichiometric part of the oxide layer; see above).

Finally, the oxide-film growth curves, $L(t) = L^{\text{ox}}(t) + L^{\text{int}}(t)$, were obtained by fitting the calculated data of $\Delta(\lambda)$ and $\Psi(\lambda)$ as function of t to the corresponding measured data and with the thicknesses of the stoichiometric Al_2O_3 top layer (L^{ox}) and the intermediate suboxide layer ($L^{\text{int}} < 0.2$ nm) as (time-dependent) fit parameters, adopting values for A^{Cauchy} (as determined for each growth curve; see above) and f^{EMA} (as determined for each metal-substrate orientation; see above).

6.4. Model description of the oxide-film growth kinetics

6.4.1. Theoretical background

After formation of a closed oxide film (i.e., at least 1 ML) on the bare Al metal surface, continued oxide-film growth can only proceed if the (charged) reactant species (*here*: O and Al ions and their vacancies, as well as electrons and electron holes) are transported through the developing oxide film towards the reacting metal/oxide and/or oxide/oxygen interfaces. At elevated temperatures (say, $T > 600$ K; cf. Refs. [8-11]), the thermal energies of the reacting species are sufficient to enable their transport through the thickening oxide film under influence of the electrochemical potential (i.e. concentration) gradients [5, 6]. However, at the relatively low oxidation temperatures considered here (i.e. $T \leq 600$ K), an additional driving force is required to enable further oxide-film growth beyond the formation of a closed oxide film.

As first postulated by Mott and Cabrera [1, 2], continued oxide-film growth on bare metal and alloy surfaces at low temperatures is realized by the diffusion of ions and electrons through the developing oxide film under influence of a surface-charge field setup by negatively-charged oxygen species adsorbed at the oxide surface. Then, adopting the so called coupled-currents constraint by Fromhold and Cook [3, 4], the corresponding net fluxes of ions and electrons (denoted by J_{ion} and J_e , respectively) are coupled by the constraint that no net electric charge is transported through the oxide film and no space charge is built-up in the developing oxide film [3, 4], i.e.

$$\sum_i e \cdot Z_i \cdot J_i = 0, \quad (6.2)$$

where e , Z_i and J_i denote the elementary charge, the effective charge in units of the elementary charge and the corresponding net flux of the i^{th} charged species, respectively.

For sufficiently thin oxide films, forward and reverse electron transport through the developing oxide film (i.e. from the Fermi level of the parent metal substrate to the electron acceptor levels of adsorbed oxygen species adsorbed at the oxide surface [5] and reverse) can take place by (i) quantum-mechanical tunnelling through the oxide band gap and/or (ii) by

thermionic (Schottky¹) emission of electrons from the Fermi level of the parent metal substrate into the empty conduction band of the oxide (cf. Refs. [5, 11]). The *net* fluxes by electron tunnelling and thermionic emission are further denoted by J_e^{tun} and J_e^{therm} , respectively. Due to the coupled (net) ion and electron fluxes, an electrostatic or so-called kinetic potential, V_k , will be established between the parent metal substrate and the chemisorbed oxygen species at the oxide-film surface, resulting in an uniform surface-charge field with strength E_k according to

$$E_k = -\frac{V_k}{L(t)}, \quad (6.3)$$

where $L(t) = L^{\text{ox}}(t) + L^{\text{int}}(t)$ is the total oxide-film thickness at time t . The surface-charge field will be directed such to enhance the rate-limiting transport of the intrinsically-slower-diffusing charged species (and to retard the intrinsically-much-faster-diffusing charged species); the relatively small unbalance between the forward and reverse currents of the intrinsically-much-faster-diffusing reactant species then provides the net current to compensate the net current due to the relatively slower diffusing reactant species.

If forward and reverse electron transport occurs at a much faster rate than the intrinsic ion transport rate, the value of the kinetic potential, V_k , approaches that of the Mott potential, V_M , according to

$$V_M = e^{-1}(\chi_0 - \chi_L), \quad (6.4)$$

where the metal/oxide work-function, χ_0 , is defined as the electron energy barrier between the Fermi level in the metal and the bottom of the conduction band in the oxide; the oxide/oxygen work-function, χ_L , is defined as the electron energy barrier between the empty

¹ Adjacent to the metal/oxide interface in the oxide film, the height of the electron energy barrier for electron transport through the oxide film (i.e. the potential energy of an electron in the oxide) is reduced due to the attractive force between the electron in the oxide and its image charge in the metal [5]. Similarly, adjacent to the oxide/oxygen interface in the oxide film, the height of the electron energy barrier for electron transport through the oxide film is reduced due to the force between the electron and the induced electronic dipole moment at the oxide surface in the adsorbed oxygen species [5]. Hence, reduction of the height of the electron energy barrier near the metal/oxide and oxide/oxygen interfaces is realized and thus higher forward and reverse fluxes due to thermionic emission occur for the very thin (< 1.5 nm) Al₂O₃ films studied here. Thermionic emission over such a reduced electron energy barrier is generally referred to as Schottky emission [5].

oxygen acceptor levels of oxygen atoms or molecules adsorbed at the oxide surface and the bottom of the conduction band in the oxide (see Fig. 1 in Ref. [11]).

On the other hand, if the intrinsic ion transport rate is much faster than the intrinsic electron transport rate, the value of the kinetic potential, V_k , approaches that of the so-called diffusion potential V_d , given by

$$V_d = \frac{k_B T}{e \cdot Z_i} \cdot \ln \left[\frac{C_i^{\text{defect}}(z=0)}{C_i^{\text{defect}}(z=L(t))} \right], \quad (6.5)$$

where k_B is the Boltzmann constant and $C_i^{\text{defect}}(z=0)$ and $C_i^{\text{defect}}(z=L(t))$ denote the defect concentrations of the diffusing i^{th} ionic species at the metal/oxide interface ($z=0$) and at the oxide/oxygen interface ($z=L(t)$), respectively.

6.4.2. Application to oxide-film growth on Al

For the initial oxide-film growth on bare Al metal substrates at low temperatures ($T \leq 600$ K), the metal cations are generally considered to be mobile and the oxygen anions to be immobile [2, 25]. Only for prolonged oxidation at higher temperatures ($T > 600$ K), the inward growth of large γ -Al₂O₃ crystallites into the parent metal substrate by inward diffusion of oxygen anions along oxide grain boundaries has been observed [36]. The oxide films grown in this study on Al{111} and Al{110} at $T \leq 600$ K are, dependent on thickness and temperature, either amorphous or single-crystalline² (see Chapters 4 and 5) and then inward oxygen diffusion along oxide-grain boundaries can be neglected. Against the above background, in this work the oxidation of the bare Al{111}, Al{100} and Al{110} substrates in the temperature range of 350 – 600 K has been modelled by adopting a coupled-currents description for transport of Al³⁺ cations and electrons (by both tunnelling and thermionic emission) through a surface-charge field (see Sec. 6.4.1).

The calculation of the theoretical oxide-film growth curves, comprising the solution of a differential equation [3-5, 11], was performed using a variable order Adams-Bashforth-Moulton multistep solver implemented in Matlab ('ode113' solver [37]). The expressions used to calculate the coupled fluxes of $J_{\text{Al}^{3+}}$ of J_e^{tun} and J_e^{therm} as function of $L(t)$ and V_k have been given in Refs. [5, 10, 11]. Since only a single *rate-limiting* energy barrier for cation transport

² The thicker crystalline oxide films grown on Al{100} at $T > 450$ K possess a two-domain γ -like-Al₂O₃ structure (Chapter 4).

(further denoted by W) is considered in the calculation of $J_{\text{Al}^{3+}}$ [5, 10, 11], the model does not distinguish if the rate-limiting barrier for cation transport is *at* the metal/oxide interface [i.e. $W^{\text{metal} \rightarrow \text{ox}}$ corresponding to the transport of cations from potential minima at the parent metal surface across the metal/oxide interface *into* potential minima (i.e. interstices) of the O anion arrangement of the oxide] or *within* the oxide film [i.e. W^{ox} corresponding to the transport of cations between adjacent potential minima of the O anion arrangement of the oxide]. The value of V_k at a given oxide-film thickness, $L(t)$, is determined by solving the differential equation (see above) by imposing the coupled-currents constraint [see Eq. (6.2)] to the calculated currents of $J_{\text{Al}^{3+}}$ of J_e^{tun} and J_e^{therm} . Fitting of the calculated to the experimental growth curves (as obtained by RISE; see Sec. 6.3), while varying one or more parameters (see below), was performed using the Nelder-Mead simplex method as implemented in Matlab [37] by minimizing the sum of squared differences between the calculated and experimental growth curves. The very initial part of the experimental oxide growth curves with $L(t) < 0.35$ nm (i.e. less than 2 oxide MLs) was excluded in the fitting, because a closed oxide film covering the entire metal surface may not have formed at this stage and interface reactions (instead of transport of reactant species across the oxide film) may be rate-limiting for the oxidation [6, 11].

For the modelling of the oxide-film growth kinetics on the basis of the coupled-currents approach presented in Sec. 6.4.1, the rate-limiting energy barrier for cation transport (W), as well as the metal/oxide (χ_0) and oxide/oxygen (χ_L) work-functions are the most sensitive fit parameters [5, 8, 11]. In addition, for the ultra-thin (< 1.5 nm) oxide films grown in this study (Sec. 6.5.3), the calculated net electron flux due to both tunnelling and Schottky emission (see footnote 1; Sec. 6.4.1) is only sensitive to the work-function difference, $\Delta\chi = \chi_0 - \chi_L$, instead of to the individual values of χ_0 and χ_L [8, 11]. Therefore, only W and χ_L were taken as fit parameters in the fitting of the calculated to the experimental growth curves; the value of χ_0 was fixed at a constant value of 1.6 eV (according to Ref. [38]; see Table 6.1). A systematic parameter study performed for the experimental growth curves analysed here (as determined by RISE; see Sec. 6.5.3) showed, indeed, that taking χ_0 (and not χ_L) as fixed is an arbitrary choice: identical calculated growth curves and values of W and the work-function difference, $\Delta\chi = \chi_0 - \chi_L$, were obtained by assigning a constant value to χ_L (and taking χ_0 as fit

parameter). Values of other parameters, which were fixed during the calculation, have been gathered in Table 6.1.

Table 6.1. Values for physical and chemical constants used in the numerical computations.

name	symbol	value	unit	reference
ionic jump distance	$2a$	0.22	nm	[39]
ionic jump frequency	$\nu_{\text{Al}^{3+}}$	10^{12}	s^{-1}	[3, 4]
electron jump frequency	ν_e	10^{14}	s^{-1}	[3, 4]
effective ion charge	$Z_{\text{Al}^{3+}}$	3		
cation defect concentration at metal/oxide interface	$C_{\text{Al}^{3+}}^{\text{defect}}(z=0)$	10^{-3}	nm^{-3}	[3, 4]
cation defect concentration at oxide/oxygen interface	$C_{\text{Al}^{3+}}^{\text{defect}}(z=L(t))$	10^{-6}	nm^{-3}	[3, 4]
relative dielectric constant of oxide	ϵ_r	3.4		[40]
product of oxygen polarizability and oxygen surface concentration	$\gamma \cdot \sigma$	10^{-20}	$\text{C}^2 \text{J}^{-1}$	[3, 4]
oxide volume per cation	∂V	0.0233	nm^3	[39]
metal/oxide work-function	χ_0	1.6	eV	[38]
relative effective electron mass	m_e^*/m_e	0.75		[41]

For the initial, very fast growth regime (corresponding to the very steep part of the oxide-film growth curves; see Figs. 6.3 and 6.4 in Sec. 6.5.3), the values of the (difference of the) metal/oxide and oxide/oxygen work-functions and the energy barrier for cation transport may differ from those attained during the subsequent growth stage (for example, as a consequence of the initial formation of a non-stoichiometric oxide phase [22]). To allow a flexible description of this initial part of the growth curve, but at the same time to limit the total number of fit parameters, sigmoidal time-dependences of the parameters W and χ_L were adopted, according to [11]:

$$W(t) = \frac{W^i - W^f}{1 + e^{(t-t_0)/\delta t}} + W^f, \quad (6.6a)$$

$$\chi_L(t) = \frac{\chi_L^i - \chi_L^f}{1 + e^{(t-t_0)/\delta t}} + \chi_L^f. \quad (6.6b)$$

This implies that the values of W and χ_L can vary between W^i and W^f and χ_L^i and χ_L^f , respectively, around the value at the so-called central time t_0 with a rate defined by δt . Finally, by taking the same values of t_0 and δt for Eqs. (6.6a) and (6.6b), a total of six fit parameters remain: i.e. W^i , W^f , χ_L^i , χ_L^f , t_0 and δt .

6.5. Results and Discussion

6.5.1. Formation of a closed oxide film

Typical examples of the dependences of the measured values of Δ and Ψ at $\lambda = 589$ nm on oxidation time (as obtained by RISE; see Sec. 6.3), as well as the result of the fitting of Δ and Ψ for $\lambda = 589$ nm, are shown in Figs. 6.1a-c for the oxidation of the bare Al{111}, Al{100} and Al{110} substrates at $T = 350$ K, respectively. For the thin oxide films considered here, the decrease of the phase-shift-dependent parameter Δ [i.e., the value of $\delta(\Delta)$] will be approximately linearly related to the corresponding increase in the oxide-film thickness (see Sec. 6.5.2 and e.g. Ref. [35]). Since Ψ is insensitive to the presence of a transparent (i.e. non-absorbing) thin-film phase between the ambient and the substrate media [13, 34], a corresponding linear relationship between a change in Ψ [i.e., $\delta(\psi)$] and the oxide-film thickness is not observed. The change of the value of Ψ for the initial interaction of oxygen with a bare metal or alloy substrate strongly depends on the dipole interactions at the concerned solid surface region [35]. For the low oxidation temperatures (up to about 450 K) on Al{111} and (to a lesser extent) on Al{110}, the value of Ψ initially drops, but subsequently increases, initially fast then more gradually, reaching a constant value within the first 500 s of oxidation (see Figs. 6.1a and c, respectively). On the other hand, for the oxidation of Al{100} in the range $T = 300 - 600$ K, as well as for the oxidation of Al{111} and Al{110} at $T > 450$ K, a continuous decrease of the value of Ψ is observed from the onset of oxidation (i.e. a subsequent increase, after the initial decrease, is not observed) attaining a nearly constant value within the first 200 s of oxidation (cf. Fig. 6.1b; in agreement with the findings in Ref. [27]).

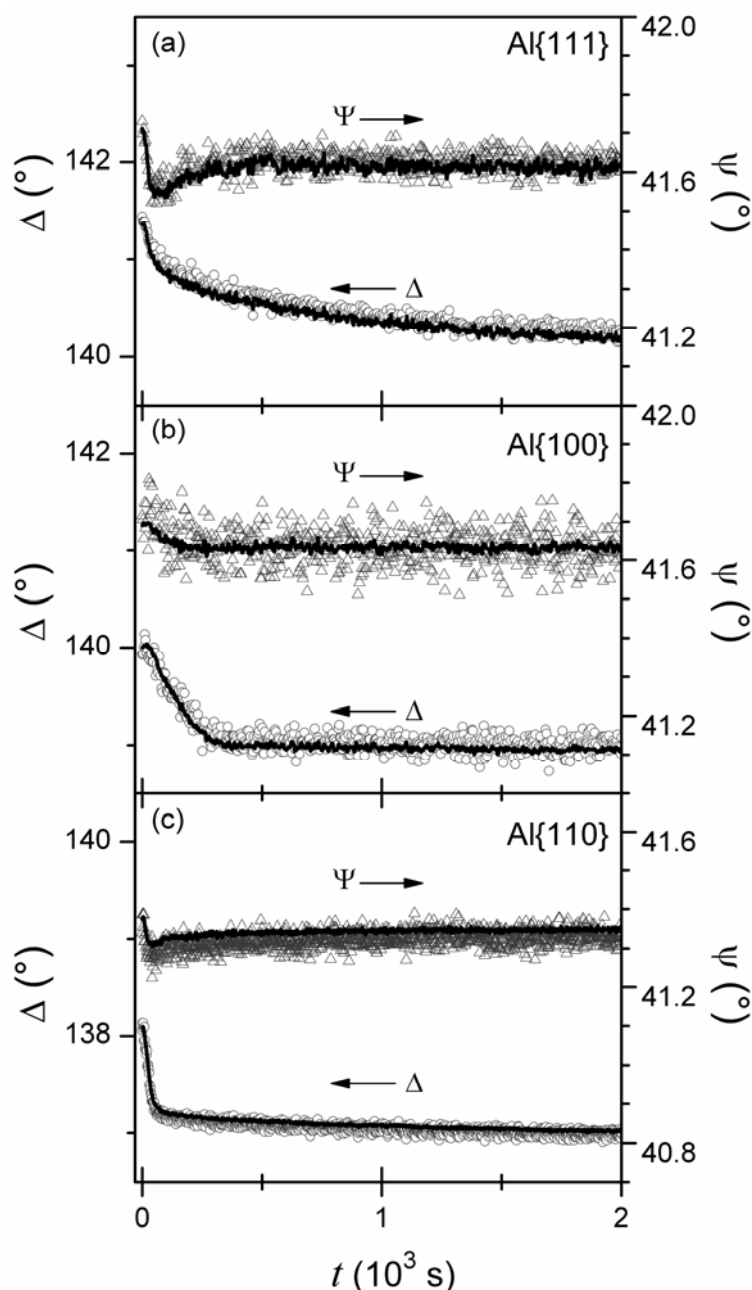


Figure 6.1. The measured ellipsometric parameters Δ and Ψ at $\lambda = 589$ nm as function of oxidation time (t) (markers, as obtained by RISE; see Sec. 6.3), as well as the corresponding results of the fitting of Δ and Ψ at $\lambda = 589$ nm (solid lines), for the oxidation of the bare (a) Al{111}, (b) Al{100} and (c) Al{110} substrates at $T = 350$ K and at $p_{\text{O}_2} = 1 \times 10^{-4}$ Pa, respectively.

The observed differences in the course of Ψ with increasing t at the onset of oxidation for the bare Al{111}, Al{100} and Al{110} substrates can be understood as a result of the competing processes of oxygen incorporation into the bare metal subsurface and on-top chemisorption of oxygen on the bare metal surface, during the initial stage of interaction of oxygen gas and the bare Al metal surface [13, 19, 20]. Oxygen incorporation is favoured over

on-top chemisorption on the less-densely packed metal surfaces (i.e. Al{100} and Al{110}) [19] and for increasing oxidation temperatures [20], and is generally accompanied by a decrease of Ψ [13, 19]. On-top chemisorption is preferred on the more densely packed metal surfaces (i.e. Al{111}) and for lower temperatures and is accompanied by an increase of Ψ .

On Al{111} the O incorporation rate exceeds the O chemisorption rate only at the very onset of oxidation leading to the observed initial decrease of Ψ ; O chemisorption becomes dominant afterwards, as associated with a subsequent increase of Ψ , which is consistent with the observed formation of an ordered (1×1) chemisorbed oxygen layer on Al{111} (see Refs. [20, 23] and references therein). As soon as a 3-dimensional oxide phase has formed the value of Ψ remains almost constant [13, 19]. With increasing temperature oxygen incorporation prevails [20, 23] and, consequently, only an initial decrease (without a subsequent increase) of Ψ is observed. For the oxidation of the more open Al{100} surface, oxygen incorporation hinders the formation of a well-defined ordered O chemisorption phase [20]; i.e. only a decrease in Ψ is observed at the onset of oxidation (Fig. 6.1b). As for the Al{100} face, initial O incorporation is expected to be dominant for the oxidation of the even more open Al{110} surface [19]. However, a reconstruction of the bare Al{110} metal surface occurs upon oxidation, resulting in the formation of a {111} faceted Al metal surface for $T > 550$ K (see Sec. 6.5.2). The observed initial decrease and subsequent increase of Ψ at the onset of oxidation on Al{110} (which is less pronounced than for Al{111}; Fig. 6.1c) indicates that very soon upon start of oxidation chemisorption predominates oxygen incorporation at the onset of oxidation on the open Al{110} face for $T \leq 450$ K (Fig. 6.1c). This suggests that a reconstruction of the Al{110} surface is already initiated at low temperatures (i.e. $T \leq 450$ K), since oxygen chemisorption is not expected to dominate on the unreconstructed (i.e. very open) Al{110} surface. For $T > 450$ K, O incorporation predominates chemisorption resulting in a continuous decrease of Ψ at the onset of oxidation for Al{110} (as for Al{111} and Al{100}; see discussion above and Refs. [20, 23]).

The average oxygen sticking coefficient on Al{111}, Al{100} and Al{110}, s , as determined in the present study for thicknesses up to 1 ML,³ was found to increase with

³ The sticking coefficient, s , is defined as the number of oxygen atoms incorporated in the oxide film per oxygen atom supplied from the gas phase. In the present study, the average number of incorporated oxygen atoms per unit time is straightforwardly determined from the constant slope of the ellipsometric growth curve (linear) up to 1 ML thickness. The corresponding number of oxygen atoms supplied from the gas phase per unit time is calculated from $2 \cdot p_{\text{O}_2} / \sqrt{2\pi \cdot m_{\text{O}_2} \cdot k_B \cdot T}$ (kinetic gas theory), where m_{O_2} is the mass of the O₂ molecule.

increasing T , because oxygen chemisorption on Al metal surfaces is a thermally activated process for $T < 600$ K [21]. The value of the sticking coefficient for the different Al substrate orientations in the studied temperature range of $T = 350 - 600$ K increases in the order: Al{100} ($0.01 \leq s \leq 0.05$) < Al{111} ($0.02 \leq s \leq 0.07$) < Al{110} (with $0.05 \leq s \leq 0.1$), in good agreement with corresponding values reported in the literature [18, 20, 21].

6.5.2. Oxidation-induced reconstruction of the Al{110} face

For the thin oxide films considered here, the decrease in $\Delta(\lambda)$ with increasing t is linearly related to the corresponding increase in the oxide-film thickness: as follows from the model fitting of the measured RISE data for $\lambda = 585$ nm (cf. Fig. 6.1), a decrease in Δ of 1° corresponds to an increase in oxide-film thickness of 0.53 ± 0.04 nm, independent of substrate orientation and oxidation temperature (in the temperature range 350 – 600 K; for Al{110} up to 550 K, see what follows). However, for Al{110} for $T > 550$ K, a minimum in the $\Delta(\lambda, t)$ curve occurs at about 200 s of oxidation due to a short increase of $\Delta(\lambda)$ after the initial steep decrease of $\Delta(\lambda)$ corresponding to the very fast initial oxidation stage (Fig. 6.2). This minimum in the $\Delta(\lambda, t)$ curve becomes more pronounced with increasing temperature for $T > 550$ K and appears to coincide with the transition from the initial, very fast to the second, slow oxide-film growth stage (Fig. 6.2). According to the above interpretation, this short increase in $\Delta(\lambda)$ at the onset of the transition to the slow growth stage would imply a decrease in oxide-film thickness (see above). Since the oxide films grown on Al{110} are still amorphous after $t = 6000$ s of oxidation at $T = 640$ K, as verified by cross-sectional HR-TEM analysis (Chapters 2 and 5), the apparent thickness decrease cannot be attributed to a densification (i.e. a reduction of free volume in the dense-random-pack O arrangement [42]) of the developing oxide film due to an amorphous-to-crystalline transition. Further, a decomposition of the oxide film by oxide dissociation and/or oxygen dissolution into the bulk metal substrate can be neglected in the studied temperature range of $550 \text{ K} < T < 650 \text{ K}$. Instead, low energy electron diffraction (LEED) and high-resolution transmission electron microscopy (HR-TEM) analysis of the oxide films grown on Al{110} at $T > 550$ K (see Chapter 5), indicate a reconstruction of the oxidizing Al{110} surface for $T > 550$ K, which is associated with the development of a {111}- faceted Al metal surface.

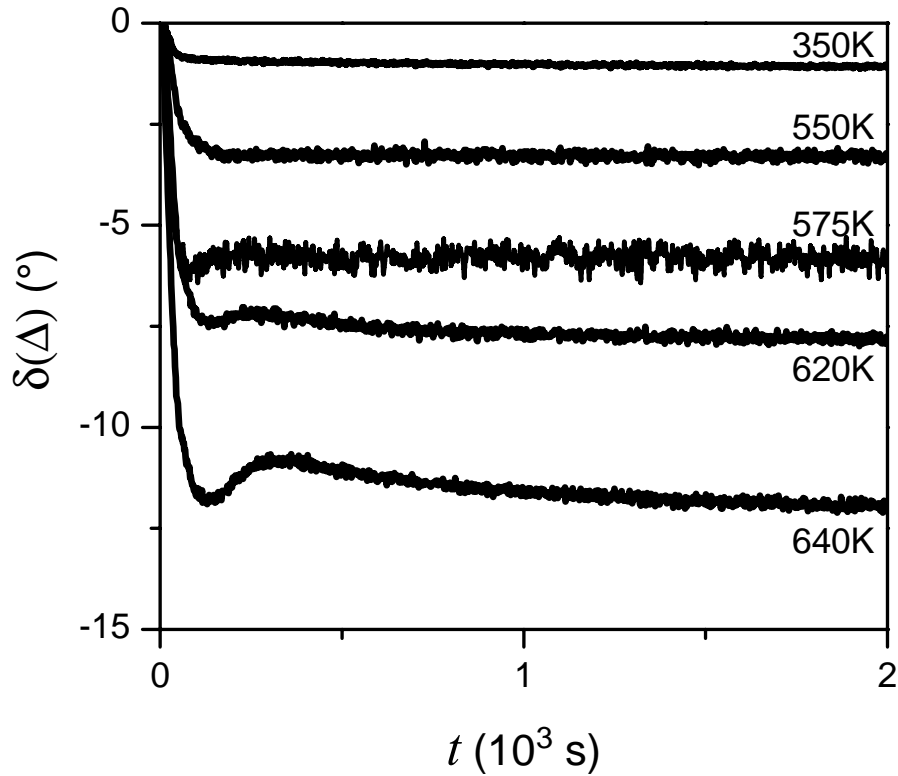


Figure 6.2. Change in the phase-shift-dependent ellipsometric parameter Δ [i.e. $\delta(\Delta)$] with increasing oxidation time (t) for the oxidation of the bare Al{110} substrate at different T and at $p_{\text{O}_2} = 1 \times 10^{-4}$ Pa.

As demonstrated by thermodynamic calculations (Chapter 5), the {111}-faceting of the original Al{110} surface is thermodynamically preferred due to the lower energy of the resulting Al{111}||*am*-Al₂O₃ interface (as compared to the original Al{110}||*am*-Al₂O₃ interface), in spite of the associated increase in total surface area of about 22%. If the amount of new oxide formed during the time-interval of the oxidation-induced reconstruction can be neglected (i.e. if faceting occurs at a much faster rate than further oxide growth), the effective increase in metal/oxide interface area by 22% must be accompanied by a similar, real decrease in the average oxide-film thickness over the (constant) RISE analysis area. Indeed, as verified by cross-sectional HR-TEM analysis (Chapter 5), the oxide-film thickness is no longer uniform after oxidation-induced reconstruction of the Al{110} surface. It is noted that the original {110} crystallographic surface of the *bare* Al substrate becomes restored after subsequent cleaning and annealing (Sec. 6.2) of the oxidized, reconstructed Al{110} surface in UHV (as verified by LEED and in agreement with thermodynamic model predictions; see Chapter 5).

6.5.3. Oxide-film growth kinetics

Some typical examples of the experimental oxide-film growth curves, as obtained by RISE (see Sec. 6.3), for the oxidation of the bare Al{111}, Al{100} and Al{110} substrates at various temperatures in the range of $T = 300 - 600$ K are shown in Figs. 6.3 and 6.4. The growth curves correspond to the sum of the thickness, $L^{\text{ox}}(t)$, of the stoichiometric Al₂O₃ top layer and the thickness, $L^{\text{int}}(t)$, of the non-stoichiometric interface 'layer', as considered in the model description of $\Delta(\lambda, t)$ and $\Psi(\lambda, t)$ for the evolving substrate/film system (Sec. 6.3 and Fig. 6.1): i.e. $L(t) = L^{\text{ox}}(t) + L^{\text{int}}(t)$. For all metal-substrate orientations and oxidation temperatures considered, the fitted value of $L^{\text{int}}(t)$ increases only during the first 120 – 180 s of oxidation and then remains constant during further growth. The constant value of L^{int} is in the range of 0.1 – 0.3 MLs for Al{111} and Al{100} (independent of T), whereas for Al{110} it increases with increasing T from 0.3 ML at 350 K to 1 ML at 600 K. The origin of this interface oxide layer with a thickness < 1 ML [as required for an accurate model description of $\Delta(\lambda, t)$ and, in particular, $\Psi(\lambda, t)$; see Sec. 6.3] is attributed to the deficient coordination of Al cations by nearest-neighbour O anions at the metal/oxide interface (Sec. 6.3), as confirmed by AR-XPS analysis performed in this project (see Chapter 5). It is recognized that the EMA description of the thin intermediate oxide layer in principle can also effectively describe any roughness present at the metal/oxide interface. However, the oxide films grown on Al{111} and Al{100} are atomically flat as confirmed by cross-sectional HR-TEM analysis (Chapter 4, [14]). Only on Al{110}, the increase of L^{int} with increasing T for Al{110} can be related to an increased roughening of the metal/oxide interface as a result of the oxidation-induced faceting of this metal surface increasing with increasing temperature (Sec. 6.5.2).

On Al{100} and Al{110} at all oxidation temperatures considered (350 – 600 K; for Al{110} up to 550 K), the oxide-film growth kinetics are characterized by an initial regime of very fast film growth, which is succeeded by a second oxidation stage in which the oxide-film growth rate becomes very small (i.e. a *near*-limiting oxide-film thickness, L^{lim} , is attained [25]; see Figs. 6.3b and c). The value of L^{lim} , as reached in the second growth stage for Al{100} and Al{110}, increases with increasing T . This passivation behaviour is typical for the oxidation of metals and alloys at low temperatures, where the rate of diffusion of cations and/or anions through the developing oxide film under influence of the chemical potential (i.e. concentration) gradient is negligibly small (Secs. 6.4 and 6.5.4).

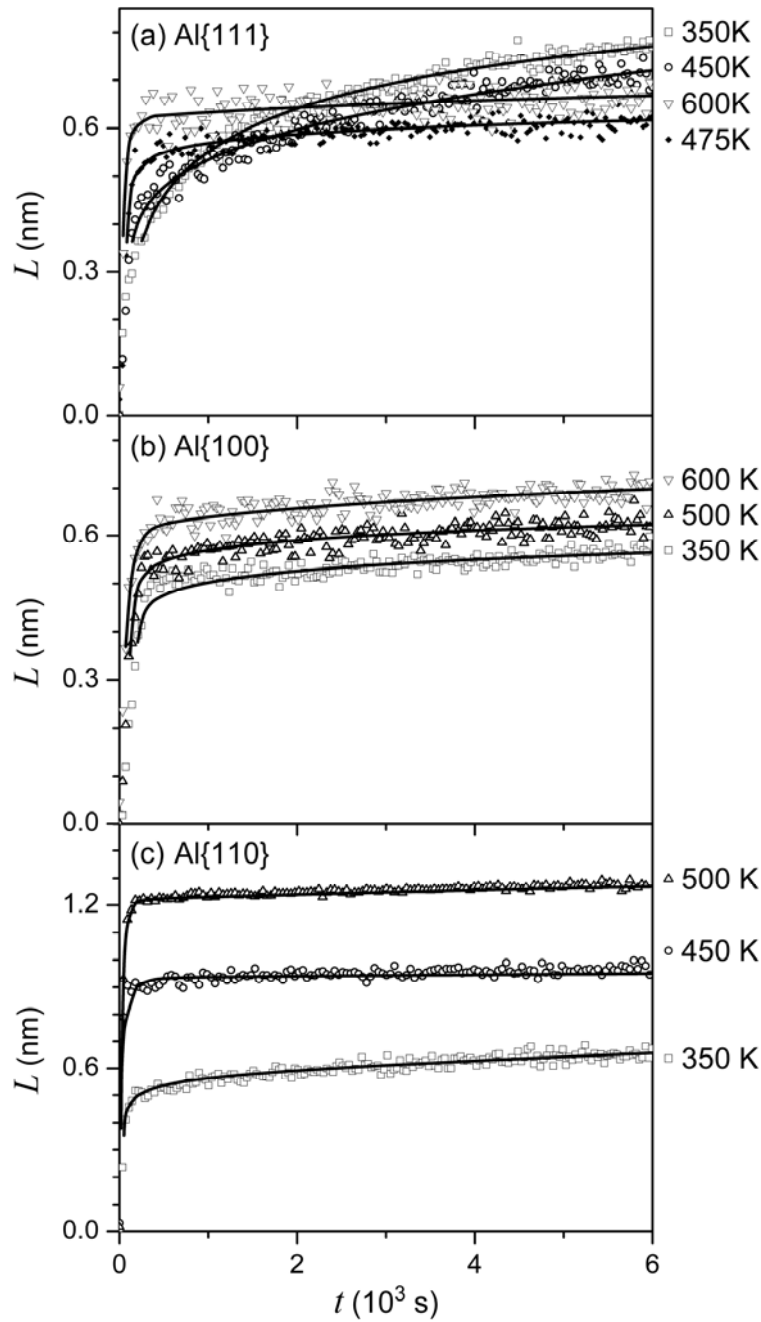


Figure 6.3. Experimental (*markers*) and fitted (*lines*) oxide-film growth curves for the oxidation of the bare (a) Al{111}, (b) Al{100} and (c) Al{110} substrate in the temperature range of $T = 350 - 600$ K at $p_{\text{O}_2} = 1 \times 10^{-4}$ Pa. The experimental data were obtained by RISE (Sec. 6.3). The theoretical growth curves were calculated on the basis of the coupled currents of cations and electrons (by both tunnelling and thermionic emission) under a surface-charge field (Sec. 6.4).

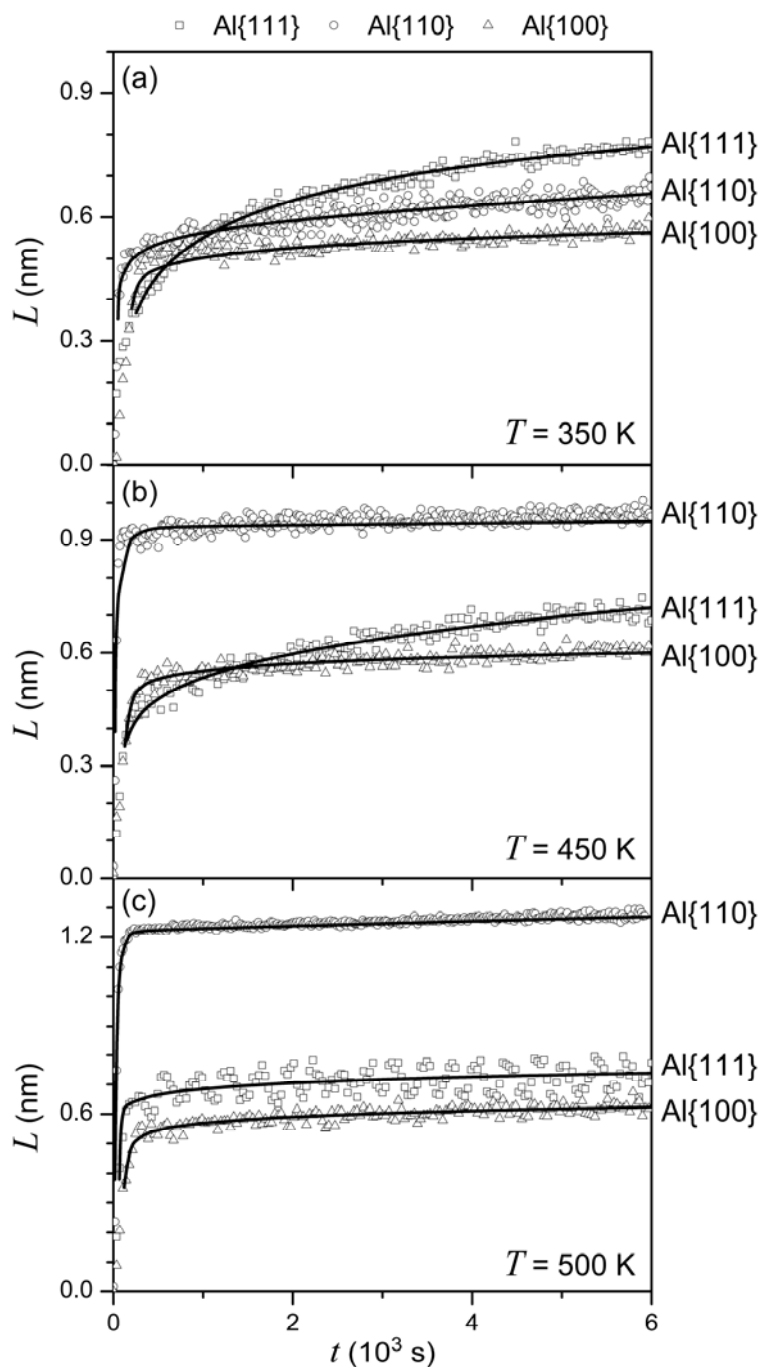


Figure 6.4. Experimental (*markers*) and fitted (*lines*) oxide-film growth curves for the oxidation of the bare Al{111}, Al{100} and Al{110} substrates at (a) 350 K, (b) 450 K and (c) 500 K and at $p_{\text{O}_2} = 1 \times 10^{-4}$ Pa. See caption of Fig. 6.3 for details.

On Al{111}, on the other hand, no distinct transition between an initial, very fast and a subsequent, very slow growth stage is observed for $T \leq 450$ K (see Fig. 6.3a): at these temperatures the initial, very fast growth rate decreases much more gradually with increasing oxidation time without approaching a near-limiting thickness (after $t = 6000$ s; see Figs. 6.4a and b). This gradual decrease of the oxide-film growth rate with increasing t becomes more

pronounced towards higher oxidation temperatures for $T \leq 450$ K (compare the growth curves in Fig. 6.3a for $T = 350$ K and $T = 450$ K for $t < 2000$ s). This growth behaviour on Al{111} leads to the unexpected *decrease* of the oxide-film thickness after $t = 6000$ s oxidation ($L^{t=6000s}$) with *increasing* temperature in the range of $T = 350 - 475$ K (as also found by AR-XPS, see Chapter 5), although the very initial oxide-film growth rate is larger for $T = 450$ K than for $T = 350$ K. For $T \geq 475$ K (i.e. above the amorphous-to-crystalline transition temperature for Al{111} for $t = 6000$ s; see Chapter 4 and Ref. [14]), the growth kinetics on Al{111} can be subdivided, as for Al{100} and Al{110}, into an initial, very fast and a second, very slow oxidation stage and, consequently, a near-limiting thickness that increases with increasing T is observed now for Al{111}, too (compare Figs. 6.3a-c and 6.4c).

The here observed and discussed differences in oxide-film growth kinetics for the different Al substrate orientations explain the discrepancies reported in the literature regarding the oxide-film thickness order for oxidized Al single-crystals with {111}, {100} and {110} surfaces [43, 44]: as follows from the present work, for example, at $T = 350$ K and $t = 500$ s the resulting oxide-film thickness increases in the order Al{111} < Al{100} < Al{110}, whereas at $T = 350$ K and $t = 6000$ s the thickness increases in the order Al{100} < Al{110} < Al{111} (see Fig. 6.4a).

6.5.4. Oxide-film growth mechanisms

Clearly, very good agreement exists between the experimental and (model fitted, see Sec. 6.4) growth curves (see Figs. 6.3 and 6.4). The corresponding rate-limiting energy barrier for cation transport, W , and the metal/oxide work-function, χ_L , as resulting from the fitting, depend on oxidation time only at the very onset of oxidation. This implies that a time-dependence of W and χ_L is required only to accurately describe the initial steep gradient of the growth curves at the onset of oxidation. Constant values of W and χ_L [corresponding to W^f and χ_L^f , respectively; see Eqs. (6.6a) and (6.6b) in Sec. 6.4.2] have been reached before the onset of the second, slower growth stage. The constant values of W^f and the work-function difference $\Delta\chi^f = \chi_0 - \chi_L^f$ (with χ_0 fixed at a constant value of 1.6 eV; see Sec. 6.4.2) have been plotted as function of T in Figs. 6.5a and b, respectively.

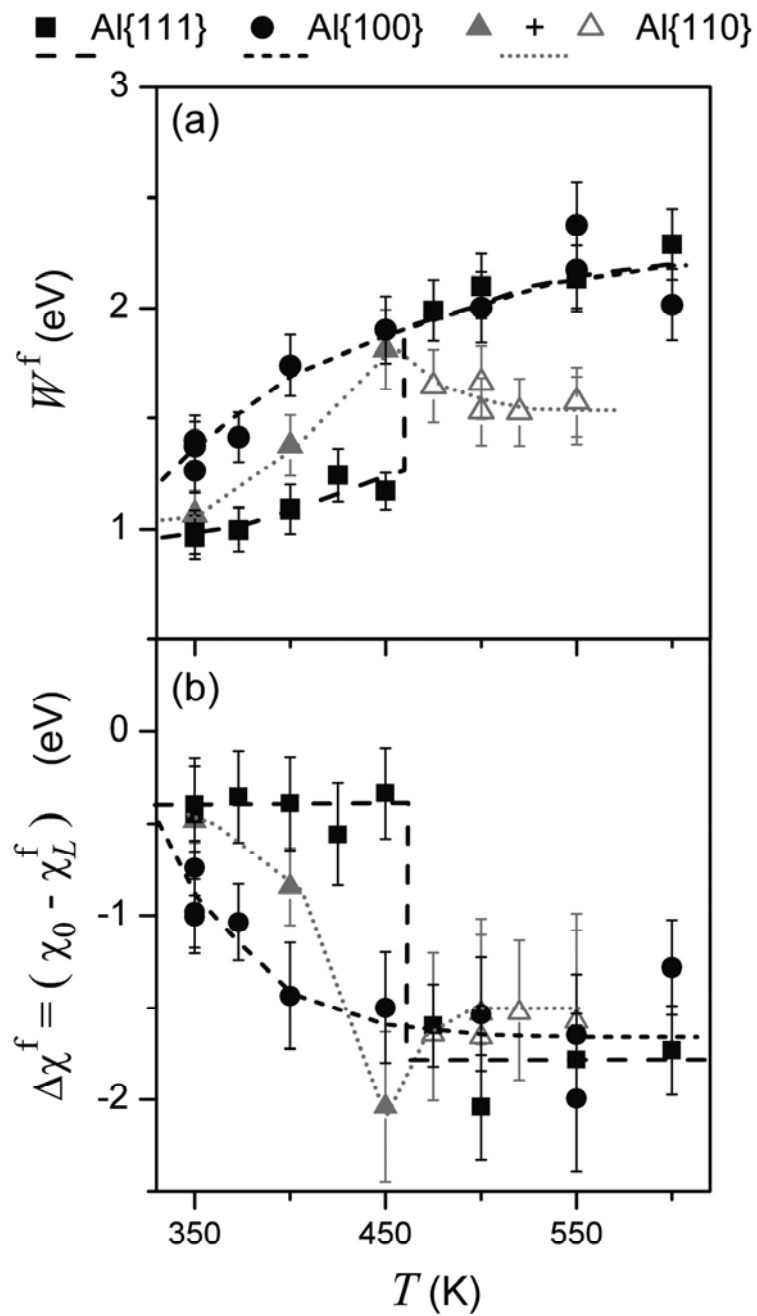


Figure 6.5. (a) Activation-energy barrier for cation transport, W^f , and (b) work-function difference, $\Delta\chi^f = \chi_0 - \chi_L^f$, as function of the temperature, T , for the oxidation of different bare Al substrates at $p_{O_2} = 1 \times 10^{-4}$ Pa. The constant (i.e. time independent) values W^f and $\Delta\chi^f$ are reached very soon upon the start of oxidation [i.e. already during the initial very fast oxidation; see Eqs. (6.6a) and (6.6b) and discussion in Sec. 6.4.2]. The dashed lines have been given to guide the eye (see text). The error bars indicate the estimated error based on the accuracy of the model fitting and the scatter in the experimental data obtained by RISE.

For all substrate orientations and temperatures studied, it was found that the kinetic potential V_k slightly deviates from the Mott potential V_M only at the very onset of growth. Further, a negative work-function difference, $\Delta\chi^f$, and thereby a negative kinetic potential

V_k , which approximately equals the Mott potential $V_M = e^{-1}(\chi_0 - \chi_L)$ [Eq. (6.4)], is maintained over the entire thickness range of the growth curves (Fig. 6.5b). This implies that the corresponding (positive) surface-charge field strength [see Eq. (6.3)] is directed such as to enhance outward cation transport (and to retard electron transport): i.e. the oxide-film growth rate is always limited by cation transport. As evidence from the small deviation of the kinetic potential from the Mott potential, it was observed that electron transport (by tunnelling and thermionic emission) only co-determines the growth rate at the very beginning of oxidation. From the data obtained by the model fitting, it follows, for the very thin (< 1.5 nm) Al_2O_3 films grown at low temperatures (as considered in this study), electron transport by thermionic (Schottky) emission also contributes to the net electron current, because of the significant reduction of the electron potential energy barriers adjacent to the metal/oxide and oxide/oxygen interfaces (see footnote 1 in Sec. 6.4.1). Consequently, the Mott potential during continued oxide-film growth is maintained by the (near-)balance between a very large, forward electron flux by tunnelling and a slightly smaller, reverse electron flux by thermionic emission (the small imbalance providing the compensation for the net cation current to satisfy the coupled currents criterion; see Sec. 6.4.1). The (positive) electric field strength, $E_k = -V_k/L(t)$, due to the (negative) Mott potential, $V_M \equiv V_k$, decreases with increasing thickness, $L(t)$. Consequently, the electric-field enhanced outward cation flux (and thus the oxide-film growth rate) has already strongly decreased at the onset of the second, slow oxidation stage on $\text{Al}\{100\}$ and $\text{Al}\{110\}$ (and on $\text{Al}\{111\}$ for $T \geq 475$ K; see Sec. 6.5.3).

As holds for the low-temperature oxidation of Fe [8] and Zr [11], oxide-film growth on $\text{Al}\{100\}$ is associated with a gradual increase of the rate-limiting activation-energy barrier for cation transport, W^f , with increasing T from $W^f \cong 1.3$ eV at $T = 350$ K to $W^f \cong 2.2$ eV at $T = 600$ K (Fig. 6.5a), which is ascribed to the amorphous-to-crystalline transformation occurring in the thickening oxide films grown at higher temperatures (in agreement with the LEED and HR-TEM analysis performed in this project; see Chapters 4 and 5). The gradual development of long-range order in the random-dense-packing of O ions (associated with oxide-film densification [42]) results in a net reduction of the average interstice dimensions experienced by the 'hopping' interstitial cations, leading to an increase in the activation-energy

barrier W^f .⁴ Simultaneously, an increase of the absolute work-function difference, $|\Delta\chi^f|$ occurs (i.e. $\Delta\chi^f$ becomes more negative from $\Delta\chi^f \cong -0.8$ eV at $T = 350$ K to $\Delta\chi^f \cong -1.6$ eV at $T = 600$ K; Fig. 6.5b), which is accompanied by a decrease of the Mott potential, V_M [see Eqs. (6.3) and (6.4)]. This decrease can be attributed to a reduction of the number of electronic defect states within the oxide band gap upon the amorphous-to-crystalline transition. It follows that, in spite of the gradual increase of W^f with increasing T , the concurrent *decrease* of the *negative* Mott potential (and thus an increase of the positive surface-charge field strength at constant L) induces the observed increase of the near-limiting thickness, L^{lim} , with increasing T (Sec. 6.5.3). Clearly, the thermal energy of the 'hopping' cations for $T \leq 600$ K is insufficient to realize further oxide-film growth beyond the near-limiting oxide-film thickness.

A similar increase of W^f and $|\Delta\chi^f|$ with increasing T was observed for Al{110} up to $T = 450$ K (as for Al{100}). [However, for more elevated temperatures $T > 450$ K, a decrease of W^f and $|\Delta\chi^f|$ was found instead, which coincides with the initiation of the oxidation-induced {111}-faceting of the original Al{110} surface (not accounted for in the present model calculations; see Sec. 6.5.2).]

On the other hand, a gradual increase of W^f with increasing T was not observed for oxide-film growth on Al{111} (Fig. 6.5a): after a relatively small initial increase of W^f with increasing T , a more or less abrupt increase of W^f occurs around $T = 450$ K, which corresponds to the temperature for the amorphous-to-crystalline transition of the oxide films grown on Al{111} for $t = 6000$ s (Chapter 4); for $T \geq 475$ K, the value of W^f then again more gradually increases with increasing T . The corresponding value of $\Delta\chi^f$ shows a similar trend (Fig. 6.5b): the value of $\Delta\chi^f$ is about constant up to $T = 450$ K ($\Delta\chi^f \sim -0.4$ eV), but then

⁴ The development of long-range order in the oxygen-ion arrangement of the oxide film during the amorphous-to-crystalline transition (associated with a reduction of free volume; see Ref. [42]) will also be accompanied with a reduction of the average cationic jump distance ($2a$), as fixed in the present model calculations (see Table 1). However, adopting in the present model calculations an, on average, 10% larger cationic jump distance for the amorphous Al₂O₃ films grown at low temperatures results in an increase of the optimized value of W^f (as obtained from the fitting) of only about 0.1 eV.

suddenly drops to value of about $\Delta\chi^f \sim -1.7$ eV for $T > 450$ K. Apparently, the amorphous-to-crystalline transition as observed upon increasing T is much more abrupt for the oxide films grown on Al{111}, as compared to those on Al{100}. This suggests that the relatively small increase of W^f with increasing T for $t = 6000$ s in the amorphous temperature regime for Al{111} is exclusively due to a slight (net) reduction of the average interstice dimensions experienced by the 'hopping' interstitial cations due to a structural relaxation of the amorphous oxide film, whereas on Al{100} a pronounced development of long-range order of the dense-random-packed O arrangement of the oxide occurs (see above).

The value of W^f in the amorphous temperature regime for Al{111} is considerably lower than that for Al{100} (Fig. 6.5a), which is another indication that the amorphous-to-crystalline transformation of the oxide film already starts at a lower temperature on Al{100}. As a result of the relatively low value of W^f for Al{111}, a near-limiting oxide-film thickness is not observed within the amorphous temperature regime (i.e. for $T \leq 450$ K). Thus, the at first sight surprising *decrease* of the thickness, $L^{t=6000s}$, with *increasing* T for the amorphous temperature regime on Al{111} (Sec. 6.5.3 and Fig. 6.3a), is due to a slight increase with temperature of the activation energy for cation transport, W^f , in combination with a constant kinetic potential due to the surface-charge field.

The values of W^f within the crystalline temperature regime $T > 450$ K are approximately equal for the γ -like- Al_2O_3 films grown on Al{111} and Al{100} (Fig. 6.5a). The crystalline oxide films on Al{111} and Al{100} both have their {111} surface parallel to the surface. Consequently, a coherent Al{111}/ γ - Al_2O_3 {111} interface develops for the epitaxial overgrowth on Al{111}, whereas an incoherent Al{100}/ γ - Al_2O_3 {111} interface is formed on Al{100} (see Chapters 4 and 5). The similar values of W^f for the γ -like- Al_2O_3 films on Al{111} and Al{100} therefore indicate that the rate-limiting activation-energy barrier for cation transport is likely located *within* the oxide film (W^{ox} ; see discussion in Sec. 6.4.2), rather than *at* the metal/oxide interface ($W^{\text{metal} \rightarrow \text{ox}}$; as previously postulated in Ref. [25]).

6.6. Conclusions

- The kinetics of ultra-thin (< 1.5 nm) oxide-film growth on bare Al{100} and Al{110} substrates in the temperature range of 350 – 600 K at $p_{\text{O}_2} = 1 \times 10^{-4}$ Pa can be subdivided into an initial, very fast and a subsequent, very slow oxidation stage. The

- latter slow oxidation stage is characterized by the occurrence of a near-limiting thickness that increases with increasing temperature.
- For the oxidation of bare Al{111} substrates up to $T = 450$ K and at $p_{\text{O}_2} = 1 \times 10^{-4}$ Pa, a distinction between an initial, very fast and a subsequent, very slow oxidation stage cannot be made. Instead, the initial oxide-film growth rate on Al{111} decreases only gradually with increasing oxidation time without that a near-limiting oxide-film thickness occurs. An unusual decrease of the oxide-film thickness with increasing T after $t = 6000$ s of oxidation is observed for $T \leq 450$ K, what can be described to a slight increase with temperature of the activation energy for cation transport. At higher temperatures $T > 450$ K, the growth kinetics on Al{111} can also (as for Al{100} and Al{110}) be subdivided into an initial, very fast and a subsequent, very slow oxidation stage (leading to a near-limiting thickness that increases with increasing temperature).
 - Upon initial interaction of oxygen gas with the bare Al{111} substrate and, to a lesser extent, with the Al{110} substrate, for $T \leq 450$ K and at $p_{\text{O}_2} = 1 \times 10^{-4}$ Pa, and apart from the very onset where incorporation dominates, on-top chemisorption of oxygen on the bare metal surface predominates over concurrent oxygen incorporation into the bare metal subsurface. For higher temperatures $T > 450$ K on Al{111} and Al{110}, as well as on Al{100} in the temperature range of 300 – 600 K, initial oxygen incorporation prevails instead. The corresponding values of the oxygen sticking coefficient are in the range of 0.01 – 0.1; the oxygen sticking coefficient increases with increasing T and in the order: Al{100} < Al{111} < Al{110}. The apparent thickness decrease for the developing oxide film after about 200 s of oxidation on Al{110} at $T > 550$ K (identified by the ellipsometric analysis) is due to the oxidation-induced reconstruction of the Al{110} surface for $T > 550$ K (resulting in the development of a {111}- faceted metal surface).
 - The thermal oxidation of Al single-crystals in the temperature regime between 350 K and 600 K can be well described by adopting coupled currents of Al³⁺ cations and electrons (by both thermionic emission and quantum mechanical tunnelling) in an uniform surface-charge field, taking the rate-limiting activation energy for cation transport, W , across the developing oxide film and the work-function difference, $\Delta\chi$, as fit parameters. It follows that the oxide-film growth rate is always limited by the electric-field enhanced cation transport through the developing oxide film. Electron transport is co-determining the oxide growth rate only at the onset of oxidation. The

surface-charge field due to the Mott potential is maintained during continued oxide-film growth by the (near-)balance between a very large, forward electron flux by tunnelling and a slightly smaller, reverse electron flux by thermionic emission.

- Due to the gradual transformation of the initial amorphous oxide film on Al{100} into γ -like-Al₂O₃ the values of the energy barrier for cation transport, W , and the Mott potential, V_M , both increase gradually with increasing oxidation temperature in the range of 350 – 600 K for Al{100}, as well as up to 450 K for Al{110}. This leads to the observed initial, very fast oxidation stage and the subsequent, very slow oxidation stage and the occurrence of a near-limiting oxide-film thickness that increases with increasing temperature. For Al{111}, the corresponding amorphous-to-crystalline transition occurs at higher temperatures, $T > 450$ K, and is more abrupt than for Al{100} and Al{110}. Consequently, within the amorphous temperature regime up to $T = 450$ K, the Mott potential remains constant and the corresponding value of the energy barrier for cation transport stays relatively low, and a near-limiting oxide-film thickness does not occur. Around the amorphous-to-crystalline transition temperature for Al{111}, the corresponding values of W and V_M change abruptly towards the corresponding values for the crystalline oxide films grown on Al{100} and Al{110} and then the same growth behaviour (i.e. an initial, very fast and subsequent, very slow oxidation stage and occurrence of a near-limiting oxide-film thickness) occurs for all substrate orientations.

References

- [1] N. F. Mott, *Trans. Faraday Soc.* **43** (1947) 429.
- [2] N. Cabrera and N. F. Mott, *Rep. Prog. Phys.* **12** (1949) 163.
- [3] A. T. Fromhold, Jr. and E. L. Cook, *Phys. Rev.* **158** (1967) 600.
- [4] A. T. Fromhold, Jr. and E. L. Cook, *Phys. Rev.* **163** (1967) 650.
- [5] A. T. Fromhold, Jr., *Theory of metal oxidation; Volume 1 – Fundamentals*, (North-Holland, Amsterdam, 1976).
- [6] E. Fromm, *Kinetics of Metal-Gas Interactions at Low Temperatures; Hydriding, Oxidation, Poisoning* (Springer, Berlin, 1998).
- [7] M. Martin and E. Fromm, *J. Alloys Compd.* **258** (1997) 7.

- [8] P. C. J. Graat, M. A. J. Somers, A. M. Vredenberg and E. J. Mittemeijer, *J. Appl. Phys.* **82** (1997) 1416.
- [9] S. J. Roosendaal, A. M. Vredenberg and F. H. P. M. Habraken, *Phys. Rev. Lett.* **84** (2000) 3366.
- [10] P. C. J. Graat, M. A. J. Somers and E. J. Mittemeijer, *Z. Metallkd.* **93** (2002) 532.
- [11] L. P. H. Jeurgens, A. Lyapin and E. J. Mittemeijer, *Acta Mater.* **53** (2005) 4871.
- [12] A. Lyapin, L. P. H. Jeurgens and E. J. Mittemeijer, *Acta Mater.* **53** (2005) 2925.
- [13] M. S. Vinodh, L. P. H. Jeurgens and E. J. Mittemeijer, *J. Appl. Phys.* **100** (2006) 044903.
- [14] F. Reichel, L. P. H. Jeurgens, G. Richter, P. A. van Aken and E. J. Mittemeijer, *Acta Mater.* **55** (2007) 6027.
- [15] L. P. H. Jeurgens, W. G. Sloof, F. D. Tichelaar and E. J. Mittemeijer, *Phys. Rev. B* **62** (2000), 4707.
- [16] B. J. H. Stadler, M. Oliveria and L. O. Bouthillette, *J. Am. Ceram. Soc.* **78** (1995) 3336.
- [17] H. Momida, T. Hamada, Y. Takagi, T. Yamamoto, T. Uda and T. Ohno, *Phys. Rev. B* **73** (2006) 054108.
- [18] P. O. Gartland, *Surf. Sci.* **62** (1977) 183.
- [19] J. Grimblot and J. M. Eldridge, *J. Electrochem. Soc.* **129** (1982) 2366.
- [20] I. P. Batra and L. Kleinman, *J. Electron Spectr. Relat. Phenom.* **33** (1984) 175.
- [21] V. Zhukov, I. Popova and J. T. Yates, Jr., *Surf. Sci.* **441** (1999) 251.
- [22] T. Kravchuk, R. Akhvediani, V. V. Gridin and A. Hoffman, *Surf. Sci.* **562** (2004) 83.
- [23] J. Trost, H. Brune, J. Witterling, R. J. Behm and G. Ertl, *J. Chem. Phys.* **108** (1998) 1740.
- [24] L. C. Ciacchi and M. C. Payne, *Phys. Rev. Lett.* **92** (2004) 176104.
- [25] L. P. H. Jeurgens, W. G. Sloof, F. D. Tichelaar and E. J. Mittemeijer, *J. Appl. Phys.* **92** (2002) 1649.
- [26] P. Hofmann, W. Wyrobisch and A. M. Bradshaw, *Surf. Sci.* **80** (1979) 344.
- [27] B. E. Hayden, W. Wyrobisch, W. Oppermann, S. Hachicha, P. Hofmann and A. M. Bradshaw, *Surf. Sci.* **109** (1981) 207.
- [28] C. Ocal, S. Ferrer and N. Garcia, *Surf. Sci.* **163** (1985) 335.
- [29] A. Hasnaoui, O. Politano, J. M. Salazar and G. Aral, *Phys. Rev. B* **73** (2006) 035427.

- [30] A. Lyapin, L. P. H. Jeurgens, P. C. J. Graat and E. J. Mittemeijer, *J. Appl. Phys.* **96** (2004) 7126.
- [31] Guide to Using WVASE32™. J. A. Woolam Co., Inc. (1997).
- [32] I. H. Malitson, F. V. Murphy and W. S. Rodney, *J. Opt. Soc. Am.* **48** (1958) 72.
- [33] R. Ahuja, J.M. Osorio-Guillen, J. Souza de Almeida, B. Holm, W. Y. Ching and B. Johansson, *J. Phys.: Condens. Matter* **16** (2004) 2891.
- [34] E. P. Gusev, E. Cartier, D. A. Buchanan, M. Gribelyuk, M. Copel, H. Okorn-Schmidt and C. D'Emic, *Microelectron. Eng.* **59** (2001) 341.
- [35] R. M. A. Azzam and N. M. Bashara, *Ellipsometry and Polarized Light*, (North-Holland, Amsterdam, 1987).
- [36] L. P. H. Jeurgens, W. G. Sloof, F. D. Tichelaar and E. J. Mittemeijer, *Thin Solid Films* **418** (2002) 89.
- [37] MATLAB version 6.1.0.450, Release 12.1 (The MathWorks Inc., Natick, 2001).
- [38] J. Kadlec and K. H. Gundlach, *Phys. Stat. Sol. A* **37** (1976) 11.
- [39] Powder Diffraction Files, Card 00-050-0741 from JCPDS-International Centre for Diffraction Data (2005).
- [40] K. Cho, *Comp. Mater. Sci.* **23** (2002) 43.
- [41] W. H. Rippard, A. C. Perrella, F. J. Albert and R. A. Buhrmann, *Phys. Rev. Lett.* **88** (2002) 046805.
- [42] P. C. Snijders, L. P. H. Jeurgens and W. G. Sloof, *Surf. Sci.* **589** (2005) 98.
- [43] J. I. Eldridge, R. J. Hussey, D. F. Mitchell and M. J. Graham, *Oxid. Met.* **30** (1988) 301.
- [44] K. Shinohara, T. Seo and H. Kyogoku, *Z. Metallkd.* **73** (1982) 774.

Chapter 7

Summary

This thesis addresses the effect of the parent metal-substrate orientation on the thermodynamics and kinetics of ultra-thin (< 5 nm) oxide-film growth on bare metals upon their exposure to oxygen gas at low temperatures (up to 650 K). As demonstrated, for such thin oxide overgrowths on their metals, the resulting oxide-film microstructures often differ from those predicted by *bulk* thermodynamics, because of the relatively large contributions of interface and surface energies to the total energetics of the various metal-substrate/oxide-film systems (Chapters 2, 3 and 4). Further, surface and interface thermodynamics can stabilize crystallographic orientation relationships (COR) with unexpected high lattice mismatches between the crystalline oxide overgrowth and the metal substrate (Chapter 4). An amorphous state for ultra-thin oxide films grown on e.g. Al, Ta or Si can be thermodynamically, instead of kinetically, preferred up to a certain critical oxide-film thickness, because of the lower sum of surface and interface energies as compared to the corresponding crystalline modification (Chapter 3). Beyond this critical oxide-film thickness, bulk thermodynamics will strive to stabilize the competing crystalline oxide phase, but the corresponding amorphous-to-crystalline transition can then be kinetically hindered by a relatively large energy barrier for nucleation of crystallization (Chapter 5). An amorphous-to-crystalline transition of the developing oxide film will affect the activation-energy barriers for ion and electron transport in the oxide, and thereby govern the oxide-film growth kinetics as function of the oxidation conditions, e.g. oxidation temperature, partial oxygen pressure and parent metal-substrate orientation (Chapter 6).

Apart from the scientific interest to investigate the, up to date largely unaddressed, effect of the parent metal-substrate orientation on the oxidation process, the achieved fundamental knowledge on the oxide-film growth kinetics and microstructure as function of the growth conditions is, at the same time, of great technological importance. For example, the specific properties of thin oxide films (e.g. electric conductivity, wear and corrosion resistance as well as thermal and mechanic stability), as used in numerous technological application areas such as microelectronics, catalysis and surface coatings, will be determined by their microstructure. In particular, the growth of either an amorphous or a coherent, single-

crystalline oxide film is desired, because of the absence of grain boundaries in both these types of oxide films. Grain boundaries in the grown oxide films may act as paths for fast atom or electron transport, thereby deteriorating material properties such as the electrical resistivity, corrosion resistance or catalytic activity. Thus, to further optimize the chemical and physical properties of the applied oxide films, a fundamental and comprehensive knowledge on the thermodynamics and kinetics of the oxide growth process is required.

To this end, a **model description** has been developed to predict the thermodynamically stable microstructure of a thin oxide film grown on its bare metal substrate as function of the oxidation conditions and the substrate orientation (Chapter 2). In the model calculations, the total energetics (i.e. surface, interface and bulk) of two competing oxide microstructures on identical metal substrates are compared, while accounting for the relaxation of elastic growth strain (due to the initial lattice mismatch between the crystalline oxide overgrowth and its metal substrate) by the introduction of misfit dislocations at the metal/oxide interface. The thermodynamic model can be applied to oxide-overgrowth/metal-substrate systems with low and high initial lattice mismatches and for oxide-film thicknesses from the (sub-) monolayer up to the micrometre range.

The model has been applied to predict whether a thin amorphous oxide film (instead of the competing crystalline modification) can be thermodynamically preferred up to a certain critical thickness for various metal/oxide systems (i.e. of Al, Cu, Ni, Cr, Fe, Mg, Zr, Ti and Si; Chapter 3). It follows that the critical oxide-film thickness, $h_{\{M_xO_y\}}^{\text{critical}}$, up to which an amorphous oxide overgrowth on its metal substrate is thermodynamically preferred, is governed by: (i) the difference in bulk Gibbs energies between the amorphous and competing crystalline oxide phase, (ii) the difference in surface energies between the amorphous and competing crystalline oxide overgrowth (as determined by the COR between the crystalline oxide overgrowth and its metal), (iii) the strength of the metal-oxygen bond for the metal/oxide system under investigation and (iv) the difference in the density of metal-oxygen bonds across the metal/oxide interface between the amorphous and competing crystalline oxide overgrowth (as also determined by the COR between the crystalline oxide overgrowth and its metal). Beyond this critical oxide-film thickness, the competing crystalline oxide overgrowth will be thermodynamically preferred, because the positive bulk Gibbs energy difference between the amorphous and the crystalline oxide overgrowth is no longer overcompensated by the more negative sum of the surface and interfacial energy differences. It follows that amorphous oxide overgrowths on Si are stable up to a thickness in the range of

40 – 80 nm (as dependent on the growth temperature and the substrate orientation). The corresponding critical oxide-film thicknesses are in the range of only several oxide monolayers (ML) on the various low-index crystallographic faces of Al, Ti and Zr, as well as on the less densely packed surfaces of Fe and Cr. For Mg and Ni, the critical oxide-film thickness is less than 1 oxide ML and therefore the initial development of an amorphous oxide phase on these metal substrates is unlikely. Finally, for Cu and densely packed Cr and Fe metal surfaces, oxide overgrowth is predicted to proceed by the direct formation and growth of a crystalline oxide phase (corresponding to a negative critical thickness value; see Fig. 7.1). These results are in qualitative agreement with the scarce number of experimental observations of the initial oxide-film microstructure on metals reported in the literature. Unfortunately, for most metal/oxide-film systems, detailed knowledge on the development of the microstructure of the initial oxide overgrowth on its bare metal (as obtained by e.g. high-resolution electron microscopy) lacks.

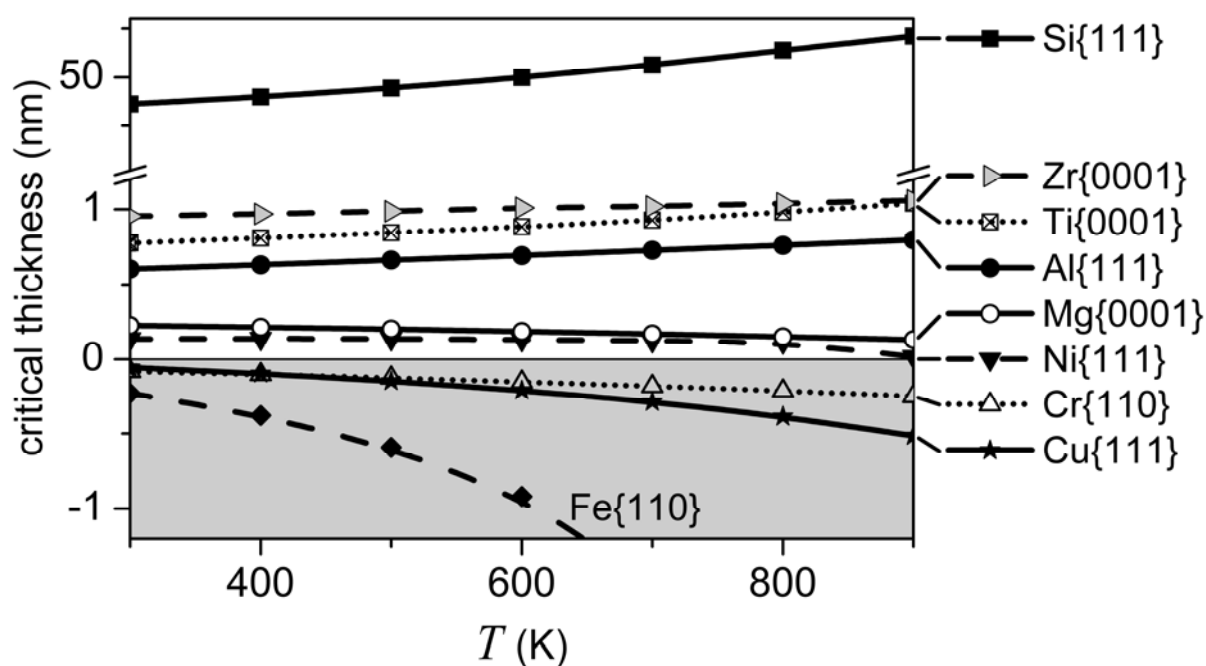


Figure 7.1. Critical thickness up to which an amorphous oxide overgrowth (instead of the corresponding crystalline oxide overgrowth) is thermodynamically preferred on the most densely packed face of a bare metal substrate as function of the growth temperature (T) for various metal/oxide systems.

In Chapter 4, the striking **experimental** observation and thermodynamic explanation of a COR of exceptionally high lattice mismatch between a $\text{Al}\{100\}$ metal substrate metal and its crystalline Al_2O_3 overgrowth is reported, which is in contrast with the general assumption that a COR corresponding with low lattice mismatch is always preferred. To this

end, polished Al single-crystals with $\{111\}$, $\{100\}$ and $\{110\}$ surface orientations were introduced in an ultra-high vacuum (UHV) system for specimen processing and analysis, which consists of three coupled UHV chambers: (i) a UHV chamber for analysis by angle-resolved X-ray photoelectron spectroscopy (XPS), (ii) a UHV chamber for specimen processing (e.g. surface cleaning, annealing and oxidation) and analysis by the low energy electron diffraction (LEED) and real-time in-situ spectroscopic ellipsometry (RISE) and (iii) a UHV chamber for thin film deposition by molecular beam epitaxy (MBE). The introduced Al single-crystals were first cleaned and outgassed by a treatment of sputter cleaning using 1 keV Ar^+ ions and simultaneous annealing at temperatures up to 450°C , while employing sample rotation to avoid sputter-induced roughening of the sample surface. After a final step of in-situ UHV annealing for 15 min at 450°C (without sputter cleaning), the obtained *bare* Al substrates are clean at their surfaces (as verified by AR-XPS) and the crystal order at their surfaces is also fully restored (as verified by LEED). Next, the bare Al substrates have been oxidized by exposure to pure oxygen gas for $t = 6000$ s in the temperature regime of $T = 350 - 650$ K at partial pressure of oxygen of $p_{\text{O}_2} = 1 \times 10^{-4}$ Pa. During the oxidation, the oxide-film growth kinetics has been established by RISE. After the oxidation, the oxide-film microstructure (e.g. thickness, composition, phase constitution, crystallinity, morphology and local chemical state of the ions) were investigated by AR-XPS and LEED. Finally, high-resolution transmission electron microscopic (HR-TEM) analysis was applied to study the microstructure and morphology of the grown oxide films on an atomic scale, as well as to establish the CORs between the crystalline oxides overgrowths and the parent metal substrates. To this end, some of the grown oxide films were sealed prior to their removal from the UHV system (i.e. prior to their exposure to atmospheric conditions) by deposition of an Al capping layer by MBE, after which a cross-sectional TEM lamella was cut from the specimens by a focussed ion beam (FIB).

Pronounced dependencies of the microstructural evolution and the growth kinetics of the oxide films on the parent metal-substrate orientation are established (see what follows). **The oxide films grown on Al $\{111\}$** for $t = 6000$ s and $T \leq 600$ K are overall stoichiometric (i.e. Al_2O_3) and have uniform thicknesses in the range of $L = 0.6 - 0.9$ nm (as determined by AR-XPS, RISE and/or HR-TEM). Furthermore, the corresponding metal/oxide interfaces are atomically flat (as evidenced from the cross-sectional HR-TEM analysis). The oxide films grown on Al $\{111\}$ are amorphous up to $T = 450$ K, whereas at higher temperatures ($T \geq 475$ K) epitaxial crystalline oxide films with a coherent metal/oxide interface develop (as

evidenced by LEED and HR-TEM; see Fig. 7.2 and Chapter 4). The amorphous oxide films on Al{111} are stable upon subsequent in-situ UHV annealing at 700 K. The thicknesses of these thermally stable, low- T amorphous Al₂O₃ films on Al{111} are in good agreement with the corresponding calculated critical thickness of $h_{\{\text{Al}_2\text{O}_3\}}^{\text{critical}} = 0.7 \pm 0.1$ nm up to which an amorphous Al₂O₃ film is thermodynamically preferred on the Al{111} substrate. The transformation of the low- T amorphous oxide films into a crystalline Al₂O₃ phase beyond the critical thickness is possibly kinetically hindered by a relatively large energy barrier for nucleation of crystallization.

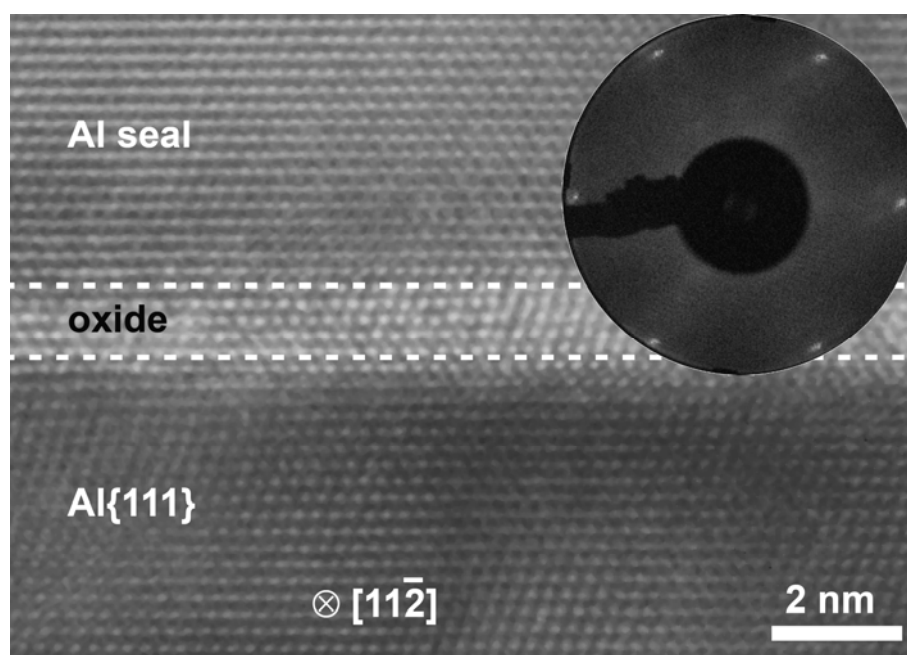


Figure 7.2. High-resolution transmission electron micrograph of the crystalline Al₂O₃ overgrowth on Al{111} after oxidation at $T = 550$ K and $p_{\text{O}_2} = 1 \times 10^{-4}$ Pa for $t = 6000$ s. The direction of the primary electron beam was along the zone axis $[11\bar{2}]$ of the Al{111} substrate, the oxide film and the Al seal. The dashed lines roughly indicate the boundaries between the oxide and the Al{111} substrate and the oxide and the Al seal, respectively. The inset shows the corresponding LEED pattern (as recorded with a primary electron energy of 53 eV) with a six-fold symmetry due to the epitaxial overgrowth of γ -Al₂O₃ on Al{111}.

At more elevated temperatures $T \geq 475$ K, an epitaxial crystalline Al₂O₃ film develops on Al{111} instead, because (i) the critical oxide-film thickness for the amorphous-to-crystalline transition has decreased as a result of a change in oxide growth mode (from layer-by-layer to island-by-layer growth) and/or (ii) oxygen incorporation predominates over on-top oxygen chemisorption for $T \geq 475$ K, thereby reducing the activation-energy barrier for nucleation of crystallization (Chapter 5). The resulting crystalline oxide, designated as γ '-

Al_2O_3 in this thesis, possesses an fcc oxygen sublattice structure with a lattice parameter similar to that of $\gamma\text{-Al}_2\text{O}_3$, but with a random distribution of cations in the interstices of the oxygen sublattice. For the crystalline $\gamma''\text{-Al}_2\text{O}_3$ overgrowth on $\text{Al}\{111\}$, the expected COR of lowest possible mismatch ($\sim 2 - 3\%$) between the $\text{Al}\{111\}$ substrate and the $\gamma''\text{-Al}_2\text{O}_3$ overgrowth is found: $\text{Al}(111)[1\bar{1}0]||\gamma''\text{-Al}_2\text{O}_3(111)[1\bar{1}0]$, with a coherent metal/oxide interface (Chapter 4).

The oxide films grown on $\text{Al}\{100\}$ for $t = 6000$ s and $T \leq 600$ K are also overall stoichiometric (i.e. Al_2O_3) have uniform thicknesses in the range of $L = 0.5 - 0.8$ nm and atomically flat metal/oxide interfaces. The oxide films grown on $\text{Al}\{100\}$ are amorphous up to $T = 400$ K, but are transformed into $\gamma''\text{-Al}_2\text{O}_3$ upon subsequent in-situ UHV annealing beyond an experimentally determined critical thickness of 0.45 ± 0.15 nm, which is somewhat lower than the corresponding calculated critical thickness of $h_{\{\text{Al}_2\text{O}_3\}}^{\text{critical}} = 0.8 \pm 0.1$ nm. At more elevated temperatures $T > 400$ K, a crystalline $\gamma''\text{-Al}_2\text{O}_3$ film with a semi-coherent metal/oxide interface develops beyond a critical thickness of about 0.2 ± 0.1 nm (as determined experimentally at $T = 550$ K). The relatively lower value of the critical oxide-film thickness on $\text{Al}\{100\}$ for $T > 400$ K (as compared to the corresponding critical thickness value for $T \leq 400$ K) is attributed to a change in oxide growth mode from layer-by-layer to island-by-layer growth (Chapter 5). For the crystalline $\gamma''\text{-Al}_2\text{O}_3$ overgrowth on $\text{Al}\{100\}$, an unexpected COR of high lattice mismatch ($> 15\%$) between the $\text{Al}\{100\}$ substrate and the $\gamma''\text{-Al}_2\text{O}_3$ overgrowth is found: $\text{Al}(100)[011]||\gamma''\text{-Al}_2\text{O}_3(111)[01\bar{1}]$, with a semi-coherent metal/oxide interface (see Fig. 7.3 and Chapter 4). The crystalline oxide overgrowth structure consists of two types of $\gamma''\text{-Al}_2\text{O}_3$ domains with their $\{111\}$ plane parallel to the surface, but rotated with respect to each other by 90° around the surface normal. As evidenced by the smearing out in rings of the LEED spots originating from the $\gamma''\text{-Al}_2\text{O}_3$ domains, relaxation of the anisotropic, tensile, elastic growth strain in the oxide overgrowth does not only occur by the formation of defects at the metal/oxide interface (presumably misfit dislocations), but also by slight, in-plane rotations of the $\gamma''\text{-Al}_2\text{O}_3$ domains (of about $\pm 4^\circ$) with respect to the aforementioned high-mismatch COR.

This striking observation of a COR of exceptionally high lattice mismatch between a metal substrate and its oxide overgrowth is in contrast with the general assumption that a COR corresponding with low lattice mismatch is preferred. However, as demonstrated here by thermodynamic model calculations (Chapter 4), the relatively large energy contributions due to residual growth strain and misfit dislocations in such thin overgrowths can be

overcompensated by the relatively low sum of the surface and interface energies. Neglecting the role of the surface energy and/or the interface energy contributions, can therefore lead to wrong theoretical predictions of CORs for ultra-thin overgrowths (Chapter 4).

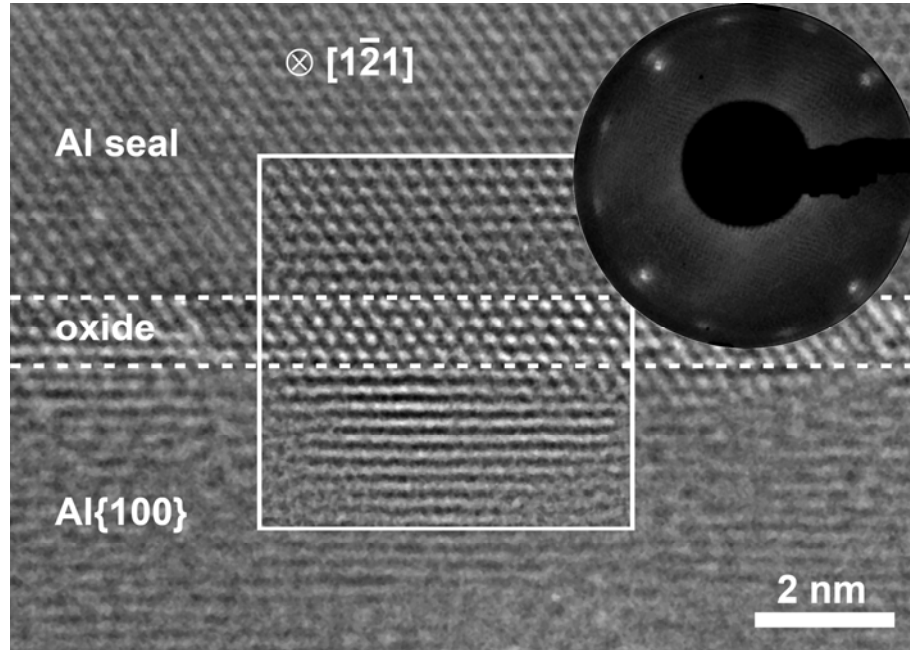


Figure 7.3. High-resolution transmission electron micrograph of the Al_2O_3 overgrowth on $\text{Al}\{100\}$ after oxidation at $T = 550$ K and $p_{\text{O}_2} = 1 \times 10^{-4}$ Pa for $t = 6000$ s. The direction of the primary electron beam was along the zone axis $[1\bar{2}1]$ of the Al capping layer and the oxide film. The area in the square represents a Fourier-filtered region of the original micrograph. The corresponding LEED pattern for $t = 120$ s (as recorded with a primary electron of energy 54 eV) shows the separate diffraction spots originating from the $\text{Al}\{100\}$ substrate (exhibiting a four-fold symmetry) and due to the two-domain structure of the $\gamma''\text{-Al}_2\text{O}_3$ oxide overgrowth (exhibiting a twelve-fold symmetry with spots located in rings).

The oxide films grown on $\text{Al}\{110\}$ for $t = 6000$ s and $T \leq 550$ K are also overall stoichiometric with uniform average thicknesses in the range of $L = 0.6 - 1.2$ nm. The oxide films are amorphous and stable upon subsequent in-situ UHV annealing at 700 K, in accordance with the relatively high value of the calculated critical oxide-film thickness on $\text{Al}\{110\}$ of $h_{\{\text{Al}_2\text{O}_3\}}^{\text{critical}} = 4.0 \pm 0.5$ nm. At more elevated temperatures $T > 550$ K, the oxide-film thickness after $t = 6000$ s increases significantly up to $L = 2.75 \pm 0.3$ nm at $T = 640$ K and then distinct LEED spots appear at the onset of oxidation, which become weaker with increasing oxidation time. As evidenced by the HR-TEM and LEED analysis, the original bare $\text{Al}\{110\}$ surface becomes reconstructed at the onset of oxidation. As demonstrated by thermodynamic model calculations (Chapter 5), the resulting $\{111\}$ - faceted oxidized metal

surface is thermodynamically preferred due to the relatively lower energy of the Al{111}/*am*-Al₂O₃ interface (as compared to the Al{110}/*am*-Al₂O₃ interfacial energy). The oxide film grown on Al{110} after prolonged oxidation at 640 K still appears predominantly amorphous in the HR-TEM analysis, which indicates that the amorphous-to-crystalline transition beyond the critical oxide-film thickness is kinetically hindered (Chapter 5).

The **kinetics of the oxide-film growth** on the bare Al{100} and Al{110} substrates in the temperature range of 350 – 600 K at $p_{\text{O}_2} = 1 \times 10^{-4}$ Pa, as experimentally established by RISE, can be subdivided into a initial, very fast and a subsequent, very slow oxidation stage, which is characterized by the occurrence of a near-limiting thickness that increases with increasing temperature (see Fig. 7.4). For the oxidation of the bare Al{111} substrate up to $T = 450$ K, a distinction between an initial, very fast and a subsequent, very slow oxidation stage cannot be made (see Fig. 7.4a). Instead, the initial oxide-film growth rate on Al{111} decreases only gradually with increasing oxidation time without the attainment of a near-limiting oxide-film thickness and an unexpected decrease of the oxide-film thickness with increasing T after $t = 6000$ s of oxidation is observed for $T \leq 450$ K (i.e. within the amorphous temperature regime). At higher temperatures $T > 450$ K (i.e. within the crystalline temperature regime), the growth kinetics on Al{111} can also (as for Al{100} and Al{110}, see Fig. 7.4 b) be subdivided into an initial, very fast and a subsequent, very slow oxidation stage with a near-limiting thickness that increases with increasing temperature (Chapter 6).

The experimental growth curves for the thermal oxidation of Al single-crystals in the temperature regime of 350 – 600 K can be accurately described by considering the coupled currents of Al³⁺ cations and electrons (by both thermionic emission and quantum mechanical tunnelling) in an uniform surface-charge field and taking the rate-limiting activation energy for cation transport, W , and the work-function difference, $\Delta\chi$, (i.e. the difference between the work-functions at the oxide/oxygen and oxide/metal interface) as fit parameters (see Fig. 7.4). It follows that the oxide-film growth rate is always limited by the diffusion of cations through the developing oxide film under influence of the surface charge field setup by chemisorbed oxygen species at the growing oxide-film surface. Electron transport is co-determining the oxide growth rate only at the onset of oxidation. The kinetic potential due to the surface-charge field is maintained during continued oxide-film growth by the (near-) balance between a very large, forward electron flux by tunnelling and a slightly smaller, reverse electron flux by thermionic emission.

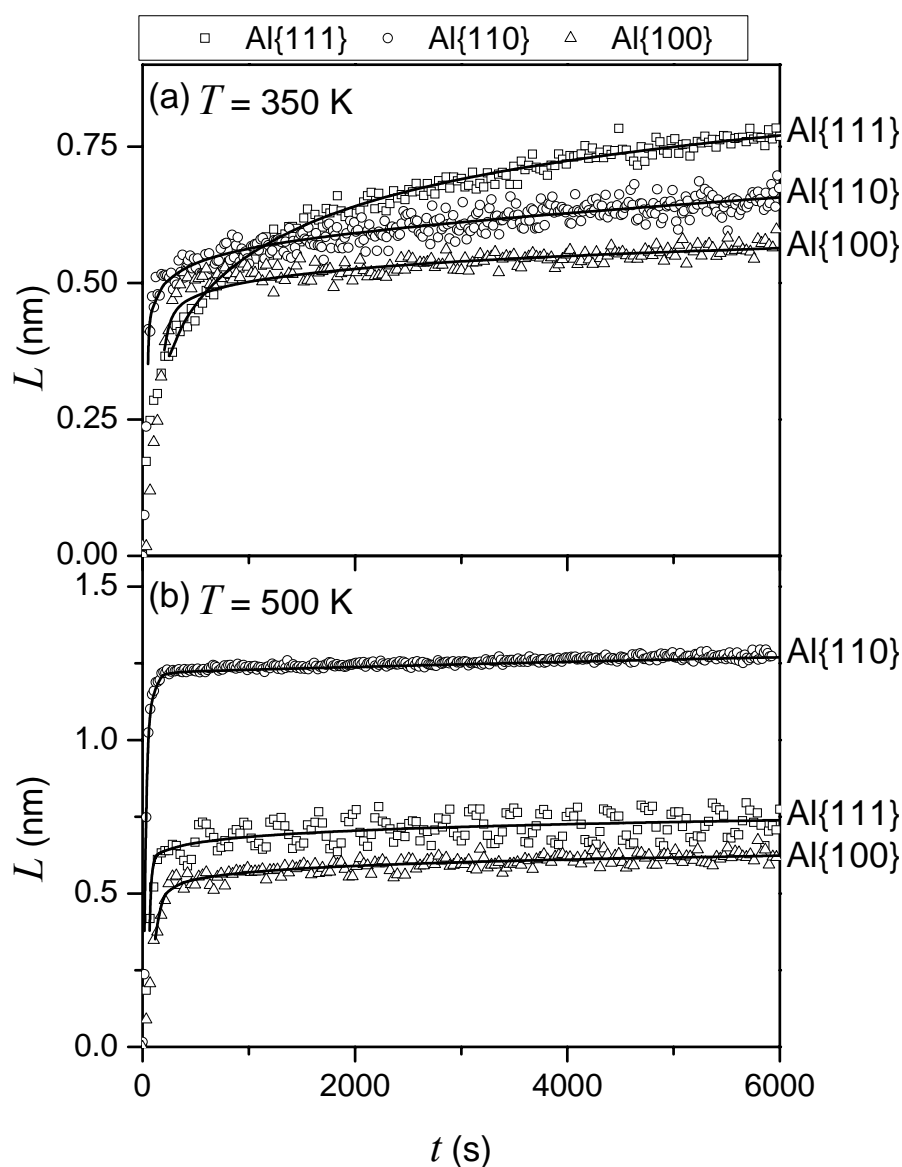


Figure 7.4. Experimental (*open markers*) and model fitted (*lines*) oxide-film growth curves for the oxidation of bare Al{111} (*squares*), Al{100} (*circles*) and Al{110} (*triangles*) substrates at (a) $T = 350$ K and (b) $T = 500$ K (all at $p_{\text{O}_2} = 1 \times 10^{-4}$ Pa). The experimental data has been obtained by RISE. The theoretical growth curves have been calculated on the basis of the coupled currents of cations and electrons (by both tunnelling and thermionic emission) under a surface-charge field.

Due to the gradual transformation of the initial amorphous oxide film on Al{100} into γ -Al₂O₃, the energy barrier for cation transport and the absolute value of the kinetic potential both increase gradually with increasing oxidation temperature in the range of 350 – 600 K for Al{100}, as well as up to 450 K for Al{110}. The relatively large energy barrier for cation transport together with the decrease of the surface-charge field strength with increasing oxide-film thickness leads to the observed initial, very fast and subsequent, very slow oxidation stage and the occurrence of a near-limiting oxide-film thickness that increases with increasing

temperature. On Al{111}, the corresponding amorphous-to-crystalline transition occurs toward higher temperatures $T > 450$ K and is more abrupt (than for Al{100} and Al{110}). Consequently, the value of the energy barrier for cation transport is relatively low within the amorphous temperature regime up to $T = 450$ K, resulting in a more gradual growth mode without the establishment of a near-limiting oxide-film thickness in the amorphous temperature regime (i.e. for $T \leq 450$ K). Around the amorphous-to-crystalline transition temperature for Al{111}, the corresponding values of the energy barrier for cation transport and the kinetic potential abruptly change towards the corresponding values for the crystalline oxide films grown on Al{100} and Al{110} and then the growth behaviour becomes independent of the metal-substrate orientation.

It is concluded that the parent metal-substrate orientation plays a decisive role for the kinetics and thermodynamics of the oxidation process. A comprehensive description of the thermodynamics of ultra-thin oxide overgrowth on bare metal substrates can only be achieved if the role of surface and the interface energy contributions is accounted for. Fundamental understanding of the initial oxide-film growth kinetics on bare metal surfaces, on the other hand, requires detailed knowledge on the microstructural evolution of the developing oxide film as function of the oxidation conditions.

Kapitel 8

Zusammenfassung in deutscher Sprache

Diese Arbeit behandelt den Einfluss der Metallsubstratorientierung auf die Thermodynamik und die Kinetik des Wachstums sehr dünner (< 5 nm) Oxidschichten auf reinen Metallen, während diese bei niedrigen Temperaturen (bis zu 650 K) reinem Sauerstoff ausgesetzt sind. Auf Grund der relativ großen Beiträge der Ober- und Grenzflächenenergien zur Gesamtenergie der entstehenden Metall-Oxidsysteme unterscheidet sich die Mikrostruktur sehr dünner Oxidschichten oft von jener Mikrostruktur, die bei vergleichsweise dicken Oxidschichten thermodynamisch stabil wäre (Kapitel 2, 3 und 4). Daher können sehr dünne, amorphe Oxidschichten, z.B. auf Al, Ta oder Si, bis zu einer gewissen kritischen Schichtdicke thermodynamisch (und nicht nur kinetisch) bevorzugt sein, weil die Summe von Ober- und Grenzflächenenergien im Vergleich zu kristallinen Oxidschichten geringer ist (Kapitel 3). Oberhalb dieser kritischen Schichtdicke sorgt der Volumenenergiebeitrag dafür, dass sich ein kristallines Oxid bildet. Eine kristallographische Orientierungsbeziehung zwischen einer kristallinen Oxidschicht und dem darunterliegenden Metallsubstrat mit ausgesprochen hoher Gitterfehlpassung kann ebenfalls durch Ober- und Grenzflächenthermodynamik stabilisiert werden (Kapitel 4). Die Phasenumwandlung von amorphen zu kristallinen Oxidschichten kann jedoch durch die Kinetik verhindert werden, wenn die nötige Aktivierungsenergie für die Keimbildung der kristallinen Phase thermisch nicht aufgebracht werden kann (Kapitel 5). Bei einer solchen Phasenumwandlung in der wachsenden Oxidschicht ändern sich auch die Aktivierungsenergien, die beim Transport von Ionen und Elektronen durch diese Oxidschicht überwunden werden müssen. Dadurch wird die Oxidationskinetik als Funktion der Oxidationsbedingungen, z.B. Temperatur, Sauerstoffpartialdruck und Substratorientierung, beeinflusst (Kapitel 6).

Neben dem wissenschaftlichen Interesse, den bis heute im Wesentlichen unbekanntem Einfluss der Substratorientierung auf die Oxidation zu untersuchen, sind die erzielten Kenntnisse über die Mikrostruktur und die Wachstumskinetik als Funktion der Oxidationsbedingungen auch von großer technologischer Bedeutung. Die besonderen Eigenschaften der dünnen Oxidschichten (wie geringe elektrische Leitfähigkeit, Korrosions- und Verschleißbeständigkeit, sowie gute thermische und mechanische Belastbarkeit), die für

zahlreiche technische Anwendungen (z.B. im Bereich der Mikroelektronik, der Katalyse oder der Oberflächenbeschichtung) benötigt werden, hängen sehr stark von der Mikrostruktur der Oxide ab. Insbesondere amorphe oder einkristalline, epitaktisch auf ihr Metallsubstrat aufgewachsene Oxidschichten sind erwünscht, da sie keine Korngrenzen aufweisen. Korngrenzen in den gewachsenen Oxidschichten stellen Pfade für den Atom- und Elektronentransport dar und verschlechtern somit Materialeigenschaften, wie den elektrischen Widerstand, die Korrosionsbeständigkeit und die katalytische Aktivität. Um die chemischen und physikalischen Eigenschaften der Oxidschichten zu optimieren, sind daher fundamentelle Kenntnisse der Thermodynamik und der Kinetik des Oxidwachstums auf reinen Metallen erforderlich.

Aus diesen Gründen ist ein **thermodynamisches Model** weiterentwickelt worden, welches die thermodynamisch stabile Mikrostruktur einer Oxidschicht als Funktion der Oxidationsbedingungen und der Substratorientierung voraussagt (Kapitel 2). Hierzu wird die gesamte freie Enthalpie (d.h. von Volumen, Oberfläche und Grenzfläche) von zwei konkurrierenden Oxidmikrostrukturen auf dem dazugehörigen, jeweils identischen Metallsubstrat verglichen. Dabei können elastische Spannungen, die beim Oxidwachstum auf Grund von Gitterfehlpassungen zwischen einem kristallinen Oxid und seinem Metallsubstrat entstehen, durch den Einbau von Gitterversetzungen an der Metall/Oxidgrenzfläche abgebaut werden. So kann das Modell auf Metall-Oxidssysteme mit geringer und hoher Gitterfehlpassung und für Oxidschichten von weniger als einer Monolage bis mehreren Mikrometern Dicke angewendet werden.

Mit Hilfe dieses Modells wird beispielsweise analysiert, ob eine dünne amorphe Oxidschicht gegenüber einer kristallinen Oxidschicht auf verschiedenen Metalloberflächen (d.h. von Al, Cu, Ni, Cr, Fe, Mg, Zr, Ti und Si; Kapitel 3) thermodynamisch bevorzugt sein kann. Außerdem wird ein möglicher Übergang von amorphem zu kristallinem Oxid bei einer kritischen Schichtdicke vorausgesagt. Die kritische Schichtdicke, bis zu welcher das amorphe Oxid thermodynamisch bevorzugt ist, hängt von der Stärke der Metall-Sauerstoffbindungen über die Metal/Oxid-Grenzfläche hinweg ab. Darüberhinaus sind die Unterschiede in der Anzahl dieser Bindungen pro Fläche, der Oberflächenenergie und der freien Bildungsenthalpie jeweils zwischen amorphem und kristallinem Oxid entscheidend. Oberhalb dieser kritischen Schichtdicke wird das kristalline Oxid favorisiert, da der höhere Volumenenergiebeitrag des amorphen Oxids im Vergleich zu kristallinem Oxid nicht mehr durch die geringeren Ober- und Grenzflächenenergien ausgeglichen werden kann. Es ist herausgefunden worden, dass auf Si amorphe Oxidschichten bis zu Schichtdicken von 40 – 80

nm (je nach Temperatur und Substratorientierung) stabil sind (siehe Abb. 8.1). Aber auch die kritischen Schichtdicken auf verschiedenen niedrig indizierten Oberflächen von Al, Ti und Zr, sowie auf relativ offen gepackten Fe- und Cr-Oberflächen entsprechen mehreren Oxidmonolagen. Auf Ni und Mg hingegen sind amorphe Oxidschichten nur im Submonolagenbereich stabil, so dass sie sich wahrscheinlich nicht beobachten lassen. Auf Cu und den dichtgepacktesten Oberflächen von Fe und Cr wird schließlich vorausgesagt, dass direkt eine kristalline Oxidschicht wächst (d.h. die berechnete kritische Schichtdicke ist negativ, siehe Abb. 8.1). Diese Ergebnisse stimmen qualitativ mit Beobachtungen aus der Literatur. Es mangelt aber leider an genauen experimentellen Beobachtungen der Mikrostruktur einer Oxidschicht als Funktion der Schichtdicke (zum Beispiel mit hochauflösender Elektronenmikroskopie), bei denen die Oxidschicht auf einem reinen Metall (d.h. ohne natürliche Oxidschicht) gewachsen ist.

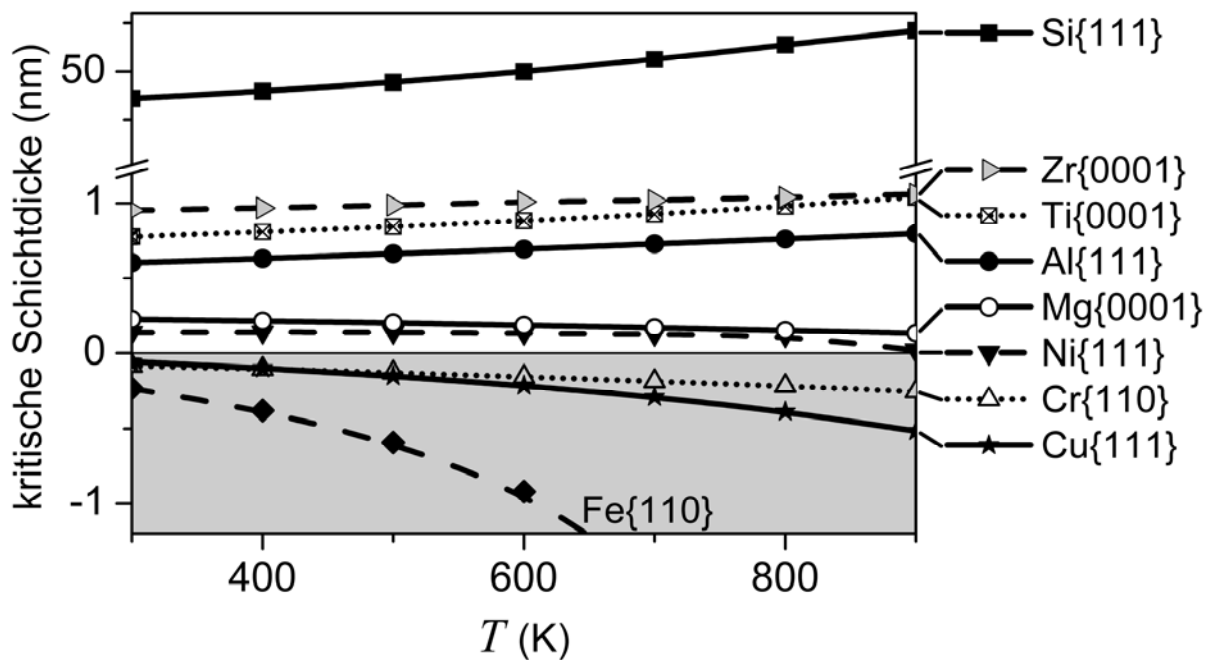


Abbildung 8.1. Kritische Schichtdicke, bis hin zu welcher eine amorphe Oxidschicht (anstelle der jeweiligen kristallinen Oxidschicht) auf den dichtgepacktesten Oberflächen der reinen Metallsubstrate thermodynamisch bevorzugt ist, als Funktion der Wachstumstemperatur (T) für einige Metall/Oxid-Systeme.

Die thermodynamische Erklärung für die außergewöhnliche **experimentelle** Beobachtung einer kristallographischen Orientierungsbeziehung mit sehr hoher Gitterfehlpassung zwischen dem Al{100}-Substrat und seinem kristallinen Oxid wird in Kapitel 4 beschrieben. Diese widerspricht der verbreiteten Annahme, dass die Orientierungsbeziehung mit der geringsten Fehlpassung immer die günstigste ist. Für die

experimentellen Untersuchungen wurden polierte Al-Einkristalle mit $\{111\}$ -, $\{100\}$ - und $\{110\}$ -Oberflächenorientierung in ein Ultrahochvakuum- (UHV-) System gebracht, welches aus drei gekoppelten Kammer besteht: (i) einer Analysenkammer für Röntgen-Photoelektronen-Spektroskopie (XPS), (ii) einer Kammer um Proben zu bearbeiten (z.B. reinigen, ausheizen oder oxidieren), sowie mittels Beugung niederenergetischer Elektronen (LEED) und spektroskopischer in-situ Echtzeitellipsometrie (RISE) zu analysieren und (iii) einer Kammer um dünne Schichten mittels Molekularstrahlepitaxie (MBE) wachsen zu lassen. Die Al-Einkristalle wurden durch Ionenätzen mit Ar^+ -Ionen einer Energie von 1 kV bei Temperaturen bis zu 450°C unter Rotation gereinigt. Dies geschah um die Proben auszugasen und die natürliche Oxidschicht zu entfernen ohne dadurch die Oberflächenrauigkeit zu erhöhen. Die einkristalline Oberfläche wurde im Anschluß durch Auslagern bei 450°C wiederhergestellt. Die so behandelten *reinen* Al-Substrate sind vollständig sauber (was mit XPS kontrolliert wird) und an der Oberfläche vollständig einkristallin (was mit LEED kontrolliert wird). Anschließend wurden die gereinigten Substrate für eine Oxidationszeit von $t = 6000$ s im Temperaturbereich von $T = 350 - 650$ K bei einem Sauerstoffpartialdruck von $p_{\text{O}_2} = 1 \times 10^{-4}$ Pa oxidiert, während die Wachstumskinetik der Oxide mittels RISE aufgenommen wurde. Nach der Oxidation wurden die so gewachsenen Oxidschichten mit Hilfe von winkelabhängiger (AR-) XPS und LEED untersucht. Um hochauflösende transmissionselektronenmikroskopische (HR-TEM) Untersuchungen der Mikrostruktur und der Morphologie der Oxidschichten außerhalb des UHV-Systems durchzuführen wurde das thermisch gewachsene Oxid mit Hilfe einer Al-Schutzschicht vor weiterer Oxidation an der Atmosphäre geschützt. Die Schutzschicht wurde im UHV-System mittels MBE aufgebracht. Aus der so präparierten Probe wurde anschließend für die HR-TEM-Untersuchungen mit Hilfe eines fokussierten Ionenstrahls (FIB) eine TEM-Lamelle geschnitten, die einen Querschnitt der Probe darstellt.

Während der Oxidation von Al-Einkristallen zeigt sich in der entstehenden Mikrostruktur und der Wachstumskinetik der Oxidschichten eine deutliche Abhängigkeit von der Metallsubstratorientierung (siehe folgende Abschnitte). Die **Oxidschichten**, die **auf Al $\{111\}$ -Einkristallen** bei der Oxidation für $t = 6000$ s bis zu einer Temperatur von $T = 600$ K wachsen, sind insgesamt stoichiometrisch (d. h. Al_2O_3) und besitzen gleichmäßige Schichtdicken zwischen $L = 0,6 - 0,9$ nm (wie mittels AR-XPS und HR-TEM herausgefunden wurde). Desweiteren zeigt die Analyse des HR-TEM-Querschnitts, dass die Metall/Oxidgrenzfläche atomar flach ist. Mit Hilfe von LEED und HR-TEM ist beobachtet

worden, dass auf Al{111} bis zu einer Temperatur von $T = 450$ K amorphe Oxidschichten wachsen, während bei höheren Temperaturen ($T \geq 475$ K) epitaktisch kristalline Oxidschichten mit kohärenter Metal/Oxidgrenzfläche entstehen (siehe Abb. 8.2).

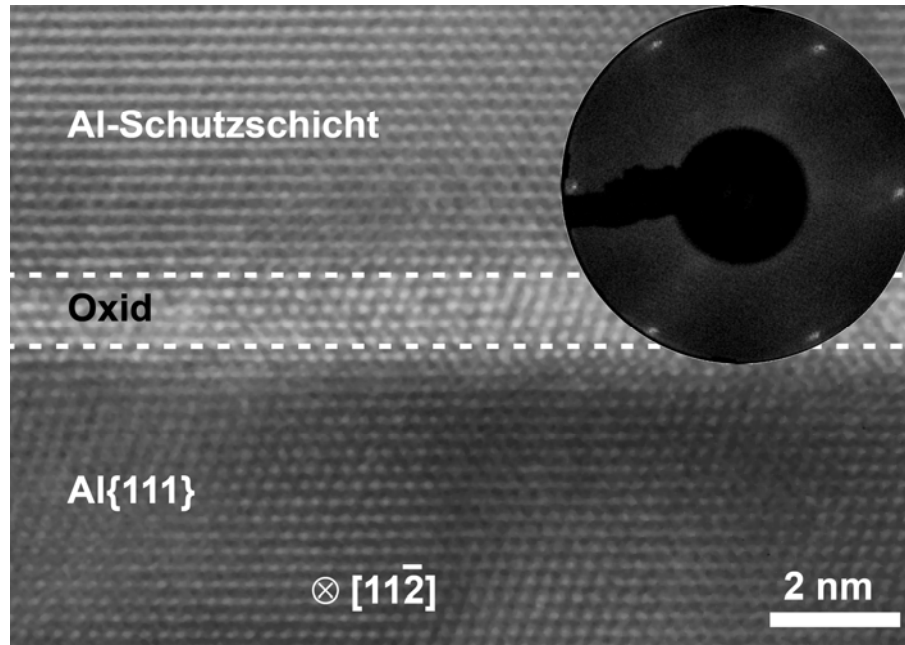


Abbildung 8.2. Hochauflösende transmissionselektronenmikroskopische Aufnahme der kristallinen Al_2O_3 -Schicht auf Al{111} nach der Oxidation für $t = 6000$ s bei $T = 550$ K und $p_{\text{O}_2} = 1 \times 10^{-4}$ Pa. Die eingestrahlenen Elektronen liefen entlang der $[11\bar{2}]$ Zonenachse des Al{111}-Substrats. Die gestrichelten Linien geben grob die Grenzflächen zwischen dem Al{100}-Substrat und dem Oxid bzw. zwischen dem Oxid und der Al-Schutzschicht an. Die eingesetzte Abbildung zeigt das dazugehörige LEED-Beugungsbild, das mit einer Primärelektronenenergie von 53 eV aufgenommen worden ist. Es zeigt sechs Beugungspunkte typisch für epitaktisch auf Al{111} aufgewachsenes Oxid.

Die amorphen Oxidschichten auf Al{111} bleiben während des Auslagerns bei 700 K im UHV amorph. Die Schichtdicke dieser stabilen amorphen Schichten stimmt relativ gut mit der entsprechenden berechneten kritischen Schichtdicke von $h_{\{\text{Al}_2\text{O}_3\}}^{\text{critical}} = (0,7 \pm 0,1)$ nm überein, bis zu welcher die amorphe Schicht thermodynamisch auf Al{111} bevorzugt ist. Die Umwandlung in kristallines Oxid oberhalb der kritischen Schichtdicke könnte kinetisch dadurch verhindert worden sein, dass die Energiebarriere für die Keimbildung der kristallinen Phase zu hoch ist. Bei höheren Temperaturen $T \geq 475$ K wächst stattdessen kristallines Oxid auf Al{111}, weil (i) die kritische Schichtdicke durch eine Änderung des Wachstumsmodus (von schichtweisem Wachstum zu Wachstum, bei dem anfänglich Inseln wachsen, welche anschließend zu Schichten geschlossen werden) gesenkt wird und/oder (ii) der Einbau von

Sauerstoff in die Metalloberfläche gegenüber der Chemisorption von Sauerstoff auf der Oberfläche für $T \geq 475$ K bevorzugt ist, was die Aktivierungsenergie für die Kristallisationskeimbildung verringert (Kapitel 5).

Das auftretende kristalline Oxid, in dieser Arbeit γ'' -Al₂O₃ genannt, enthält ein kubisch-flächenzentriertes Sauerstoffanionengitter mit einer Gitterkonstante ähnlich der von γ -Al₂O₃, aber mit dem Unterschied, dass die Al³⁺ Kationen im Gitter unregelmäßiger verteilt sind. Die kristallographische Orientierungsbeziehung zwischen dem Al{111}-Substrat und der kristallinen γ'' -Al₂O₃-Schicht lautet: Al(111)[1 $\bar{1}$ 0] || γ'' -Al₂O₃(111)[1 $\bar{1}$ 0] und entspricht der erwarteten Orientierungsbeziehung mit geringst möglicher Gitterfehlpassung (~ 2 – 3%) zwischen Al{111} und der γ'' -Al₂O₃-Schicht (Kapitel 4).

Oxidschichten, die durch $t = 6000$ s Oxidation bei $T \leq 600$ K **auf Al{100}-Einkristallen** erzeugt wurden, sind stöchiometrisch, haben eine gleichmäßige Schichtdicke von $L = 0,5 - 0,8$ nm und eine atomar glatte Metall/Oxidgrenzfläche. Sie sind bis zu einer Temperatur von $T = 400$ K amorph, wandeln sich während des Auslagerns bei 700 K im UHV aber in γ'' -Al₂O₃ um, wenn sie die experimentell bestimmte kritische Schichtdicke von $0,45 \pm 0,15$ nm überschreiten. Die experimentell bestimmte kritische Schichtdicke ist somit etwas geringer als die entsprechend Berechnete von $h_{\{\text{Al}_2\text{O}_3\}}^{\text{critical}} = (0,8 \pm 0,1)$ nm. Bei etwas höheren Temperaturen von $T > 400$ K entsteht eine kristalline Oxidschicht mit semi-kohärenter Metall/Oxidgrenzfläche oberhalb einer kritischen Schichtdicke von ungefähr $(0,2 \pm 0,1)$ nm (was experimentell bei $T = 550$ K herausgefunden wurde). Dass die kritische Schichtdicke bei höheren Temperaturen geringer ist als bei niedrigeren, hängt mit der Änderung im Wachstumsmodus vom schichtweisen Wachstum zu Inselwachstum (welches in Schichtwachstum übergeht) zusammen (Kapitel 5). Für die kristallinen Oxidschichten auf Al{100} wird nicht die erwartete Orientierungsbeziehung mit geringer Fehlpassung zwischen dem Metallsubstrat und dem kristallinen Oxid beobachtet, sondern eine Orientierungsbeziehung mit sehr großer Fehlpassung ($> 15\%$): Al(100)[011] || γ'' -Al₂O₃(111)[01 $\bar{1}$] (siehe Abb. 8.3 und Kapitel 4). Mittels thermodynamischer Berechnungen kann festgestellt werden, dass die experimentell beobachtete Orientierungsbeziehung hoher Fehlpassung gegenüber der vorher erwarteten Beziehung mit niedriger Fehlpassung zwischen Al{100} und seiner kristallinen Oxidschicht thermodynamisch begünstigt ist. Entscheidend sind dabei die höhere Anzahl von Metall-Sauerstoffbindungen über die Metall/Oxidgrenzfläche hinweg und die geringere Oberflächenenergie bei der Orientierungsbeziehung hoher Fehlpassung im Vergleich zu

derjenigen niedriger Fehlpassung. Durch diese werden die höheren Fehlpassungsenergiebeiträge mehr als aufgewogen. Wenn Ober- und Grenzflächenenergien vernachlässigt werden, kann dies zu falschen theoretischen Voraussagen der Orientierungsbeziehungen zwischen einem Metall und einer dünnen Oxidschicht führen (Kapitel 4).

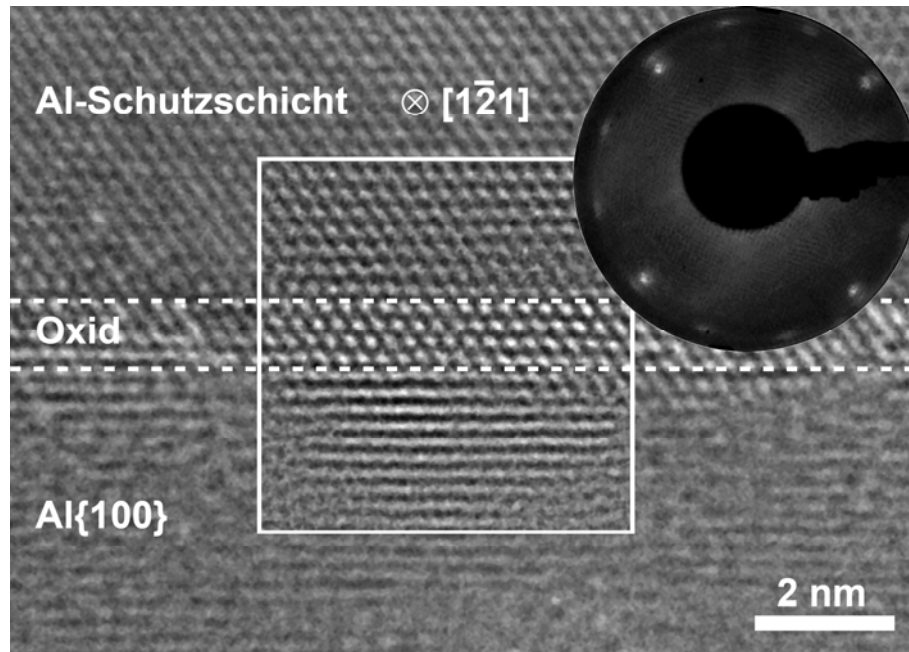


Abbildung 8.3. Hochauflösende transmissionselektronenmikroskopische Aufnahme der Oxidschicht auf Al{100} nach der Oxidation für $t = 6000$ s bei $T = 550$ K und $p_{\text{O}_2} = 1 \times 10^{-4}$ Pa. Die Richtung der eingestrahlenen Elektronen entspricht der $[1\bar{2}1]$ Zonenachse der Al-Schutzschicht und des Oxids. Das Quadrat in der Mitte der Abbildung kennzeichnet einen Fourier-gefilterten Bereich der Originalaufnahme. Die oben rechts eingesetzte Abbildung zeigt das dazugehörige LEED-Beugungsbild, das (mit einer Primärelektronenenergie von 54 eV) von dem Al{100}-Substrat nach $t = 120$ s Oxidation aufgenommen worden ist. Es zeigt vier Beugungspunkte des Al{100}-Substrats und zwölf Beugungspunkte, die durch zwei Gruppen von γ'' -Al₂O₃-Domänen mit {111}-Oberfläche verursacht werden.

Die **Oxidschichten auf Al{110}-Einkristallen**, die durch $t = 6000$ s Oxidation bei $T \leq 550$ K erzeugt wurden, sind auch stochiometrisch und besitzen eine gleichmäßige Schichtdicke von $L = 0,6 - 1,2$ nm. Die Oxidschichten sind sowohl nach der Oxidation als auch nach dem Auslagern bei 700 K im UHV amorph in Übereinstimmung mit der berechneten kritischen Schichtdicke von $h_{\{\text{Al}_2\text{O}_3\}}^{\text{critical}} = (4,0 \pm 0,5)$ nm. Bei höheren Temperaturen von $T > 550$ K steigt die erreichte Oxidschichtdicke nach $t = 6000$ s erheblich bis auf $L = (2,75 \pm 0,3)$ nm bei $T = 640$ K an. Außerdem erscheinen LEED-Reflexe im Beugungsbild, die

mit zunehmender Oxidationszeit schwächer werden. Bei der Analyse der LEED und HR-TEM Ergebnisse stellt sich heraus, dass die Al{110}-Oberfläche zu Beginn der Oxidation facettiert. Die sich ergebenden {111}-Facetten an der Oberfläche sind, wie thermodynamischen Berechnungen zeigen, gegenüber der glatten oxidierten Al{110} bevorzugt, da die Al{111}/am-Al₂O₃-Grenzfläche eine geringere Grenzflächenenergie als die Al{110}/am-Al₂O₃-Grenzfläche aufweist. Die Oxidschicht auf dem facettierten Substrat erscheint in der HR-TEM-Aufnahme auch bei einer Oxidationstemperatur von $T = 640$ K überwiegend amorph, was darauf hinweist, dass die Umwandlung von amorphem zu kristallinem Oxid oberhalb der kritischen Schichtdicke kinetisch verhindert ist (Kapitel 5).

Die **Kinetik des Oxidschichtwachstums**, die experimentell mit RISE aufgenommen worden ist, zeigt, dass die Al{100}- und Al{110}-Substrate im Temperaturbereich $T = 350 - 600$ K bei $p_{\text{O}_2} = 1 \times 10^{-4}$ Pa anfänglich sehr schnell oxidieren, bevor das Oxidwachstum anschließend fast vollständig zum Erliegen kommt und eine nahezu limitierende (d. h. kaum noch ansteigende) Oxidschichtdicke erreicht wird (siehe Abb. 8.4). Diese nahezu limitierende Oxidschichtdicke steigt mit zunehmender Oxidationstemperatur an. Im Gegensatz zu den offeneren Al{100}- und Al{110}-Oberflächen wächst die Oxidschicht auf der dichtgepacktesten Al{111}-Oberfläche bei $T \leq 450$ K im Anfangstadium langsamer. Anschließend nimmt die Oxidationsrate aber nur allmählich ab, so dass auch nach Oxidation von $t = 6000$ s keine (nahezu) konstante Oxidschichtdicke erreicht wird (siehe Abb. 8.4). Außerdem nimmt die Oxidschichtdicke auf Al{111} im amorphen Temperaturbereich ($T = 350 - 450$ K) unerwartet mit steigender Temperatur ab. Bei höheren Temperaturen von $T \geq 475$ K (im kristallinen Temperaturbereich) findet man auf Al{111}-Substraten Oxidwachstum, das analog zu den anderen Substraten in zwei Wachstumsbereiche von anfänglich sehr schnellem und anschließend sehr langsamem Oxidwachstum unterverteilt werden kann. Dabei entsteht eine Oxidschicht mit nahezu limitierender Oxidschichtdicke, die mit zunehmender Temperatur ansteigt (Kapitel 6).

Die experimentell gefundenen Wachstumskurven für die thermische Oxidation von Al-Einkristallen im Temperaturbereich von $T = 350 - 600$ K können sehr gut durch das sogenannte Modell gekoppelter Ströme modelliert werden (siehe Abb. 8.4), wenn der Transport von Al³⁺-Kationen und Elektronen (über quantenmechanisches Tunneln und thermionische Emission) unter Einfluss eines gleichmäßigen Oberflächenladungsfeldes betrachtet wird. Dabei werden die Aktivierungsenergiebarriere für den Kationentransport, \mathcal{W} , sowie die Differenz zwischen den Austrittsarbeiten an der Oxid/Sauerstoffgrenzfläche und der

Metall/Oxidgrenzfläche, $\Delta\chi$, als Fitparameter verwendet. Aus den Modellberechnungen resultiert, dass der Kationentransport durch die Oxidschicht unter Einfluss des Oberflächenladungsfeldes, das durch die an der Oberfläche chemisorbierten Sauerstoffteilchen entsteht, für das Oxidwachstum geschwindigkeitslimitierend ist. Währenddessen ist der Elektronentransport nur in den Anfangsstadien der Oxidation mitbestimmend. Da der sehr starke Vorwärtsfluss von Elektronen per Tunnelmechanismus durch den nur wenig schwächeren entgegengesetzten Elektronenfluss per thermionische Emission fast aufgehoben wird, wird ein konstantes kinetisches Potential des elektrischen Feldes während des Oxidwachstums aufrecht erhalten.

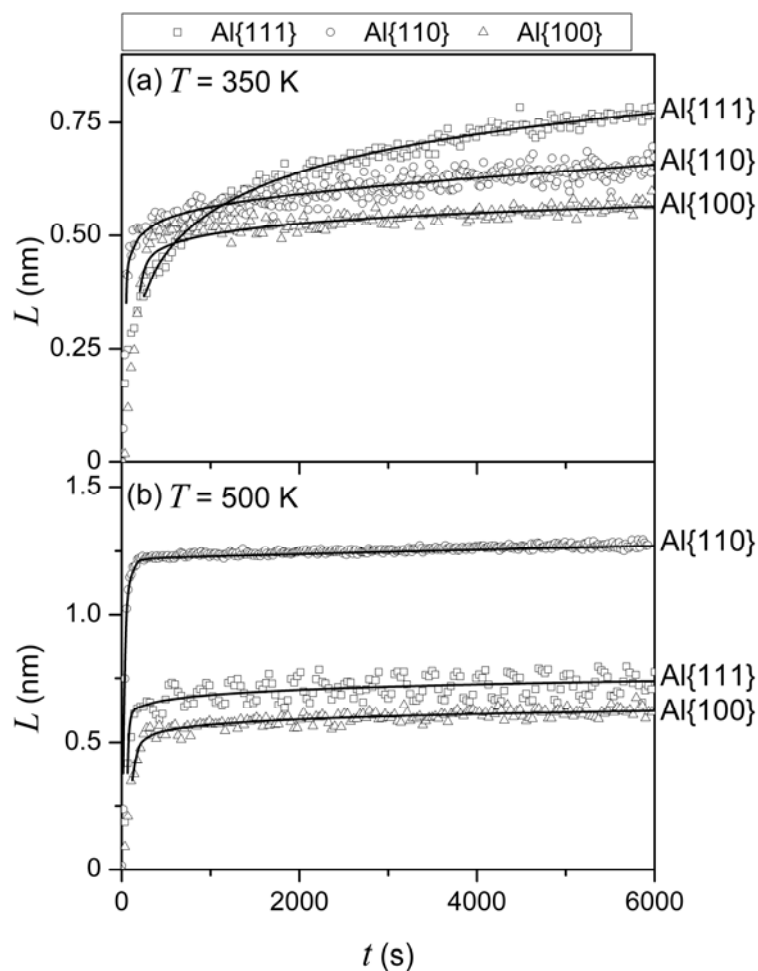


Abbildung 8.4. Experimentell beobachtete (*offene Symbole*) und modellberechnete (*Linien*) Wachstumskurven der Oxidschichten, die bei der Oxidation von $\text{Al}\{111\}$ - (*Quadrate*), $\text{Al}\{100\}$ - (*Kreise*) und $\text{Al}\{110\}$ -Substraten (*Dreiecke*) für $t = 6000\text{ s}$ bei (a) $T = 350\text{ K}$ bzw. (b) $T = 500\text{ K}$ (alle bei $p_{\text{O}_2} = 1 \times 10^{-4}\text{ Pa}$) erzeugt wurden. Die experimentellen Kurven sind mit RISE aufgenommen worden. Die theoretischen Kurven sind mit Hilfe des Modells - auf Grundlage gekoppelter Ströme von Kationen und Elektronen unter Einfluss eines Oberflächenladungsfeldes - berechnet.

Durch die fortlaufende Umwandlung von amorphem zu kristallinem Oxid auf Al{100} steigen die Aktivierungsenergiebarriere für den Kationentransport sowie das kinetische Potential des Oberflächenladungsfeldes (d.h. der Betrag der Differenz zwischen den Austrittsarbeiten an der Oxid/Sauerstoffgrenzfläche und der Metall/Oxidgrenzfläche) mit steigender Temperatur auf Al{100}-Substraten im Temperaturbereich von $T = 350 - 600$ K (sowie auf Al{110}-Substraten bis zu $T = 450$ K) kontinuierlich an. Die relativ hohe Barriere des Kationentransports führt zusammen mit dem Abschwächen des kinetischen Potentials mit zunehmender Oxidschichtdicke zu der beobachteten starken Abnahme der Oxidationsgeschwindigkeit (nach dem anfänglich sehr schnellen Wachstum) und der nahezu limitierenden Oxidschichtdicke. Auf Al{111} findet der entsprechende Übergang von amorph zu kristallin erst bei höheren Temperaturen $T \geq 450$ K statt und ist abrupter als auf Al{100} und Al{110}. Daraus folgt, dass die Energiebarriere für den Kationentransport im amorphen Temperaturbereich bis zu $T = 450$ K relativ niedrig ist und deshalb bei kontinuierlichem Wachstum auch nach $t = 6000$ s Oxidation keine limitierende Schichtdicke erreicht wird. Bei der Umwandlungstemperatur von amorph nach kristallin verändern sich die Werte der Energiebarriere für den Kationentransport und das kinetische Potential schlagartig zu denjenigen Werten, die für die Oxidschichten auf Al{100} beobachtet werden. Erst dann ist das Oxidwachstum nahezu unabhängig von der Metallsubstratorientierung.

Zusammenfassend spielt der Einfluss der Substratorientierung eine entscheidende Rolle für die Kinetik und die Thermodynamik des Oxidationsablaufes. Eine umfassende Beschreibung der Thermodynamik sehr dünner Oxidschichten auf reinen Metalloberflächen kann nur dann gelingen, wenn die Energiebeiträge von Ober- und Metall/Oxidgrenzflächen berücksichtigt werden. Grundlegendes Verständnis der Oxidwachstumskinetik verlangt außerdem, dass die mikrostrukturelle Entwicklung in der wachsenden Oxidschicht als Funktion der Oxidationsbedingungen einschließlich der Metallsubstratorientierung vollständig bekannt ist.

Symbols and abbreviations

Symbols

a	lattice parameter / spacing	C_{ijkl}	stiffness tensor
\bar{a}	residual lattice spacing	C	Tougaard background constant
\tilde{a}^0	unstrained lattice parameter at T_0	χ	ratio of surface areas of crystalline and amorphous oxide cells
A	molar area	χ_0	metal/oxide work-function
A_O	molar area per oxygen ion	χ_L	oxide/oxygen work-function
A^{Cauchy}	Cauchy parameter	d	dislocation distance
α	thermal expansion coefficient	D	Tougaard background constant
α	XPS detection angle (with respect to surface normal)	Δ	ellipsometric parameter
\bar{b}	Burgers vector	e	elementary charge
B	parameter in SIO	E	energy
B^{Cauchy}	Cauchy parameter	E_g	band gap
B	Tougaard background constant	E^{lattice}	lattice energy
β	parameter in SIO	E_k	strength of surface-charge field
β'	parameter in Ball approach	$\bar{\epsilon}_{ij}$	residual strain tensor (and its contributions)
$\beta_{\text{Al } 2p}$	anisotropy of Al 2p photoionization cross-section	ϵ_r	relative dielectric constant
$\beta_{\text{O } 1s}$	anisotropy of O 1s photoionization cross-section	η	tolerance limit in XPS quantification
c	(reference) lattice parameter / spacing	f	mismatch
C^{defect}	defect concentration	f^{EMA}	EMA-fraction
C	molar density	G	Gibbs energy
C^{sub}	molar density in the substrate	ΔG^f	Gibbs energy of formation
C^{ovl}	molar density in the oxide overlayer	γ	(surface or interface) energy per unit area
C^{Cauchy}	Cauchy parameter	$\gamma_{M\text{-amb}}$	surface energy of M in contact with the ambient per unit area

$\gamma_{M\text{-vac}}$	surface energy of M in contact with the vacuum per unit area	λ	wavelength
$\gamma_{M\text{-}M_xO_y}$	metal/oxide interface energy per unit area (and its contributions denoted by superscript indices)	λ^{eff}	effective attenuation length
$(\gamma \cdot \sigma)$	product of oxygen polarizability and oxygen surface concentration	$\lambda_{M,\text{met}}^{\text{sub}}$	λ^{eff} of substrate photoelectrons traversing in the substrate
h	thickness of oxide cell in thermodynamic model	$\lambda_{M,\text{met}}^{\text{ovl}}$	λ^{eff} of substrate photoelectrons traversing in the oxide overlayer
h^{critical}	critical oxide-film thickness	$\lambda_{M,\text{ox}}^{\text{ovl}}$	λ^{eff} of photoelectrons originating from oxidic M ions and traversing in the oxide
h	Planck's quantum	$\lambda_{O,\text{ox}}^{\text{ovl}}$	λ^{eff} of photoelectrons originating from oxidic O ions and traversing in the oxide
H	enthalpy	m	mass
ΔH^{f}	enthalpy of formation	m_e	electron mass
H^{fuse}	enthalpy of fusion	m_e^*	effective electron mass
$\Delta H_{O\text{ in } \langle M \rangle}^{\infty}$	enthalpy of mixing at infinite dilution of 1 mol O in a metal	M	metal
I	(PLZ) intensity	M_xO_y	oxide
J_{ion}	ion flux	μ	interfacial shear modulus
J_e^{therm}	electron flux by thermionic emission	μ'	modified interfacial shear modulus for Ball approach
J_e^{tun}	electron flux by tunnelling	μ^{el}	shear modulus
k_B	Boltzmann's constant	n	refractive index
k	extinction coefficient	N_A	Avogadro constant
K	XPS instrumental factor	N_{M-O}^{NN}	molar number of broken, near-neighbouring metal-oxygen bonds per unit surface area
l	length of oxide cell in thermodynamic model	ν^{el}	Poisson ratio
L	oxide-film thickness	ν	frequency
L^{int}	thickness of the interface oxide	$\nu_{\text{Al}^{3+}}$	Al cation jump frequency
L^{lim}	(near-) limiting thickness	ν_e	electron jump frequency
L^{ox}	thickness of the stoichiometric oxide film	p	geometric fraction describing shape of Wigner-Seitz cell
λ^{av}	average elastic modulus		

p_{O_2}	partial pressure of oxygen	∂V	oxide volume per cation
P	dislocation vernier period	V_{d}	diffusion potential
P_{BP}	intrinsic bulk plasmon probability	V_{k}	kinetic potential
ψ	angle between incident X-rays and detected photoelectrons	V_{M}	Mott potential
Ψ	ellipsometric parameter	W_0	amplitude of interfacial potential
q	strain field radius (EXTR)	$W(\alpha, \psi)$	AR-XPS asymmetry factor of the photoionization cross- section
R	dislocation field cut-off radius (VOLT)	W	energy barrier for cation transport
ρ	density	x	atom fraction
s	sticking coefficient	X_n	n^{th} subshell of core-level shell X
S	entropy	y	atom fraction
$\bar{\sigma}_{ij}$	stress tensor (and its contributions)	z	depth (below a surface)
σ	photoionization cross-section	z^{eff}	effective depth
t	oxidation time	Z	charge in units of e
T	oxidation temperature	ζ	parameter in APPR
T_0	standard temperature (298 K)	{ }	amorphous state
T^{m}	melting temperature	⟨ ⟩	crystalline state
V	molar volume		

Abbreviations

<i>am</i>	amorphous
APPR	first approximation (approach)
AR-XPS	angle-resolved X-ray photoelectron spectroscopy
BE	binding energy
COR	crystallographic orientation relationship
EAL	effective attenuation length
EMA	effective medium approach
EXTR	extrapolation (approach)
FIB	focussed ion beam
FWHM	full width at half maximum
HR-TEM	high-resolution transmission electron microscopy
KE	kinetic energy
LDD	large dislocation distance (approach)
LEED	low energy electron diffraction
LLS	linear least squares
MBE	molecular beam epitaxy
ML	monolayer
n.a.	not available
PZL	primary zero loss
RHEED	reflection high energy electron diffraction
RISE	real-time in-situ spectroscopic ellipsometry
SIO	semi-infinite overgrowth (approach)
UHV	ultra-high vacuum
UPS	ultraviolet photoelectron spectroscopy
VOLT	Volterra (approach)

List of publications

1. F. Reichel, L. P. H. Jeurgens and E. J. Mittemeijer, *Modeling compositional changes in binary solid solutions under ion bombardment: Application to the Ar⁺ bombardment of MgAl alloys*, Phys. Rev. B **73** (2006) 024103.
2. F. Reichel, L. P. H. Jeurgens and E. J. Mittemeijer, *Thermodynamic model of oxide overgrowth on bare metals: Relaxation of growth strain by plastic deformation*, Phys. Rev. B **74** (2006) 144103 (Chapter 2 of this thesis).
3. F. Reichel, L. P. H. Jeurgens, G. Richter, P. A. van Aken and E. J. Mittemeijer, *The origin of high mismatch orientation relationships for ultra-thin oxide overgrowths*, Acta Mater. **55** (2007) 6027 (Chapter 4 of this thesis).
4. F. Reichel, L. P. H. Jeurgens and E. J. Mittemeijer, *Thermodynamic modeling of the initial microstructural evolution of oxide films grown on bare copper*, Thin Solid Films (2007) in press.
5. F. Reichel, L. P. H. Jeurgens and E. J. Mittemeijer, *The role of the initial oxide-film microstructure on the passivation behaviour of metal surfaces*, Surf. Interface Anal. (2007) in press.
6. L. P. H. Jeurgens, F. Reichel, S. Frank, G. Richter and E. J. Mittemeijer, *On the development of long-range order in ultra-thin amorphous Al₂O₃ films upon their transformation into crystalline γ -Al₂O₃*, Surf. Interface Anal. (2007) in press.
7. F. Reichel, L. P. H. Jeurgens and E. J. Mittemeijer, *Model predictions on the thermodynamic stability of amorphous oxide overgrowths on metals*, (2007) in press (Chapter 3 of this thesis).
8. F. Reichel, L. P. H. Jeurgens, G. Richter and E. J. Mittemeijer, *The amorphous-to-crystalline transition for oxide overgrowths on Al substrates*, (2007) submitted (Chapter 5 of this thesis).
9. F. Reichel, L. P. H. Jeurgens and E. J. Mittemeijer, *The effect of substrate orientation on the kinetics of ultra-thin oxide-film growth on Al single-crystals*, (2007) submitted (Chapter 6 of this thesis).

Danksagung

Die vorliegende Arbeit wurde am Institut für Metallkunde der Universität Stuttgart und am Max-Planck-Institut für Metallforschung, Stuttgart, angefertigt. An dieser Stelle möchte ich all denen danken, die zum Gelingen dieser Arbeit beigetragen haben.

An erster Stelle möchte ich mich bei Herrn Prof. Dr. Ir. E. J. Mittemeijer, meinem Doktorvater, für die Aufnahme in seine Abteilung, die Überlassung des interessanten Themas und das in mich gesetzte Vertrauen bedanken. Sein außergewöhnliches Engagement und die regelmäßigen Diskussionen waren von sehr großer Bedeutung für den Erfolg dieser Arbeit.

Herrn Prof. Dr. Dr. hc. M. Rühle danke ich für die freundliche Übernahme des Mitberichts, sowie Herrn Prof. Dr. F. Aldinger für die Zusage den Prüfungsvorsitz zu übernehmen.

Mein besonderer Dank geht an meinen täglichen Betreuer Dr. Lars P. H. Jeurgens für die stete Unterstützung und unermüdliche Diskussionsbereitschaft. Seine wertvollen Ratschläge waren für die erfolgreiche Durchführung und das Abschließen dieser Arbeit unerlässlich.

Herzlich danken möchte ich auch allen Mitarbeitern des Max-Planck-Instituts für Metallforschung, insbesondere den Kollegen der Abteilung Mittemeijer, für die Unterstützung und die angenehme Arbeitsatmosphäre. Namentlich möchte ich mich bei Michaela Wieland und Bernd Siegle für die experimentelle Unterstützung bedanken und bei Dr. Gunther Richter für die Durchführung der HR-TEM Untersuchungen.

Nicht zuletzt bedanke ich mich bei meinen Eltern und Geschwistern, sowie bei Sven, für die persönliche Unterstützung.

Curriculum Vitae

Persönliche Daten

Name Friederike Reichel
geboren am 04.01.1980 in Aachen
Staatsangehörigkeit deutsch

Schulbildung

1986–1989 Grundschule, Erlenschule Witten
1989–1990 Grundschule Baltmannsweiler
1990–1999 Theodor-Heuss-Gymnasium, Esslingen a.N.
mit dem Abschluss: Allgemeine Hochschulreife

Studium

1999–2004 Studium im Diplomstudiengang Werkstoffwissenschaft an der
Universität Stuttgart
mit dem Abschluss: Diplom Ingenieurin
2004 Diplomarbeit am Institut für Metallkunde der Universität Stuttgart mit
dem Thema „Der Effekt der Substratoberflächenkondition auf die
Anfangsstadien der thermischen Oxidation von MgAl-Legierungen“
Hauptberichter: Prof. Dr. Ir. E. J. Mittemeijer

Promotion

2004-2007 Max-Planck-Institut für Metallforschung, Stuttgart
und Institut für Metallkunde der Universität Stuttgart
Thema: „The effect of substrate orientation on the kinetics and
thermodynamics of initial oxide-film growth on metals“
Hauptberichter: Prof. Dr. Ir. E. J. Mittemeijer